The Environmental Optimisation of the Iron Ore Sintering Process

Swansea University
Prifysgol Abertawe

Matthew Rhys Wilcox

COLLEGE OF ENGINEERING

SWANSEA UNIVERSITY

This thesis is submitted in partial fulfilment of the requirements of the degree of Doctor of Engineering

March 2023

I. ABSTRACT

Iron ore sintering is an established thermal agglomeration process where fine iron ores are fused together to produce a coarser product which is a suitable burden material for blast furnaces. Due to the scale of blast furnace demands, a typical steelworks sinter plant can produce thousands of tonnes of sinter every day which in turn results in the formation of significant quantities of dusts. The majority of these dusts will be captured and reused in the process due to their iron content. However, dusts released to atmosphere can create environmental concerns and they can also be problematic to the sintering process itself. This thesis considers two major aspects related to the optimisation of environmental emissions from blast furnace sinter production; namely sinter dusts and the addition of recycled steelmaking material by-products (reverts) back into the sintering process.

Firstly, considering sinter dusts, these are removed from the exhaust stream using processes including electrostatic precipitators (ESPs). But the dusts must be removed from ESP plates to maintain dust removal efficiency. The dusts consist of sinter sub-components and metal chlorides. Although an established method for removing chlorides from the dusts, following an industrial scale trial carried out by Tata Steel UK, in this thesis, experiments have been carried out to optimise the water washing process of sinter plant waste dust. This involved varying parameters such as washing time, agitation speed and liquid to solid ratios. Initial tests confirmed that > 95 % of soluble chlorides within the dusts can be mobilised by water washing with only one wash under standard operating conditions. Experiments were then carried out to assess whether the washing solution could be effectively recycled to wash more dusts. Results showed that the washing solution could still mobilise chloride from the dust for up to ten cycles, although there was decline in effectiveness at later cycles. One issue noted during these experiments was the hydrophobicity of ESP dust, making it harder to work with during washing and even allowing some dust to apparently remain dry after washing. To combat this, more dust washing experiments were then carried out which featured the inclusion of surfactants, the aim being for the surfactants to mitigate the hydrophobic effects. Three surfactants were tested, each of varying properties, and all showed positive impacts to the processing of the dust, TX-100 being the most effective. More detailed analysis of the surfactants outside of a dust washing setting was also undertaken and confirmed that TX-100 was more effective at tackling the dusts hydrophobicity.

Upon completion of dust washing experiments, tests were undertaken using a pilot-scale sinter pot to better establish the impacts of sintering before and after washing the dusts. These results showed impacts on sinter strength and dust production when including both dust types, although utilising the washed dust appeared to result in higher dust emissions. Furthermore, both dusts were then micro-pelletised and sintered alongside sinter blends with the same dust content, to establish if reducing the fines content in the sinter blend could allow their use at higher rates. These showed that pelletising the dusts greatly improved the sinter bed permeability, aided sinter strength and reduced dust emissions.

Overall, this thesis considers the environmental optimisation of raw material sintering for steel manufacturing, focusing on the remediation and recycling of input materials. Investigating how these processes can be improved and identifying any impacts on process quality, product quality and dust emissions.

II. DECLARATIONS

1. **This work has not previously been accepted in substance for any degree and is not being concurrently submitted in candidature for any degree.**

Signed.....[redacted].....

Date.....**31/03/23**.....

2. **This thesis is the result of my own investigations, except where otherwise stated. Other sources are acknowledged by footnotes giving explicit references. A bibliography is appended.**

Signed.....[redacted].....

Date.....**31/03/23**.....

3. **I hereby give consent for my thesis, if accepted, to be available for photocopying and for inter-library loan, and for the title and summary to be made available to outside organisations.**

Signed.....[redacted].....

Date.....**31/03/23**.....

4. **The University's ethical procedures have been followed and, where appropriate, that ethical approval has been granted.**

Signed.....[redacted].....

Date.....**31/03/23**.....

III ACKNOWLEDGEMENTS

Firstly, I would like to acknowledge my academic supervisor Professor Peter Holliman for his unwavering support and guidance, ability to answer any question I could think of and his seemingly endless supply of cat memes to brighten almost every email he sent.

I'd like to thank my industrial supervisors, Dr David Anderson and Jamie Barrett, for always being on hand to provide support and guidance. Furthermore, I thank Dr Kevyn Bevan, Dr Christopher Melvin and Ryan Davies of Tata Steel UK for their time and support throughout my project.

I'm grateful to the hard-working staff of the Materials and Manufacturing Academy of Swansea University for supporting my project. The CEMEG research group who were always on hand to offer help and support, particularly Dr Eurig Jones who offered up his experience and much of his time to help me throughout my project.

I acknowledge that this research project was made possible through funding from the European Social Fund and the Welsh European Funding Office via the Welsh Government, Swansea University EPSRC impact acceleration account, and Tata Steel UK.

My parents, Mary and Tony, for supporting me throughout my whole life as I would never have made it to this point without you.

Finally, I'd like to thank my partner Hannah for being there every step of the way throughout my project whilst offering support, never ending patience and love.

CONTENTS

LIST OF FIGURES

LIST OF TABLES

1. INTRODUCTION

1.1 Background

The steel making industry forms a significant part of the global economy with more than 1,950 Mt of steel produced globally in 2021 alone, an increase of 3.8 % on 2020 (1). Sintering of iron ore is a crucial pre-blast furnace preparation stage within integrated steel works all over the world, the process allows fine and lower grade ores to be utilised in blast furnace hot metal production, a schematic representation is shown in Figure 1.1.

After granulation the sinter mixture is charged to the sinter strand, this is a moving metal grate that carries the sinter mixture under the ignition hood. The ignition hood is located at the start of the sinter strand and typically emits temperatures in the range of 1300 – 1480 °C, this heats the top of the sinter bed. Below the sinter strand are wind boxes which draw the flame front through the sinter bed using flow rates between 333,000 – 1,600,000 Nm^3/hr, depending on plant size. Modern sinter plants utilise layers of sinter material approximately 400 – 600 mm in depth. Below this is a 30 – 50 mm layer of recycled sinter which has two functions. Firstly, it stops the raw sinter mix from falling through the strand grate and, secondly, it also protects the grate from the intense heat. As the sinter bed moves down the strand the flame front travels through the bed, whilst the high temperatures fuse the raw sinter mix to form the finished sinter product. At the point where the sinter bed reaches the end of the strand the entire mixture will have been sintered. It then falls into a mechanical breaker where it is crushed to a desired size. Once cooled the sinter is then ready to be charged to the blast furnace (2).

Port Talbot has been home to ironmaking for centuries, dating back to at least 1253 when monks of Margam Abbey began a small foundry working pig iron (3). Today Tata Steel UK operate one of the largest integrated steelworks in Europe from Port Talbot and produce approximately 5 MT of steel every year. The site is a key part of the regional economy and directly employs around 4,000 people whilst indirectly supporting thousands of other local jobs. The two blast furnaces on the site operate with the majority of their ferrous burden arising from the sites sinter plant. Maintaining reliable productions rates and sinter quality is therefore key to the site's overall operation.

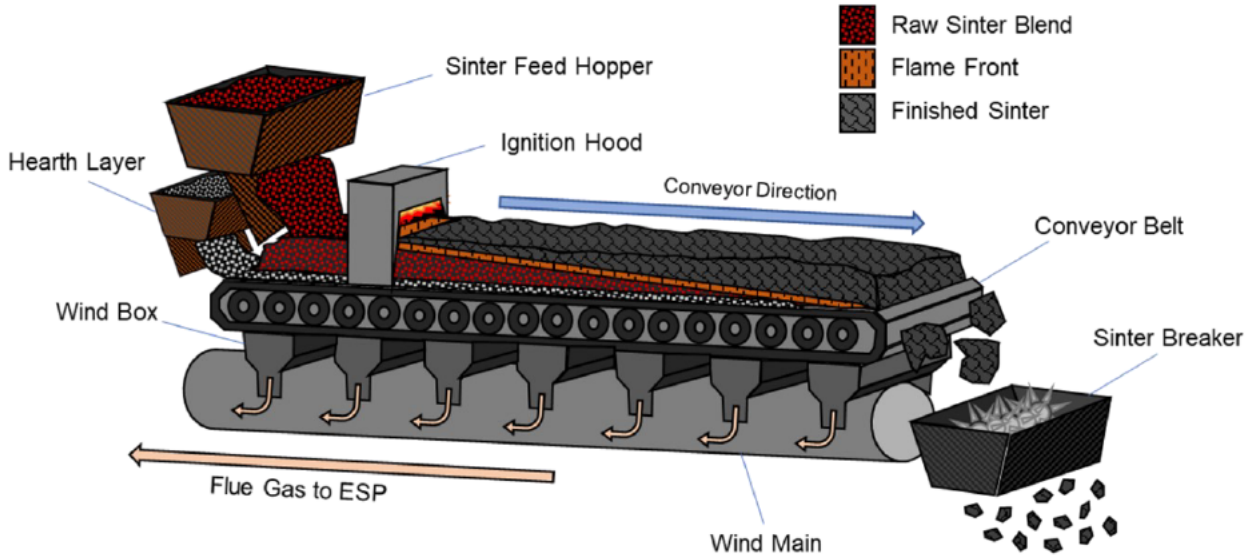

Figure 1.1 Schematic diagram of a typical iron ore sinter plant.

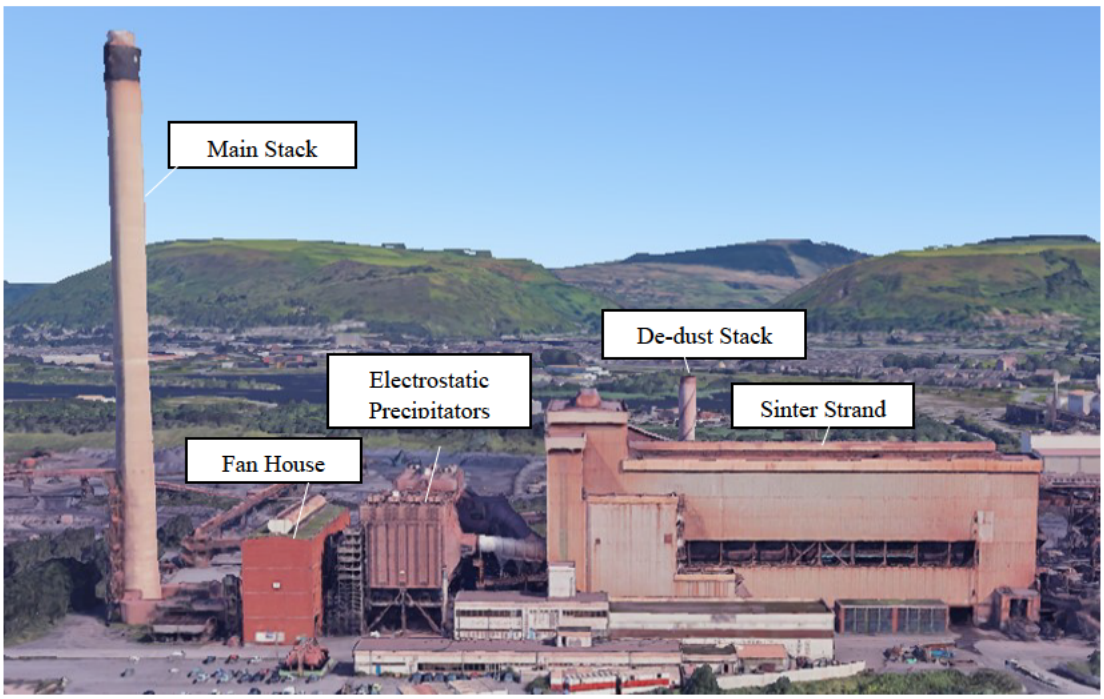

Figure 1.2 Composite image of Tata Steel UK's Port Talbot sinter plant with key parts labelled.

1.2 Environmental Issues Associated with Sintering

The sintering process has previously been ranked as the second worst industrial emitter of pollutants, only behind the combustion of municipal solid waste (4). As previously mentioned, global steel production is still increasing year on year, at the same time national and international emission reduction targets puts significant pressure on plants, such as Tata Steel UK's Port Talbot site, to make their steelmaking process more environmentally friendly.

The sintering process has been shown to release the most dusts of any stage of the steelmaking process, with previous work indicating it accounts for approximately 45 % of all steelmaking dust emissions. Some of the other common pollutants associated with iron ore sintering include emissions of carbon dioxide, dioxins, polychlorinated biphenyls (PCB), polycyclic aromatic hydrocarbon (PAH), acidic gases and alkali metals (5). These pollutants have long been associated with environmental and human health issues.

Dioxins accumulate in the environment before entering the body through the food-chain, they have been linked with certain cancers. Research has shown lifetime average daily doses and associated cancer risk were higher in sinter plant workers and people living in close proximity to sinter plants when compared to residents living away from sinter plants (6). Steelworks have previously been shown to be significant sources of dioxin-like PCBs (7). The "Belgian dioxin crisis" relates to a 1999 event where animal feed contaminated with dioxins and PCBs entered the food chain. It is estimated that this event may eventually lead to between 44 and 8,316 excess cancer deaths, sub-optimal neurological function in children, thyroid hormone fluctuation, T cell population variation in the bloodstream and vitamin K deficiency in new-borns (8).

Studies have shown that dust emissions are also harmful to health, particles ≤ 2.5 microns in diameter ($PM_{2.5}$) can enter the pulmonary alveoli and has the ability to penetrate blood vessels into the bloodstream whilst particles ≤ 10 microns in diameter (PM_{10}) have been shown to enter the respiratory system. $PM_{2.5}$ has been linked with premature death, cardiovascular issues, lung diseases and cancer (9). They also negatively impact the local environment and community.

There is now a range of established abatement techniques which reduce emissions of varying origins and composition. These include electrostatic precipitators, bag filters, wet scrubbing and injection of compounds such as urea. Sinter plant dusts which are arrested

from waste gas streams using electrostatic precipitators (ESP dust) are commonly recycled into the sintering process, however the significant chloride content of ESP dust and its ultra-fine size can result in operational issues. Some plants water wash their ESP dust to lower the chloride content and micro-pelletisation of fine materials has previously been carried out to counter these issues, these processes will be outlined in more detail in section 2.1.

1.3 Research Questions

1. Can existing methods of water washing sinter plant dusts be optimised, reducing energy and resource consumption whilst maintaining an effective washing process?
2. What are the impacts on the sintering process when including high concentrations of both washed and unwashed sinter plant dusts?
3. Does the micro-pelletisation of fine ores and reverts enable higher concentrations to be utilised whilst avoiding detrimental process, product and environmental impacts?

1.4 Thesis Structure

Chapter 2 – Comprehensive literature review focusing on sinter plant ESP dusts, previous research into the washing of ESP dust, sintering experiments utilising by-product materials and the impact of micro-pelletising fine materials on the sintering process.

Chapter 3 – Details all experimental methods and techniques used in this project.

Chapter 4 – investigations into the water washing of ESP dust. Assessing whether washing solutions can be recycled to reduce freshwater consumption, the addition of surfactants to the process and impact of varying key parameters of washing effectiveness.

Chapter 5 – Detailed study on the impact of surfactants at varying concentrations on the wettability of ESP dust, focusing on water contact angle measurements.

Chapter 6 – Sinter pot research which investigates the impacts of adding high concentrations of both washed and unwashed ESP dust to sinter blends and testing of an initial micro-pellet material.

Chapter 7 – Further sinter pot testing of ESP dusts at higher concentrations and the equivalent concentrations in micro-pellet form, a different by-product was also tested in the same fashion.

Chapter 8 – Conclusions and recommendations for future work.

2. LITERATURE REVIEW

2.1 Sinter Plant Dusts

Approximately 4kg of metal dusts ranging from 0.46 – 46.1 µm in size are produced for every 1T of steel created during integrated steel making. These dusts typically consist of K, Na, Ca, Mg, Zn, Pb, Fe, O and C (10). In 2015 global crude steel output was 1,621 MT and has risen every year since reaching 1,951 MT in 2021 (1), an increase of ~ 20 %. This means that in 2021 there were roughly 7.8 MT of waste dusts produced as a by-product of steelmaking. As 70 – 850 g of dust are produced for every T of sinter (11), it is one of the most significant sources of dust pollution in the steelmaking process. Dust emissions can be classified as $PM_{2.5}$ if they have an aerodynamic diameter of < 2.5 µm or PM_{10} if the aerodynamic diameter lies between 2.5 – 10 µm (9,12). Figure 2.1 shows examples of sinter plant ESP dust particle size distribution from two studies showing 2 sets of peaks with one being ~ 1 µm and the other ~ 100 µm, which as previously mentioned can be detrimental to human health.

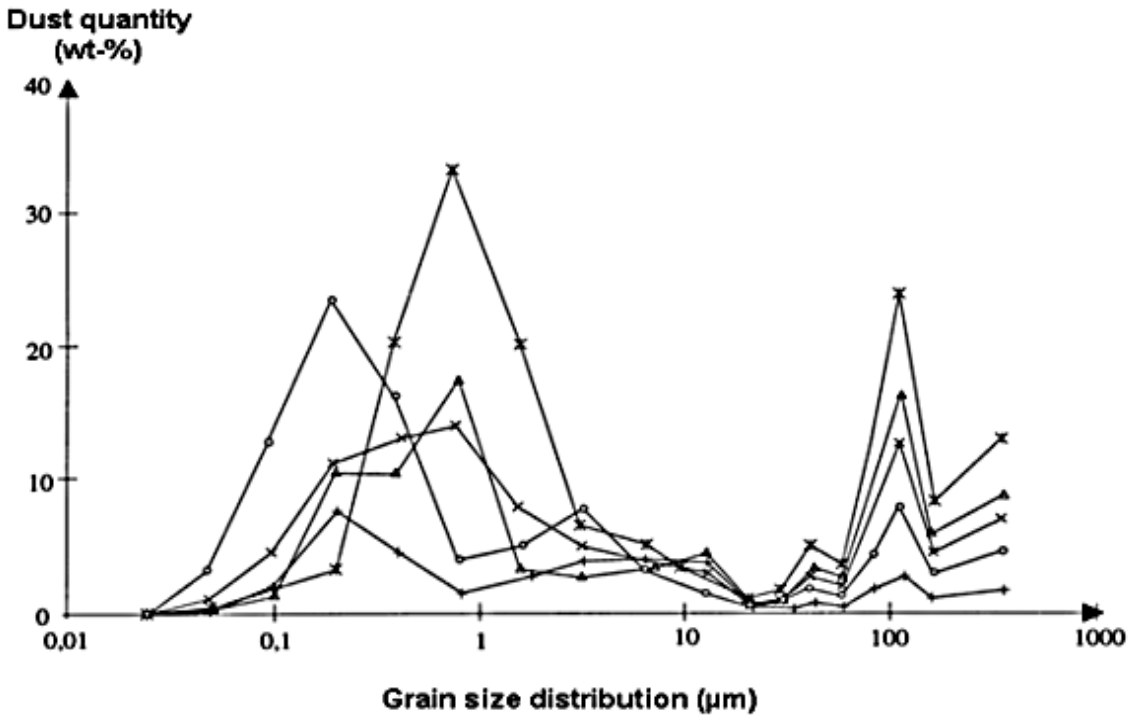

Figure 2.1 Grain size and weight distribution of sinter dusts from various sinter plants (2).

Sinter plant dust has been found to host by far the most chlorides when compared to other sinter blend materials such as fuels, reverts, fluxes and iron ores (13). The presence of chlorides in the sintering process gives rise to several undesirable consequences. These include contributing to the formation of pollutants such as PCDD/Fs and WHO-12 PCBs (13), blast furnace complications (14) & lowering ESP efficiency resulting in higher dust emissions (11). Chloride exists predominantly in the form of KCl however various other chlorides such as NaCl, PbCl and RbCl have also been recorded in sinter plant ESP dusts (15).

2.1.1 Electrostatic Precipitators

Electrostatic precipitators (ESP) are a common abatement method used to ensure sinter dust is not released into the atmosphere, due to their simple design and high efficiency rates (16). Dust collected by ESPs is referred to as ESP dust.

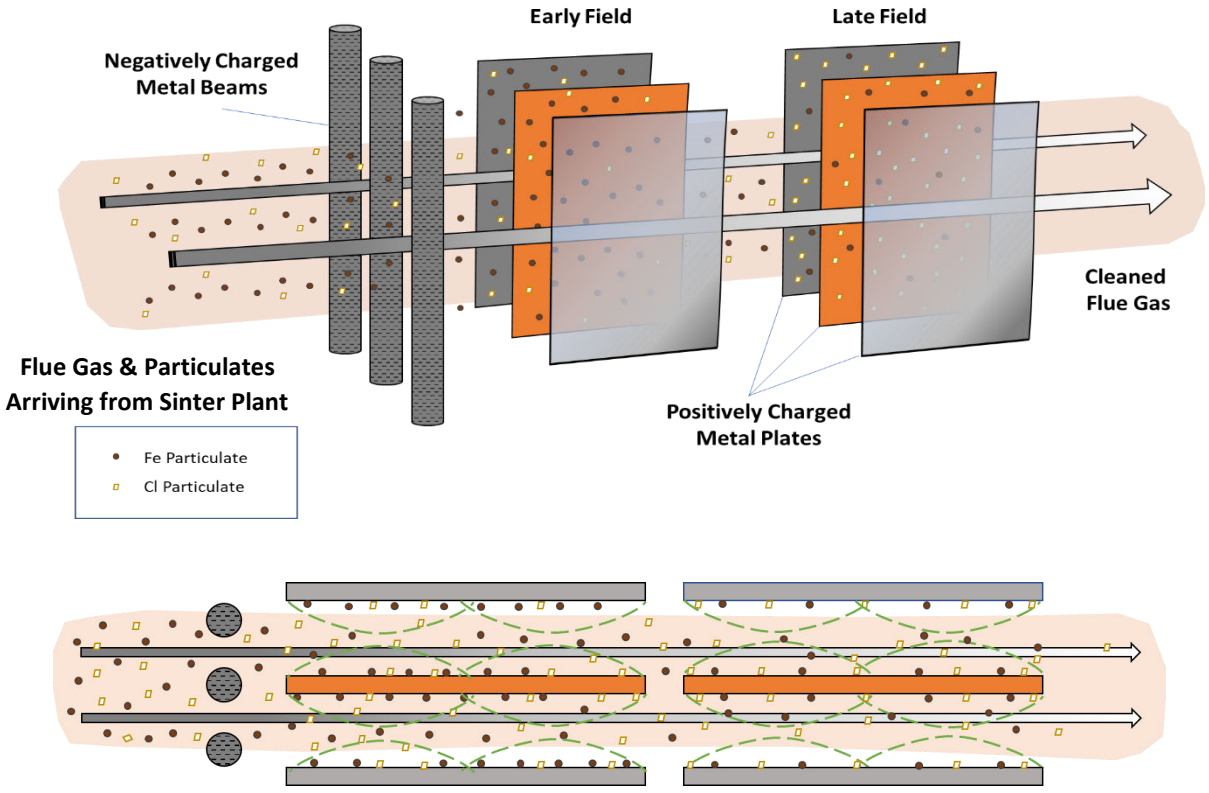

Figure 2.2 Schematic diagram of an electrostatic precipitator system. 2.2b. Aerial schematic of electrostatic precipitator highlighting pulsed corona discharge and particle capture. Source: Author, adapted from Vehlow 2015 (16).

Electrostatic precipitators use an electric field to collect dust from waste gas streams. This is done as these revert dusts often contain high levels elements such as Fe (approx. 22 wt.% (10)) making them valuable secondary materials and to minimise emissions to the environment. An electrical field is generated with a voltage of approximately 50 to 100 kV (17) so that a negative charge originates from central metal wires and a positive charge emanates from the surrounding collector plates. As the dust-laden gases pass through the ESP system, they are ionised and pick up either a positive or negative charge. Negatively charged ions move towards the collector plates and may collide with dust particles. This imparts the negative charge to the dust particle, which is then drawn to the collecting plates, shown in figure 2.2. The plates are periodically agitated or "rapped" so the dust build up falls into hoppers (17). Although removal rates for 10 μm sized particles exceeds 99.5 %, this can be improved by employing wet ESP systems, this requires cleaning the plates with water rather than rapping (2). However, ESP dust also usually contains high levels of chlorides and other undesirable constituents (Pb, Ni, Zn etc) (2). The coarse dusts can be collected by ESPs at a high efficiency; however, the finer chloride rich dusts can create an insulating layer over the ESP plates due to their high resistivity (10^{12} and 10^{13} Ω cm) (2) and ESPs have been shown to struggle with capture of 0.1 – 1.0 μm dust particles (12). Over time this chloride build-up can lead to significant reductions in ESP efficiencies. Effective treatment of these dusts can remove chlorides producing a much more Fe rich material which can be reused in the sintering process with less environmental and engineering issues.

Chlorides are often seen as the main negative component associated with ESP dusts. It has been reported that these form during the sintering process due to the presence of silico-aluminates in the iron ore (feldspar, mica etc) which then react in the reducing atmosphere and high temperatures (potassium has a melting point of 774 °C; the sinter process reaches temperatures >1200 °C) (10). Alkali metals exist predominantly in the form of NaCl and KCl, these vaporise during the sintering process to release chlorides (18), this makes the formation of chlorides during the sintering process hard to avoid completely but it can be mitigated.

Previous studies have shown that the composition of ESP dust varies significantly between ESP fields. (19,20). Cl concentrations tend to increase in later electrostatic fields and conversely Fe content decreases, as seen in Figure 2.3. This has led to suggestions that late field ESP dust should not be recycled into the raw sinter feed without prior remediation. For example, flue gas hosting KCl may contribute to corrosion of equipment if water condenses in the system (19).

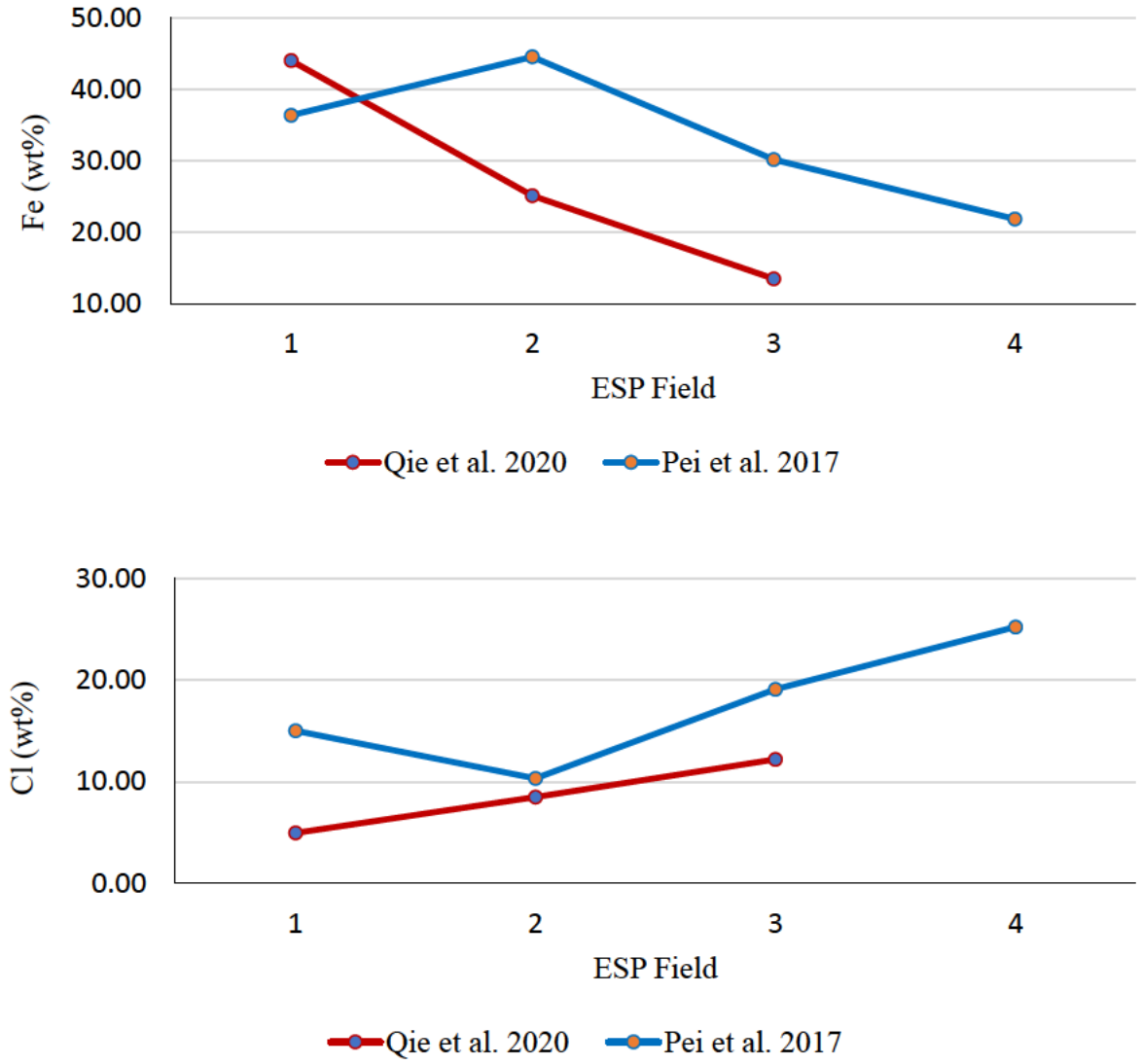

Figure 2.3 Graphs shows variation in iron content (top) and chloride content of ESP dust through ESP fields (19,20).

2.1.2 ESP Dust Chloride & Heavy Metal Leaching

Sintering dusts are often recycled in the steel industry due to their high Fe and C content. However, this complex and variable material also hosts various hazardous components such as Cl, Pb, Zn, K and Na. Reusing the dust without further processing can lead to impact on blast furnace performance (12), contribute to pollutant formation during sintering, such as dioxins or PCBs (22,23), and reduce ESP efficiency leading to higher dust emissions.

Although the presence of chlorides in iron ore sintering is often inevitable, as it is often present at low concentrations in iron ores, steps can be taken to reduce the overall chloride content of the blend. Previous work has reported various methods that have been shown to reduce chloride levels once the dust is captured (acid leaching, water washing etc) (24). Many integrated steelworks will reuse ESP dust without making any attempt to purge chlorides etc which not only increases negative environmental emission rates but as previously described, has also been shown to reduce electrostatic precipitator efficiency leading to higher dust emissions (16). The chloride content is also dependant on the stage of the sintering process. Dust emitted from the sinter strand itself host no or very low levels of chlorides and other pollutants whereas the finer dust produced during sintering is much more problematic (10).

Water washing of sinter plant ESP dust is an established technique to remove undesirable chlorides from the dust (10,14,24). As iron ore sinter plants can produce > 20 T of ESP dust each day this requires substantial amounts of water to effectively treat the dusts using current methods (liquid: solid ratios vary from 2:1 to 10:1 (10,24–26), this also results in large amounts of effluent water which must be dealt with. Water washing sintering dusts also presents the opportunity to extract undesirable heavy metals such as Pb, Cd, Zn.

Previous work often uses complicated and expensive methods to extract KCl from ESP dust. Peng, Zhang and Guo (2009) used a jacketed PMMA reactor with 4 baffles using counter-current leaching to remove KCl, sodium sulphide was added to the leachate solution to remove heavy metals (10). Zhan and Guo (2013) used a simpler method of adding approx. 5 g of ESP dust to 100 mL of deionised water in a conical flask before stirring for 10 minutes. This process was repeated another 4 times meaning 500 mL of deionised water was used to wash 5 g of dust over the course of approximately 1 hour (24). Factors such as stirring speed and water temperature were found to impact leaching rates

A pilot plant was set up in Poland with the aim of washing sintering dusts through a multistage process, shown in Figure 2.4, involving the “thickening” of the washing solution (27). Initially heavy metals (Pb, Zn, Cd & Tl) are precipitated with the addition of sodium hydroxide followed by sodium sulphide. Once heavy metals are lowered to trace levels the main solid components still in the solution are mostly Na, K, Cl and S which amount to ~ 10 % total dissolved solids.

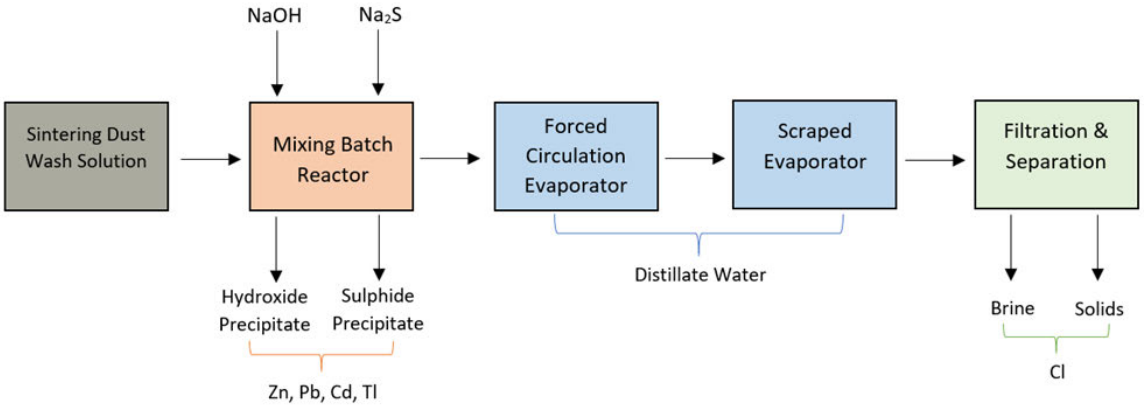

Figure 2.4 Flow diagram of leaching process for chloride removal from ESP dust (24)

Heavy metals leaching rates were > 98 %. This small-scale pilot study demonstrated the potential for sintering dust washing solution treatment at a capacity of 1 m^3/day or 1,000 L/day. Some of the key considerations identified relating to the washing of sintering dust were precise control of sulphide concentration to prevent H_2S release, S_2- ion concentration controls the amount of Na_2S added and treatment volumes of 100 kg/h to 100,000 kg/h may be achieved (27). The final solids produced were ~ 92 % NaCl with the remainder comprised of K, S, and trace elements.

The steel industry has also moved towards tackling this issue on industrial scales, demonstrating the level of interest and potential for water washing sinter plant ESP dust. A potassium chloride plant with a capacity of 10,000 t/year of sintering dust was built in Tangshan, China (24) and Tata Steel UK undertook an industrial-scale by-product washing trial in 2018 (28). During the Tata Steel UK trial key objectives included evaluating the recycling of washing solutions, equipment, material flows, system performance, logistics, water consumption, effluent quality and chloride leaching rate. The trial utilised a single leaching stage in an agitated tank followed by dewatering using a hydro-cyclone, followed by a centrifuge to remove additional solids. 33.3 T of ESP dust were utilised in total.

The compositional variability of ESP dust was clear during this trial, the maximum chloride level measured in ESP dust prior to washing was ~ 22,000 ppm compared to the minimum of ~ 3,000 ppm. However, the trials had the desired effect with dust chloride levels regularly dropping by > 90 % after washing and promising results were also seen when recycling the washing water to wash more dust (28). These trials and industrial set ups show that the process can be operated at large scales using existing processes although further work could be done to improve and optimise the process.

2.1.3 Hydrophobicity of ESP Dust

Hydrophobicity is a property of materials that do not mix with water, originating from Latin meaning "fear of water" (29). It has been established that sinter plant ESP dust displays hydrophobic characteristics when in contact with water, the dust migrates and behaves almost perfectly non-wetting (14,30,31). It is thought that the hydrophobicity of the ESP dust is related to the surface chemical composition, rather than physical structures as seen in other materials such as coal or melting slag or the particle itself (30). Whilst the dust particle itself is hydrophilic, these hydrophilic surface groups attract the hydrophobic *n*-alkyl chains/aromatic groups resulting in a hydrophobic shell. If a water droplet is rolled in ESP dust it will form a "liquid marble", this is when fluid is encapsulated by a powder due to high contact angles and lateral capillary forces (32). The contact angle of ESP dust was previously observed as 96.4 °, dropping to 93.2 ° after 105 s (30). A contact angle of > 90 ° is classified as highly hydrophobic.

Surfactants have been used previously to tackle hydrophobicity in industrial practices. Water spray suppression of coal dust is a common technique used in the coal mining industry (33). This is done to avoid hazards such as explosions and coal workers' pneumoconiosis (CWP), CWP cases still increase year on year in developed countries such as the USA and China making it a significant issue in the industry (34). Surfactants have been added to the spray to reduce water surface tension and the coal dusts hydrophobicity, making the suppression more effective (35). Brij 35 has been used to improve washing of non-aqueous phase liquid (NAPL) contaminated soils with a minimal environmental impact by using bio-degradable and low toxicity surfactants (36). In another study soils contaminated with Pb from mining operations have been successfully treated using environmentally friendly soap

nut saponin, up to 48 % of Pb was removed after one wash which rose to 80 % after a further 2 cycles (37). The ability to use environmentally friendly surfactants rather than chemical reagents would make disposal of washing waters easier.

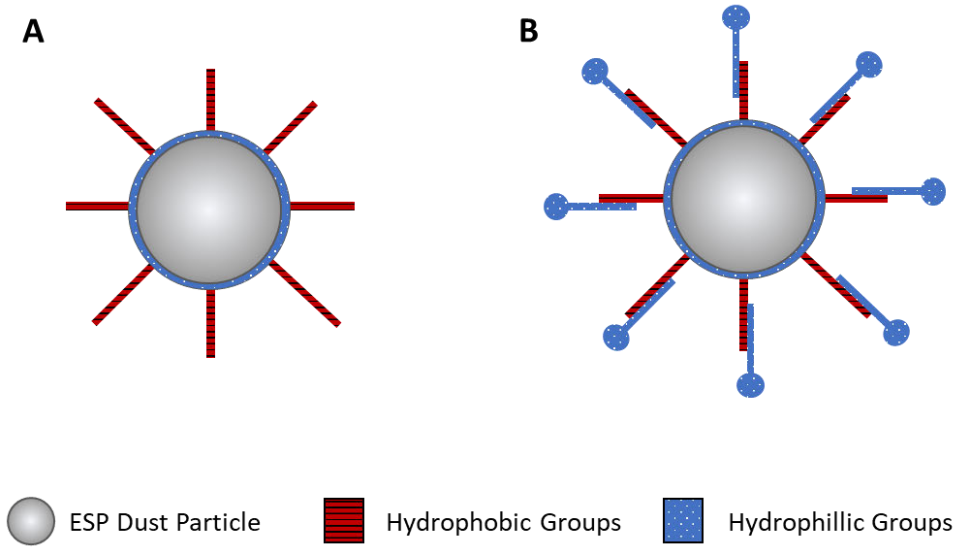

Figure 2.5 Schematic diagram showing impact of surfactants on hydrophobic particles.

Surfactants work by hydrophilic groups linking to hydrophobic groups, resulting in an hydrophilic shell which aids wetting, seen in figure 2.5. They have been used in sinter plant dust washing experiments previously with the aim of assessing if they can improve washing effectiveness. Cetyltrimethylammonium bromide (CTAB), sodium dodecylsulfate (SDS) and polyoxymethylene octyl phenyl ether (TX-100) represented cationic, anionic and non-ionic, that were trialled respectively. These surfactants were trialled by stirring the sintering dust mixture at 600 rpm for 10 minutes at room temperature with a liquid to solid ratio of 5:1. Although overall the use of surfactants appeared to reduce the hydrophobic behaviour of the dust, there was significant variance between surfactants and dosage. A mere 0.02 % dose of TX-100 increased the proportion of wetted dust particles from 59.5 % to 84.3 %, when using 0.2 % of SDS & TX-100 the wetted solids proportion rose to 92.1 % & 95.3 % respectively. However, adding 0.2 % of CTAB only resulted in the wetting of approximately 70 % of total solids, indicating that anionic and non-ionic surfactants are more effective.

Variations on the washing method were also conducted that changed stirring rate, time and temperature, some examples are shown in Table 2.1. It was shown that when using 0.2 % of TX-100 a higher proportion of solids would be wetted even when using a lower stirring speed, temperature, and time. The highest percentage of solids wetted without surfactants was 92.37 %, but this required 15 minutes of stirring at 900 rpm, both relatively high values for those parameters. Adding 0.2% of TX-100 allowed for more dust particles to become wetted whilst washing at 600 rpm for only 10 minutes. Indicating that the use of surfactants could have the benefits of saving time & energy required for effective washing.

Table 2.1 Examples of parameter variation of ESP dust washing tests and their impact on the percentage of wetted solids (30).

Test	Temp. (°C)	Stirring Rate (rpm)	Time (mins)	Wetted solids (%)
19	25	900	15	92.37
17	50	95	10	29.05
0.2 % TX-100	25	600	10	95.30

2.1.4 Potential Elemental Targets for Recovery

Various precious elements have been previously detected in iron ore sinter plant flue dust such as rubidium and silver (15,38). More common yet valuable constituents are also present in high levels such as potassium chloride which could be used as agricultural fertiliser. Multi-stage processes have previously been established with a focus on removing chlorides but also extracting other economically attractive components e.g. rubidium & potassium chloride fertiliser, examples of previous work will be discussed in this section.

2.1.4.1 Iron

Once washed the remaining solids can be filtered from the solution and recycled into the sintering process. Typically, most of this material consists of Fe phases such as Fe_2O_3 and Fe_3O_4. Total Fe content of sinter plant dust can reach up to 60 % (39), however as outlined in Figure 2.1 these dusts are often 100 µm or less in sizing, which is problematic for their recycling at integrated steelworks. Despite the undesirable sizing sinter plant dusts are commonly recycled into sinter plant feed blends in industry (40). Washing of the dusts would remove soluble impurities, such as chlorides, resulting in a more Fe rich material for the sinter plant.

2.1.4.2 Potassium Chloride

Potassium chloride is used in agriculture to encourage crop growth. Without further addition of potassium soils will reach a nutrient deficit which inhibits plant growth (26). In 2022 the EU imported 2.5 MT of potassium based fertilisers, or 88 % of its total consumption, whilst prices were 110 % higher than that of 2018 (41). This trend is likely to continue due to an increasing global population and therefore an increasing food requirement (42). The predominant source of KCl fertiliser is through the mining of potash (potassium compounds and potassium-bearing materials), approximately 90% of mined potash is used in the production of fertilisers (43). There is a total potassium fertiliser global surplus of ~ 8 MT but as shown in Table 2.2 there are various global regions with negative demands. Natural deposits are a finite resource which means other sources are desperately required to help support areas with little or no naturally occurring potash sources.

Table 2.2 Global regions with negative potassium fertiliser demand balances, all values represent million tonnages unless stated otherwise. Negative values indicate demand that outstrips regional production (41)

Global Region	2018	2020	2022	Total Demand Increase
Africa	-1.02	-1.10	-1.19	14.5%
Latin America & Caribbean	-6.68	-7.07	-7.50	10.8%
South Asia	-3.78	-4.19	-4.61	17.9%
East Asia	-10.66	-11.07	-11.47	7.0%
Central Europe	-8.73	-9.01	-9.42	7.3%
Oceania	-0.44	-0.44	-0.45	2.9%

Proven industrial sources of potassium fertiliser from waste materials include cement mills, biomass fly ash combustion & iron ore sinter plants (44). Industrial plants treat cement kiln dusts with K_2O levels between 53 – 66 %. Several papers have previously proven the existence and potential for extraction of KCl from iron ore sintering dust (10,24,26,44) and, as previously mentioned, a KCl extraction plant with capacity of 10,000 T/year sinter dust has been established in China showing industrial-scale applicability (26). As the KCl can be easily mobilised from sinter plant ESP dust and it represents the main target of washing processes there is significant scope for the extraction of KCl.

2.1.4.3 Rubidium

Rubidium is of particular interest due to its scarcity, difficulty of extraction from traditional sources and high economic value. Although Rb can be readily found in crustal rocks at trace levels, the traditional source is hypersaline lake brines with concentrations of approximately 100 mg/L (15). It has many technological applications including defence, medical and engineering. Rubidium does not form its own principal minerals and therefore does not have ore deposits. This means that although it is the 16th most common metal in the Earth's crust (45), at 78ppm, and more common than metals such as copper and zinc it is not commercially mined in the traditional sense. Due to this disparity in mineral deposits approximately only 2 – 4 T/year of rubidium are produced globally, compared to 13 MT of zinc and 20 MT of copper in 2019 (46).

One of the reasons rubidium does not form its own minerals is that due to similar ionic radius' (45), naturally occurring rubidium tends to form tiny substitutions of potassium in potassium-based minerals, such as Lepidolite and Zinnwaldite (47). Other sources include pollucite, biotite, feldspar, seawater & hypersaline lake brines. However, the main body of reserves are found in Australia, Canada, China and Namibia and are believed to total less than 200,000 tons. This scarcity encourages recovery from waste or other sources previously considered uneconomical (46).

As rubidium is not the primary target in mining operations targeting minerals such as Lepidolite, there is often costly and complex secondary processing required to extract rubidium (46,48). In the case of brines there are significant reserves however issues arise when considering low concentrations, often < 100 mg/L, and significant quantities of interfering elements such as potassium and chloride (48,49).

Table 2.3 XRF results for raw and washed ESP sample material & key PSD data (15)

XRF Results of Raw Dust											
Element	Cl	K	Pb	Fe	Na	S	Ca	Cu	Zn	**Rb**	Mg
Content (wt %)	33.38	20.51	16.02	4.85	4.39	3.49	0.92	0.77	0.47	**0.30**	0.16
XRF Results of Water Washed Dust											
Element	Cl	K	Pb	Fe	Na	S	Ca	Cu	Zn	**Rb**	Mg
Content (wt %)	2.05	2.70	31.41	9.57	0.44	-	1.37	-	0.08	**0.03**	0.26
Change After Washing (%)	96.93	93.43	1.97	1.41	94.99	-	25.80	-	91.65	**95.24**	16.31

Previously rubidium was detected at a concentration of 0.3 wt% in ESP dust from a sintering plant at Panzhihua Iron & Steel works in Sichuan Province, China, shown in Table 2.3. A total recovery rate of Rb was 58.26%, and the purity of RbCl products that were obtained after evaporation crystallization was 99.5%. Although the recovery rate could be improved, this process has proven the potential for extraction of high purity rubidium from iron ore sintering dusts. Future work should attempt to increase recovery rates whilst reducing levels of water used during the process. 1,136 mg/L of Rb detected in the final eluate is also of note as typical salt lake brines, the principal global source of rubidium, tend to host approximately 740 mg/L (15).

2.2 Sinter Pot Research

Sinter pots are essentially small-scale pilot sinter plants and have long provided a great opportunity to conduct novel sintering research (50,51). Although they do not mimic the traditional sinter strand conveyor belt system, they do replicate the process of vertical flame front propagation through a bed of raw sinter blend, seen in Figure 2.6, and produce sinter which can be analysed further.

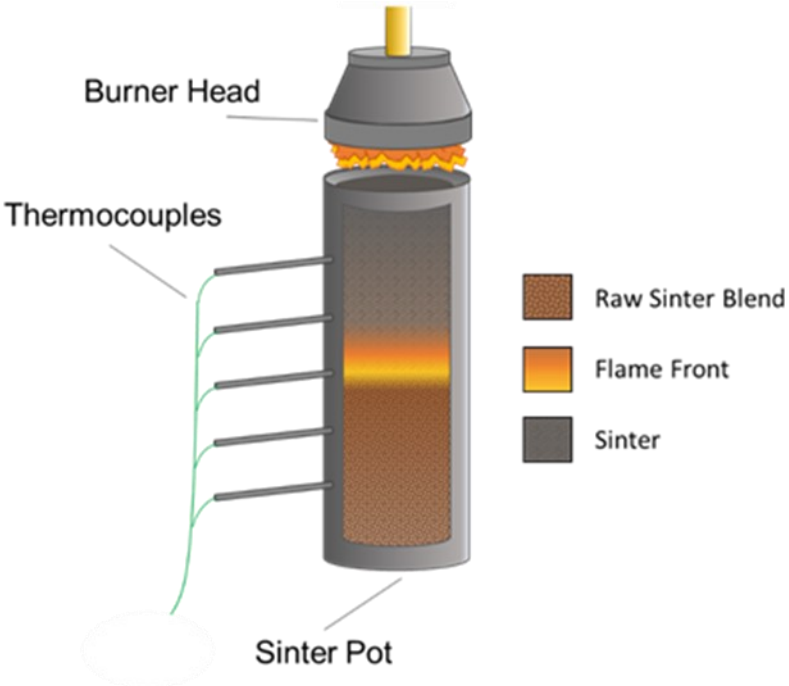

Figure 2.6 Schematic diagram of the Tata Steel UK sinter pot. Source: Author.

The size and shape can vary however typically a standard sinter pot is cylindrical and ranges from 10 – 30 cm in diameter and 50 – 100 cm in height. Previously sinter pots have been used industrially to trial sinter blends before large-scale use, environmental research has been completed focusing on emission reduction (52,53) and numerous studies have assessed the impact of physical/operational variation on final sinter properties (54).

The sinter pot at Tata Steel UK's Port Talbot site was commissioned in 2018 and has since been used to support industrial testing and academic research. This section will outline key parameters that influence the sintering process and resultant sinter. It will also discuss relevant previous research that has been carried out using similar facilities.

2.2.1 Granulation, Moisture Content and Permeability

One of the first steps in the sintering process is the granulation of raw materials. This involves adding water to the sinter blend and mixing it in a granulation vessel, such as a drum. The granulation stage of iron ore sintering is a crucial step to achieve economical and high-quality sinter production. Often a variety of ores will be used in a single sinter blend mixture, each with varying chemical properties and particle size distributions

During this process adhering particles, defined as < 0.5 mm in size, form an adhering layer around larger particles know as nuclei particles. The ratio between adhering particles and nuclei particles has been found to be a key particle characteristic impacting granulation performance (55–57). The ratio between nuclei and adhering particles is known as the PSD ratio and will be a key consideration during testing to encourage effective granulation.

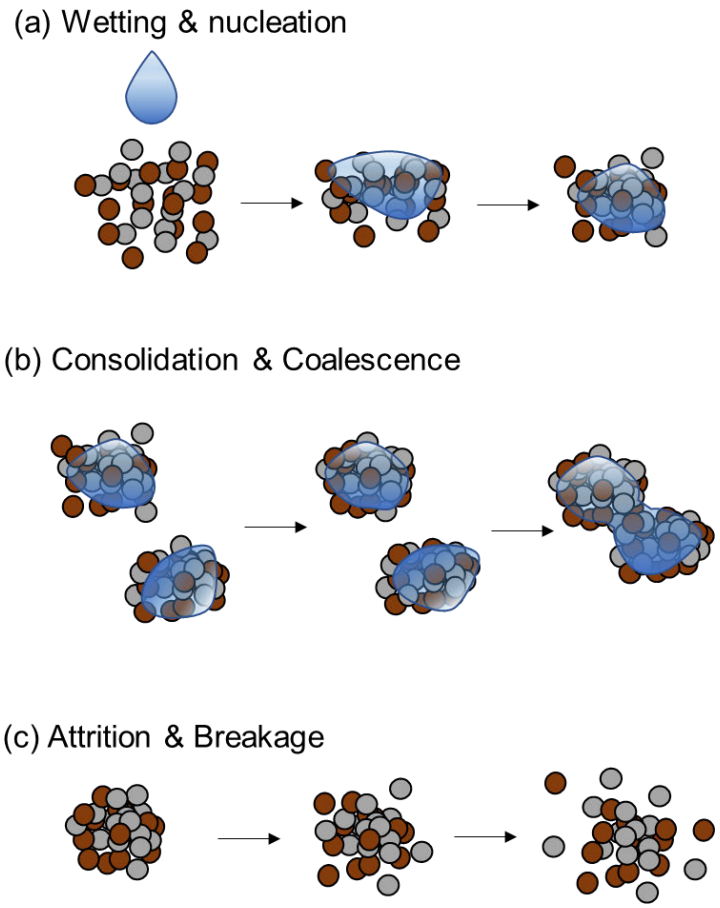

Figure 2.7 Schematic diagram showing granulation processes. Adapted from (58).

Non-adhering particles can coalesce, as shown in Figure 2.7, although this is not as desirable as granulation layering around a nucleus due to reduced strength which is shown in part c of Figure 2.7. Moisture content is a key factor relating to the granulation of the raw sinter blend. If moisture content is too low and the adhering particles will fail to form a layer around nuclei particles, whereas excess amounts of moisture can result in slurry formation which will drastically reduce air flow during sintering. A blend that is too wet will also impede the flame front propagation through the sinter bed, impacting sinter quality or requiring higher fuel rates. Previous research showed that by modifying the moisture content of the blend flame front speed, sinter productivity and product sinter microstructures can vary significantly (59). The inclusion of high amounts of fine-grained ores has also been shown to be negatively impacting granulation by hindering the dispersion of moisture through the blend (60).

Wettability is a key property relating to adhering fines in granulation (61), something that has been noted as an issue for ESP dust previously, as described in section

2.1.3. Potential to have granulation issues with ESP dust, particularly raw ESP dust which is fine grained and has hydrophobic properties. Hydrophobic powders are known to impact granulation in various ways. A mechanism known as “preferential nucleation”, shown in figure 2.8, has been suggested to explain this behaviour during granulation. Hydrophilic particles initially will preferentially nucleate which are then followed by hydrophobic particles. During granulation this structure changes as mechanical collisions push the hydrophobic particles further into the granule, this action is further promoted with increasing granulation speed (62).

A study in the pharmaceutical field supported a key finding of previous work indicating that average granule size decreases as the proportion of hydrophobic powder increases (63). This was thought to be due to weaker liquid bridges coupled with the smaller nuclei formed because of a lack of a semi-saturated surface layer, smaller granules are also themselves more liable to degrade and break.

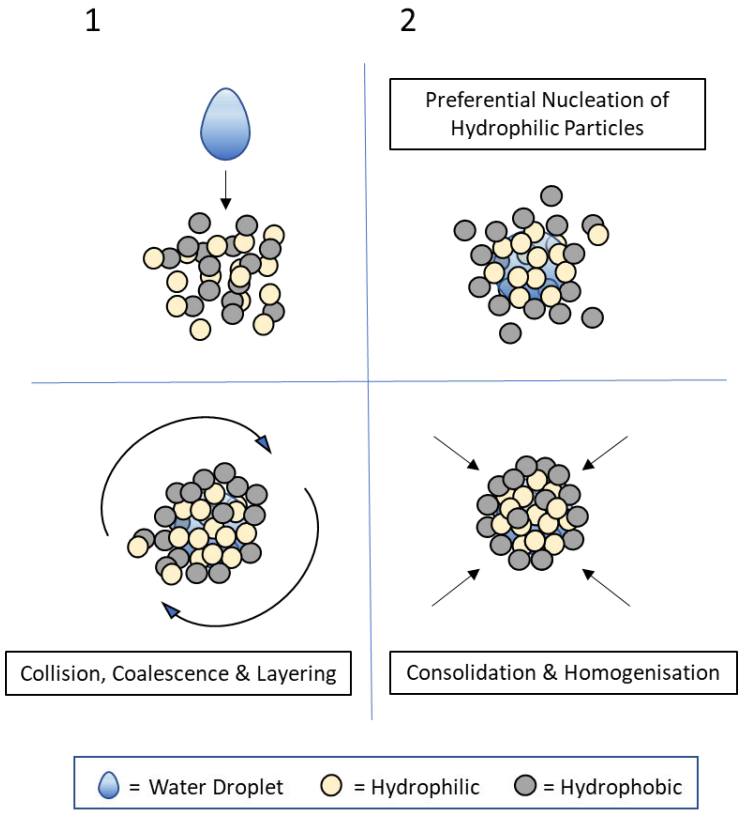

Figure 2.8 Schematic diagram showing theoretical preferential nucleation of hydrophilic particles. Adapted from (62).

As previously mentioned, permeability during the sintering process is heavily linked to the granulation of the mixture. Low permeability will impact flame front speed during sintering, impact temperatures and in turn the sinter product. Granule size, void fraction and PSD ratio have all previously been shown to impact the permeability of sintering bed (64).

2.2.2 Influence of Raw Materials

A typical sinter blend can contain up to 20 raw materials, each with their own individual chemistry and properties. The total bulk chemistry created by these blends is crucial to determining many parameters of both the sintering process itself and resultant sinter quality. This section will outline the key types of materials commonly utilised in iron ore sintering and how they impact the process.

2.2.2.1 Iron Ores

Iron ores are purchased from all over the world and from a range of geological deposits. The phases present in iron ores have significant impacts on sintering, such as wustite (FeO), haematite (Fe_2O_3) and magnetite (Fe_3O_4).

FeO is an indicator of the thermal state of the sintering process and is employed as a quality control tool at many sinter plants globally (65). FeO content has also previously been shown to impact reducibility, productivity, and sinter strength (66), previous sinter pot research showed that an FeO content of 8.5 – 10 % produced the best sinter across these parameters.

Blends using high amounts of magnetite rich ores or concentrates rely on the formation of magnetite-magnetite grains to form via diffusional bonding. This occurs at high temperatures of 1350 – 1370 °C, meaning higher fuel rates may be required to reach and maintain this temperature (67). If these temperatures are not reached when using magnetite rich blends, the sinter produced may be weak and display poor tumble test results.

Whereas the utilisation of higher rates of haematite ores, particularly with a basicity (CaO/SiO_2) of > 2, can result in a sinter rich in calcium ferrites (SFCA) at temperatures below 1300 °C, producing a high strength sinter. It has also been found that using higher levels of haematite ores compared to magnetite ores results in better productivity, fuel rates and sinter strength (68).

Poor reducibility can hinder blast furnace productivity which will reduce liquid hot metal output and potentially lead to increased fuelling, meaning higher costs and emissions. Sinter strength is important during handling and burdening of blast furnaces, the sinter will undergo compaction and abrasion during these processes. If it is weak, it will break down, resulting in less sinter reaching the furnaces and breakdown in the furnace itself will result in a reduction in permeability.

2.2.2.2 Fluxes

The role of fluxes in the sinter blend is to aid the agglomeration, production of the liquid phase during peak temperature sintering (69) and also impacts both microstructure and chemistry of the finished sinter product (70). As mentioned, sinter basicity is calculated by dividing the CaO content by the SiO_2. content, previous research has shown strong links to sinter strength and reducibility. One study showed that as sinter basicity was increased so did the sinter productivity and reducibility (71). The same study also showed that higher basicity promotes the formation of silico-ferrites of calcium and alumina (SFCA) and calcium ferrites (CF) structures. These form when lime and iron oxide react to form calcium ferrite, which then melts and reacts with silica to form a melt and iron oxide.

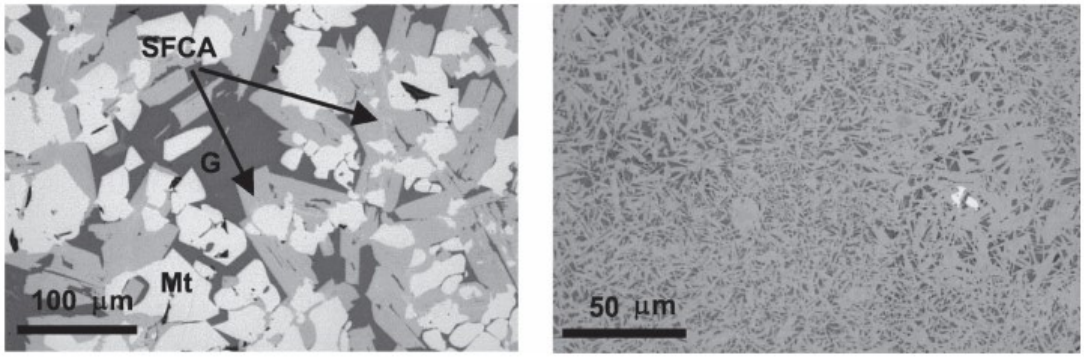

Figure 2.9 Typical SFCA structure (left) and SCFA-I matrix structure (right) G = glassy quench melt & Mt = magnetite.(72).

SFCA refers to a group of minerals consisting of over 19 variations. These variations are largely morphological (platy, blocky, fibrous etc) and linked to factors such as cooling, chemical composition, kinetics and melt viscosity, examples shown in Figure 2.9. Higher basicity values promote SCFA formation and lower basicity promotes SCFA-I formation.

Previous research found that SFCAs form early on in the sintering process at low temperatures, before breaking down into a melt and haematite at ~ 1300 °C.

2.2.2.3 Fuel

Absolutely crucial to the sintering process is the fuel content. Without the fuel combustion cannot take place, and therefore the raw materials cannot thermally agglomerate to produce iron ore sinter. Fuels used in sintering should have high calorific values and low volatile matter (73). A common fuel in iron ore sintering is coke breeze, this is a by-product from blast furnace coke production which usually occurs within integrated steelworks, as it does in Port Talbot. Breeze is typically < 3 mm and has unique combustion, mechanical and structural characteristics which make it suited for iron ore sintering (74). Fuelling therefore greatly impacts the behaviour of the flame front's speed, width, and temperature. All of which will control the quality of the sinter produced from the process (75).

2.2.3 Reverts in Sinter Pot Testing

Iron rich steelmaking biproducts that are recycled account for ~ 20 % of sintering raw materials (21). The reuse of iron rich waste products can save money whilst also contributing to the circular economy. Waste products from other industries, such as municipal waste fly ash (76), have also been utilised in sinter pot experiments.

A recent study assesses the use of 4 iron-bearing biproducts (Blast furnace flue dust, steel slag tailings, mill scale and ESP dust) and their impact on sinter quality, NO_x emissions and SO_2 emissions (21).

Table 2.4 List of the chemical compositions and sizing of the test revert materials (21).

Varieties	**T.Fe**	**FeO**	**CaO**	**MgO**	**SiO_2**	**K_2O**	**Na_2O**	**S**	**C**	**Cl**	**N**
Blast furnace dust	28.7	5.2	4.51	1.27	5.8	0.25	0.16	0.34	20.2	1.23	0.27
Steel slag tailings	17.8	9.2	40	7.97	8.13	0.04	0.059	0.16	0.85	–	–
Mill scale	71.9	48	0.22	0.07	1.23	0.05	0.076	0.07	1.78	–	–
ESP 1st electric field	44	2.3	7.08	1.97	4.82	8.25	1.87	0.69	2.23	4.96	0.14
ESP 2nd electric field	25.1	2.5	3.86	1.37	3.04	17	1.8	0.46	2.17	8.49	0.2
ESP 3rd electric field	13.5	2.6	4.42	1.62	2	19	3.23	1.55	1.79	12.2	0.33

Fe content is shown to vary significantly between materials with a maximum of 71.9 % and a minimum of 13.5 % for the mill scale and 3rd electric field ESP dust respectively. The sulphur content of the 3rd field ESP dust was also significantly higher than the other materials at 1.55 %, this is thought to be due to the presence of unburnt coke particles. Chloride increases with the fields as would be expected. The amount of ESP dust from each field used in testing was of equal quantity. These reverts were blended with iron ores, fluxes and sinter pot tests were undertaken with 1 %, 2 % and 5 % of reverts within the blend. A control test was also undertaken with no reverts added, moisture of the blends was 8 %.

Blast furnace flue dust has previously also been recycled into sinter pot experiments in a separate study and found to be a suitable replacement of coke due to the almost equal replacement of C. However, the use of blast furnace dust also increased SO_2 emissions during sinter pot testing by approximately 85 % (77). Similar results were seen in this study as SO_2 emissions rose in every test featuring reverts and continued to rise as revert concentration increased (21). A rise of 26 % in SO_2 emissions was seen when using 3 % ESP dust compared

to the control test, this was the highest increase of any revert. The sinter dust test also saw the greatest increase in NOx emissions at 21.9 % whereas the steel slag tailings saw a reduction of 11.5 %. As can be seen in table 2.4 the N content is relatively high in ESP dust and is highest in 3rd field dust, as is S and Cl. This indicates that where possible latter field ESP dust should not be included in revert recycling without further processing. Figure 2.10 shows the difference in sinter tumbler strength between 3% revert loaded sinter.

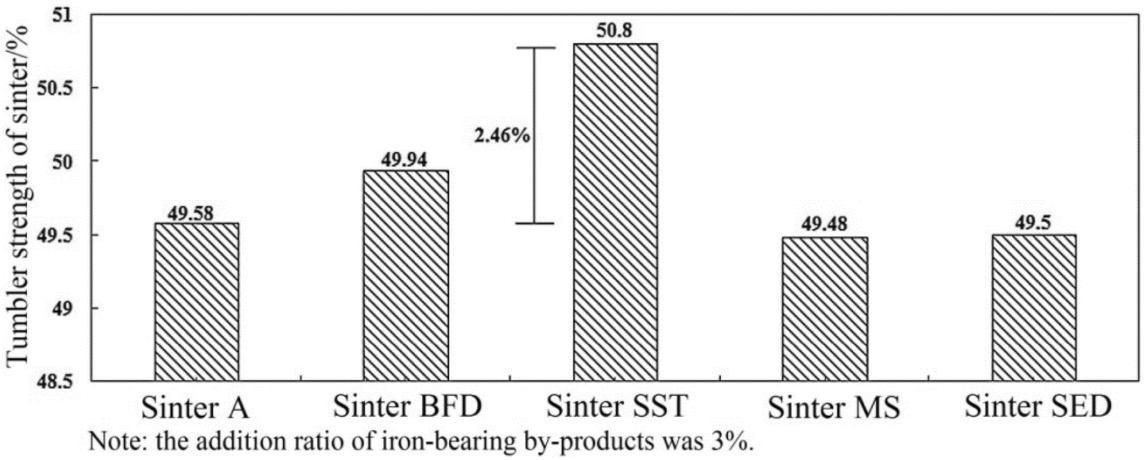

Figure 2.10 Tumble strength of sinters produced featuring 3 % of various reverts in the respective blends. Sinter A = no reverts, BFD = blast furnace dust, SST = Steel slag tailings, MS = millscale, SED = sinter ESP dust (21).

ESP dust sinter performed worst with 49.5 %, however this is only 2.46 % less than the best result which was obtained by steel slag tailing sinter. This research demonstrates no significant impact between the different reverts on tumble strength when used at 3 % concentration.

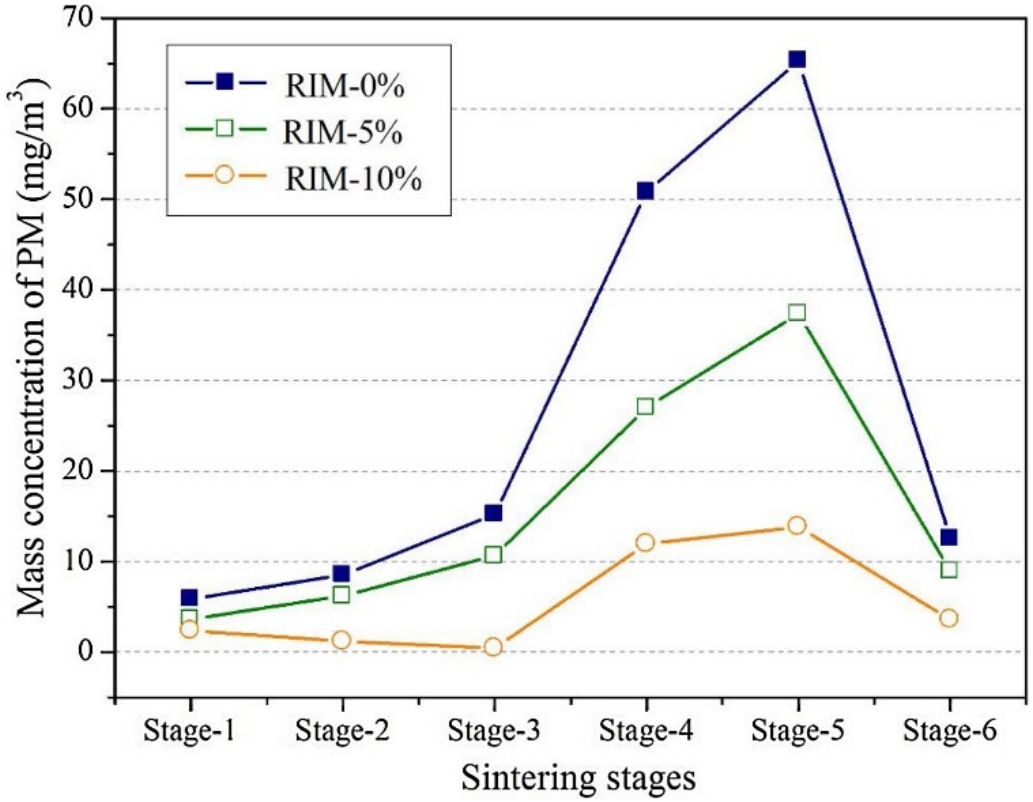

Figure 2.11 Graph showing difference in PM emissions during sintering between tests featuring different levels of revert materials. Stage 1 = ignition phase, stage 2/3/4 = middle sintering i.e. between ignition and before gas temperature inflection point, stage 5 = first half of sharp gas temperature rise & stage 6 = second half of gas peak and plateau.

This research also found fluctuations in emissions of hazardous elements and $PM_{2.5}$ particles throughout the sintering process. The experiment divided the total sintering time into stages based on waste gas temperature, outlined in the Figure 2.11 caption. This shows a similar trend between 0 %, 5 % and 10 % however $PM_{2.5}$ emissions are seen to significantly increase as revert levels increase. The particulate emission rates were found to considerably increase between stages 4 & 5, this is likely due to the reduction of the wet zone in the sinter bed (78). There is a sudden release of hazardous elements and $PM_{2.5}$ between stages 4 – 5 is speculated to be caused by a potential for the sinter bed to store $PM_{2.5}$ before an intensive release which may be temperature controlled Figure 2.12.

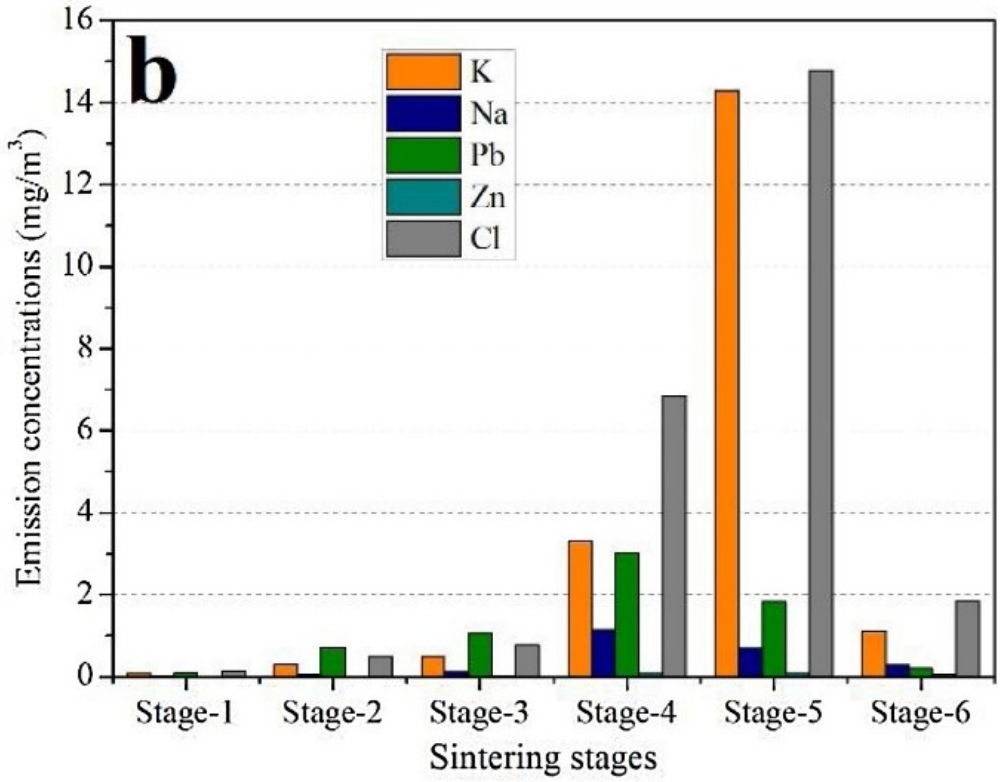

Figure 2.12 Bar chart showing variation in chemistry of emissions during sintering tests

The same study also assessed the impact of material distribution on emissions, as previously discussed the release of $PM_{2.5}$ and hazardous emissions is not uniform during sintering. If the release of these unwanted constituents can be concentrated this could lead to more economical and efficient cleaning of flue gas. Separate granulation of materials was undertaken to allow testing of various distributions during sintering, these are schematically represented in Figure 2.13.

Compared with Case-1, distributing reverts in different sintering layers decreased the sintering speed, yield, tumbler index and sinter productivity. However, out of the altered distributions Case-5 showed results most analogous to Case-1. Sinter from Case-5 also showed decreases in hazardous elements to the extent where it was comparable to sinter produced using 0 % reverts. Figure 2.13 Shows that the distribution used in Case-5 encouraged intensive release of $PM_{2.5}$ and hazardous elements in stages 5 and 6 of the sintering process. The ability to control and therefore lower the volume of gas requiring intensive remediation to approximately one third of the total flue gas.

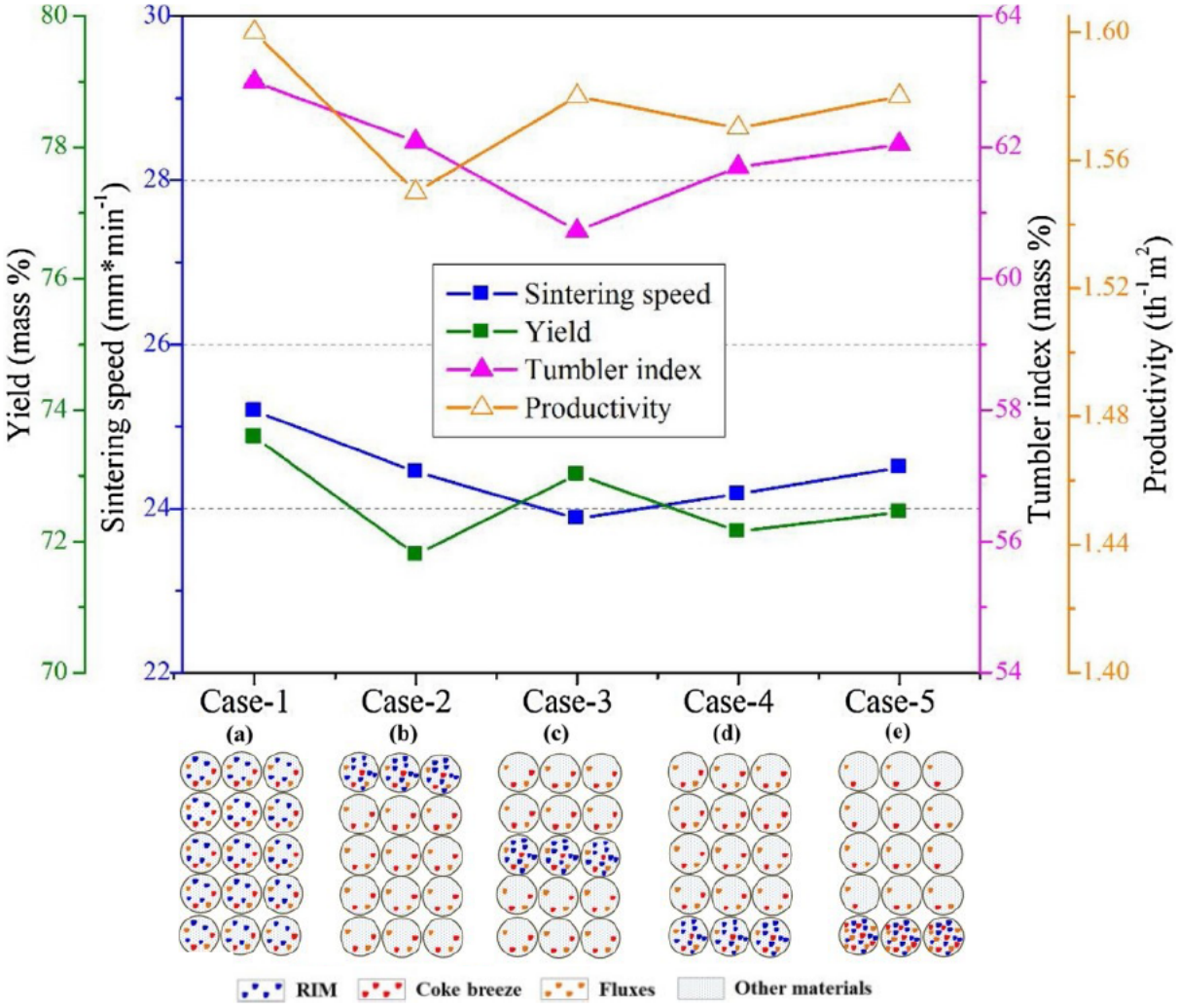

Figure 2.13 Graph comparing yield, sintering speed, tumbler index and productivity between cases. (a) Case-1: Uniform distribution (b) Case-2: reverts concentrated at top layer (c) Case-3: reverts concentrated in the middle layer (d) Case-4: reverts concentrated in the base (e) Case-5: reverts concentrated at the base with added fuel and CaO (20).

Another common revert material arising from within integrated steelworks is basic oxygen steelmaking (BOS) slurry, as the name suggests this ferrous dust material originates from the BOS stage of the process. Due to the injection of oxygen into the liquid hot metal and turbulent rheological conditions, fine material is ejected from the BOS vessel. Then as with sinter plant ESP dust, the fines must be arrested from the waste gas stream (79). The high Fe content of BOS slurry means it is desirable to recycle the material through the sinter plant, however the proportion of zinc in the material is often a limiting factor. The zinc level has been shown to be linked to galvanised scrap addition at the BOS plant (80).

At Tata Steel UK's Port Talbot site BOS slurry is produced and filter pressed to reduce moisture content. Providing the moisture and zinc content is low enough the material is routinely recycled through the site's sinter plant.

2.2.4 Micro-pellet Sintering

As previously described sinter bed permeability is crucial to achieving effective sintering, this being heavily linked to granulation and raw material particle size ratio. As many common steelmaking revert materials, such as sinter plant ESP dust and BOS plant slurry, are finely sized, the concentration that can be included in sintering blends is limited. Increasing concentration beyond these levels, which will vary between plants and blends, will detrimentally impact the permeability of the bed (81).

Previous work has investigated the micro-pelletisation of fine iron ores and concentrates to avoid this negative impact on blend permeability (82–84) and found promising results. By agglomerating the fines prior to sinter blend granulation, higher concentrations can be used without recording a negative impact on the blend's permeability and therefore sintering process. Some previous research has been completed with a focus on revert pelletisation although this is still an underdeveloped field of study (85,86).

3. EXPERIMENTAL METHODS

3.1 ESP Dust Washing Methodology

This section details the methodology of sinter plant ESP dust washing undertaken. As discussed in the literature review, water washing of sinter plant ESP dust is an established treatment method for the removal of chlorides. The research outlined in this section aimed to build on previous work by diversifying methodology and testing a range of washing parameters such as washing time, speeds, and liquid to solid ratios. The addition of surfactants was also tested, whilst TX-100 has been shown to be effective in combatting the hydrophobicity of ESP dust it is relatively expensive and has associated hazards. Alternative surfactants were tested alongside TX-100 to compare their effectiveness. The methodology of each of these variations will be outlined individually.

All ESP dust samples used during these experiments were supplied by Tata Steel UK, arising from their Port Talbot sinter plant and sampled by Tata Steel UK staff.

3.1.1 Gravity Recycle Method

This methodology did not involve any action of agitation or stirring, this was done to ascertain if ESP dust could be effectively water washed in a low energy setting. A 12.5 mm Whatman grade 1 filter paper was placed in a glass sintered buchner funnel (Scientific Glass Laboratories, U.K) before being wetted using deionised water, to ensure an effective seal. A rubber flask seal was placed into the top of a borosilicate glass narrow neck Erlenmeyer Flask (Fisher Scientific, U.K) before the buckner funnel was carefully inserted. The flask was then connected to a KNF LABOPORT Mini Diaphragm Vacuum Pump N 96 (ProfiLab24, Germany) using a rubber line, the pump was then turned on to full power for at least 10 seconds to remove excess moisture. The funnel and filter paper were then securely clamped above a different Erlenmeyer Flask, which would act as the collection vessel during testing. 100 g ± 0.5 of ESP dust was added to a weighing boat using a metal spatula before being weighed to 3 decimal places using a OHAUS Scout scale and was then placed in the buchner funnel. A volumetric flask was used to measure out 500 ml of deionised water, this was then added to the funnel by hand at a steady and consistent rate. The mixture was then allowed to filter naturally without any agitation over the course of 24 hours, shown in figure 3.1.

The filter paper holding the washed dust sample was removed from the funnel and the washed solids transferred to a weighing boat. After zeroing the scales using an identical weighing boat, the boat containing the washed solids was weighed 3 times and averaged. The solids were then transferred to an aluminium tray and dried at 105 °C for 24 hours. A 10 ml sample of the washing solution was retained in a glass vial with the rest of the washing solution being using for further washing cycles. 1 drop of nitric acid was added to each 10 ml sample vial. These steps were then repeated for a further 4 cycles, between each cycle all equipment was thoroughly washed using tap water, acetone and deionised water. After the fifth cycle the entire washing solution was retained in a borosilicate sample jar with several drops of nitric acid added before being stored in a fridge.

3.1.2 Stirred Solution Recycle Method

In this experiment the dust and water mixture was mechanically stirred before being vacuum filtered. 100 g ± 0.5 of ESP dust was weighed out using the OHAUS Scout scales. The dust was then added to a borosilicate glass 600 ml beaker (RS PRO, UK) before 500 ml of deionised water, which was measured out using a volumetric flask, was then added to the beaker. The stirrer arm of the IKA Eurostar 60 Digital Constant-Speed Mixer (Cole-Parmer, U.K) was carefully lowered into the mixture and positioned approximately 1 “ from the central base of the beaker. Samples were then washed at 400 rpm for 10 minutes, determined as baseline parameters from literature. Once complete the stirrer arm was removed and cleaned with acetone and deionised water.

A 12.5 mm Whatman grade 1 filter paper (Amazon, UK) was wetted using deionised water, to ensure an effective seal, before being placed in a glass sintered buchner funnel (Scientific Glass Laboratories, U.K). A rubber flask seal was placed into the top of a borosilicate glass narrow neck Erlenmeyer Flask (Fisher Scientific, U.K) before the buchner funnel was carefully inserted. The flask was then connected to a KNF LABOPORT Mini Diaphragm Vacuum Pump N 96 (ProfiLab24, Germany) using a rubber line, the pump was turned on to full power for at least 10 seconds to remove excess moisture. At this point the flask was switched for a dry flask.

During vacuum filtration, experiments were timed using a stopwatch. After filtering for at least 2 minutes on full power, or 30 seconds after all visible liquids had been extracted, the filter paper holding the washed dust sample was removed from the funnel and the washed solids transferred to a weighing boat, this is shown in figure 3.1. After zeroing the scales using an identical weighing boat, the boat containing the washed solids was weighed 3 times and averaged. The solids were then transferred to an aluminium tray and dried at 105 °C for 24 hours. A 10 ml sample of the washing solution was retained in a glass vial with the rest of the washing solution being using for further washing cycles. 1 drop of nitric acid was added to each 10 ml sample vial. These steps were then repeated for a further 4 cycles, between each cycle all equipment was thoroughly washed using tap water, acetone and deionised water. After the fifth cycle the entire washing solution was retained in a borosilicate sample jar with several drops of nitric acid added before being stored in a fridge. Later these same methods were repeated but extended to a total of 10 washing cycles.

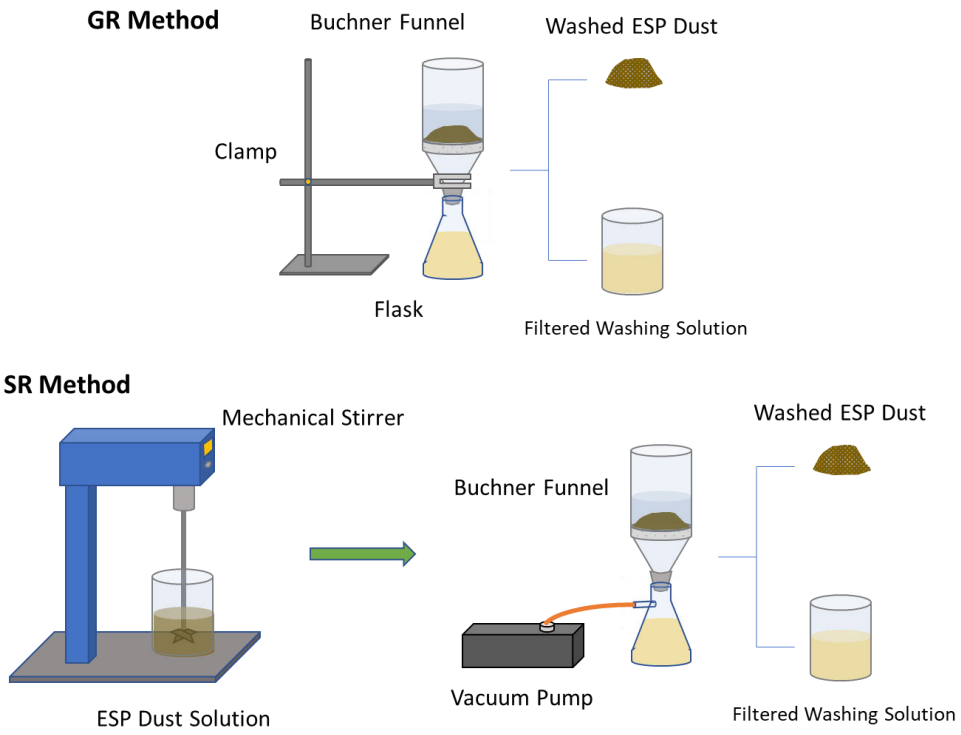

Figure 3.1 Schematic diagram illustrating the methodology for the gravity recycle (GR) and stirred recycle (SR) ESP dust washing methods.

3.1.3 Stirred Solids Recycle Method

In this set of tests, the ESP dust solids were retained after each wash and recycled, rather than the washing solution. Deionised water being replaced after each cycle to assess what proportion of chlorides remained in the sample after each washing cycle. After filtering the samples 10.0 g of wet ESP dust was sampled and all of the washing solution retained for analysis. The remainder of the solids were then washed again using the same methodology, this was repeated for a total of 5 washing cycles. Other than this the same methodology was followed as is described in section 2.1.2.

3.1.4 Stirred Recycle with Surfactants Method

Again, this method followed the same methodology as section 2.1.2 but with the addition of surfactants to the solution prior to washing. 3 surfactants were tested in total, these being organic soap nut powder (Living Naturally, UK), sodium xylene sulfonate (Mistral Industrial Chemicals, UK) and Triton X-100 (Alfa-Aesar). Surfactants were measured out and added to a beaker in the required concentration before 500 ml of deionised water was added. The mixture was then stirred for 10 minutes at 100 rpm. As the soap nut powder was a solid, this mixture was vacuum filtered prior to dust washing. Initially two surfactant concentrations were tested, 0.2 % and 2.0 % alongside a controlled sample using deionised water. Later these same methods were repeated but extended to a total of 10 washing cycles for both 0.2 % and 2.0 % surfactant concentrations.

3.1.5 Separation of Heavy and Light Solids

Due to observations from previously described experiments these tests were carried out to determine the impact of the surfactants tested on the solids during washing. The same washing methods were used to wash the samples as described in section 3.1.4, although the only concentration tested was 2.0 % of surfactants. After washing, the mixture was very slowly poured into the buchner funnel for filtration, to only move the buoyant ‘light’ particles, leaving the settled ‘heavy’ particles at the bottom of the beaker. Once vacuum filtration had been completed the filter papers were carefully removed to preserve their surfaces. Photographs were also taken at this point of the filter papers and beakers. The filter papers were then imaged using a VHX-7000 digital microscope (Keyence, UK).

3.1.6 Water Contact Angle Analysis

Water contact angle and surface tension tests were carried out using a mounted camera with FT32 software. 10.0 g of ESP dust sampled were measured out using OHAUS Scout scales and were placed on a glass slide before another glass slide was placed on top and gently compressed to create a level surface. The top slide was removed and then the dust laden slide was placed on the sample stage. The stage was manually adjusted to ensure the ESP bed was in focus and at the correct height for imaging. All glass slides used for the sample bed preparation were washed with acetone and deionised water prior to use and between samples. A disposable syringe was used to apply a droplet of solution to the sample, shown in figure 3.2.

The software was used to determine the required time and frame rate, which varied depending on experiments between 10 seconds – 10 minutes and 1/s – 20/s respectively. 5 seconds was added to the required time to allow the solution droplet to be added, once the test was completed the exact moment of contact could be determined using the FT32 software and experiment timing was recorded from this point. Surface tension analysis was carried out using an L2004 Contact Angle Goniometer (Osilla, UK). Data then being analysed using Osilla Contact Angle v4.1.

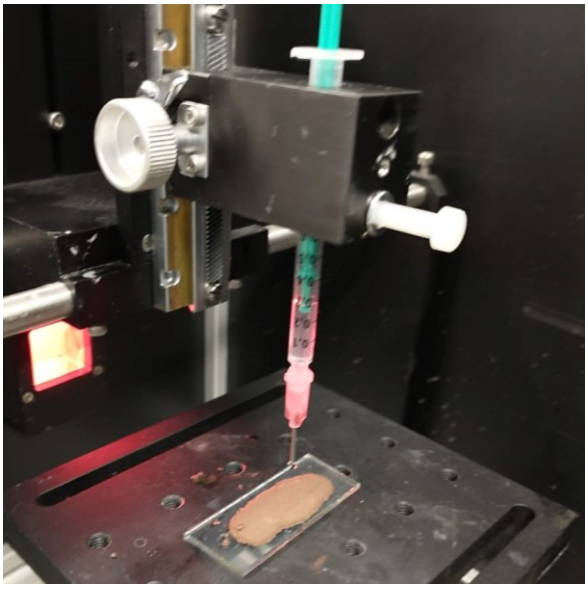

Figure 3.2 Image showing standard set up for water contact analysis.

3.2 Sinter Pot Methodology

Methods used during sinter pot experiments are outlined in the following section. Competency training was undertaken and passed prior to experimental work in accordance with Tata Steel UK policy. Sinter pots are an established experimental method in iron ore sintering field, providing an opportunity to replicate sintering conditions at a laboratory scale. This section details sample preparation, sinter pot operation and specific post analysis undertaken.

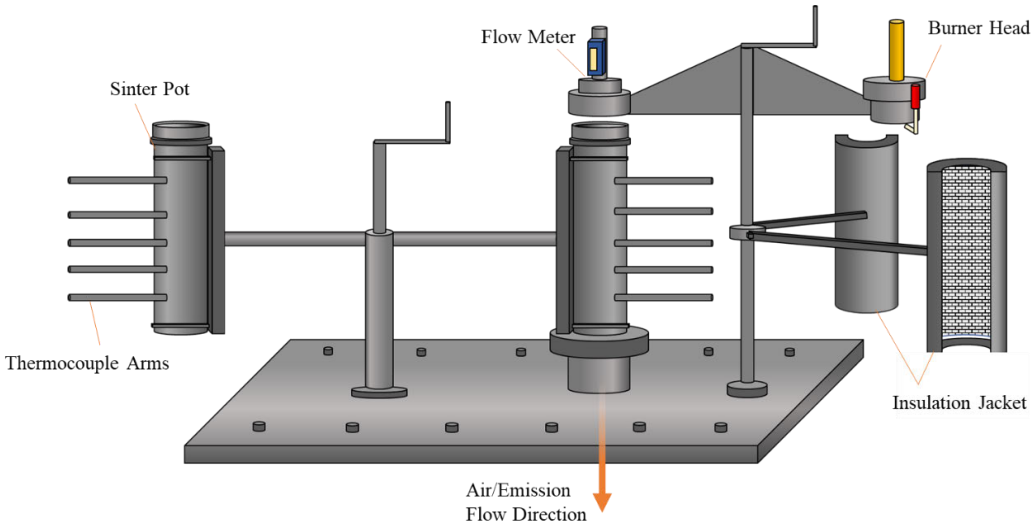

Figure 3.3 Sinter pot schematic highlighting key features.

A sinter pot replicates the conditions of iron ore sintering as would be recorded in an industrial sinter plant. The main difference being in a sinter pot the sintering occurs in a static condition and utilises a core of sinter blend. The blend is charged into the cylindrical sinter pot, shown in figure 3.3, before being ignited from the top using the burner head, a fan is then used to create negative pressure which draws the flame front through the sinter blend which results in reactions taking place and agglomerated sinter forming. Thermocouples are placed into the thermocouple arms and record temperatures throughout the test. The flow meter is also secured to the top of the sinter pot to monitor air flow during testing.

3.2.1 Preparation

Iron ores, fluxes, fuels and revert materials were provided by Tata Steel Port Talbot for testing, as seen in Figure 3.4. Raw materials were stored in plastic barrels in a shipping container before use. Samples were collected in galvanised buckets or trays before being dried for at least 24 hours at approximately 100˚C in Pickstone drying ovens at Tata Steel Port Talbot sample preparation labs. After drying, iron ores were screened by hand to < 5 mm, whereas coke breeze and fluxes were screened to < 3 mm to ensure a homogenous sample, examples are shown in figure 3.4.

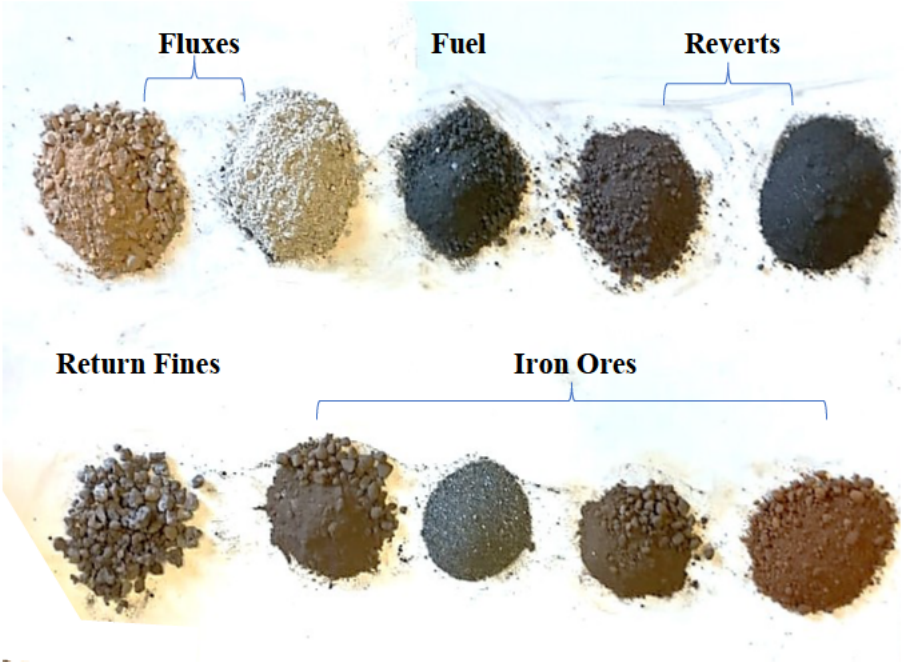

Figure 3.4 An example of dried and screened iron ores, fluxes, fuels and reverts.

As can be seen in figure 3.5, without screening there could be some fragments as large as > 20 mm which would impact granulation and airflow during testing, this also replicates processes at industrial scale.

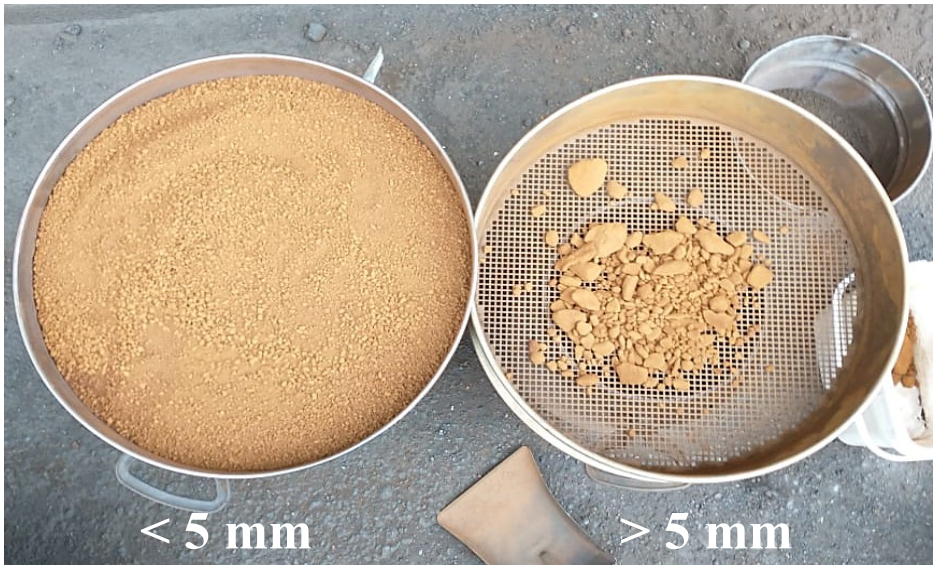

Figure 3.5 Iron ore after drying and screening to < 5 mm (left) and oversized particles (right).

The dried and sized materials were then mixed according to the required sinter blend specifications, these can be found in their respective sections. Minebea Intec Signum 1 weighing scales were used to weigh out the materials before they were mixed in a Belle Maxi 140 (Altrad, UK) cement mixer, shown in figure 3.6, which was placed at a 30˚ angle, for 2 minutes to create the raw sinter blend.

Typically a moisture optimisation test is undertaken to determine the optimal moisture content for this specific raw blend, to achieve this a range of typical moisture contents are tested on each blend. After mixing, approximately 10 g of the raw sinter blend was taken for moisture testing using a HB43 Halogen Moisture Analyser (Mettler Toledo, UK), seen in figure 3.6, to determine the blend's baseline moisture content, this was repeated 3 times and averaged to improve reliability. Once the moisture content values were recorded and averaged, the required water volume was calculated to achieve the desired moisture content for granulation.

The water was supplied by Tata Steel Sampling Laboratories and measured out using glass volumetric cylinders before being added to a SO402 handheld water sprayer (Solo, UK) which was pressurised manually with 70 pumps. A further 75 ml of water was added to the sprayer, this is to account for residual water which remains after spraying in accordance with Tata Steel UK training.

$$\textbf{Required Water Volume (ml)} \;=\; 16{,}000\ (g) \times \left(\frac{Required\ Water\ Content\ (\%)}{100}\right)$$

Equation 1 Required water volume for sinter blend granulation.

Figure 3.6 Altrad Belle Maxi 140 Cement Mixer (left), Mettler Toledo HB43 Halogen Moisture Analyser & Gladstone Engineering G94 Special Granulator (right).

The raw sinter blend was then added to the G94 Special Granulator (Gladstone Engineering), shown in figure 3.6, the water was added whilst the drum rotates at its standardised speed until there is no water being emitted by the Solo sprayer. The dimensions of the drum itself are r = 18.25 cm & l = 40.0 cm with a volume of 41,854 cm^3. Once all the water was added, the wetted blend was then allowed to granulate for a further 5 minutes, after granulation the drum is removed and the granulated blend was emptied into the SP-1 Universal Splitter riffle box (Gilson, UK), seen in figure 3.7, so the sample can be split into 2 batches of approximately 8 kg, any remaining mixture can be retained for analysis.

Figure 3.7 Gilson SP-1 Universal Splitter riffle box being used to split granulated samples (left) & one tray after splitting (right).

3.2.2 Sinter Pot Charging

A metal grate is placed at the bottom of the sinter pot to support samples and approximately 400 g of hearth layer (sinter with a PSD of 10 – 16 mm) is added to prevent new sinter fusing to the grate, both shown in Figure 3.8. The sinter pot is then carefully charged using a galvanised steel hand scoop, rotating the direction of charging by 90 ° with each scoop to avoid preferential packing. Charging continues until the granulated blend fills the sinter pot, a ruler was then used to carefully smooth over the top. As the sinter pot is now charged and ready for testing it is lowered securely into position using the nearby handle.

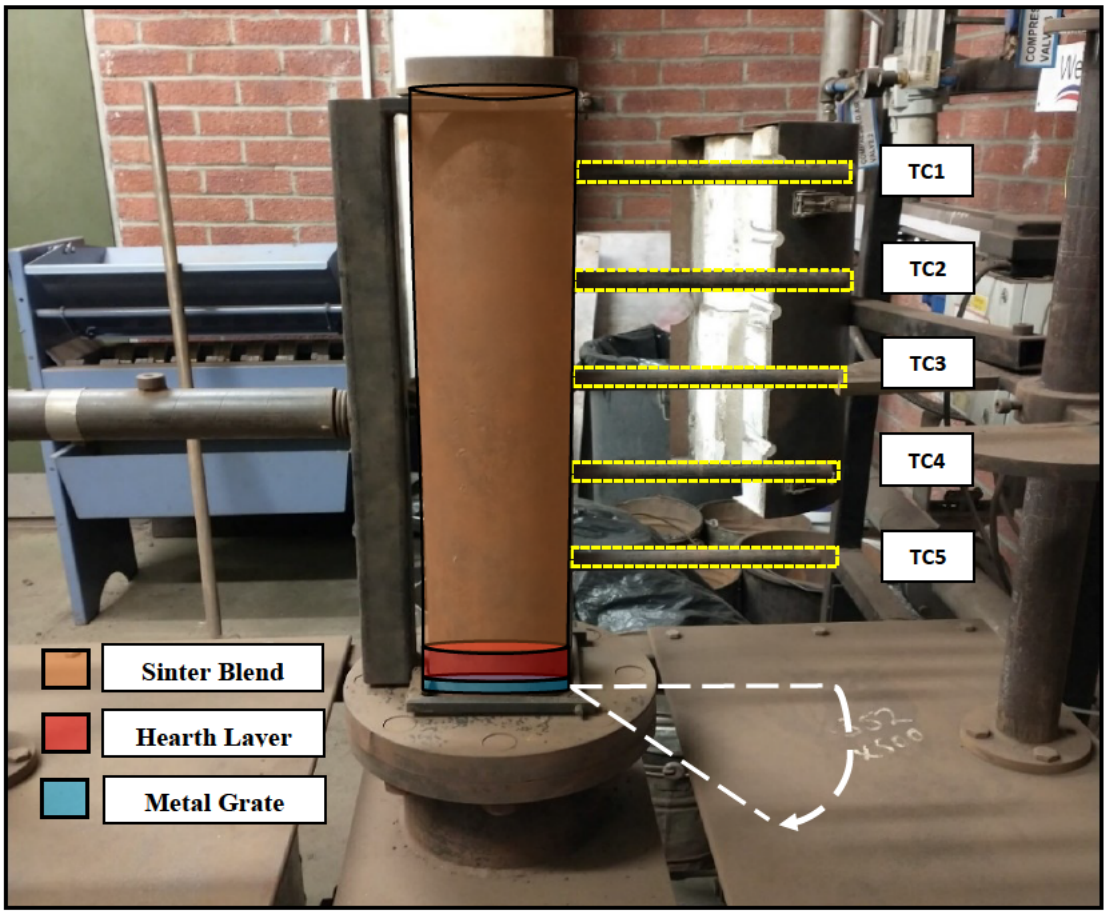

Figure 3.8 Annotated image of sinter pot with positions of sinter, hearth layer, metal grate and thermocouples highlighted. White dashed lines indicate how sinter pot is rotated. Source: Author.

3.2.3 Sintering Testing

Prior to the sintering of the granulated blend the gaseous permeability of the sinter bed within the sinter pot at ambient temperature must be quantified. This is important as the permeability directly relates to the sintering process, the air flow draws the flame front through the sinter bed allowing the sintering to occur. To conduct cold permeability tests the VPFlowScope flowmeter was fastened to the top of the sinter pot and rubber seals were placed into thermocouple arms to create a closed system, see Figure 3.9. The fan is turned on to create negative pressure and once the pressure read 100 mbar air flow data was logged for approximately 5 minutes to measure cold permeability.

After cold permeability testing is concluded, the flowmeter was carefully switched for the burner head, taking care not to disrupt the sinter pot which could influence consolidation & permeability. The rubber seals were removed from the thermocouple arms before rotating the sinter pot, shown in Figure 3.8. A thin metal rod is inserted into the thermocouple arms to create a small void in the sinter bed for the protective ceramic thermocouple casings. Thermocouples are now inserted with rubber seals to restore the closed system & the insulating jacket is secured around the pot. At this point the refractory insulation jacket was secured around the sinter pot.

Figure 3.9 Images of sinter pot prior to sintering test.

The fan is then again turned on and once the flowmeter read 100 mbar pressure all air/gas valves were opened, and the burner head ignited. After burning for 1 minute the gas/air valves were closed which ended the ignition process. At this point, the flow meter was reattached in place of the burner head. The sintering test runs until all thermocouples read < 100 ˚C. To conclude the test thermocouples were removed from the arms and the sinter pot can be discharged. The sinter pot was unlocked from the testing position before being moved so it lay above a wheelbarrow. The sinter pot was then rotated 180 ° so that it was upside down and the sinter removed manually. An image was taken of the sinter in the wheelbarrow prior to any further handling, shown in figure 3.10.

.

Figure 3.10 Image of sinter produced during testing.

3.2.4 PSD/Mechanical Sieving

Sinter produced during testing was allowed to cool at ambient room temperature for at least 1 hr before being processed. The sinter sample is then added to the top of a vibrating particle size distribution sieve shown in Figure 3.11. After the lid is secured, the machine was turned on for 2 minutes. Size fractions of > 40 mm, 40 - 25 mm, 25 - 16 mm, 10 – 5 mm. 5 – 1 mm and < 1 mm can then be removed in turn and weighed using Minebea Intec Signum 1 weighing scales. Approximately 400 g from the 16 – 25 mm sizing is retained for RDI analysis, 400 g of 10 – 16 mm for HOSIM and 50 g for elemental analysis.

Raw blend and sinter samples were submitted to Tata Steel Port Talbot sample analysis labs for XRF & reduction disintegration index (RDI) testing. XRF analysis was completed using a Malvern Panalytical Axios FAST XRF. This is standard procedure for sinter pot work carried out at Tata Steel.

Figure 3.11 Mechanical sieve used for particle size distribution analysis of sinter.

3.2.5 Blast Furnace Simulation Test (HOSIM)

This test simulates the top/middle part of the blast furnace, or indirect reduction, and was carried out at the Steel and Metals Institute of Swansea University. The sinter sample was screened to a sizing of 10 – 15 mm before 500.0 g (+/- 0.5 g) was weighed out using an OHAUS Scout scale. The weighed sample was then transferred to the MM 6000 HOSIM reaction tube which was in the tripod. Once the vessel is loaded and the lid is secured, the lifting tackle is used to lower the vessel into the electric oven, all shown in Figure 3.12. Then the weight of the total vessel is recorded before final safety checks and the closing of the doors. At this point the sample weight, tFe content and FeO content are input to the control panel. This allows the HOSIM rig to calculate the gas flow rates and length of test stages. After the initial heating stage the scale was zeroed so any further changes can be recorded.

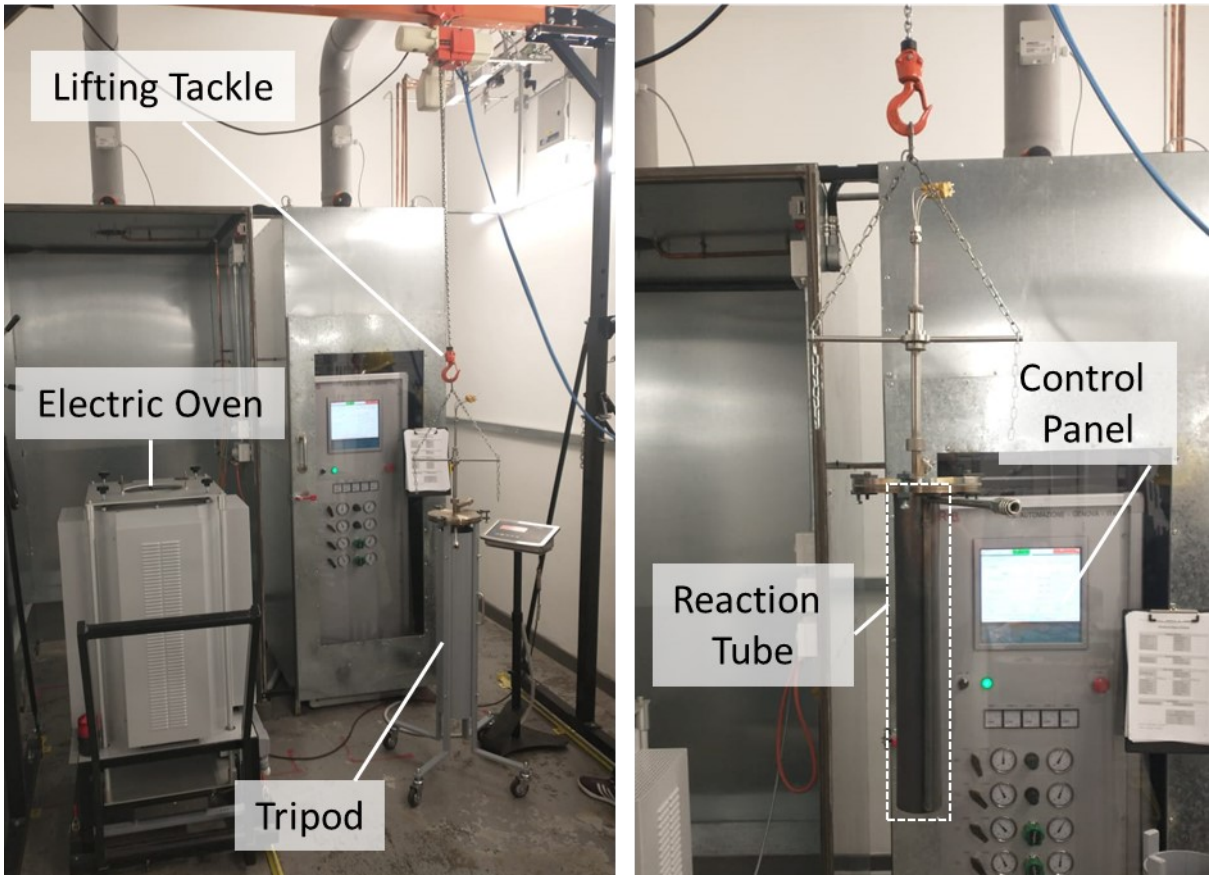

Figure 3.12 Annotated pictures of the MM 6000 machine.

3.2.6 HOSIM Tumble Testing

Tumble tests are carried out on samples after the HOSIM test using a T.B 3000, Figure 3.13, supplied by R.B Automazione. Initially the sample is mechanically sieved for 2 minutes using an Endecotts EFL 300 sieve shaker on a power setting of 80 %. This sized the sample to > 6.35 mm, 6.35 – 3.15 mm, 3.15 – 1.00 mm, 1.00 – 0.50mm and < 0.50 mm. Individual sizings were carefully discharged from the sieve to a collection plate, the sieve was checked to ensure all material was transferred. Each sizing's weight was recorded to 3 decimal places using OHAUS Scout weighing scales. The whole sample is then reunited in the T.B 3000 drum before the lid is secured and the drum is secured to the rotating arm. The tumble test itself consists of 300 revolutions at a rate of 30 revolutions a minute. Once complete, the sample is again sieved with the Endecotts EFL 300 and the mass of each sizing was again recorded. The disintergration index was then calculated using the following equation:

$$Disintergration\ Index\ = (\frac{Sum\ of\ Mass\ of\ 3\ Smallest\ Sizings}{Total\ Sample\ Mass}) \ x\ 100$$

Equation 2 Disintegration index calculation.

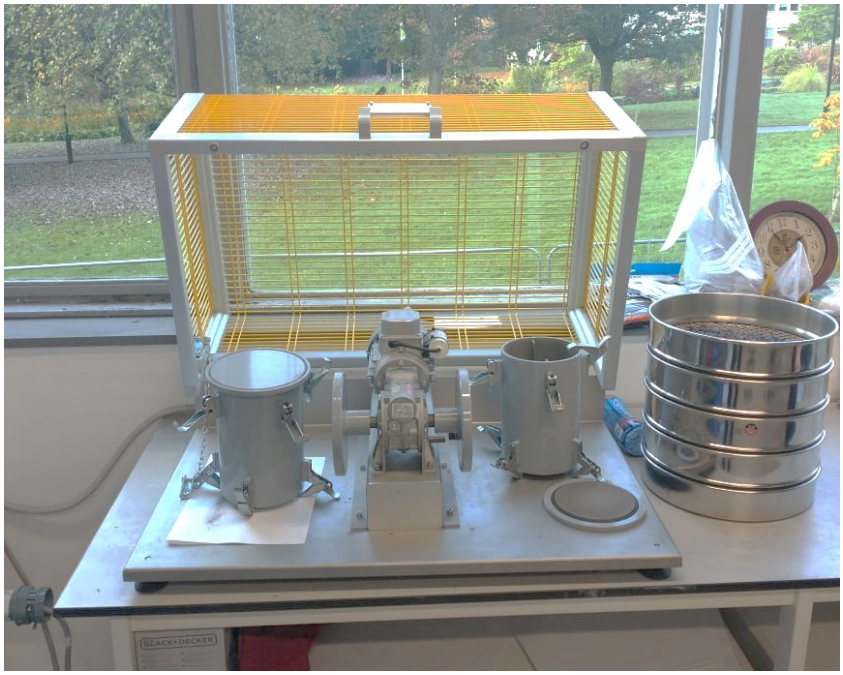

Figure 3.13 T.B 3000 tumbler system used for disintegration testing.

3.2.7 Sinter Microscopy

Sinter samples measuring no more than 30 mm x 30 mm x 30 mm in size were selected to be mounted in Bakelite resin using the Opal410 hot mounting equipment, Figure 3.14. Cold mounting is a more suitable technique for iron ore sinter due to its strength and porosity however this was the only method available at the time of analysis. The sinter sample was placed on the hydraulic mount before being lowered into position. Approximately 50 g of Bakelite resin powder was then added to the chamber, after this the chamber was locked. The OPAL140 was then heated to 180 °C before being held at this temperature for 4 minutes, followed by a cooling period of a further 4 minutes. Once the resin had cooled to room temperature it was removed from the OPAL140.

Figure 3.14 OPAL 410 (ATA, Germany) electrohydraulic hot mounting equipment with conductive Bakelite resin powder (top left), Struers LaboPol-5 (top right), Struers Labopol-1 (bottom left) & Zeiss Primotech Microscope.

A Struers LaboPol-5 was then used to polish the sample, polishing pads with roughness levels of 1200 gsm – 100 gsm were used at varying time intervals at a speed of 200 rpm. 1, 2, 4, 8, 16 minutes as the polishing pad became finer. Tap water was constantly sprayed onto the polishing pad during use. After each round of polishing, the sample was washed with water and ethanol before being dried with a hairdryer. It was then observed under the Zeiss Primotech microscope to ensure it was ready for the next grade of polishing pad.

The next step involved the LaboPol-1, 6 micron and 1 micron polishing pads were used. When each pad was attached to the LaboPol-1 a water-based diamond lubricant (Chloeren Technology, Germany) was applied, before turning the machine on at a speed of 200 rpm to evenly distribute the lubricant. This was followed by the addition of either 6 micron or 1 micron water-based diamond suspension solution (Met Prep Ltd., UK). The sample was then manually held in position, as can be seen in figure 3.15, with minimal pressure applied to ensure an even polish.

Figure 3.15 Resin mounted sinter sample after polishing process.

3.3 Analytical Techniques

3.3.1 X-Ray Fluorescence

During X-ray fluorescence analysis, an x-ray is fired at the sample material, marked as 1 in Figure 3.16. Electrons can be expelled by their atomic shells by the incoming x-ray, marked by 2 in Figure 3.16, which results in the remaining electrons reconfiguring to become stable once more, as can be seen at point 3 in Figure 3.16. Since an electron of a higher energy will replace the electron ejected from a lower energy shell, a characteristic x-ray is emitted as shown at point 4 of Figure 3.16. This characteristic x-ray is what is analysed to determine the element being analysed (87).

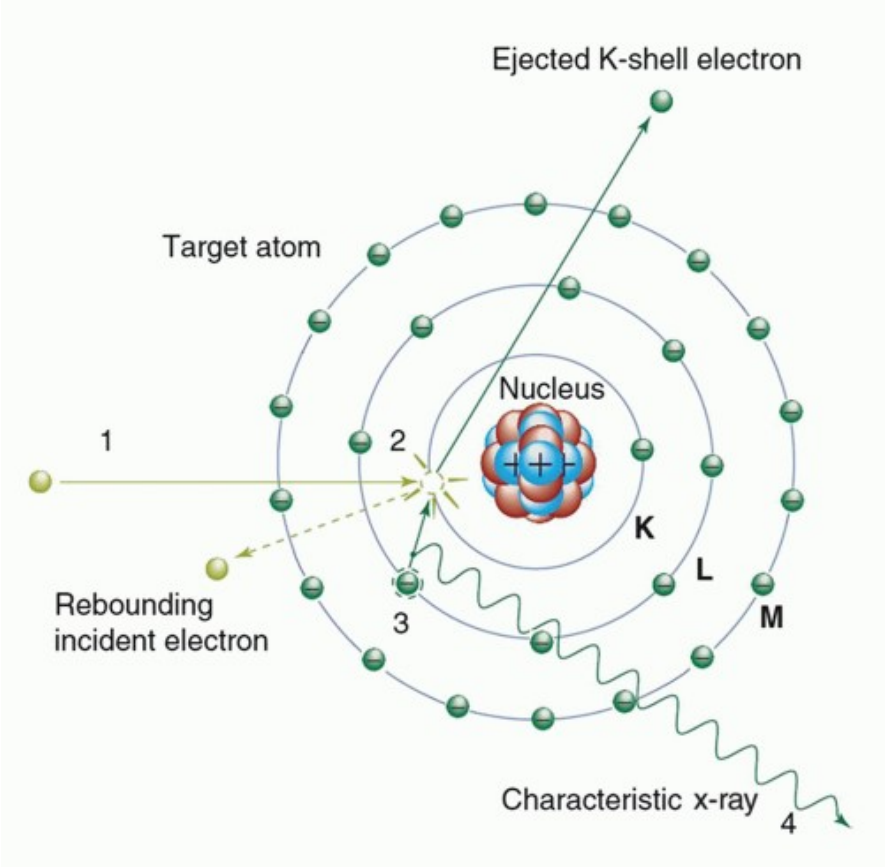

Figure 3.16 Schematic diagram illustrating the process of x-ray fluorescence analysis (87).

A X-MET7500 Handheld XRF Analyser (Oxford Instruments, UK) was used for X-ray fluorescence (XRF) analysis. The scanning time was set to 20 seconds for all samples and each sample was scanned 3 times before the results were averaged. Plastic sample containers were used when required, based on sample form, however a blank scan was taken using an empty sample container prior to analysis.

3.3.2 Ion Chromatography Analysis

A Thermo Scientific Dionex Integrion HPIC Ion Chromatography Instrument with Chromeleon v6.8 software was used for ion chromatography analysis. Standards were mixed at required concentrations and kept for a maximum of one month, before any samples were tested a blank (deionised water) and 4 standards were analysed to calibrate the equipment. Thermo Scientific eluent was used, all preparation instructions were followed, and eluent was changed at least once a month.

Samples were manually injected using disposable syringes, a new syringe was used for each sample. A pump pushes the sample through to the analytical column where its ions are separated using the ion exchange process. This produces a chromatogram peak which can be analysed to determine ion concentration, this process is shown in figure 3.17.

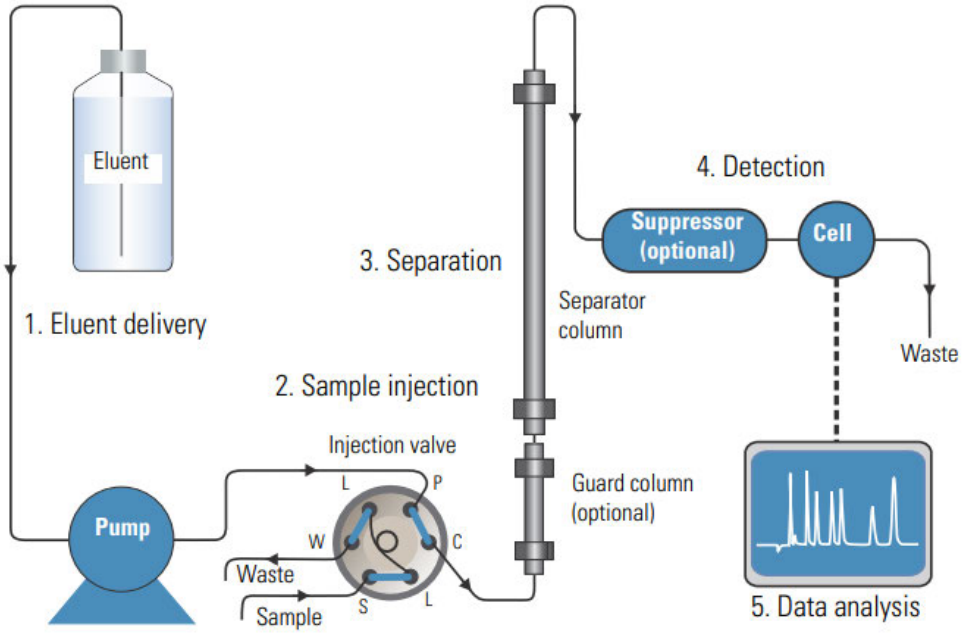

Figure 3.17 Schematic diagram of the Dionex Integrion HPIC system (88).

3.3.3 Microwave Plasma Atomic Emission Spectrometry

Microwave plasma atomic emission spectrometry (MP-AES) works by converting liquid samples to an aerosol form, this aerosol is then directed into a nitrogen plasma chamber with temperatures of approximately 5000 K. At this point atomisation of the aerosol takes place and elements are then detected and separated by a monochromator system. This allows a broad range of elements and their concentrations to be detected (89).

MP-AES analysis was carried out using an Agilent Technologies 4200 MP-AES, in accordance with operating training the MP-AES was allowed to stabilise for one hour before use. Target elements for analysis were selected depending on the samples being tested. Sample uptake flow rate was determined by the lowest recommended flow rate depending on the target element. Standard pump speeds of 15 rpm were always used, and 3 measurements were recorded for each sample. Between switching samples, the uptake tubing would be rinsed using deionised water several times. A 1000 mg/L ICP Mult-element Standard Solution IV (Merck Centripur, UK) and a 1000 mg/L ICP Rb Standard (Merck Centripur, UK) were the standards utilised. A blank sample, consisting of deionised water, and standards of 2 ppm, 4 ppm, 6 ppm, 8 ppm and 10 ppm were prepared for calibration.

Samples were prepared for ion chromatography analysis by dilution using deionised water in volumetric flasks. As the elemental concentration of samples varied, the dilution also varied to ensure the samples fell within the measurable range.

3.3.4 Scanning Electron Microscopy

To achieve scanning electron microscopy (SEM) a metallic filament is heated within the microscope which fires a beam of electrons, this beam is focused and directed by electromagnetic lenses toward the target sample. As the electron beam contacts the sample electrons will be emitted from the said sample, specialised detectors then collect these electrons and convert them to a signal which produce an image.

The SEM used for this analysis was an EVO LS25 (Zeiss, UK). 15kV acceleration voltage and a working distance of 10mm were used as baseline analysis parameters unless stated otherwise. Dust and fine samples were secured to sample staging using double sided adhesive carbon tape (Agar Scientific Ltd., UK), once the tape had been attached the dust sample was

poured from the respective sample vial. A cannister of compressed air was then used to remove loose particles to avoid damage to the SEM under vacuum. Nitrile gloves were worn throughout this process to avoid contamination. Large solid samples were prepared by being clamped to respective sample stages.

Energy dispersive x-ray spectroscopy (EDS) was carried out using the EVO LS25 which were then analysed using AZtec software (Oxford Instruments, UK). Target elements were selected based on specific samples and scans were run for a minimum of 15 minutes to achieve good standard deviation in spectra.

4. SINTER PLANT ELECTROSTATIC PRECIPITATOR DUST WASHING ENHANCEMENT & OPTIMISATION

4.1 Introduction

Recycling of unwashed ESP dust in the sintering process has been shown to contribute to dioxin formation through de novo synthesis (23), reduced ESP dust removal efficiency whilst also having negative impacts on the blast furnace at later process stages (90). The use of water to wash sinter plant ESP dust is an established remediation technique, as established in the literature review section 2.1.2. The main aim of the process is the mobilisation of chloride, resulting in a final product more appropriate for sintering. Although an established technique, there is certainly room for it to be improved and optimised to increase efficiency. Recycling of washing water and the addition of surfactants are two potential ways to achieve this. The research described in this chapter focuses on assessing the viability of recycling ESP dust washing water up to 10 times and how including surfactants in the washing water can aid the process.

4.1.1 Initial Testing

The first experiment carried out was designed to determine how effective “low energy” methods can be, compared to the “high energy” more common methods seen in literature. The low energy method involved simply allowing water to filter through the ESP dust naturally over time, aiming to simulate natural attenuation, such as rainfall in a stockyard, whereas the high energy method involved mechanical stirring before vacuum filtration, as can be seen in figure 3.1.

Once the testing was completed there was an immediate difference in the colouration of the two samples. As can be seen in Figure 4.1, there was a clear yellow discolouration to the high energy solution, whereas the low energy solution only had a slight tint of yellow discolouration. The solutions were then analysed using ion chromatography to determine the chloride content, the results of which can be seen in Figure 4.2. There is again an obvious difference between the low energy and high energy sample measurements. Whilst both sets of data trend positively after each cycle, the low energy samples recorded significantly lower chloride values when compared to the high energy samples. The average amount of chloride

mobilised from each cycle for the low energy test being 583 mg/L (± 49) compared to 2,287 mg/L (± 123) in the high energy test. After the 5 cycles this resulted in a Cl concentration in the high energy washing water of 11,933 mg/L (± 615) compared to only 2,914 mg/L (± 247) in the low energy washing water.

It also appears that the mobilisation rate increases after the first few rounds of recycling washing water. During the high energy experiment, the first cycle averaged 1,566 mg/L (± 177) whereas the fifth cycle averaged 3,644 mg/L (± 305). The low energy test also displayed a similar trend, with an average of 474 mg/L (± 127) Cl after the first recycle detected in the water compared to 1,104 mg/L (± 141) after the five cycles.

Figure 4.1 Image of ESP dust washing solutions after 5 cycles from low energy (left) and high energy (right) washing experiments.

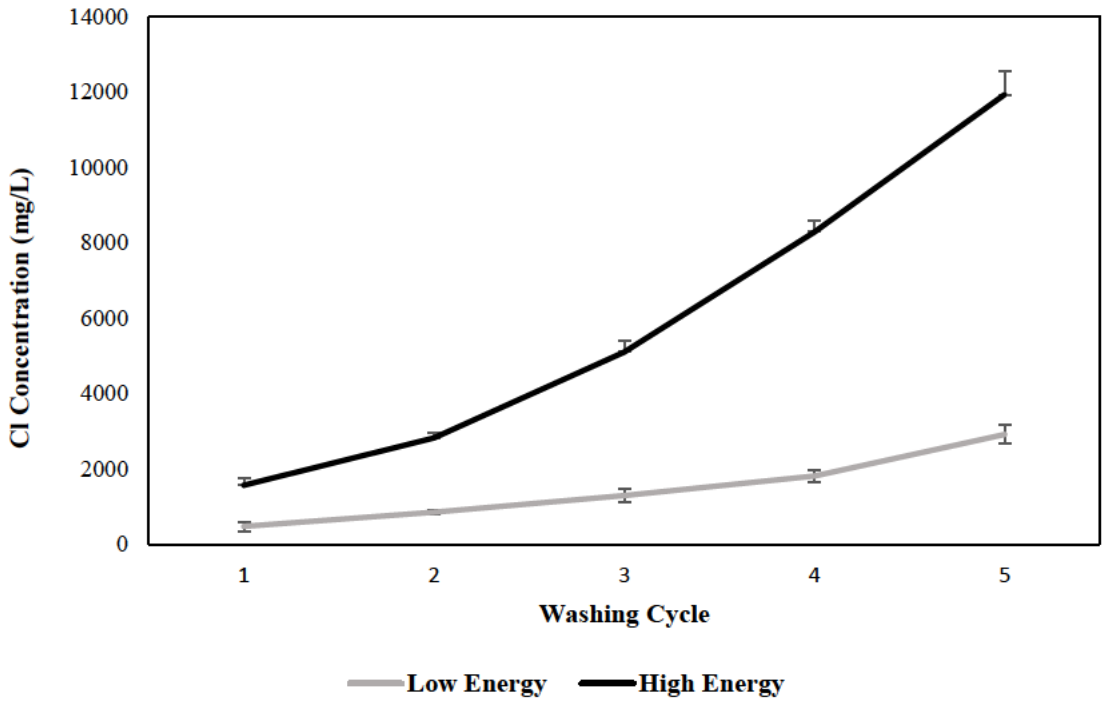

Figure 4.2 Line chart showing Cl concentrations over 5 cycles for low and high energy washing methods.

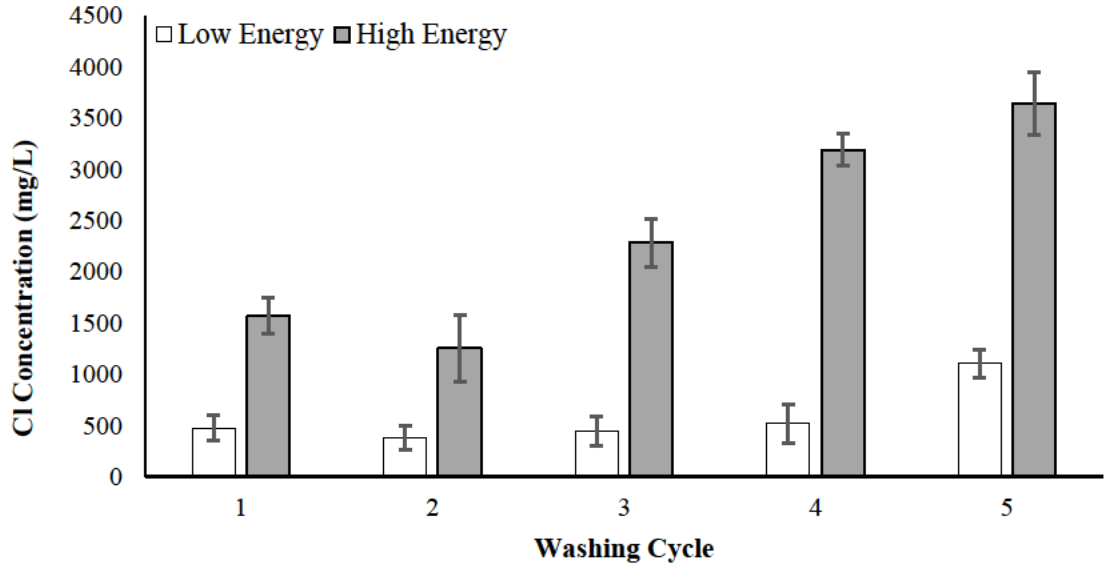

Figure 4.3 Comparison bar chart illustrating the difference in cumulative average chloride mobilisation over 5 cycles from high and low energy ESP washing tests.

The mass of the dust samples was measured before washing, immediately after washing and after being dried, the results of which are displayed in Figure 4.4 and Figure 4.5. Initially the data was plotted as a comparison bar chart, however it was then decided that a stacked bar chart can highlight the differences between the two samples more concisely. Therefore, stacked bar charts will be used to plot remaining dust mass data.

The most notable difference is in the dried weight, where the high energy washed solids lost 6.38 g and the low energy washed solids only lost 2.81 g, compared to their starting weights. This suggests more material was mobilised in the washing when using the high energy method, the high energy process resulted in more than double the mass loss of the low energy process. The high energy washed dust sample was also 1.43 g heavier on average when measured immediately after washing. This indicates that the washing was more effective as the dust from the high energy sample contained more water as it had overcome the hydrophobic property of the ESP dust.

The moisture content of the wet samples was calculated based on the difference between the wet weight and the dry weight, as per Equation 3. The results were a moisture content of 9.89 % for the low energy washed sample and 15.75 % for the high energy washed dust. This further emphasises how the high energy washing method better wets the dust samples compared to the low energy method.

$$moisture\ content\ (\%) = \frac{(wet\ mass - dry\ mass)\ (g)}{dry\ mass\ (g)} \times 100$$

Equation 3 Moisture content calculation for ESP dust samples after washing.

Figure 4.6 highlights how both rubidium and lead concentrations follow similar mobilisation patterns to that of chloride seen in Figure 4.2, the high energy method resulting in significantly greater mobilisation relative to the low energy method. Rubidium concentrations peaked at 324 mg/L (± 25) after the 5 high energy cycles, compared to 73 mg/L (± 8) in the low energy experiment. The same trend was seen when measuring lead, which peaked at 191 mg/L after high energy washing, as opposed to 41 mg/L in the low energy experiment.

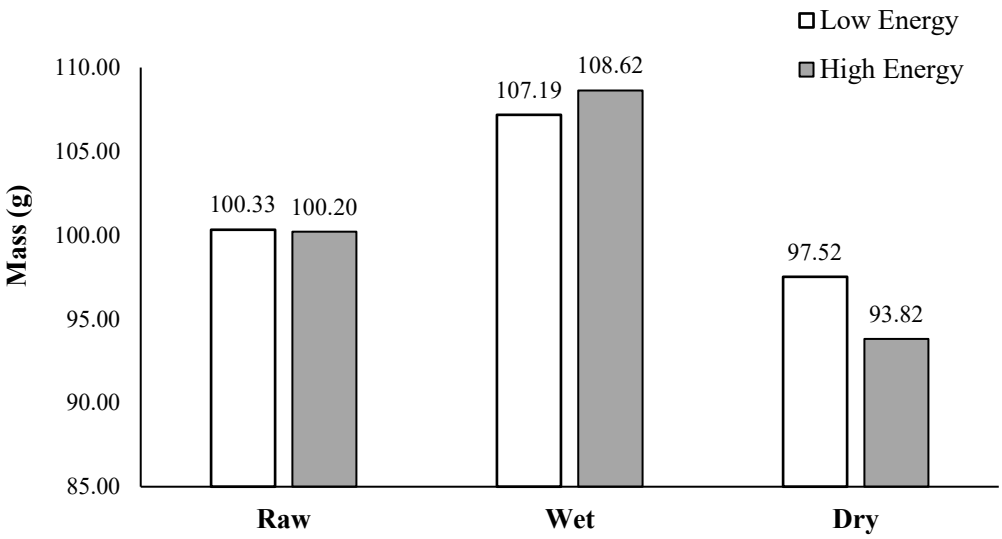

Figure 4.4 Comparison bar chart illustrating the difference in mass before washing, after washing and after drying for high and low energy dust samples. All error within ± 0.2.

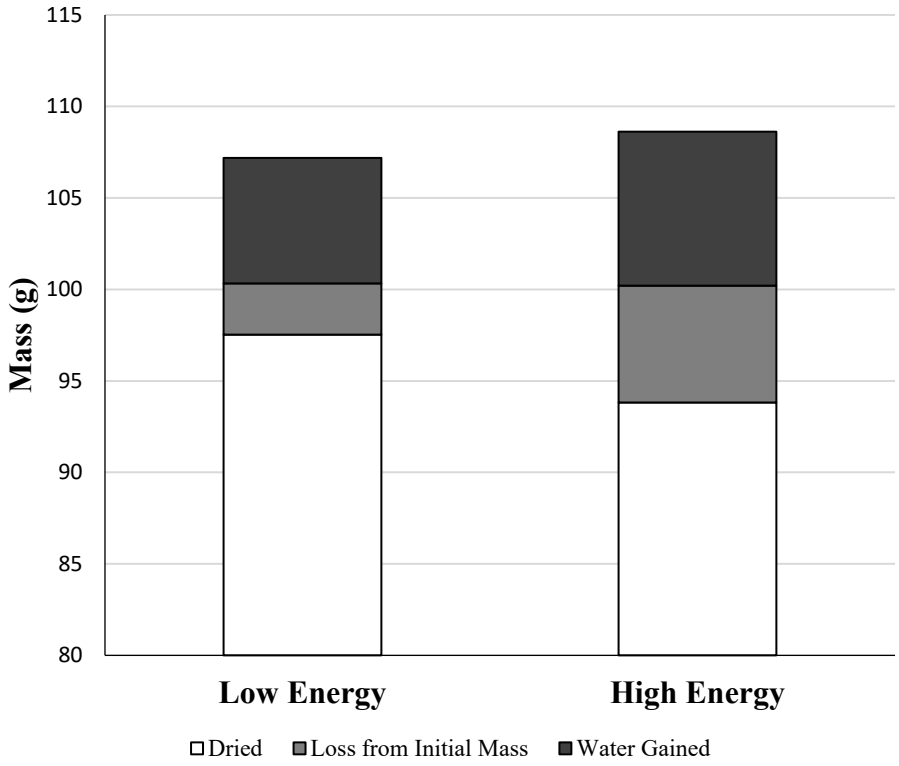

Figure 4.5 Stacked bar chart illustrating the difference in mass before washing, after washing and after drying for high and low energy dust samples. Y axis begins at 80 g.

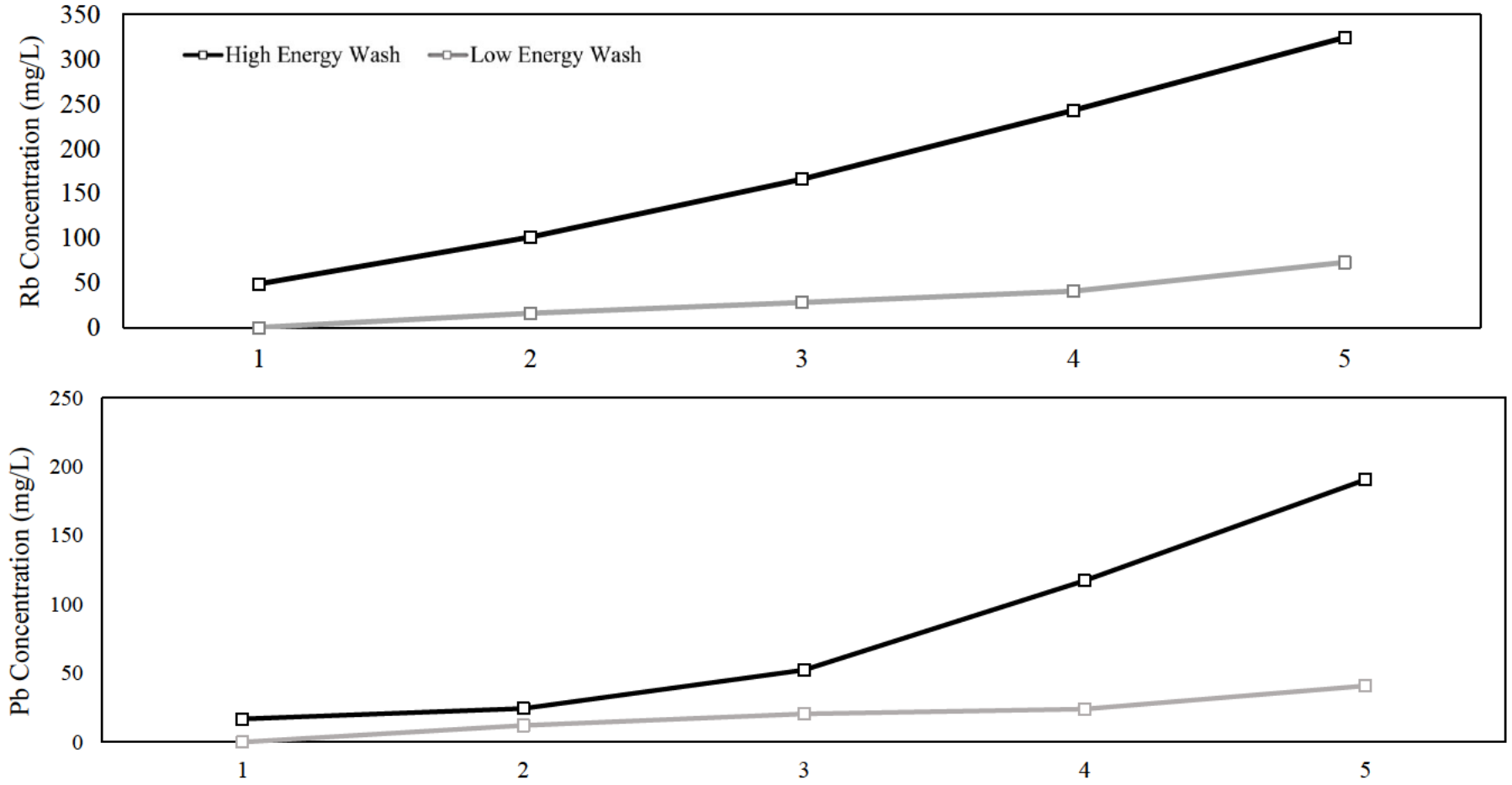

Figure 4.6 Line graphs showing Rb concentration (top) and Pb concentration (bottom) after 5 cycles of ESP dust washing.

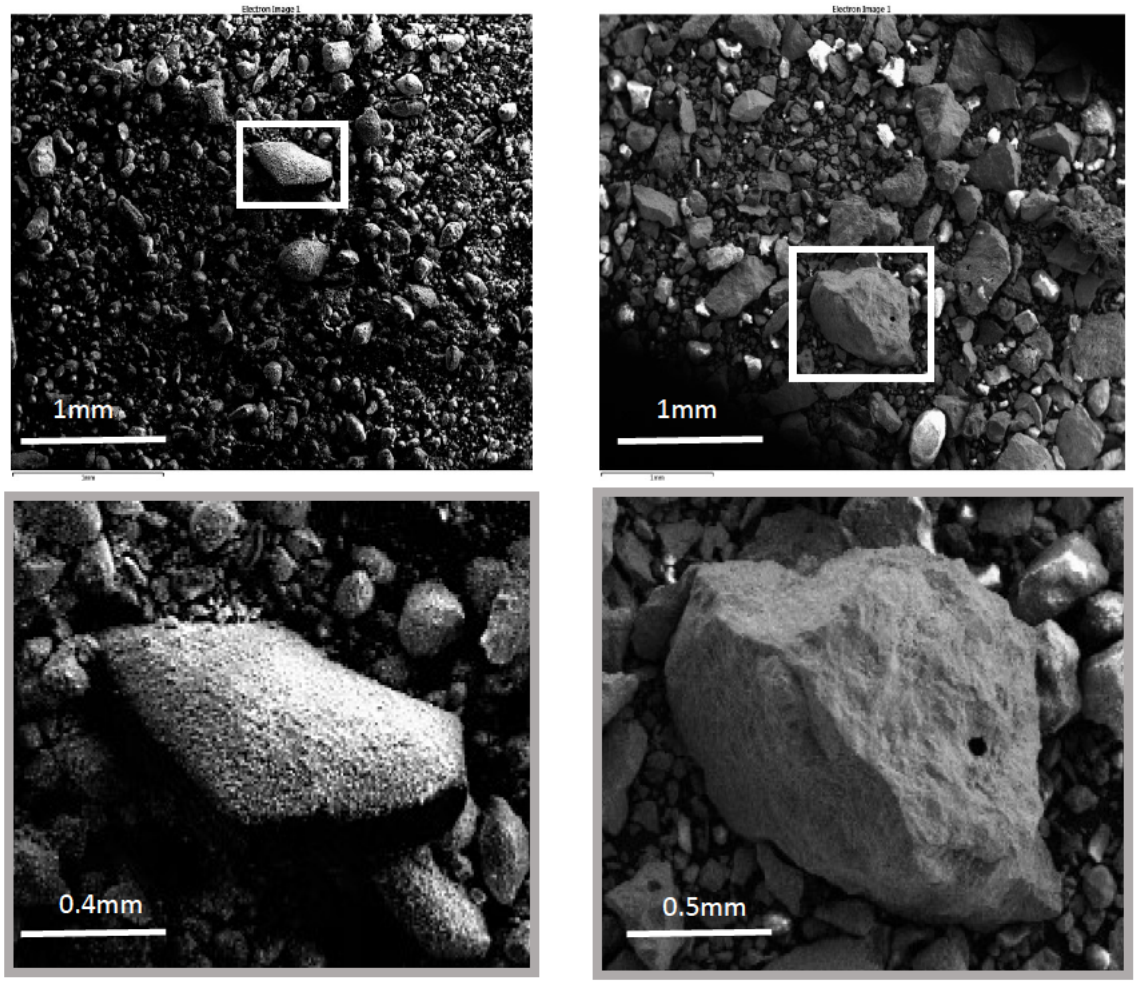

Figure 4.7 SEM images of raw ESP dust (left) and washed ESP dust (right) with zoomed portions highlighted below.

SEM images in figure 4.7 highlight the morphological features of ESP dust before and after washing. The top image shows the heterogenous sizing and shape of the material, with particles ranging from nearly 1 mm in length to < 0.1 mm. Two squares highlight specific particles, which are then shown at a higher magnification below. These magnified particles show differences in the surfaces of the dust particles before and after washing. In the raw dust they appear to be coated in much finer particles, whereas after washing, the surface features are much clearer with features such as holes and more contrast is visible. The top right image of the washed dust clearly shows a range of coloured particles, owing to the mixture of materials in the dust. This pattern of differences was seen consistently throughout samples analysed using this method.

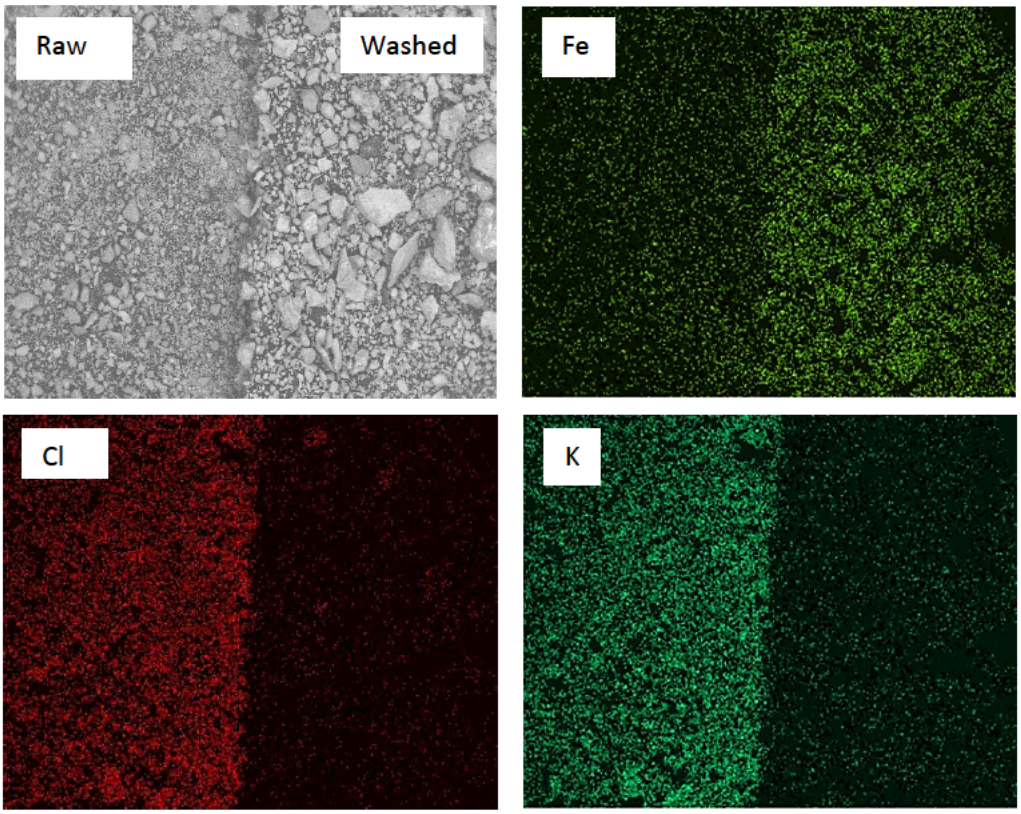

Figure 4.8 SEM image of raw and washed ESP (top left) with accompanying EDS scan results for Fe, Cl & K. images.

An SEM sample was prepared featuring raw and washed ESP dust alongside each other, to highlight chemical difference during EDS analysis. Figure 4.8 shows the results which shows the impact of washing on prevalence of iron, chloride, and potassium. Iron becomes more apparent after washing, indicating that it is coated by materials which can be mobilised by washing. Both chloride and potassium all but disappear after washing, indicating that they could be two of the elements coating the larger iron particles. An effect also seen physically in figure 4.7.

The results of this experiment indicate that the high energy washing method is far more effective over at least 5 cycles of washing, when compared to the low energy method. These results led to further testing where the recycling of ESP dust washing water was extended beyond 5 cycles using the high energy method.

4.1.2 Recycling ESP Dust Solids

An alternate test was designed where instead of recycling the washing solution after each wash, the ESP dust solids were recycled and washed with fresh water each time. This was done to support other chemical analysis (SEM EDS, XRF etc) carried out on the raw and washed ESP dust samples showing significant changes to the chemistry of the ESP dust before and after water washing. This also investigates whether there is any value in washing the same dust sample more than once, or if one wash is sufficient to remove the bulk of target elements.

Figure 4.9 clearly shows that chloride is the most dominant element mobilised of the three; with 1,580.0 mg/L (± 434.7) mobilised on average compared to 80.4 mg/L (± 17.7) rubidium and 23.7 mg/L (± 9.5) of lead. It is also clear that most of the elemental mobilisation occurs during the first cycle of washing. When quantified we see that on average, 94.7 % (± 0.8) of all chloride and 91.4 % (± 3.3) of all rubidium mobilisation in this test occurred after just 1 washing cycle. Compared to only 68.1 % (± 11.7) of lead after one wash. After a second wash chloride rose to 99.5 % (± 1.5), rubidium to 97.9 % (± 5.5) and lead recorded 81.8 % (± 16.6).

This lends further support to the idea that rubidium is closely linked to chloride minerals within the ESP dust, as these two elements appear to behave in a similar way during the test. Lead appeared harder to mobilise with water washing, with only approximately 80 % of the total being mobilised after 2 washes, whereas both chloride and rubidium were ≥ 98 % of total mobilisation at this stage. Indicating that if Pb is a target element for removal from ESP dust, further water washing, or alternate methods may be required.

Although there is variation in the total concentrations of chlorides mobilised in these tests due to the heterogenous nature of the ESP dust, the results seem to indicate the impact of washing is consistent. In these tests the chloride concentration in the water after 1 wash ranged between 1235 – 2068 mg/L but the proportion of chloride mobilised after 1 wash was between 94.1 – 95.6 % of the total.

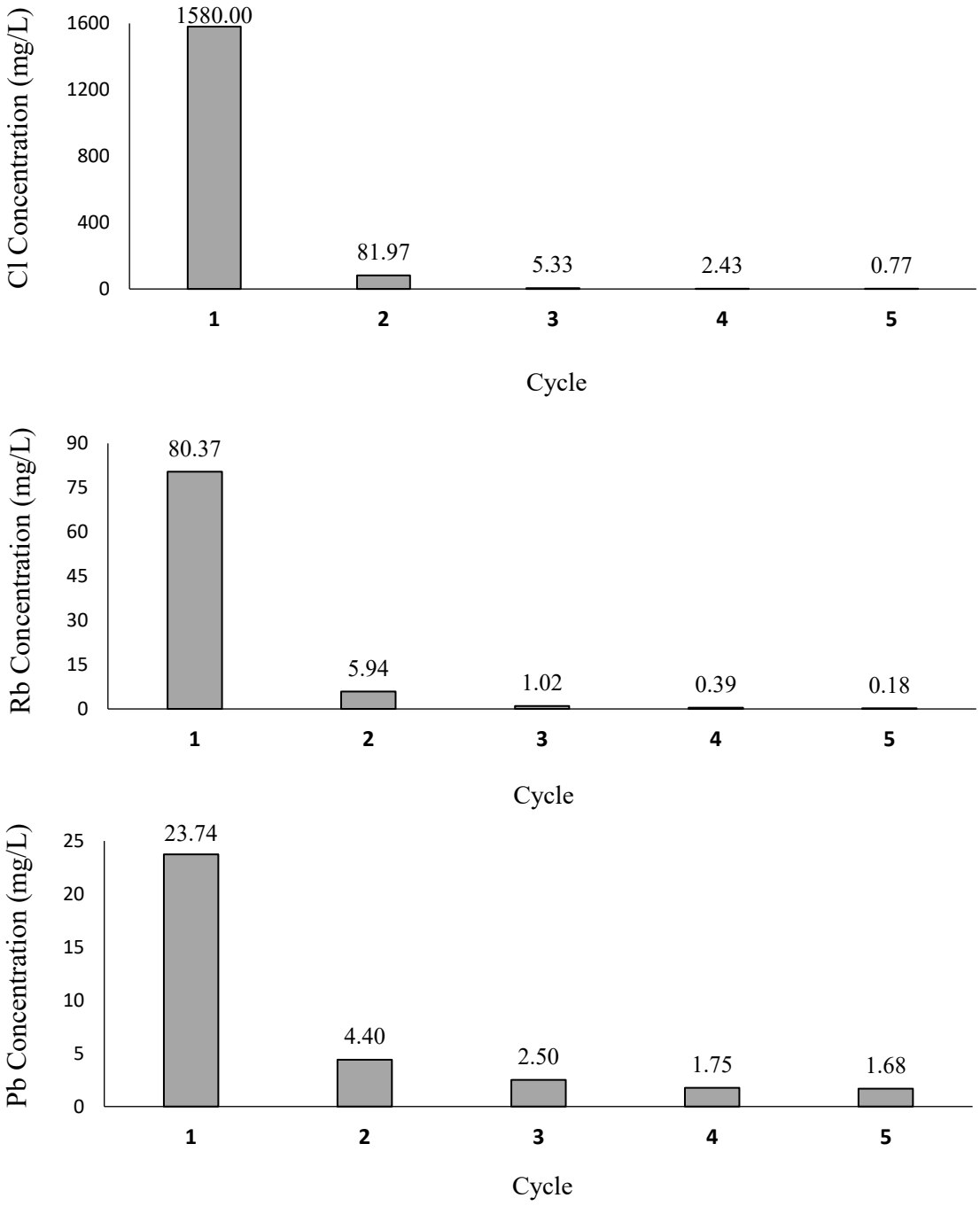

Figure 4.9 Three bar charts showing Cl (top), Rb (middle) and Pb (bottom) concentrations in washing solution when the same ESP dust sample is washed with fresh water in 5 separate cycles.

When assessing the results from mass monitoring throughout the test, figure 4.10 , the most notable drop in mass is seen after round 1 (R1). This being 6.81 g (± 1.39), compared to an average of just 2.51 g (± 0.46) for R2 – R5, this is likely due to the high proportion of soluble elements mobilised after the initial round. With most of the other mass loss due to larger particles being lost during the washing and filtering process.

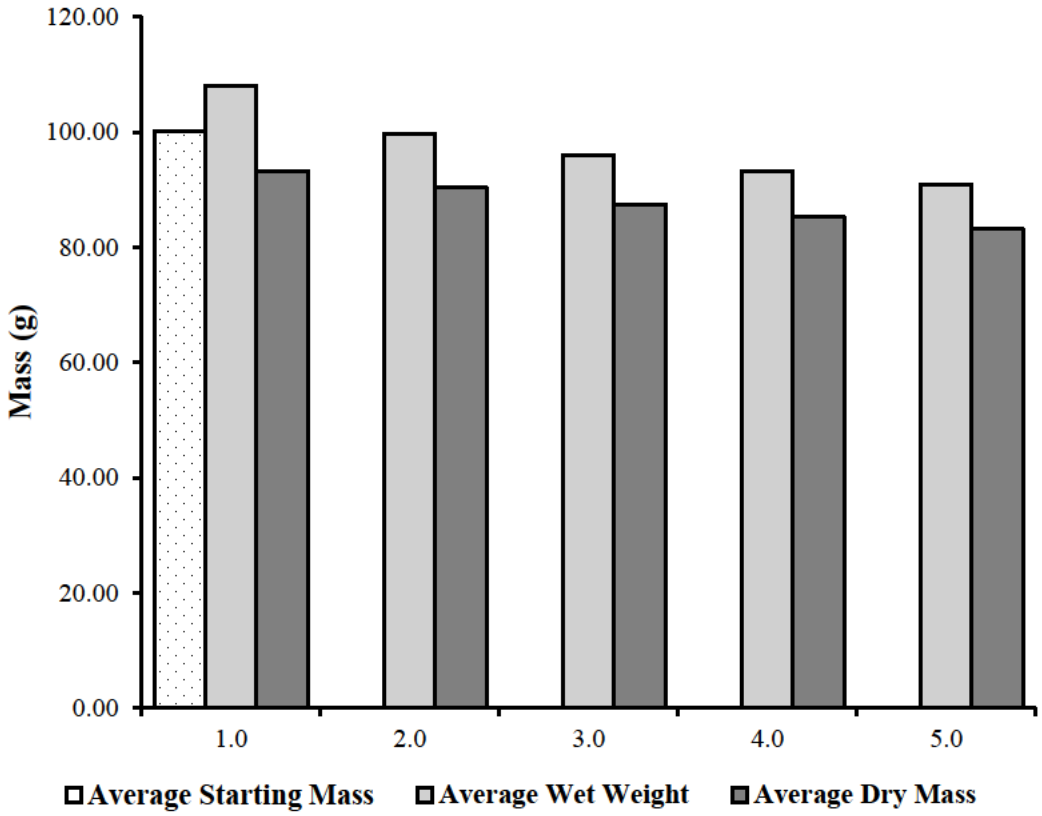

Figure 4.10 Comparison bar chart showing mass data for recycled solid washing experiments.

4.1.3 Extended ESP Dust Washing Water Recycling

Based on the results from the initial sets of testing, which indicated recycling of ESP washing water can be effective for at least 5 cycles, it was then determined that the recycling of ESP dust washing water should be extended to 10 cycles. The aim being to identify if there is a point where the solutions become saturated with soluble elements, requiring the recycling treatment to be restarted with fresh water.

As was done previously, the mass of each sample was measured before, immediately after washing and after drying was completed, this was done to determine the moisture content of the material. The extended test involved 10 stages of recycling the washing water to new ESP dust each time, this was repeated 3 times in total with values being averaged out for each set of tests before finally being averaged once more.

The average initial mass of dust tested was 100.3 g (± 0.26), after washing the mass of wet dust was then at an average of 107.50 g (± 1.57), indicating an average increase of approximately 7.17 g. After being dried the average mass of samples fell by approximately 14.56 g to 92.95 g (±1.45), which is an average of 7.38 g less than the sample's initial mass. Following Equation 3, this results in an average moisture content of 15.70 % over the course of the extended recycle.

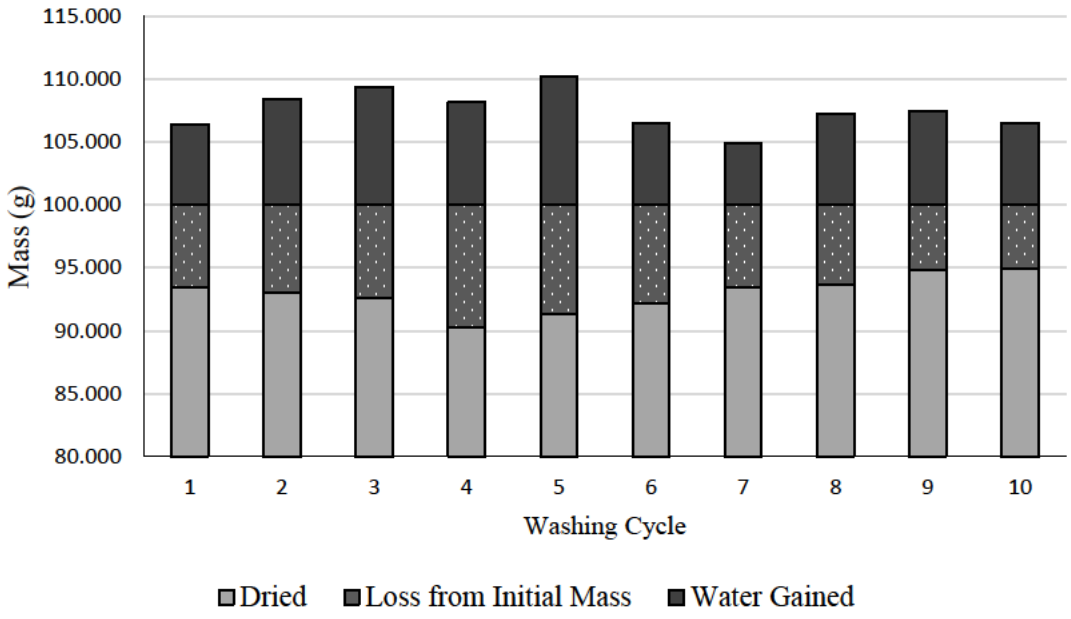

Figure 4.11 Stacked bar chart showing mass change throughout extended ESP dust wash recycling test.

Both the wet and dried average values have similar standard deviations, being within 0.12 g of each other. However, figure 4.11 shows how the mass lost and water gained vary throughout the test cycles, the largest differences in both water uptake and mass loss being between cycles 5 and 7. During cycle 5 the mass increased by 5.30 g more compared to that of cycle 7, indicating that the sample was wetter. The moisture content of samples for cycles 5 and 7 respectively was 20.63 % & 12.27 %. Cycle 5 had the second highest mass loss of 8.68 g, whereas during cycle 7 the dust sample only lost 6.60 g.

There also appears to be more significant water uptake and mass loss over the first 5 cycles of the test compared to the latter 5. Between cycles 1 - 5 the average wet mass was 108.51 g (± 1.40), which was 2.01 g greater than the average of 106.50 g (± 1.02) recorded between cycles 6 – 10. Comparing mass loss between the average wet mass and the average dried mass for cycles 1 – 5 & 6 – 10 shows drops of 16.38 g and 12.73 g respectively. Meaning that on average, tests between cycles 1 – 5, lost 3.65 g more mass than those that came after. This may be due to the solution becoming saturated during the tests, inhibiting its ability to dissolve elements.

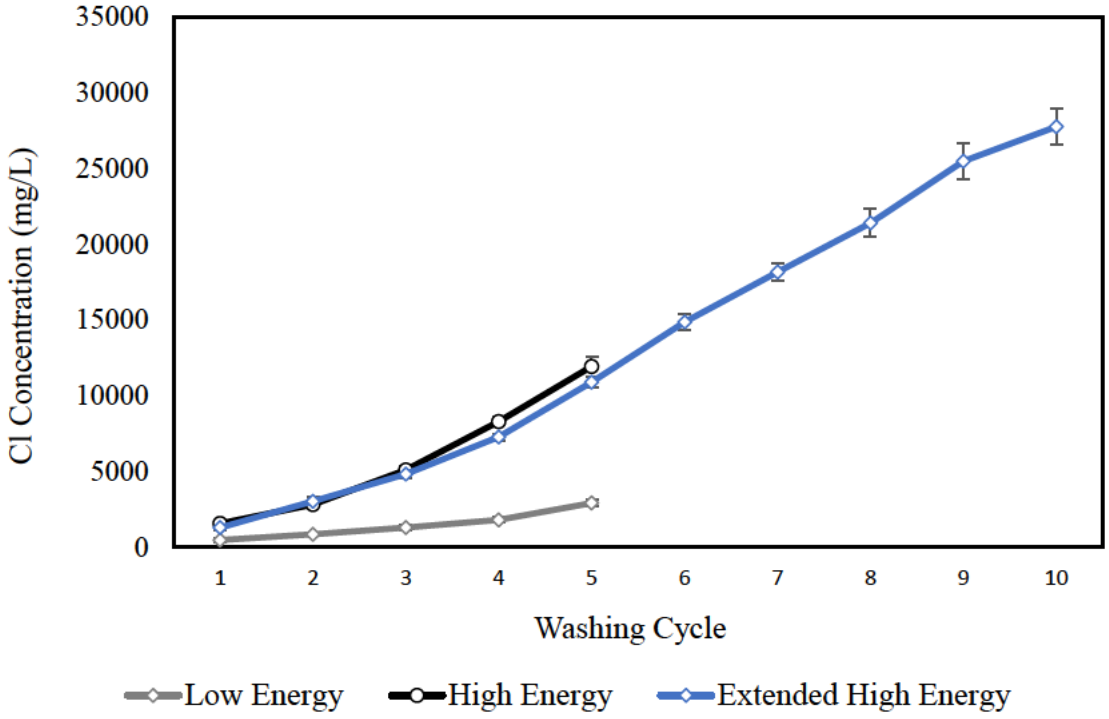

Figure 4.12 Line chart comparing chloride concentrations in low energy washing, high energy washing and extended high energy washing tests.

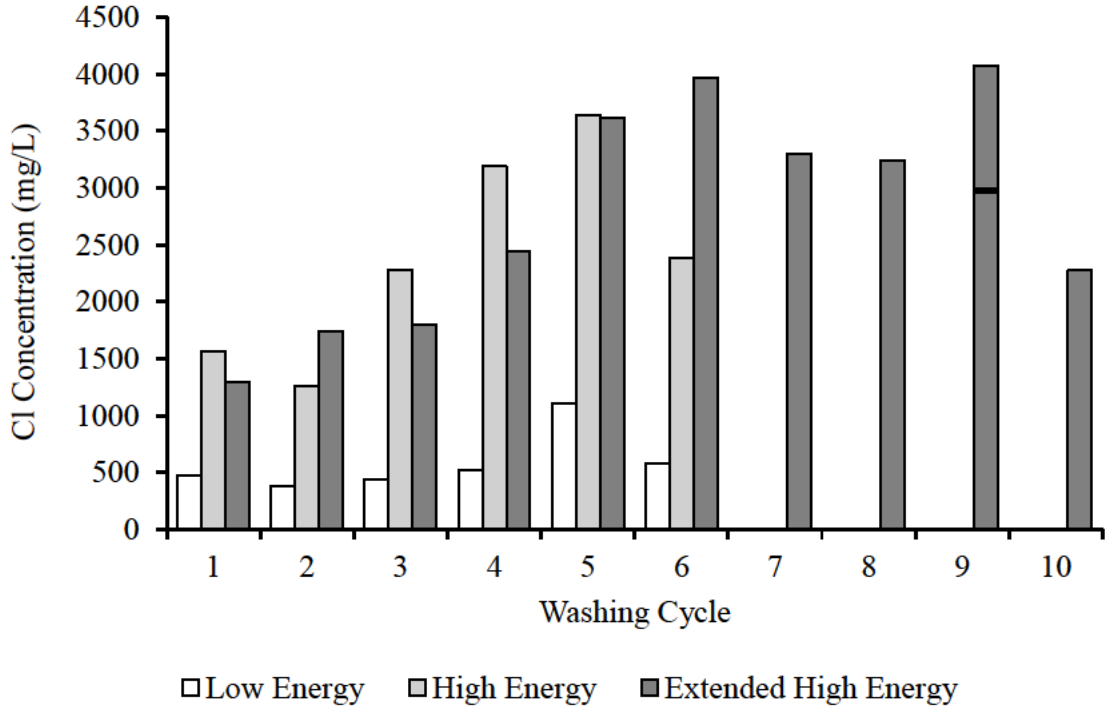

Figure 4.13 Comparison bar chart showing how much Cl was mobilised after each cycle (not cumulative) in low energy, high energy and extended high energy washing tests.

Analysis of the washing solution over the 10 cycles during the extended high energy washing test indicates that it follows a similar trajectory to the original high energy test, even beyond 5 cycles. This is clear in Figure 4.12, where both high energy tests far outperform the low energy test. There also appears to be only a slight decline in effectiveness of washing in the later cycles of 9 – 10.

The peak value after 10 cycles in the extended high energy test reached 27,750 mg/L (± 1168.30) compared to 11,933 mg/L (± 615.11) after 5 cycles in the previous high energy test. This represents an increase of 232.54 % by extending the test to 10 cycles, indicating that it is worthwhile to continue testing for 10 cycles. The variability in the data increases with the number of cycles, in the extended high energy recycle the 3 most variable cycles were 8, 9 & 10. These cycles recorded standard deviations of 940.83 mg/L, 1195.2 mg/L & 1168.3 mg/L respectively. Compared to standard deviations of just 211.24 mg/L in cycle 1, 248.6 mg/L in cycle 2 & 279.55 mg/L in cycle 3.

The amount of chloride mobilised during each cycle is displayed in Figure 4.13, as opposed to the cumulative total in Figure 4.12. Cycle 9 in the extended test clearly has the highest value, an average of 4,076 mg/L (±1989.5) however this is a very high standard deviation. This is caused by one of the tests increasing by 6,255 mg/L compared to the repeats which rose by 3618 mg/L and 2356 mg/L, the standard deviation of the two repeats being ± 892 mg/L. This is still a significant variation however it is much lower than the original for cycle 9. Potentially indicating that the reading of 6,255 mg/L was an outlier in the data as it was the highest value recorded in these tests. The second greatest single increase of chloride was 4,139 mg/L, coming in a cycle 6 test. When ignoring this outlier value, the average mobilisation in cycle 9 drops to 2,987 mg/L, this level is marked on Figure 4.13 with a black line and appears to fit the trend observed between cycles 7 – 10 much better.

The average amount of chloride mobilised between all cycles was 2,666 mg/L (± 424), whereas the lowest average value recorded was 1292 mg/L (± 211) in the initial cycle of washing and cycle 6 held the greatest average mobilisation of 3972 mg/L (± 145). An observation from the first cycle of washing was that some of the dust appeared dry, see Figure 4.14, even after the mechanically assisted water washing. This is likely an effect of the dust's hydrophobic properties, although seemingly this effect is lessened when recycling washing solutions as mobilisation values were higher in every other cycle.

Although there is a clear positive trend in Figure 4.12, when comparing it to the net mobilisations in each cycle seen in Figure 4.13 another trend becomes apparent. After accounting for the outlier value in cycle 9, the overall trend of the graph appears to be a largely steady increase in the amount of chloride mobilised until cycle 6 before the values begin to reduce until cycle 10. This could be an indication that after approximately 6 recycles of the washing solution the effectiveness of the washing begins to reduce. However, the amount of chloride mobilised after cycle 6 averaged 2,950 mg/L (± 470), whereas for the cycles that preceded cycle 6 the average value was 2,178 mg/L (± 902). This may indicate that although there is a reduction in the effectiveness of chloride mobilisation, it is still more effective than early cycles.

This test has supported the findings of the previous work, Figure 4.2, again indicating that high energy washing is more effective and that it the washing solution can be recycled more than 5 cycles effectively.

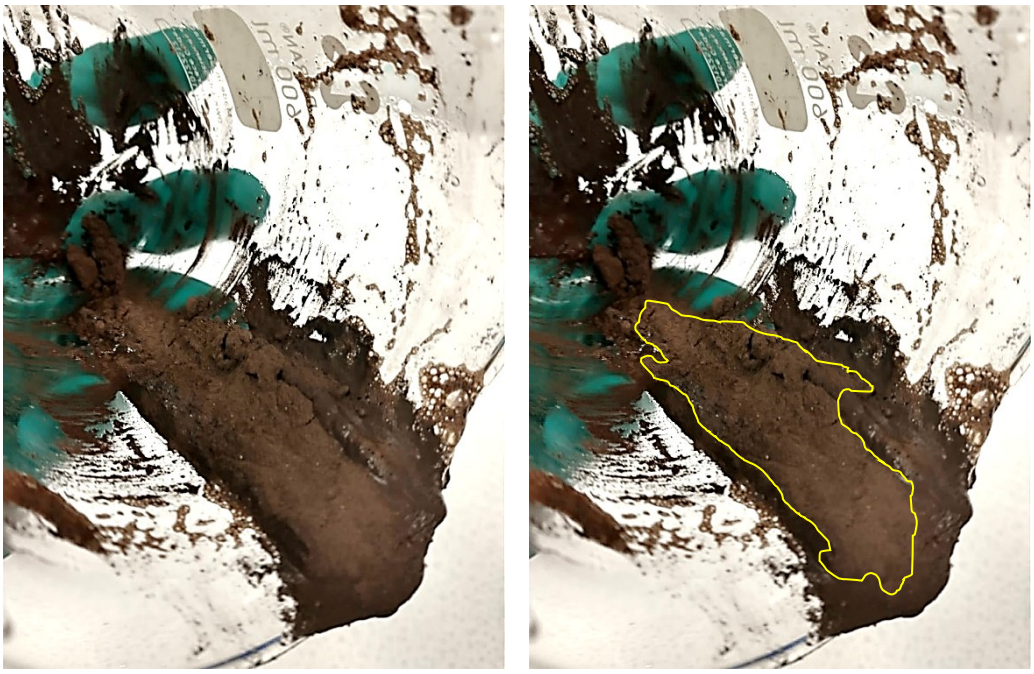

Figure 4.14 Images of ESP dust after first cycle of washing. Original image (left) & edited image to highlight dry portion of dust which remained unwashed.

Rubidium concentrations again followed the trend of chloride when extended to a 10-cycle washing experiment, as can be seen in figure 4.15, as they continued to increase with each cycle and more than doubling its concentration of 361 mg/L from cycle 5 to 858 mg/L after the final cycle. The average increase in rubidium between rounds was 85.8 mg/L (± 35), with the smallest rise being 55 mg/L compared to a maximum of 151 mg/L. These results further indicate that the rubidium present in ESP dust is linked to chloride.

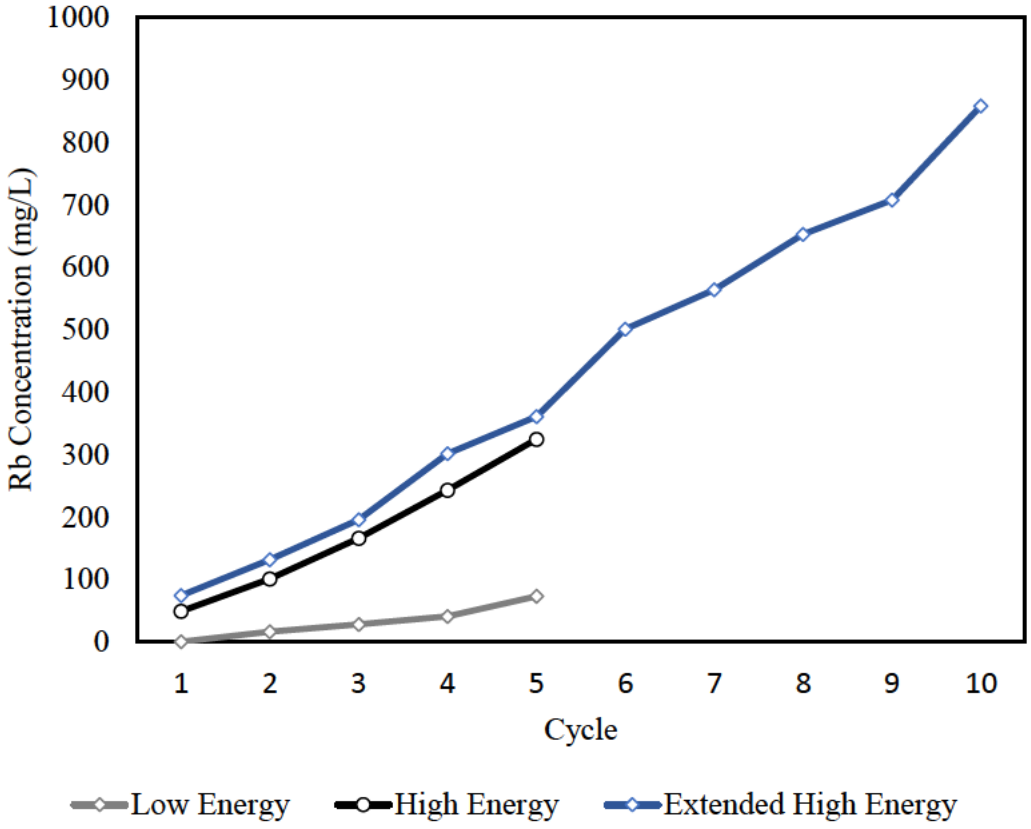

Figure 4.15 Line chart comparing rubidium concentrations in low energy, high energy and extended high energy washing tests.

4.1.4 Addition of Surfactants

At this point in the research, it was determined that including additives, such as surfactants and hydrotropes, to the washing solution may improve washing efficiency. This was to overcome the hydrophobic properties of the ESP dust, as observed in Figure 4.14. Previously outlined in section 2.1.3, the additives selected were TX-100, sodium xylene sulfonate and soap nut powder. TX-100 was selected as it has previously been used in ESP dust washing to tackle hydrophobicity, whereas sodium xylene sulfonate and soap nut were chosen to trial cheaper and less hazardous alternatives. Table 4.1 shows the varying prices and hazards of the additives, these properties would be important when potentially applying this research to an industrial scale.

Table 4.1 Comparison of additives selected for ESP dust washing tests. Prices correct as of time of purchase.

Surfactant	Additive Type	Price (per kg / L)	Hazards
Triton X-100	Liquid Surfactant	£ 47	Corrosive, hazardous, harmful to environment
Sodium Xylene Sulfonate	Liquid Hydrotrope	£ 16	Hazardous
Soap Nut Powder	Solid Surfactant	£ 16	None

4.1.4.1 Initial Tests with Surfactants

Each additive was tested at a concentration of 0.2 %, a baseline deduced from previous research (30), over a 5-cycle test alongside a control test which only used deionised water. The aim being to determine whether the TX-100 which had been previously tested at 0.2% could be directly substituted with alternatives and achieve the same results.

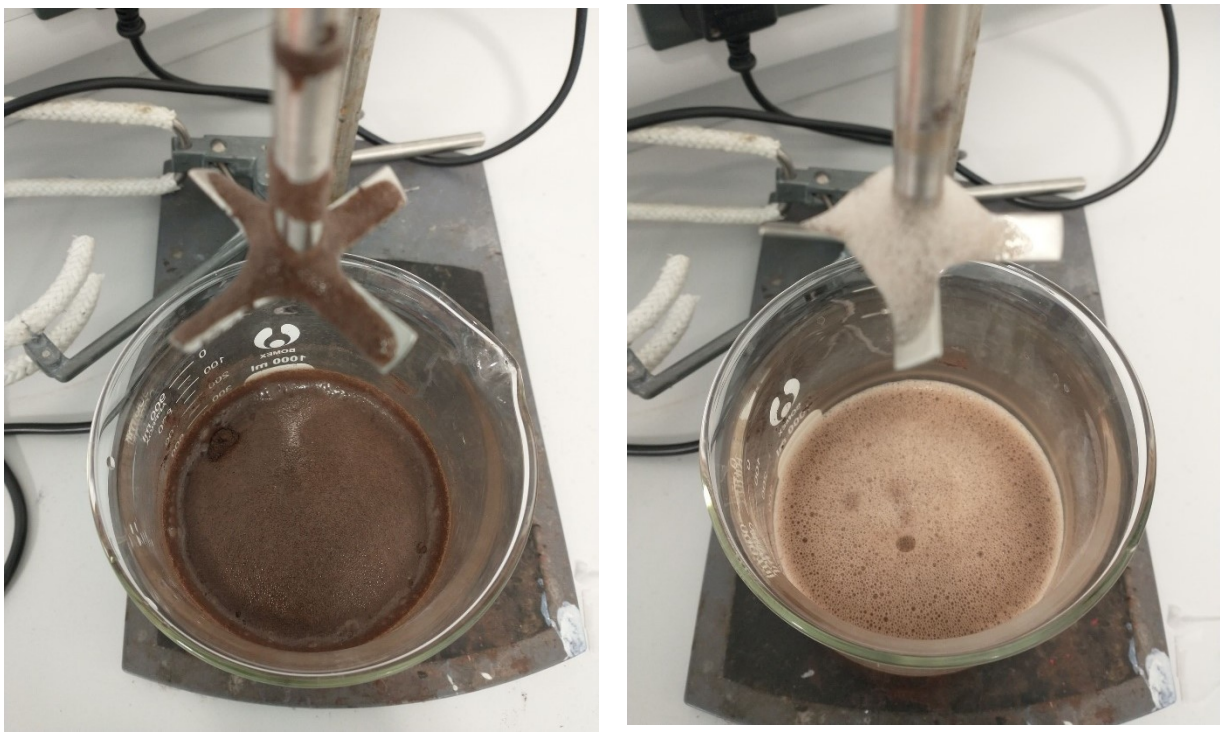

Figure 4.16 Images showing impact of additive addition on ESP dust washing process. Left image showing water washing and the right shows with additives.

One notable impact of including additives in the ESP dust washing process was the improvement to processability and handling of the solution. When running the control test with just water, as was seen in previous tests, the solution after washing was hard to transfer to the filter and behaved like wet sand. Often large portions of dust would cling to the base of the beaker, dry dust was common to be seen, wet dust would cling to the sides of the beaker and the stirrer head, which can be seen in Figure 4.16. Other observations included more retained water in the mixture compared to additive mixtures, seemingly losing more solids during transfers (washing & filtering), however these effects appeared to lessen as more cycles were completed.

The tests including additives however behaved strikingly differently, as can be seen in Figure 4.16 immediately after washing. The surface bubbles are much clearer when using additives and there is no dust clinging to the stirrer head. Transferring the solutions for filtering was significantly more efficient, with the wet mixture being easily moved with very little left behind. Filtering was also faster when using additives compared to the control test. There were however some observations which should be considered when using additives in mechanically stirred washing. The mixture would bubble much more during stirring, potentially to a negative level if either the concentration is too high or the stirring too aggressive. During filtration also, as they were allowed to filter for at least one minute*, if the solution had fully filtered before this

then bubbles would begin to stream through the filter. This is likely due to residual additives in the filter, but these bubbles could end up moving up the tubing towards the vacuum, this could potentially cause damage to equipment if not addressed. These observations will be considered when moving forward with research.

Analysis of dust mass during testing showed similar trends to what had been previously observed and Figure 4.17 shows that most of the tests appear to have behaved similarly. The general trend being that the amount of water retained by the sample increased with the number of cycles, however more detailed analysis of the figures, shown in Table 4.2, reveals some points of interest.

In terms of average moisture content, the control sample recorded 15.60 % (± 1.91), which was followed by the very similar values of 15.65 % (± 2.31) and 16.10 (± 2.59) for the soap nut and sodium xylene sulfonate respectively. The test including TX-100 however had an average of 18.98 (± 2.33). Whilst ± 2.33 is a significant standard deviation for the average moisture content value after washing, all samples had standard deviations between 1.91 – 2.59 %. Potentially indicating that significant standard deviation is to be expected in these tests and is a property of the process.

The TX-100 sample also reported the maximum moisture content of 21.96 % and the highest minimum moisture content of 16.81 %, meaning the lowest moisture content recorded in the TX-100 test exceeded the average values of the control, soap nut and sodium xylene sulfonate. The lowest moisture content recorded in all of the tests was 12.76 % in the control sample, again closely followed by sodium xylene sulfonate and soap nut respectively. It appears that TX-100 has a significant impact on the moisture content level of ESP dust in small-scale washing tests, greater than that of other additives tested.

All the samples had very similar average wet masses, lying between 108.07 g (± 1.17) - 108.88 g (± 0.98), and maximum wet masses which were between 109.36 g – 110.42 g. The minimum wet mass however had more of a spread between the tests, as can be seen in table 6 where the control had the lowest minimum of 106.34 g and the TX-100 test had the greatest minimum of 107.95 g, a difference of 1.16 g. This may be due to the hydrophobicity of the ESP dust inhibiting washing with only water, a hypothesis supported by the moisture content test results.

Table 4.2 Summary of results from the initial ESP dust washing tests featuring a control and 0.2 % of additives as described in the table. SXS = Sodium Xylene Sulfonate.

	Control	0.2 % TX-100	0.2 % Soap Nut	0.2 % SXS
Average Wet Mass (g)	108.29 (± 1.19)	108.88 (± 0.98)	108.07 (± 1.17)	108.39 (± 1.22)
Max Wet Mass (g)	109.36	110.42	109.98	109.87
Minimum Wet Mass (g)	106.34	107.95	107.15	106.93
Average Dry Mass (g)	93.69 (± 0.59)	91.53 (± 1.12)	93.46 (± 1.18)	93.33 (± 1.03)
Max Dry Mass (g)	94.31	92.77	94.77	94.55
Minimum Dry Mass (g)	92.84	90.31	91.95	91.98
Average Moisture Content (%)	15.60 (± 1.91)	18.98 (± 2.33)	15.65 (± 2.31)	16.1 (± 2.59)
Max Moisture Content (%)	17.79	21.96	18.83	19.45
Min Moisture Content (%)	12.76	16.81	13.23	13.09

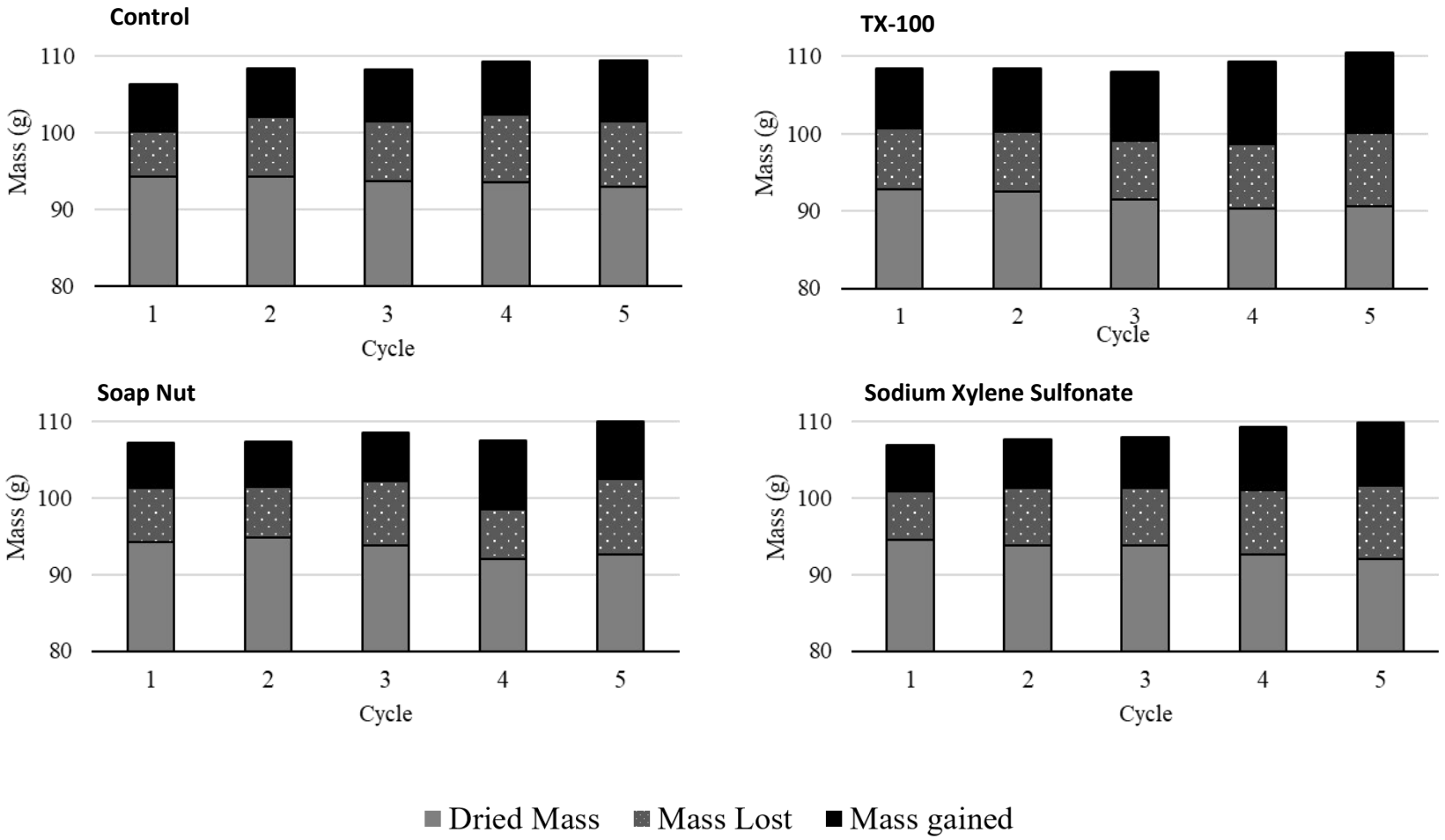

Figure 4.17 Dust mass data before, during and washing for additive washing trials and water control. All graphs start from 80 g on Y axis.

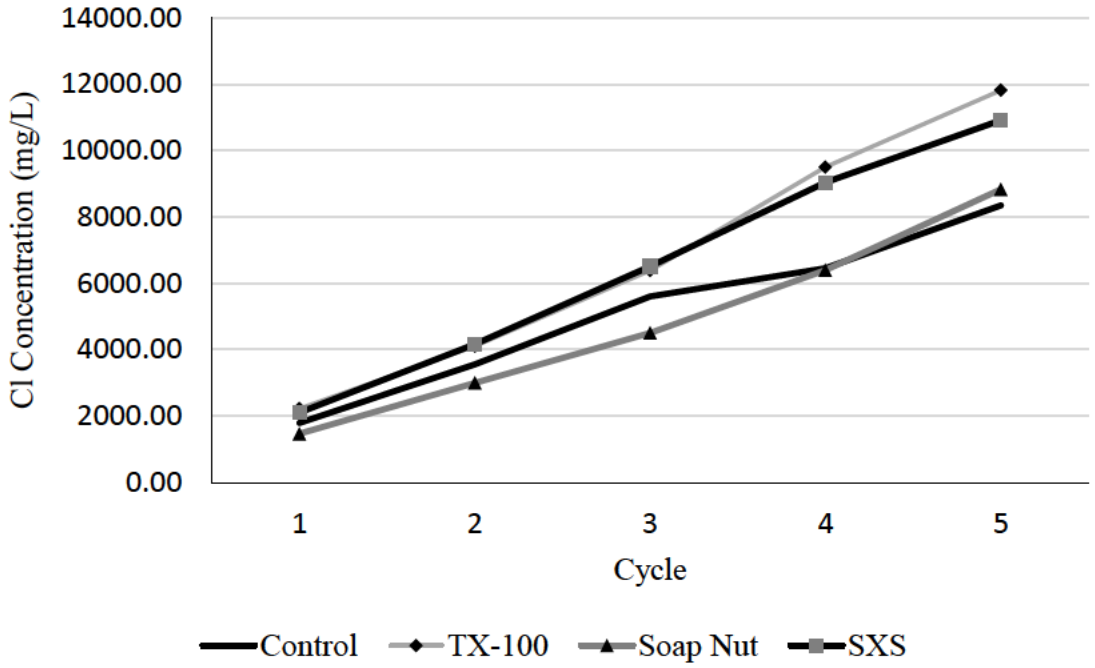

Figure 4.18 Line chart showing chloride concentrations in washing solution samples from initial 0.2 % additive washing trials. (Based off 1 test, samples tested multiple times).

Analysis of the chloride concentration within the washing solution samples is shown in figure 4.18. By the final cycle of the test TX-100 has the greatest average concentration of all samples, this being 11,820 mg/L (± 70.71). Although, during the test it is obvious in figure 4.21 that the sample containing sodium xylene sulfonate very closely follows the behaviour of the TX-100 sample before diverging after cycle 3. Resulting in the sodium xylene sulfonate reading an average of 10,916 mg/L (± 40), approximately 904 mg/L or 8.0 % lower than the TX-100 sample.

The remaining two samples, the water control test and the 0.2 % soap nut, appear to have performed significantly worse than the two samples. From the initial cycle it can be seen that they were lagging behind in terms of concentration and they do not recover this deficit throughout the duration of the test. The baseline test appeared to be outperforming the soap nut sample, until cycle 3 where it only increased by 845 mg/L (± 4), compared to an average of 1876 mg/L (± 129) seen between the other control test cycles. As a drop off such as this is not seen in the other samples tested this could be other results of the hydrophobicity, it was noted that there was dry dust visible in this test after the washing stage, such as that in Figure 4.14.

If the samples are split into two groups based on their performance, the lesser group being the control and soap nuts samples, whereas the more effective group included the TX-100 and sodium xylene sulfonate. The lesser group recorded average peak concentrations after 5 cycles of 8,592.00 mg/L (± 342), whereas the more effective group averaged peak

concentrations of 11,368 mg/L (± 639). This is a significant difference, meaning the control and soap nut approximately mobilised 2,776 mg/L, or approximately 24 %, less chloride from the ESP dust over 5 cycles. Rubidium concentrations in the washing solutions were also tested after this experiment, the results of which are shown in Figure 4.19.

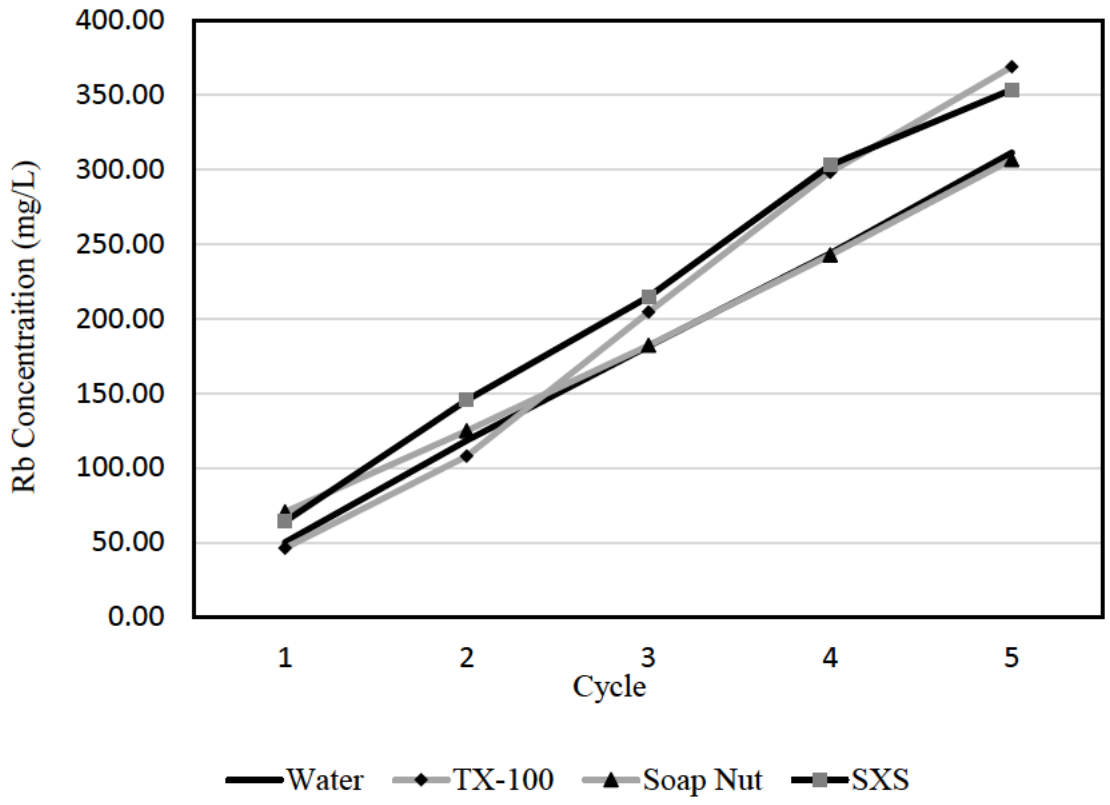

Figure 4.19 Line graph comparing rubidium concentrations between samples from initial additive ESP dust washing experiments.

The initial observation when looking at Figure 4.19 is that it shares a strong resemblance to the chloride concentrations recorded in the same samples. With TX-100 and sodium xylene sulfonate recording the highest average values of 369 mg/L (± 49) & 354 mg/L (± 9) respectively. Compared to the lower values of 307 mg/L (± 15) and 311 mg/L (± 24) for soap nut and water respectively. A point of note is the high variability recorded in the TX-100, the three results recorded from this test were 314 mg/L, 385 mg/L & 408 mg/L. It is hard to label the 314 mg/L an outlier, as it is within the range of overall results, however when discounting it the TX-100 rubidium concentration rises to 397 mg/L (± 16). The variation for this figure appears much more in line with the other tests, although as noted, the 314 mg/L is within the range of 286 – 408 mg/L recorded between all tests.

Table 4.3 Summary of average rubidium mobilised after each cycle during initial additives ESP dust washing experiments.

(mg/L)	1	2	3	4	5
Water	50.00	68.33	63.33	62.00	67.67
TX-100	46.13	61.67	96.53	94.00	70.67
Soap Nut	70.33	54.33	57.33	60.67	64.00
SXS	64.00	81.33	69.33	88.33	50.67

The average amount of rubidium mobilised between each washing cycle ranged between 46 mg/L to 96.53 mg/L, as shown in Table 4.3. The average amount of rubidium mobilised across all tests rose from a low of 58 mg/L (± 11) in cycle 1 to 63 mg/L (± 9), with the highest average mobilisation across all tests being 76 mg/L (± 17) which occurred after cycle 4. TX-100 unsurprisingly had the highest average mobilisation per cycle of 74 mg/L (± 21), whereas soap nut had the lowest value of 61 mg/L (± 6).

These results indicate that the addition additives such as surfactants and hydrotropes improve the processability of ESP dust during water washing. TX-100 and sodium xylene sulfonate, even at low concentrations of 0.2 %, can be effective in mobilising chloride and rubidium from ESP dust during washing. Based on these initial tests the addition of soap nut appears to have minimal impact on chloride mobilisation, although there did appear to be an improvement in the processability of the material during washing. It was decided that the test would be extended to 10 cycles, as was done previously.

4.1.4.2 Extended Additive ESP Dust Washing

As with the initial additive ESP dust washing tests, it was found that when using the additives, the processability of the washing process was much improved compared to washing with only water. This included less particles sticking to washing equipment (e.g., stirrers, beakers), easier transfer from washing beaker to filter funnel and faster filtering. Further time will be spent investigating the physical impacts of including additives in ESP dust washing in a later section.

Chloride concentration data from the experiment which extended the 0.2 % additive cycles from 5 to 10 are shown in Figure 4.21, alongside data from the extended control test. As with other tests, the general trend is an increase in chloride concentrations as more washing cycles are completed. This experiment however appears to show that the control test, utilising only water, was the least effective as it trails behind the other tests for the duration of 10 cycles. Soap nut appears more effective on average compared to previous tests; however, it is still the worst performing additive. After closely following the TX-100 and sodium xylene sulfonate performance between rounds 1 – 5 it begins to lag behind and slowly converge with water.

This effect can be seen in the rate of mobilisation over the last 5 cycles. Falling by approximately 17 % from 3,458 mg/L (± 553) per cycle over cycles 1 – 5 to 2,893 mg/L (± 519) per cycle between cycles 6 – 10. The control test however was the only one to increase its mobilisation rate per cycle in the latter half of the experiment, rising by approximately 54 % from 2,178 mg/L (± 902) per cycle to 3,372 mg/L (± 722) per cycle. The greatest average chloride mobilisation over all tests was seen in the 0.2 % TX-100 experiment, with an average of 3,596 mg/L (± 693) per cycle across all tests. Figure 4.22 also further highlights the slow start for the water test, with the water test mobilising approximately 1694 mg/L less on average when compared to the tests featuring additives between cycles 1 – 4. The water test then begins to fall in line with the additive samples, potentially indicating the change in pH and soluble elements aid the water to mobilise chloride.

In figure 4.21 the control test peaked at 27,750 mg/L (± 1168) after 10 cycles, compared to 31,756 mg/L (± 916) in the 0.2 % soap nut test, 34,784 mg/L (± 459) for the 0.2 % sodium xylene sulfonate and 35964 mg/L (± 1005) in the test featuring 0.2 % TX-100. Seemingly indicating that additives do aid the mobilisation of chloride from ESP dust during water washing, with TX-100 and sodium xylene being the most effective.

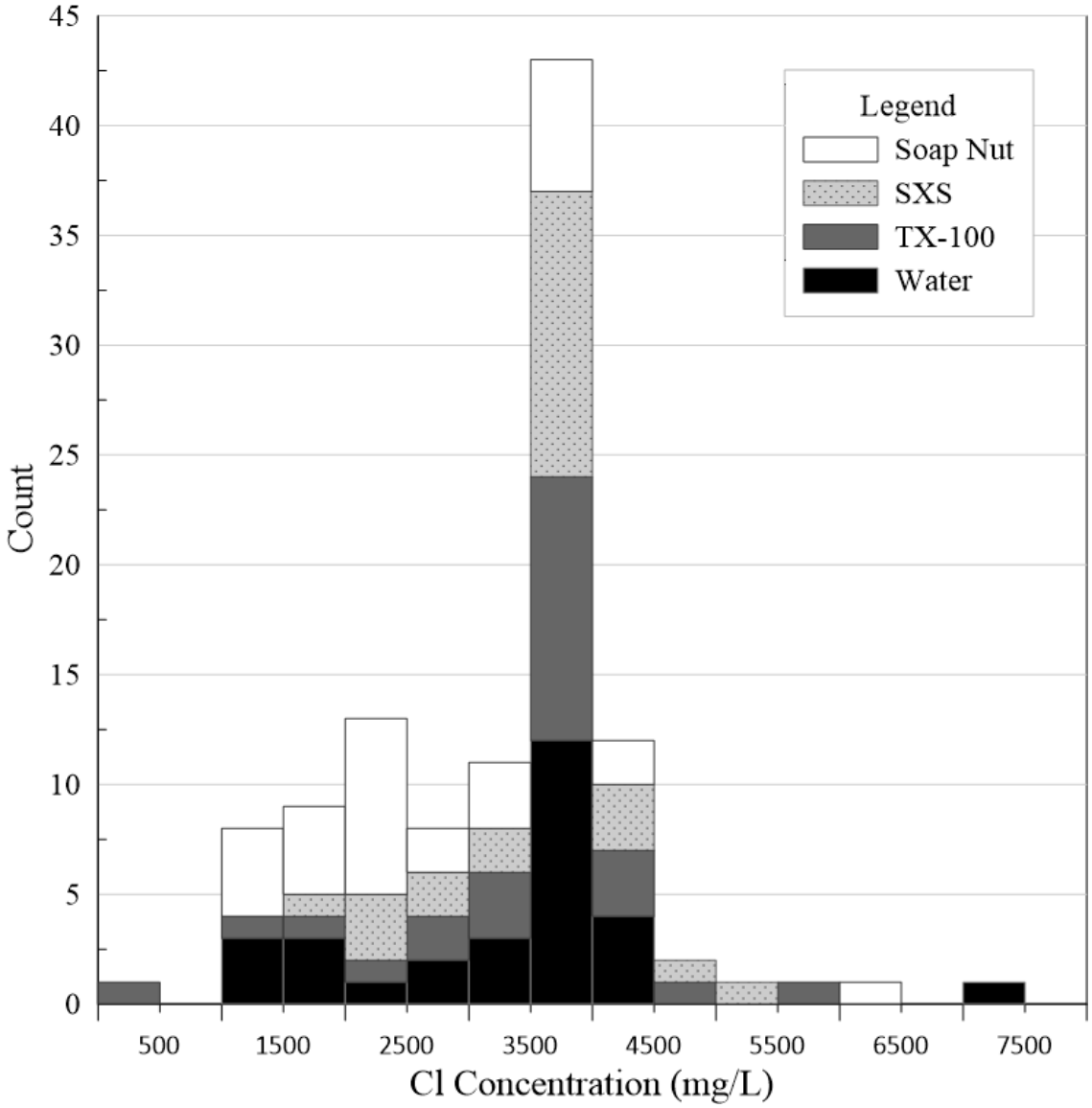

Figure 4.20 Stacked histogram showing distribution of chloride mobilisation for each wash cycle tested.

When analysing the data there appears to be washing cycles where the process is ineffective. This has been noted previously in this research, often they could be linked to tests where dry dust after washing was observed. Figure 4.20 displays a histogram of all results from this series of tests, illustrating the distribution of the chloride mobilisations in terms of concentrations and frequency.

With the median of this dataset being 3,558 mg/L, the lower and upper limits for outliers would be approximately 1925 mg/L and 5,192 mg/L respectively. Meaning 92 of the 111 values fall within this range, of the outliers 15 of the 19 fell below the lower limit, indicating that the

data has a negative skew. By far the most densely populated concentration bracket is 3500 – 4000 mg/L with 43 counts, and when expanding this to 3000 – 4500 mg/L the count rises to 66 which is just over half of the total values. This supports other analysis indicating ESP chloride concentrations

The tests which exceeded the upper limit may not necessarily be seen as a negative, as these are instances of high mobilisation which would be an attractive prospect when washing ESP dust although the cause of these instances needs to be understood. As mentioned however, 15 of the 19 outliers are found to be under the lower limit, this is something which would impact washing efficiency on larger scales and also needs to be understood. Of these 15 lower limit outliers 7 occur within the first 3 cycles of the water experiment and a further 4 occurred in the last 3 cycles of the soap nut test. This obviously feeds into the trend seen in Figure 4.22.

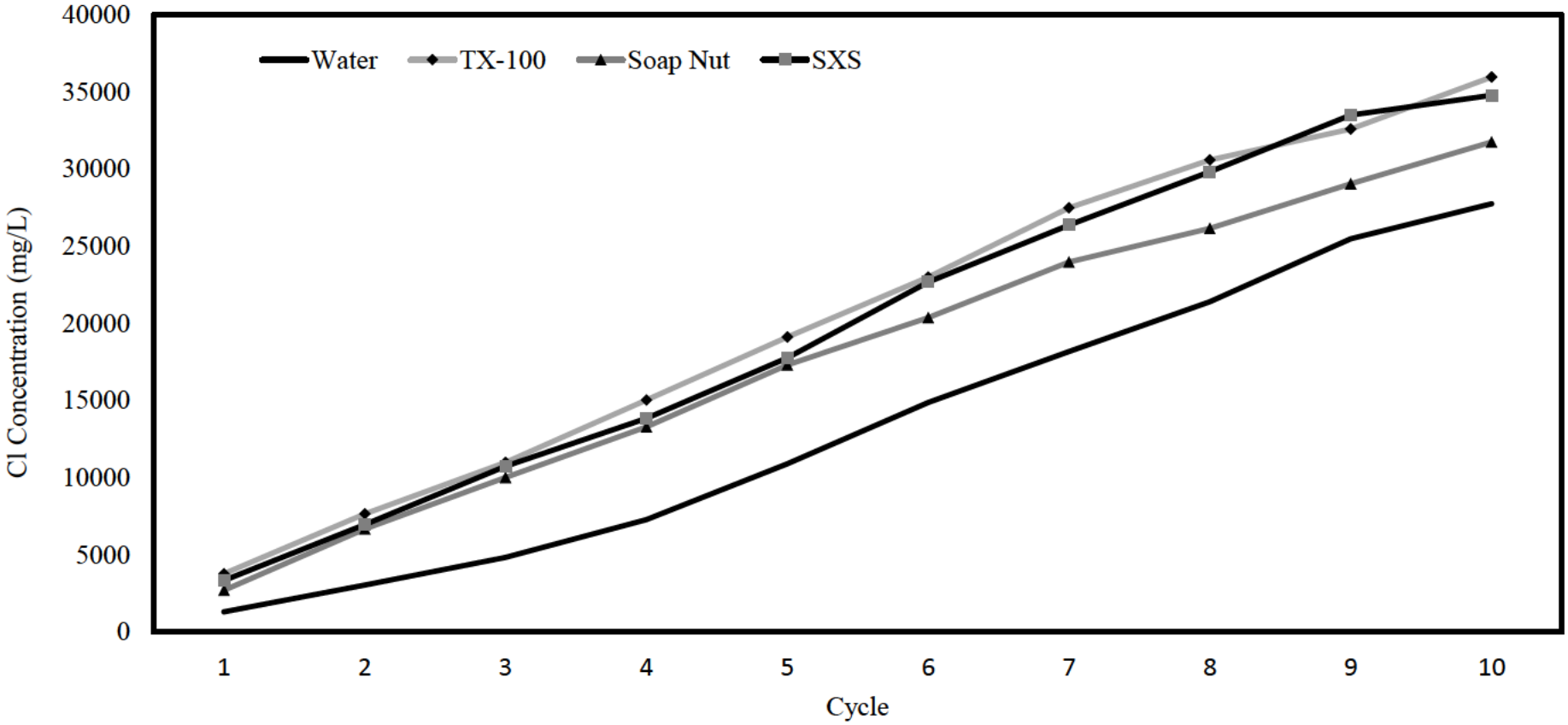

Figure 4.21 Line chart showing chloride concentrations from extended washing tests featuring 0.2 % additives and a water control.

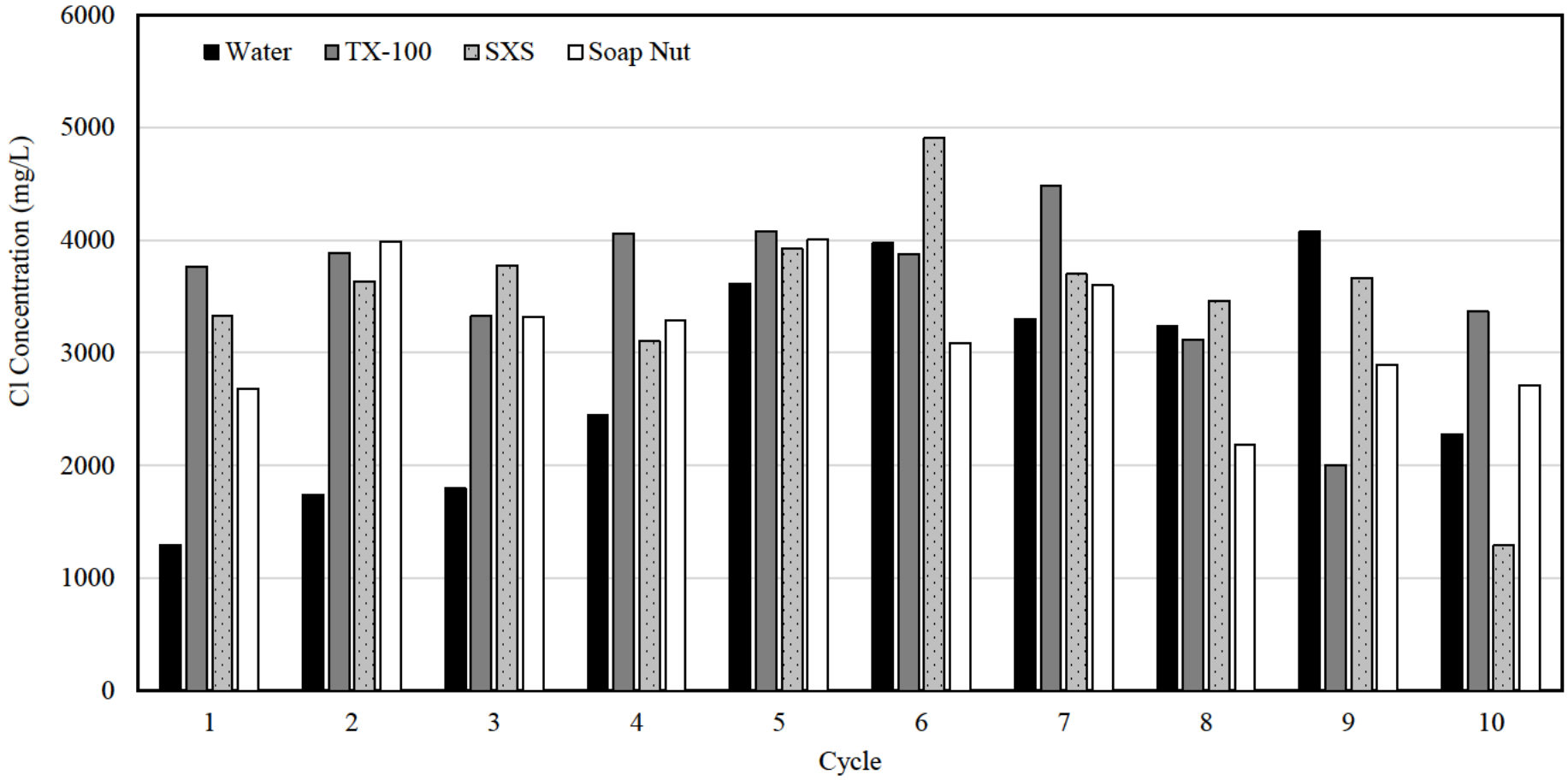

Figure 4.22 Comparison bar chart highlighting chloride mobilisation between cycles during the 0.2 % additive extended trial.

4.1.4.3 High Concentration Extended Tests

Following the 0.2 % additive 10 round washing experiments the test was repeated however the additive concentration was increased to 2.0 %. This substantial increase in surfactant concentration was chosen to highlight any significant improvements in dust washing, which could then be investigated using lower concentrations to find optimal concentration. As with all other tests featuring additives, observations during testing were that the process appeared much easier when compared to using only water although the increase in concentration did not seem to result in an improvement in processability.

Chloride concentration in washing solutions over the course of 10 cycles are shown in Figure 4.23 and once again TX-100 mobilised the most chloride throughout the test. The sodium xylene sulfonate solution is again the second most effective solution, whereas the soap nut solution appears less effective as it closely follows the water test.

The final value for the 2.0 % TX-100 solution after the 10 cycles being 38,034 mg/L (± 4,669), which is approximately 37 % greater than the water control test which recorded 27,750 mg/L (± 1168). When compared to the 0.2 % TX-100 test the increase to 2.0 % also appears to have had a slight impact on chloride mobilisation, as it rose from 35,964 mg/L (± 1005) or approximately 7 %. Variability however brings both the 0.2 % and 2.0 % solutions closer in terms of total chloride mobilised. These results further support the addition of TX-100 to ESP dust washing processes, both to improve processability and to increase chloride mobilisation rates. However, increasing the concentration utilised to 2.0 % may not prove cost effective at industrial scale.

The sodium xylene sulfonate solution peaked at 32,987 mg/L (± 1097) after 10 cycles, approximately 18 % more when compared to the control test. However, interestingly this was approximately 5 % less than the 0.2 % sodium xylene sulfonate test. When accounting for the variability in each sample however, the 0.2 % lower limit is 34,325 mg/L and the upper limit for the 2.0 % reaches 34,084 mg/L, a difference of only 241 mg/L or approximately 0.7 % of each samples total.

Soap nut appears to have significantly dropped from the 0.2 % test. It should be noted that the sample from cycle 8 from test 1 was lost before it could be analysed for chloride concentration. However, test 1 recorded significantly lower results compared to repeats 2 & 3, meaning the loss of this lower value for cycle 8 raised the overall average. This is clear in Figure 4.23 as there is a sudden spike in chloride concentration. The results from the 2.0 % soap nut

repeats were 19,216 mg/L, 31,214 mg/L and 32,730 mg/L for repeats 1 – 3 respectively. When discounting results from repeat 1, the overall average for 2.0 % soap nut rises from 27,720 mg/L (± 7,404) to 31,972 mg/L (± 1072). This would therefore show the addition of 2.0 % soap nut does improve chloride mobilisation when compared to only using water by approximately 15 %. In comparison the 0.2 % soap nut solution test measured 31,756 mg/L (± 916) after 10 cycles, indicating that increasing soap nut from 0.2 % to 2.0 % has almost no impact on chloride mobilisation but the addition of soap nut does improve chloride mobilisation when compared to water.

The amount of chloride mobilised between each round was calculated and is displayed in histogram format in Figure 4.24. Whilst all 3 distributions are different, the soap nut sample appears the most unique. It has a bimodal distribution with a negative skew, whereas both the TX-100 and the sodium xylene sulfonate samples have much more normal distributions, with the TX-100 appearing to have a slightly more normal distribution. The most common bracket of chloride concentration in both the TX-100 and sodium xylene sulfonate was between 3,500 mg/L – 4,000 mg/L. These samples had counts of 8 and 10 cycle washing within this bracket respectively, compared to just 4 in the soap nut sample. The most populous bracket for the soap nut sample was the 3,000 mg/L – 3,500 mg/L range with a count of 7.

When analysing the median of the data to identify outliers there are 3 that occur in the TX-100 test, 2 negative and 1 positive. Due to its relatively normal distribution this low number of outliers would be expected and indicates the mobilisation when using TX-100 is more consistent, potentially overcoming hydrophobicity more effectively than the other additives. By comparison, sodium xylene sulfonate has 6 negative outliers from the median and 2 positives. Soap nut again has far more outliers compared to TX-100, 12 in total with 9 being negative and 3 being positive. This distribution of outliers can be seen as an indicator of effectiveness, as negative outliers indicate the sample being less effective in mobilising chloride from ESP dust. These results also line up with results seen in Figure 4.23, where TX-100 is the most effective and soap nut is the least.

Though Figure 4.24 shows the distribution of wash cycle chloride concentrations, it does not show at which point in the 10-cycle washing process these occurred. Until cycle 5 the control test, featuring only water, mobilised the least chloride of all samples, however in cycles 5, 6, 7 and 10 water does outperform the 2.0 % soap nut. Cycle 8 appears to be the most effective cycle across all additive wash cycles, with an average of 4,857 mg/L (± 448). Overall,

however there appears to be not strong trends across the dataset, which further highlights the variability of ESP dust washing at this scale.

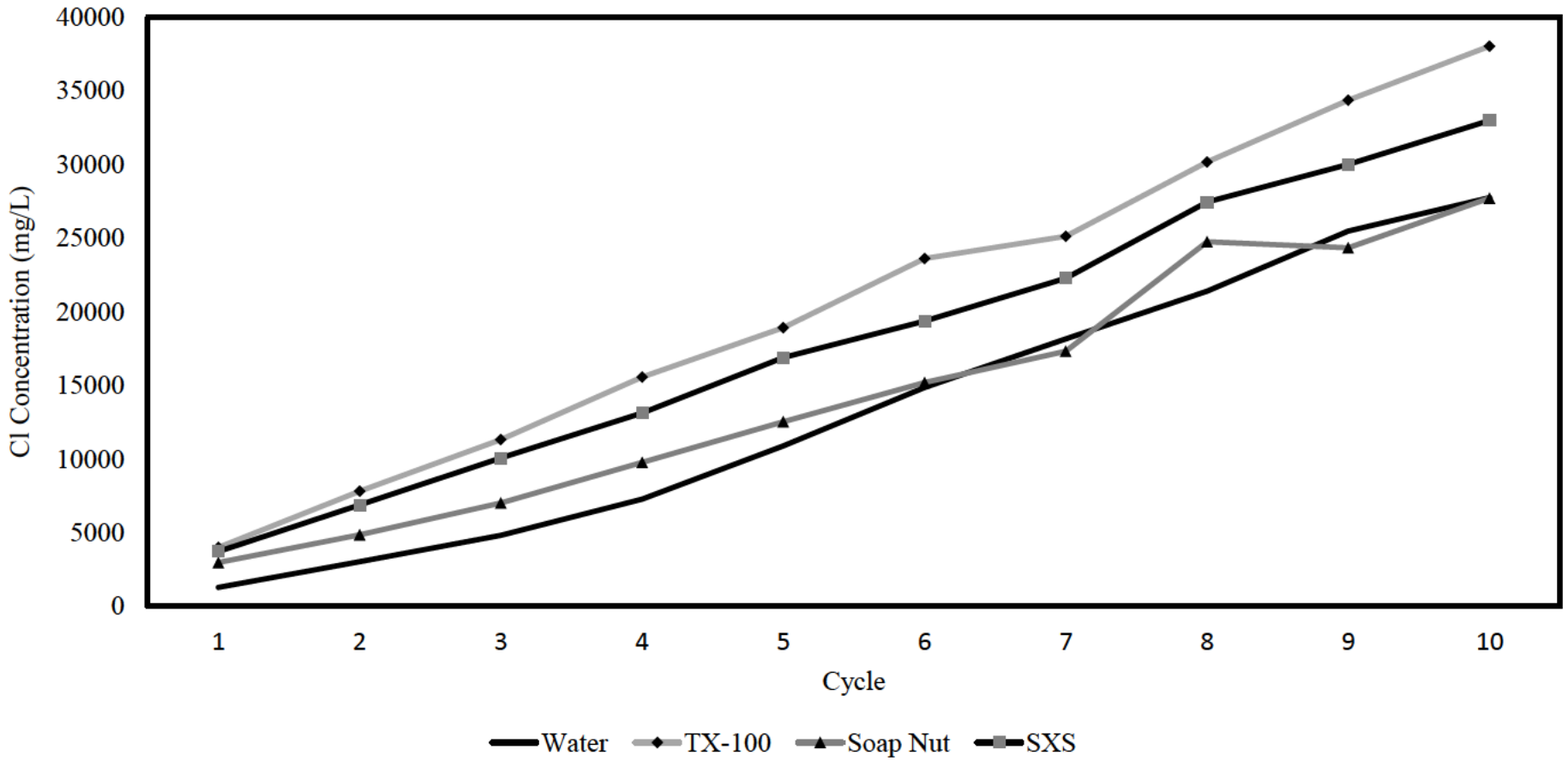

Figure 4.23 Line graph illustrating total chloride mobilisation over 10 ESP dust washing cycles for water, 2.0 % TX-100, 2.0 % soap nut and 2.0 % sodium xylene sulfonate (SXS).

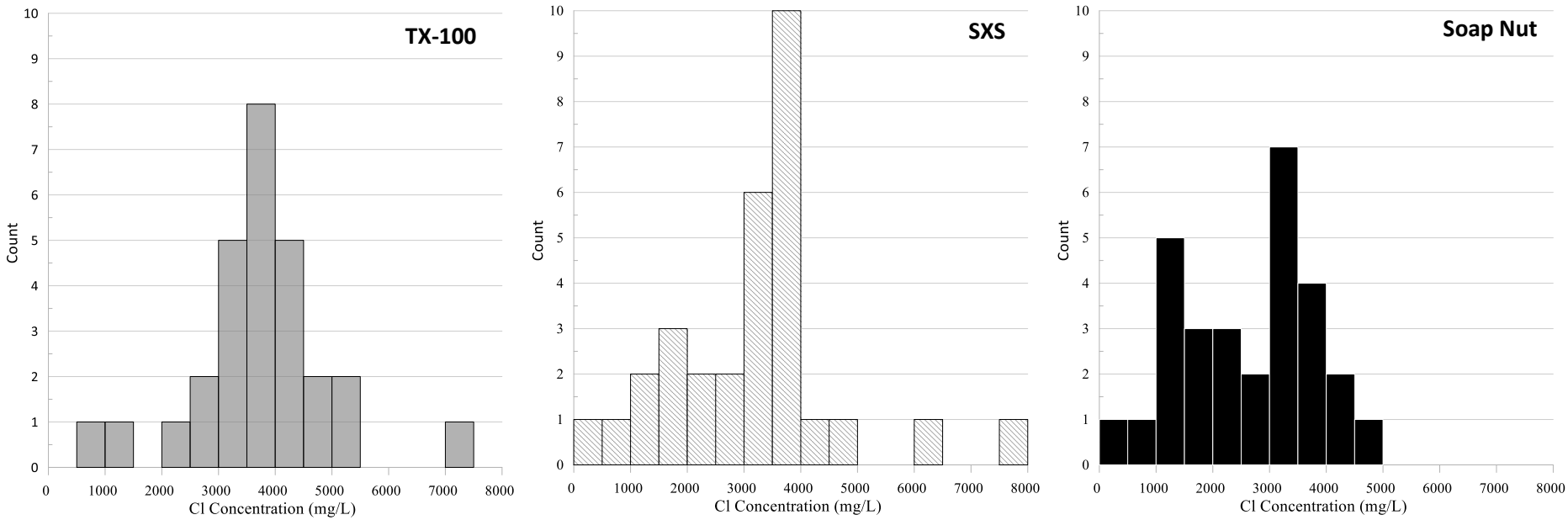

Figure 4.24 Histograms highlighting distribution of chloride mobilisation between rounds for TX-100, sodium xylene sulfonate (SXS) and soap nut.

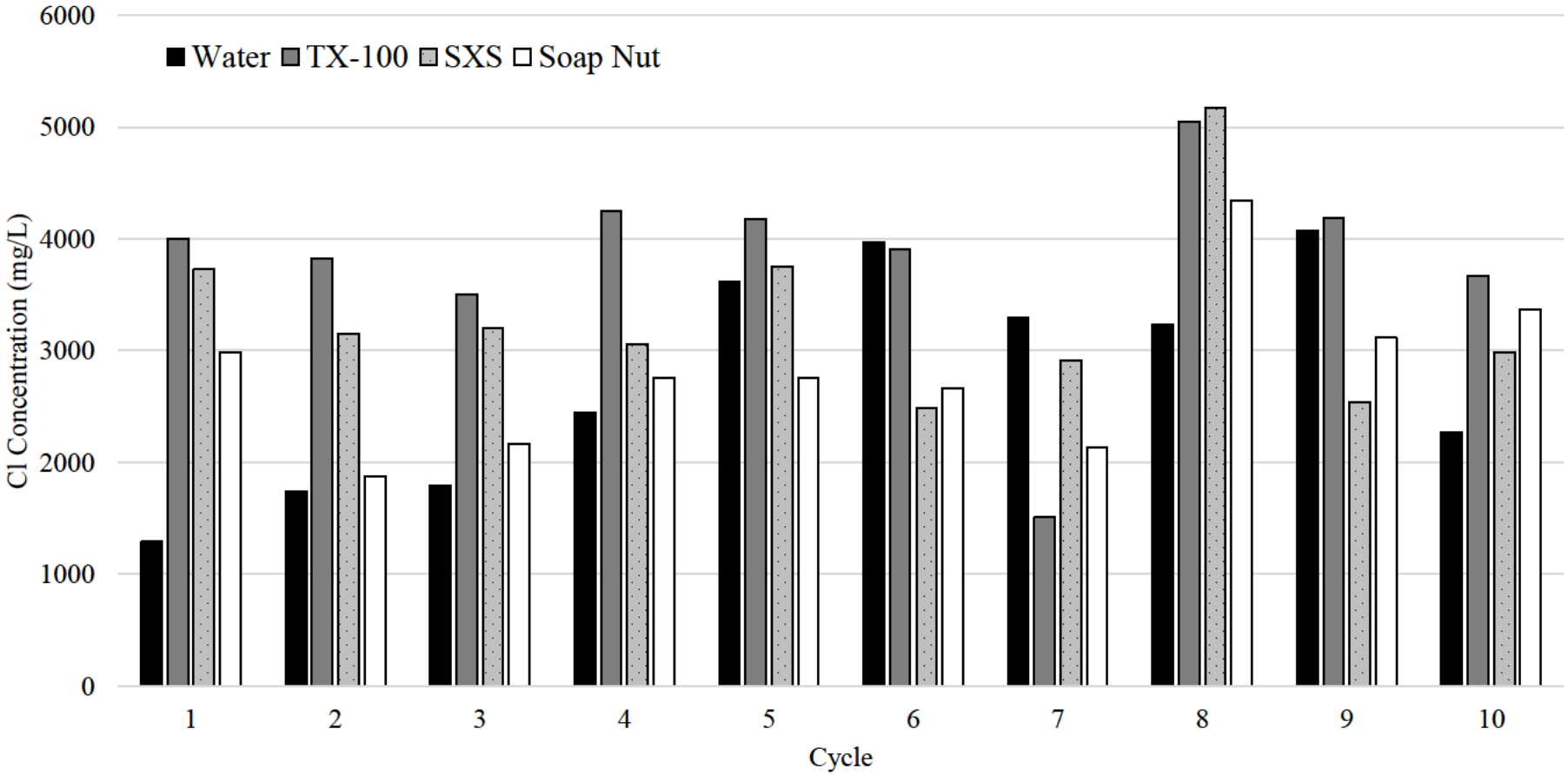

Figure 4.25 Comparison bar chart highlighting chloride mobilisation between cycles during the 2.0 % additive extended trial.

4.1.4.4 Separation of Heavy and Light Solids

After carrying out significant testing featuring additives and noticing differences in processing and solids resulting from filtering in other work, testing was carried out focusing on the impact of additives on solids filtered. The findings will be discussed in this section.

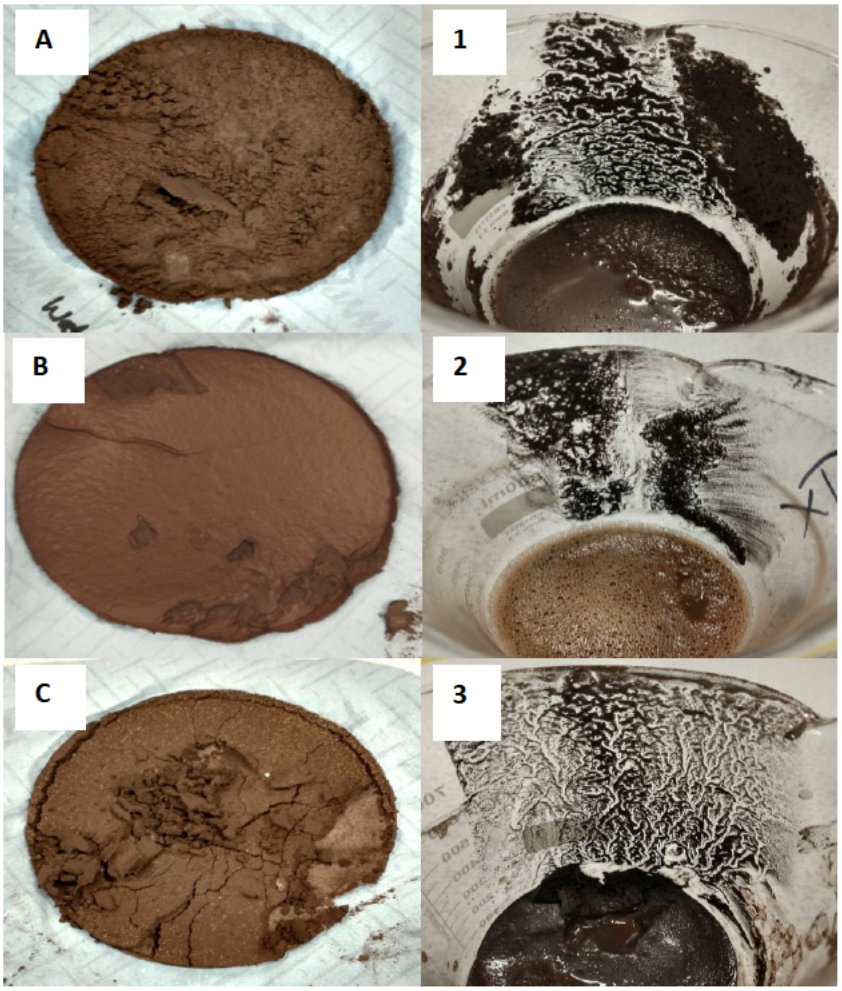

Figure 4.26 Images from testing highlighting differences in 'light' and 'heavy' particles. A/1 Water, B/2 TX-100, C/3 Soap Nut.

When using pure deionised water, a poorly mixed split solution was observed when pouring, a mixture of water and a mirky brown viscous solution. Dry hydrophobic surface dust particles could be seen before, during and after pouring. The mixture filtered within 2 minutes, like soap nut. The pour pattern left in the beaker appeared different to other tests and significant amounts of dust could be seen around the whole glass, something not observed in the tests featuring surfactants. The filtered solids settled roughly topographically speaking and were still slightly wet.

When 2.0 % TX-100 was added to the washing solution there were significant visible differences, rather than a split solution it resulted in one mirky brown viscous solution. Similar to part of the split solution seen in the other tests. The filtering stage was notably slower in this test, exceeding 3 minutes, with lots of bubbles in the solution. The material captured on the filter resulted in a smooth and shiny surface. The beaker's pour pattern was again unique when compared to the other test, shown in image 2 of Figure 4.26, showing a dominant channel rather than intricate smaller pathways. Resulting filtered solids had a sheen and formed a smooth surface. Lots of bubbles and moisture could be seen in remaining heavy solids, significantly more than in other tests.

The solution featuring 2.0 % soap nut also appeared split whilst transferring it to the filter funnel: a clear, yellow liquid and a more viscous brown solution. This solution also filtered very efficiently, however there were no hydrophobic particles observed. After pouring it was noticed that a dendritic pattern remained in the beaker. The filtered material was dry, smooth, matte and soap nut particles were visible within the filtered solids. Image C of Figure 4.26 it is clear that the solids are dry, cracking easily even when only being carefully transferred for imaging.

All samples were then dried at 100 °C for 24 hours to remove any residual moisture. Once this was completed, samples of each material were taken for imaging with a Keyence microscope which are shown in figure 4.27.

The heavy portion of the TX-100 and soap nut samples appear similar, appearing to consist of a much more significant proportion of larger particles compared to the light images. These angular particles vary in size but are dominated by particles in the range of 50 – 250 μm and are silver-metallic and iron oxide orange in colour. There appears to be some visible soap nut particles in the bottom left of the soap nut heavy image, although clearly more soap nut particles ended up in the light portion, likely due to their low density. In contrast, the water heavy particles appear to have much less void space between them, a higher proportion of smaller particles and the iron oxide orange colour seems to dominate the image. This may indicate less effective washing.

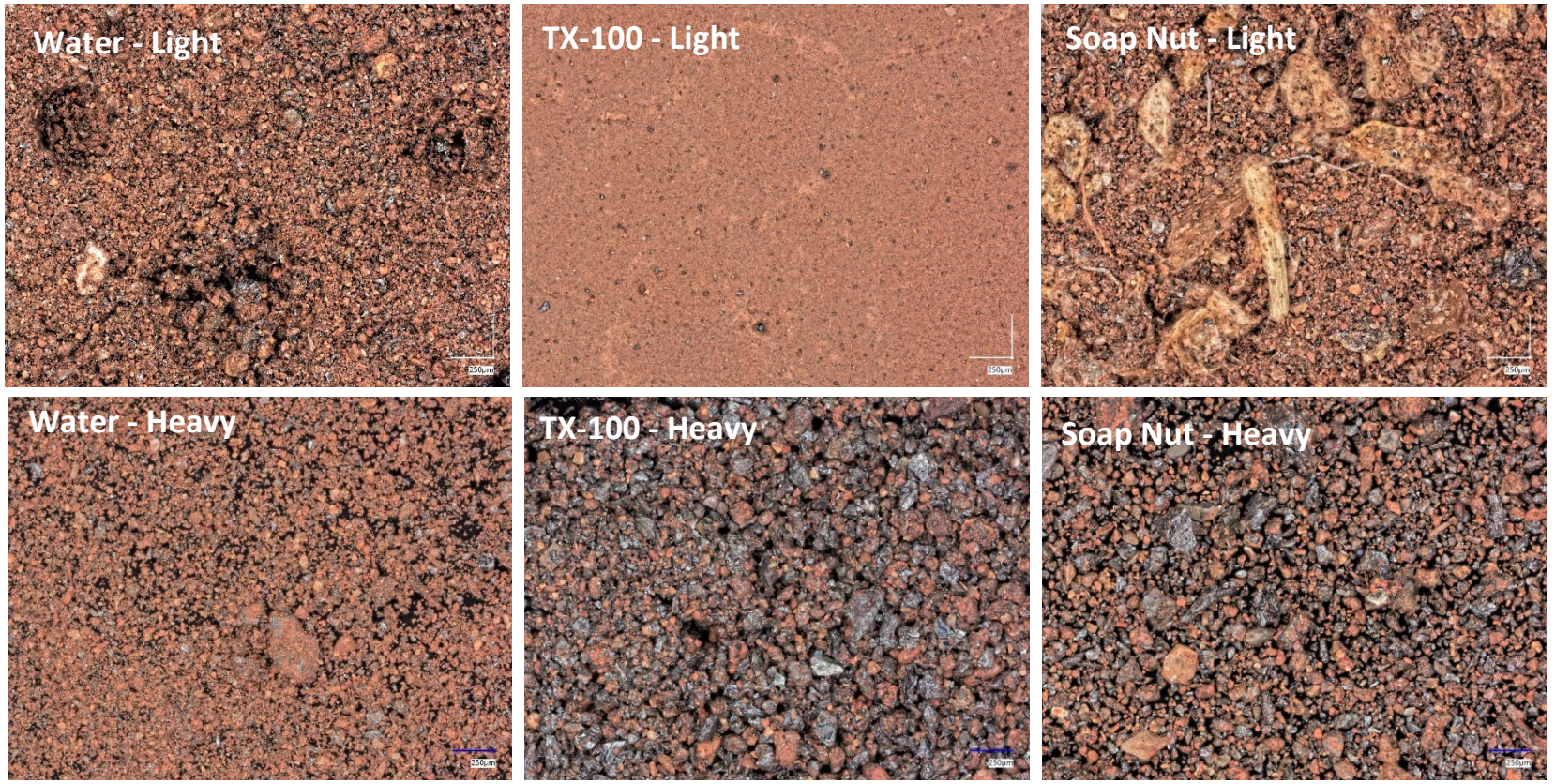

Figure 4.27 Keyence microscope images of 'heavy' & 'light' ESP dust solids. All images are 250 µm scale.

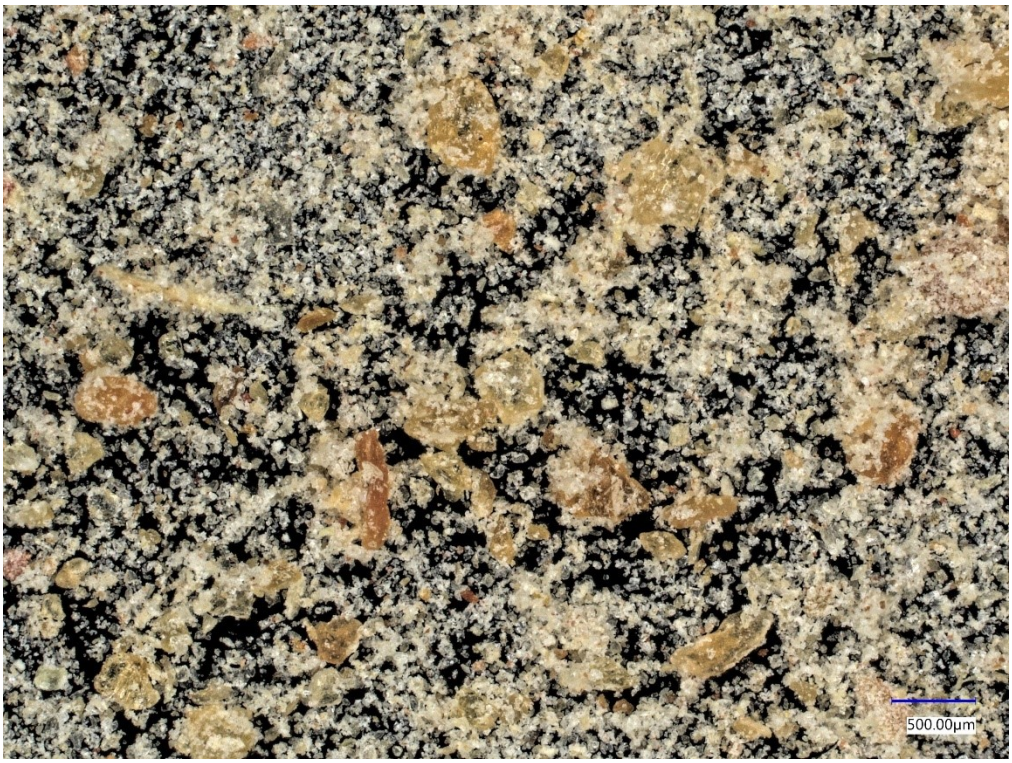

Figure 4.28 Keyence microscope image of raw soap nut particles. 500 µm scale.

The 'light' elements from all samples initially appear different to each other, with the TX-100 sample being the complete standout. In the soap nut image, the large soap nut particles are clearly spread throughout, being larger and lighter in colour than the matrix, see figure 3.29 for Keyence images of raw soap nut. However, the matrix surrounding the soap nut particles appears fairly similar to that observed in the light water image. This matrix consisting of ultra-fine (< 100 µm) angular, heterogenous, orange particles with some larger (> 250 µm) silver-metallic or white particles present.

As mentioned, the TX-100 light image does not share the matrix with the other two images. Instead, it appears more homogenous and consisting of a surface with no voids between particles. There are some sporadic particles throughout the surface, which appear similar to those seen in the other images. It was also noted that there appeared to be some white lines across the surface, which were only visible using the Keyence microscope. Further inspection of these showed that they appeared to form polygonal crust structures across the surface, as is highlighted in figure 4.29. The 5 structures highlighted show that although they varied in size and shape, they appeared throughout the sample and were found to be protruding from the largely flat surface. Figure 4.31 shows a small area of the surface which featured the polygonal structures, where 3 intersecting lines can be seen. A small portion of this was then 3D mapped to assess the height, the polygonal crust is clear in the 3D map and appears to be raised by approximately 4-

12 µm from the baseline surface. A larger particle can be seen towards the top left side of the 3D map, near the distance marker 89.56 um, indicating the structures are of analogous heights to these sporadic particles.

This structure could be analogous to anhydrite/gypsum salt crust structures found in sabkhas, such as the Matti Sabkha (see figure 4.29) (91); these are desert salt pans where the evaporative conditions and shallow saline waters give rise to salt crust structure formation (92–94). Anhydrite ($CaSO_4$) being a white crystalline mineral formed by evaporation consisting of calcium sulphate. As was observed in the sample, they often do not form coherently or homogenously, which is thought to be due to variations in aquifer groundwater flows (91). This could explain the varied distribution seen in the TX-100 sample as any water would not have been equally distributed and therefore elemental concentrations and evaporation rates would vary.

Figure 4.29 Example of salt crust structures in Matti Sabkha (left) & sabkha in UAE. Source: Goodall et al. 2000/Google images.

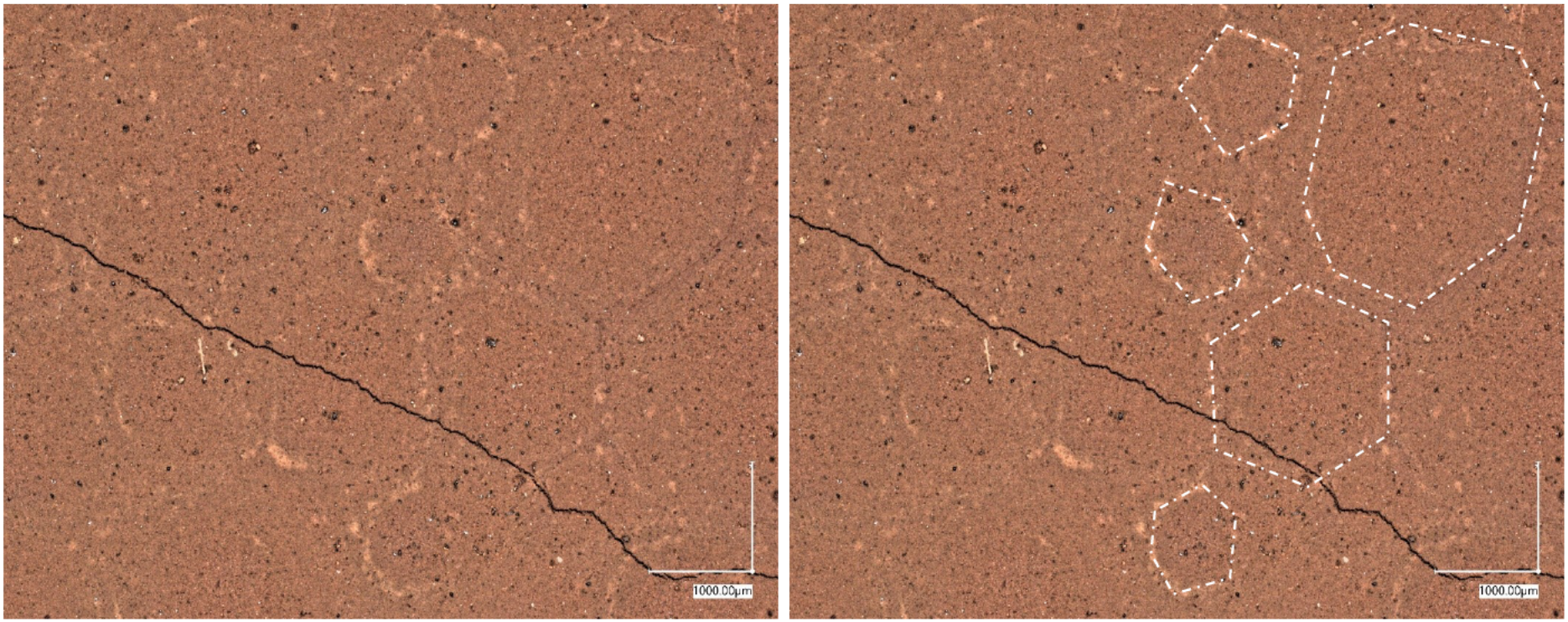

Figure 4.29 Keyence microscope images of chicken wire structure observed on TX-100 light surface. Original image (left) and edited image to the highlight the structures varying size, shape and distribution (right). 1000 µm scale.

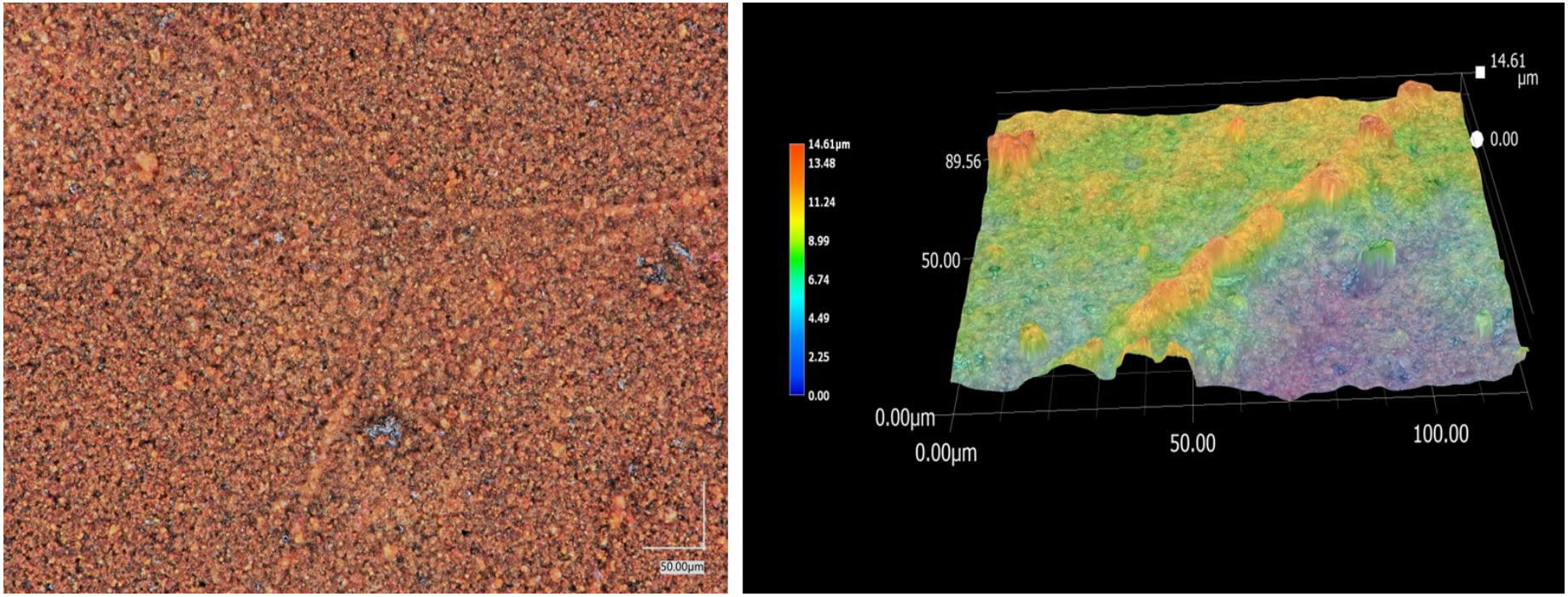

Figure 4.30 Keyence microscope image and 3D map of chicken wire structure on TX-100 light surface. 50 µm scale for image and 14.61 µm scale for 3D map.

Following the image analysis chemical analysis was undertaken on samples from the heavy and light solids from each sample group (water, TX-100 & soap nut). The results are shown in table 3.4. Compared to the unwashed ESP dust; all samples displayed increased Fe and Ca concentrations. This is likely due to the dissolution of K, the second largest constituent at 19.70 %, and other soluble elements such as Cl.

Comparison of Fe levels between all the heavy and light samples shows that the heavy samples contain approximately 8.0 % more Fe on average, heavy recording an average 88.78 % to the 80.73 % average in the light samples. Ca concentrations are seen to be higher on average in the lighter samples, measuring an average of 16.80 % compared to 9.93 % in the heavy samples.

Table 4.4 Summary of XRF results from testing of heavy and light ESP dust, alongside unwashed ESP dust data.

Name	ESP Dust	Water Light	Water Heavy	TX heavy	TX Light	SN Light	SN Heavy
Ca	7.36%	14.51%	10.37%	10.77%	17.75%	18.13%	8.65%
Mn	0.42%	0.44%	0.36%	0.41%	0.42%	0.41%	0.43%
Fe	**68.98%**	**83.46%**	**88.33%**	**87.86%**	**79.49%**	**79.24%**	**90.15%**
Cu	0.12%	0.02%	0.00%	0.00%	0.03%	0.03%	0.00%
Zn	0.17%	0.08%	0.05%	0.05%	0.12%	0.12%	0.03%
As	0.23%	0.00%	0.00%	0.00%	0.00%	0.00%	0.00%
Rb	0.35%	0.03%	0.04%	0.04%	0.03%	0.04%	0.03%
Cd	0.26%	0.09%	0.05%	0.04%	0.17%	0.13%	0.03%
Pb	2.01%	0.92%	0.53%	0.41%	1.59%	1.52%	0.28%
K	19.70%	0.00%	0.00%	0.00%	0.00%	0.00%	0.00%

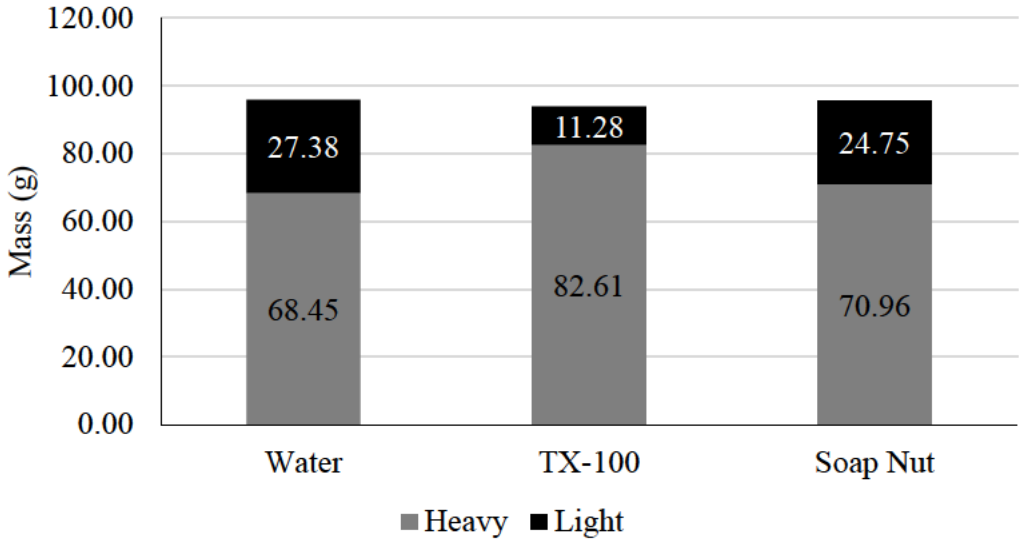

Figure 4.31 Stacked bar chart showing heavy and light particle masses for all tests.

4.1.4.5 Time Variation Washing

A short experiment was undertaken to assess the impact of including 2.0 % soap nut and TX-100 in ESP dust washing tests where time and stir speed are varied. Despite earlier testing indicating that the addition of soap nut may not be as effective when compared to TX-100 or sodium xylene sulfonate, soap nut was included in this branch of testing to determine if altering the washing parameters can improve its effectiveness and therefore its viability. The aim is to identify which of these parameters has a bigger impact on the washing process.

It is clear from initial viewing of figure 4.33 that the TX-100 mobilised more chloride, as has been observed in other testing. The average increase when using TX-100 instead of soap nut under the same stir speed and time was approximately 39 %, with the greatest difference being approximately 64 % seen in varying stir speeds whilst washing time was held at 5 minutes. This impact was more visible when using higher speeds over the 5 minutes; at 600 rpm TX-100 mobilised approximately 76 % more chloride and at 400 rpm this was approximately 85 %, compared to just a 33 % increase at 200 rpm. This impact is lessened when time is increased to 10/15 minutes, with the greatest other increase between the soap nut and TX-100 being approximately 36 % in the 400 rpm 10 minutes tests. Indicating that TX-100 could be useful if washing for shorter time periods.

When focusing on the speed variation both table 3.5 and figure 3.34 show that increasing speed mobilised more chloride, regardless of the additive used. The average increase in chloride mobilised when increasing the speed from 200 rpm to 600 rpm was 1514 mg/L (± 611). The time variation also produced interesting results, every test lasting 15 minutes mobilised between 1410 mg/L – 4900 mg/L more chloride compared to tests only 5 minutes in length, with an average of 1298 mg/L (± 508). These results indicate that the addition of 2 % TX-100 enhances ESP dust washing even at low stir speeds or washing times. They also appear to show that whilst increasing stir speed and washing time improve chloride mobilisation, stir speed appears to have a greater impact.

Table 4.5 Summary of results from parameter variation washing tests.

(mg/L)	5 minutes	10 minutes	15 minutes
2% Soap Nut & 600 rpm	1849	3551	3874
2% TX100 & 600 rpm	3237	4580	4900
2% Soap Nut & 400 rpm	1605	2496	3064
2% TX100 & 400 rpm	2962	3388	3613
2% Soap Nut & 200 rpm	1410	1936	2378
2% TX100 & 200 rpm	1881	2401	2904

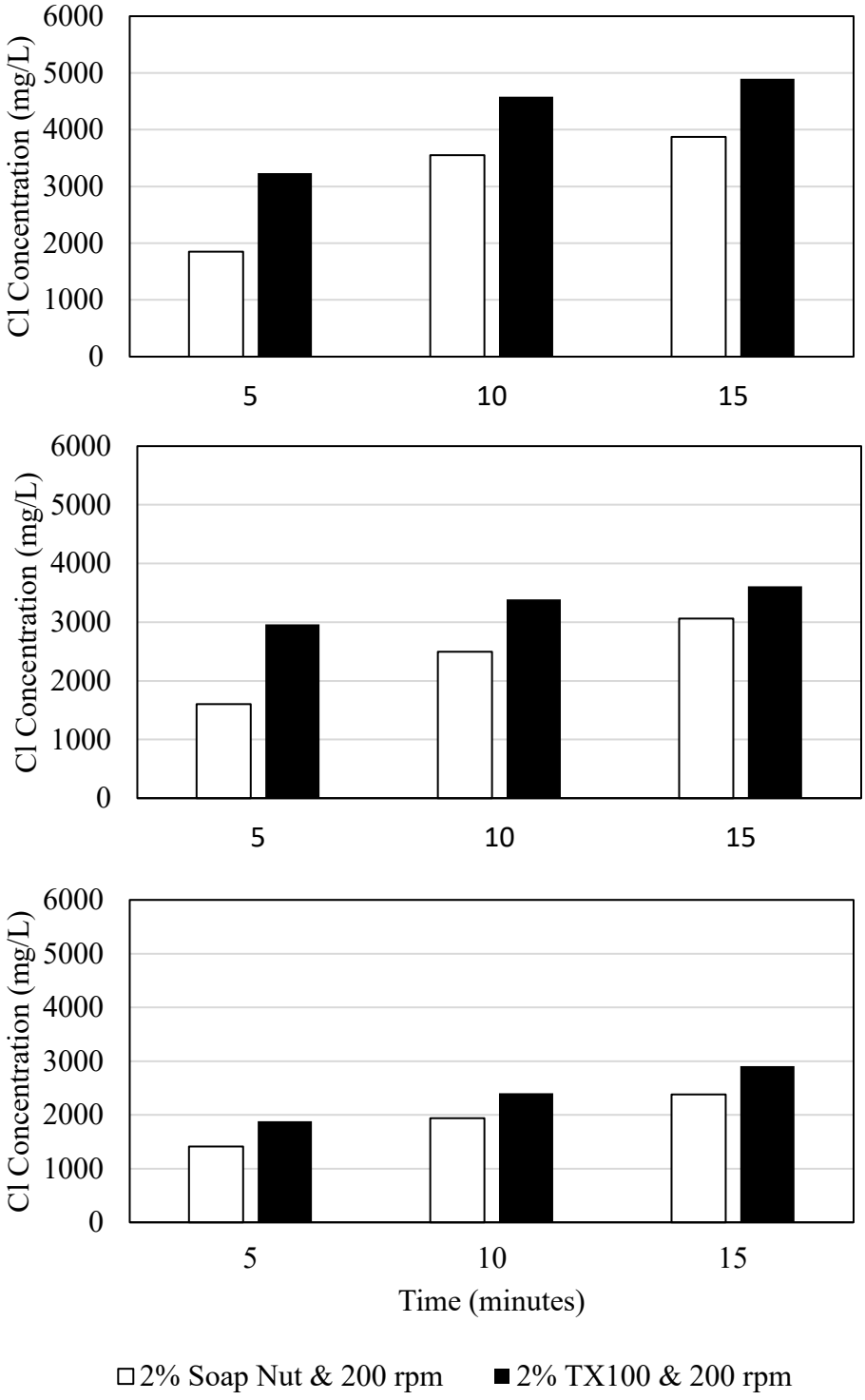

Figure 4.32 Comparison bar graph displaying difference in chloride concentrations when time is varied between 5 – 15 m & stir speed between 200 – 600 rpm.

4.1.5 Conclusions & Discussion

The results from these experiments show that water washing can remove approximately 95 % of chloride from ESP dust in a single wash. The trialled low energy method was shown to be vastly inferior to the high energy method featuring mechanical stirring. However, a hydrophobic effect was noted during early experiments, where significant portions of the dust would remain dry after the washing process. This results in variation in the amounts of chloride mobilised and was prominent when only washing with water.

Recycling of ESP dust washing solution is an effective method of reducing water consumption and the volume of water requiring down pipe treatment. Chloride is still mobilised in the tenth cycle at an effective rate; however, it does appear to be slowly declining after approximately the seventh cycle. Potentially meaning it may be better to halt the recycling process at this point.

The additives tested, TX-100, soap nut and sodium xylene sulfonate, all aided the processability of the ESP dust which could be beneficial on an industrial scale. TX-100 repeatably appeared to mobilise more chloride from the ESP dust compared to the other additives and control tests featuring only water, as is clear in figure 4.36. This is likely due to the additives overcoming the hydrophobic effect of the ESP dust, resulting in higher average chloride mobilisations. There was no clear benefit observed when increasing concentrations from 0.2 % to 2.0 %, whilst chloride mobilisation did appear higher with greater concentration of additives, the variability of the results made this finding unreliable. This increase in concentration would also increase cost, as projected in table 10.

The additives did appear to behave differently, which should be a consideration for any upscaling of their use in this capacity. Whilst soap nut did not appear to be as effective as sodium xylene sulfonate or TX-100, it is the most environmentally friendly option which raises its appeal.

The ESP dust, as has been previously noted, is a highly variable material in terms of its chemical composition. This can be due to changes in input materials, plant operating conditions, sampling or which ESP field captured the dust. This variation was observed even in this small-scale testing.

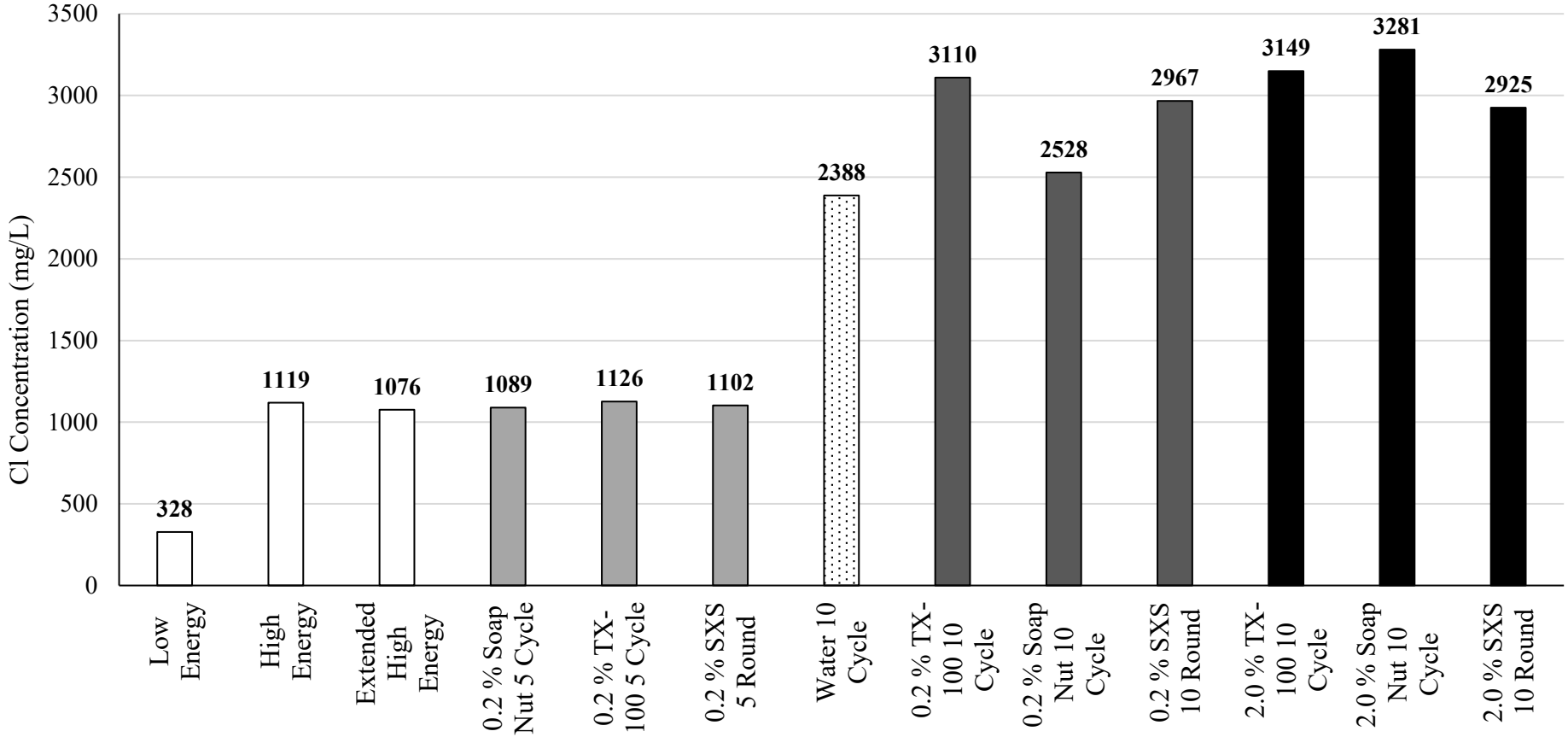

Figure 4.33 Summary bar chart displaying final chloride concentrations from all tests. Bar colours/patterns indicate which suite of experiments they belong to.

The summary of parameter variation & cost estimations for inclusion of additive in plant-scale ESP dust washing are provided in table 3.5 and 3.6. They assume a daily dust production of 15 – 25 T/day. They show the importance of determining the correct amount of additives required and the liquid to solid ratio, before fully scaling the use of additives, using 2.0 % TX-100 for example could cost approximately £235,000 a day based on 25 T of dust being treated with 250,000 L of water. Whereas in this same scenario, soap nut or sodium xylene sulfonate would cost approximately £80,000, a saving of approximately 66 %.

Table 4.6 Summary of expected range of washing conditions for solid tonnage, required water volumes and required additive volumes.

Dust/day (T)		15	25
Water Volume Required (L)	1 to 1	15,000	25,000
	5 to 1	75,000	125,000
	10 to 1	150,000	250,000
Additive Volume Required (L/kg)	0.2%	30	50
		150	250
		300	500
	2.00%	300	500
		1500	2500
		3000	5000

Although experiments in this chapter involved a liquid to solid ratio of 5: 1, by recycling the water for 10 cycles this ratio effectively becomes 0.5: 1. This could lower the cost of TX-100 to £11,750 per day from £235,000 per day, based on the scenario of 25 T of dust and 2.0 % TX-100 being used. As results in this chapter have shown there is a negligible difference between using 0.2 % and 2.0 % TX-100 in the process, this would further reduce the cost in this scenario to £1,175 per day.

Sodium xylene sulfonate was often the second-best performer in terms of chloride mobilisation and is significantly cheaper than TX-100, £16 / L compared to £44 / L respectively. Meaning that approximately it would cost between £240 - £400 per day to wash 15 – 25 T of ESP dust using a concentration of 0.2 %.

Soap nut, although found not to be as effective in improving chloride mobilisation, does aid the processability of the ESP dust during washing. Soap nut is also environmentally friendly, minimising any risk to operators or the environment from use.

Table 3.6 Summary of costing predictions for additive use in a range of scenarios.

Concentration	Ratio	TX-100		Soap Nut / SXS	
		15	25	15	25
0.20%	1 : 1	£1,410	£2,350	£480	£800
	5 : 1	£7,050	£11,750	£2,400	£4,000
	10 : 1	£14,100	£23,500	£4,800	£8,000
2.00%	1 : 1	£14,100	£23,500	£4,800	£8,000
	5 : 1	£70,500	£117,500	£24,000	£40,000
	10 : 1	£141,000	£235,000	£48,000	£80,000

This provides an annual estimate of £88,000 – £146,000 for including 0.2 % of soap nut or sodium xylene sulfonate, compared to £260,000 - £430,000 for the inclusion of 0.2 % TX-100 in the washing solution. This is assuming approximately 5,500 – 9,000 T of ESP dust being treated annually and recycling of the washing solution for 10 cycles. If the same conditions were kept without recycling the washing solution, these estimates would rise 10-fold, to approximately £880,000 – £1.5 m and £2.5 m - £4.3 m respectively.

Whilst water washing of ESP dust has been shown to be effective at washing chloride from ESP dust, recycling of the water could save vast resources.

This work carried out the recycling of ESP dust washing solutions reused the solution up to 10 times. Findings indicate that the solution is suitable to this level of recycling, with chloride being mobilised even after 10 cycles.

Hydrophobicity is a known issue with ESP dust. For this reason 3 additives were tested during washing; TX-100, sodium xylene sulfonate and soap nut. The additives were either surfactants or hydrotropes, meaning they have hydrophilic components which fix to the ESP dust's

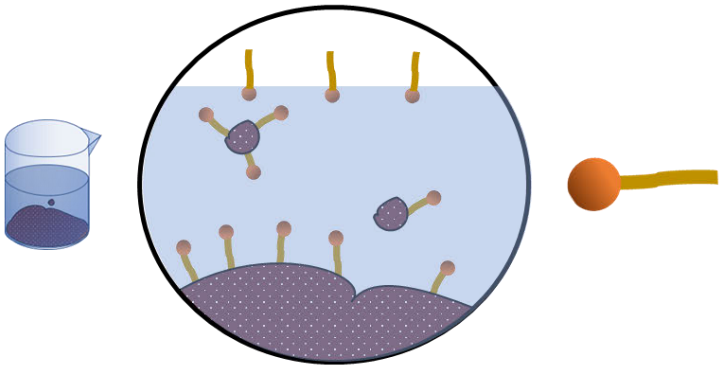

ESP dust in water with additives

Results showed that using the additives greatly improved the handling and processability of the ESP dust during washing and filtration. TX-100 was the most effective at mobilising chloride from the ESP dust although due to its affordability and low environmental impact soap nut could also be considered an alternative.

Figure 4.34 Summary diagram illustrating key findings from this chapter, relating to washing solution recycling and additive use.

5. CONTACT ANGLE ANALYSIS

Previous research has shown ESP dust to be hydrophobic (30). This is important in the context of this thesis because water is the primary solvent used in the treatment of ESP dust. Whilst water contact angle analysis (WCA) gives an average value across the area of the droplet being measured, by using a standardised procedure it does provide quantitative analysis of a materials wettability related to a given solution (30) The work described in this section considers detailed analyses on the water contact angle of ESP dust under different conditions (e.g., repeated washing using the same water solution or changing the ESP dust sample . The data studied also include what impact the washing of ESP dust and varying surfactant concentrations have on water contact angle of the dust. The surface tension of surfactants at varying concentrations has also been tested to calculate the critical micelle concentration.

5.1 Water Contact Angle on ESP Dust & WESP Dust

Initially, water contact angles were measured over 90 s with both the ESP dust and WESP dust samples. The initial water contact was determined from the first image of a stable droplet taken in the test. The resulting water contact angle behaviour was dramatically different between the dust. For example, the ESP dust's initial water contact angle averaged 145 ° (± 4) compared to 128 ° (± 6) for the droplet on WESP dust. This represents a difference in average initial contact angle of 17 ° or 11.6 %. These contact angles classify the materials as hydrophobic and are approaching superhydrophobic classification of > 150 ° (95). However, although they display relatively similar initial contact angles this was not consistent over time. For example, the stability of the droplets on the ESP/WESP dust samples varied significantly. It was noticeable that the water droplets retained their shape and contact angle value for far longer on the ESP dust compared to the WESP dust. To illustrate this, Figure 4.1 plots the difference in water contact angle between droplets on ESP dust and WESP dust over 90 s from initial contact, with WCA measurements taken every 10 s. The contact angle of the droplets on ESP dust steadily dropped by an average of 7 °/min (± 2), with an overall reduction of 11 ° (± 3) over 90 s resulting in a final average contact angle of 134 ° (± 6). By comparison, the WESP dust showed an average decline of 85 °/min (± 4), resulting in the total collapse of the droplet toward the end of the 90 s period. Figure 4.1 clearly shows that

the ESP dust WCA decline was also much more consistent compared to the WESP dust, which featured significant fluctuation over the first 40 s. The averaged standard deviation of the WCA measurements for the duration of the tests show that ESP dust was more stable with 6 ° compared to 9 ° in the WESP test. Over the 0 – 40 s period the WESP dust test was particularly variable, with an average standard deviation of 13 ° although this constrained to 4 for the 50 – 90 s portion of the test. By comparison the ESP dust test had average standard deviations of 5 ° and 6 ° for the same periods respectively. This may be caused by the removal of hydrophobic surface groups during water washing and the heterogenous physical/surface properties of the ESP/WESP dust becoming more exposed, resulting in unstable early measurements before converging to a more consistent trend after stabilising. This initial test highlighted a clear difference in WCA behaviour between ESP and WESP dust, more than likely related to the water washing of ESP dust.

Due to these initial results, the test was repeated and extended to 5 minutes, to better determine the longevity of the water droplet on the ESP dust surface. Figure 4.2 demonstrates a clear similarity to the trends observed in Figure 4.1, with ESP dust steadily declining over the 5 minutes and the WESP dust dropping faster before reaching a WCA of 0 ° after 2 minutes. The initial water contact angle for ESP dust in this test averaged to 146 ° (± 3) compared to the 128 ° (± 4) recorded in the WESP dust test. The water droplet on the ESP dust surface declined by an average of 7 °/min (± 0.4), leading to an average total loss of 33 ° (± 2) and an average final water contact angle of 113 ° (± 2) after 5 minutes. For the droplets measured on WESP dust the rate of WCA decline was 7 °/min (± 4), resulting in a total collapse of the droplet, as previously mentioned. As can be seen in Figure 4.1.2, there was variation in the early stages of the tests for both the ESP and WESP dust, although this was more pronounced in the WESP dust. This can be quantified in terms of standard deviation. For example, during the 30 – 90 s stage of each test, the standard variation averaged 5 ° in the ESP dust test and 11 ° in the WESP dust, the most variable point in either test being after 30 s in the WESP test being 17 °. The ESP dust tests then became more stable and uniform for the remainder of the test, as standard deviation lowered to 2 ° on average between 120 – 300 s.

Both tests highlight the impact of water washing ESP dust, which appears to have a significant impact on the materials surface energy and therefore water droplets WCA. Mechanically stirring the dust in water, as discussed in section 3.0, has been shown to

dissolve water soluble elements more effectively from the ESP dust. Potentially indicating that water washing of ESP dust also mobilises the hydrophobic constituents of the ESP dust, further supporting speculation of a chemical cause for the hydrophobicity. Previous research has suggested the presence of hydrophobic functional groups on the surface of ESP dust which form a "hydrophobic shell" (30).

As two tests had now been completed over 90 seconds and 5 minutes without reaching a point of collapse for the droplet on ESP dust, a further test was carried out over the course of an hour. Water contact angle was recorded every 60 seconds for an hour, the results can be seen in Figure 4.3. Overall, although there is some fluctuation, there is a gentle negative trend throughout the data as the WCA slowly falls over the test. The average initial WCA recorded in these tests was 144.15 ° (± 3.25), with an average rate of decline of 1.18 °/min (± 0.07) resulting in a final average WCA of 77.05 ° (± 2.35) after an hour. This highlights the hydrophobicity of ESP dust even over prolonged periods of time, but it does indicate that over time the surface energy does decrease.

The differences in water contact angle can also be seen visually in Figure 4.4, where the droplet on ESP dust appears largely similar after 5 minutes compared to the droplet on WESP dust which has rapidly declined over just 50 seconds. Both cases appear to show a dust 'scaling' effect, where the dust particles begin to envelope the droplets, this can be seen in the images in Figure 5.4. This was observed during almost every test although it varied between ESP and WESP dust samples. For example, whilst this effect is much more pronounced in the WESP dust so that, after only just 20 s, the dust has almost completely blocked out the light source behind the droplet in Figure 5.4. Whereas it takes 2 minutes for the effect to be visible on the droplet on the ESP dust. Although the effect continues to envelope the droplet on the ESP dust, the light source is still visible after 5 minutes with only slight obstruction from dust particles. Slightly larger particles can also be seen around the silhouette of each droplet.

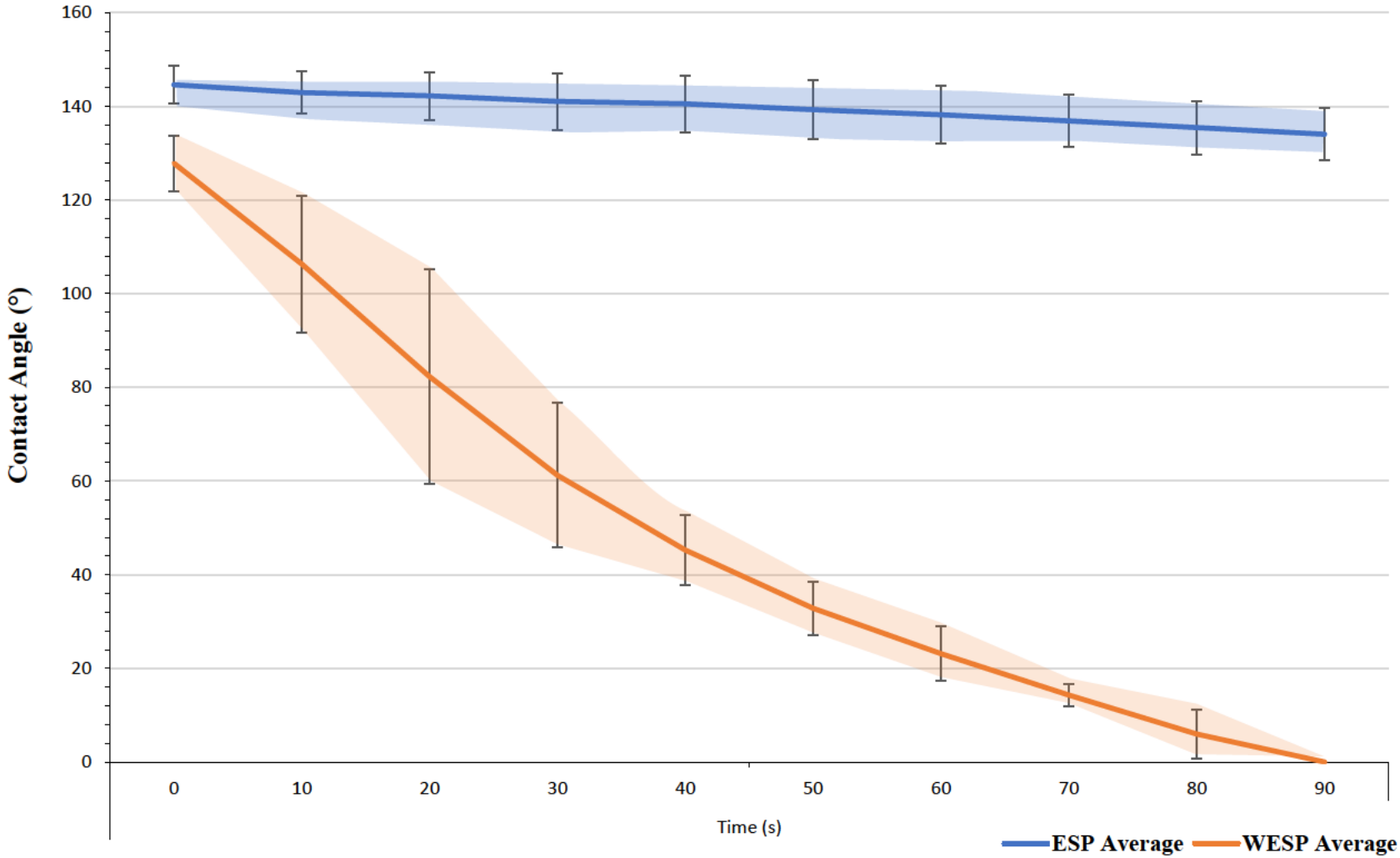

Figure 5.1 Graph depicting change in water contact angle of water droplets on ESP & WESP dust over 90 seconds.

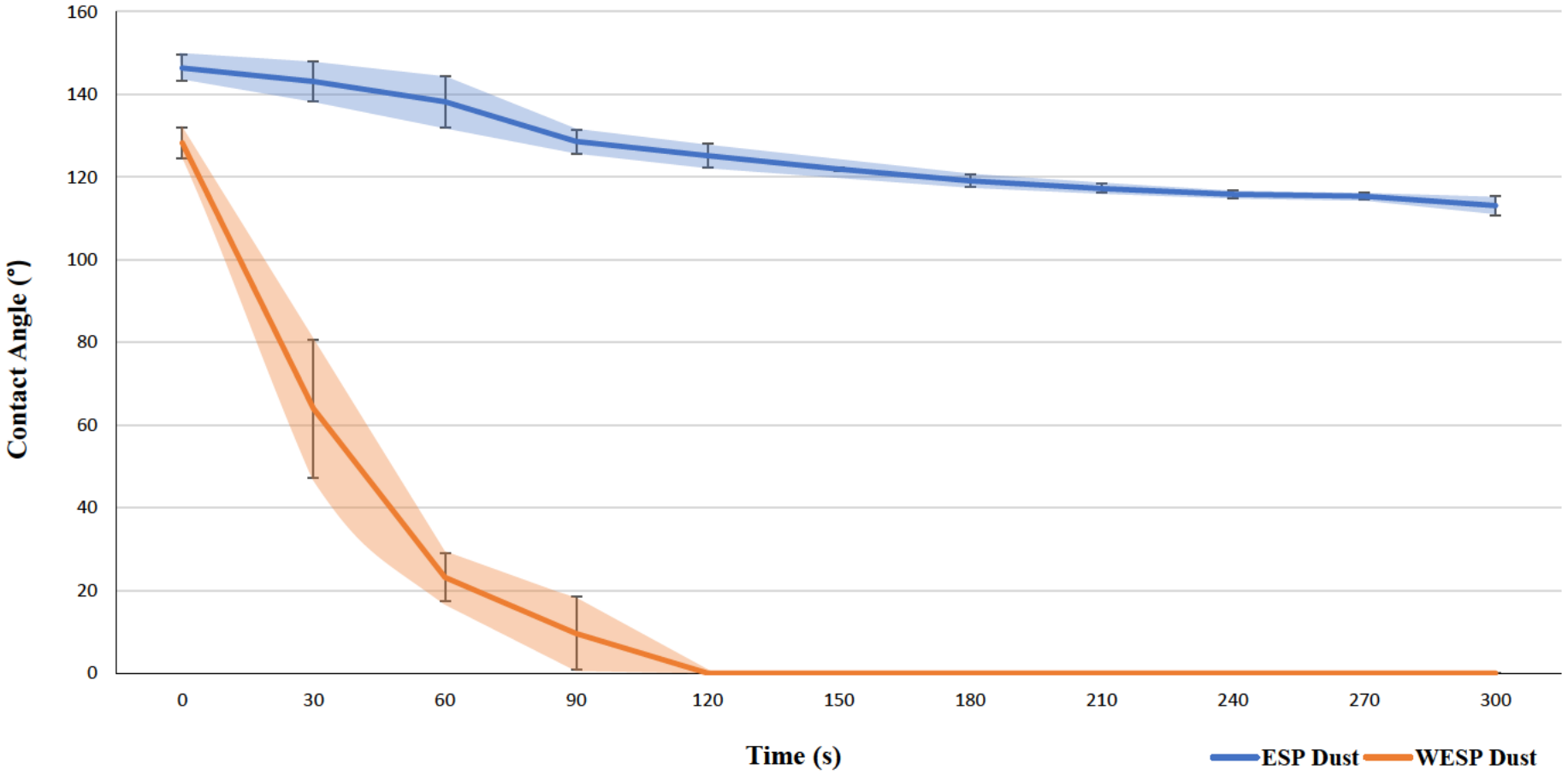

Figure 5.2 Graph depicting change in water contact angle of water droplets on ESP & WESP dust over 5 minutes.

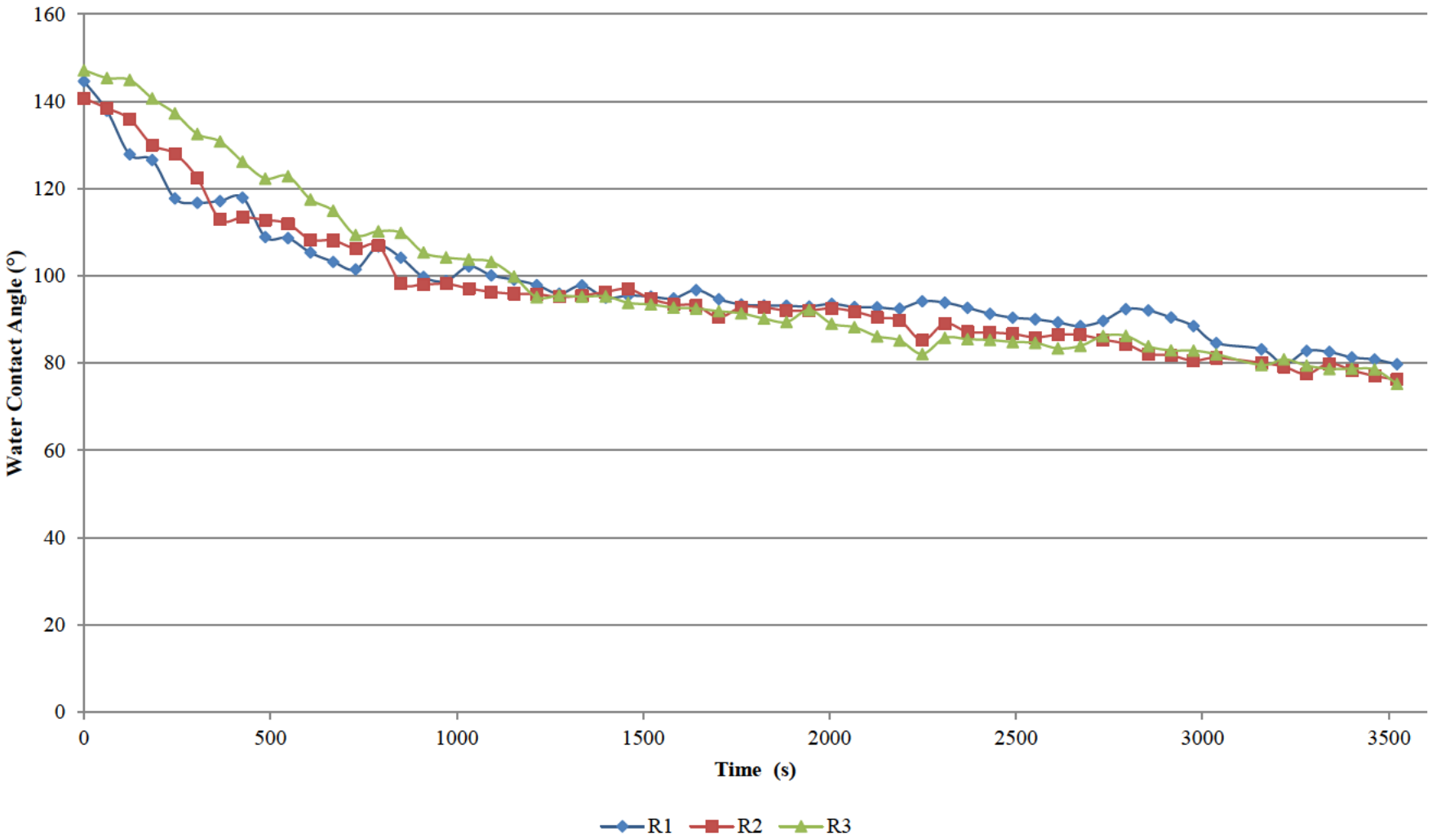

Figure 5.3 Graph depicting change in water contact angle of water droplets on ESP dust over time.

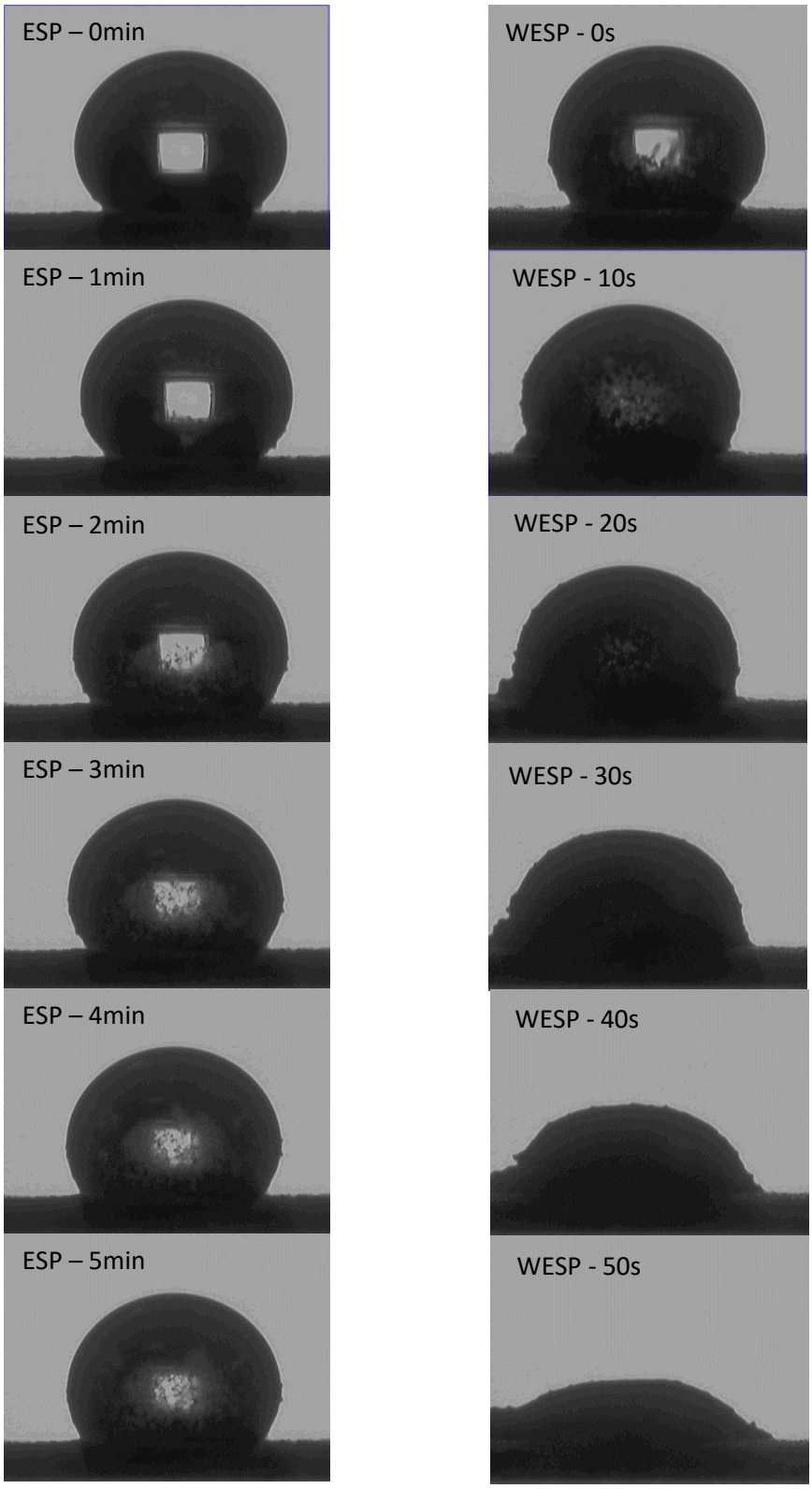

Figure 5.4 Images from water contact angle tests on ESP and WESP dust. Sample and image time are denoted on images.

5.2 Surfactant Solution Contact Angles on Glass

After initially testing pure water droplets on the dust samples, solutions containing varying concentrations of surfactants tested in section 3.0 were then tested on ESP dust. The aim here was to determine if surfactants can impact the water contact angle and wettability of the ESP dust, after initial results indicated the dust is highly hydrophobic. From an industrially perspective, being able to decrease washing time or improve the effectiveness of dust washing are both important factors when washing dusts on a large scale. In these tests solutions were first tested on a glass slide to produce a standardised baseline before testing on samples.

The first thing that stands out in Figure 5.5 is that the two samples featuring 0.2 % and 2.0 % TX-100 displayed substantially lower contact angles throughout the test compared to the other solutions tested. For example, the TX-100 solutions both recorded the two lowest initial contact angles of 14 ° and 10 °, compared to a significantly higher average of 59 ° across the other 5 solutions tested. The two TX-100 tests also had the biggest change in contact angle in terms of percentage compared to the initial contact angle, 0.2 % TX-100 falling by 90 % and 2 % by 88 % over 10 minutes. By comparison, it is interesting to note that the 2.0 % soap nut and 2.0 % sodium xylene sulfonate solutions have the highest initial water contact angles, 69 ° and 68 ° respectively. But, over the course of the test they become the lowest, excluding the TX-100 solutions. This represents a 71 % decline in the contact angle of the 2.0 % soap nut solution and a 67 % decline for the 2.0 % sodium xylene sulfonate solution over the course of 10 minutes when compared to their initial WCA value. These results make clear that TX-100 has the biggest impact on contact angle of solution droplets on a controlled surface and that increasing concentration from 0.2 % to 2.0 % achieves no significant impact.

The 0.2 % soap nut test displayed a similar data over the course of 10 minutes to that seen in the 2.0 % soap nut test, declining more rapidly initially before plateauing. However, the overall decline is significantly lower when compared to the 2.0% test, only losing 22 ° during the test meaning when increasing the soap nut concentration from 0.2 % to 2.0 % there is an approximately a 2.2 x increase in the contact angle decline. By comparison, the increase in impact when increasing the TX-100 concentration was less pronounced, further indicating that TX-100 is more effective at much lower concentrations.

The data for the water droplet was similar to that of the 0.2 % soap nut and 0.2 % sodium xylene sulfonate tests. All three recording test's initial contact angles within the range of 49 – 59

° which converged during the test to be approximately 40 ° after 10 minutes. The biggest change in these three tests is seen in the 0.2 % soap nut test, dropping by 38 % which is nearly double that of the water and 0.2 % sodium xylene sulfonate. However, the 0.2 % sodium xylene sulfonate and soap nut solutions appear to be slowly diverging from the water sample's trajectory in figure 5.5 towards the end of the test, indicating that these surfactants do have a slight impact on the water contact angle even at a low concentration. This would be expected as the surfactants should combat the ESP dust's hydrophobic shell, reducing the contact angle.

Overall, this test clearly demonstrated that the TX-100 surfactant appears to have the biggest impact on water contact angle on a controlled surface, even at 0.2 %. Higher concentrations of soap nut and sodium xylene sulfonate were shown to be effective, though still significantly less than even 0.2 % TX-100. Whereas the 0.2 % concentrations of soap nut and sodium xylene sulfonate behave more like water, with little observable impact. The greater impact seen from TX-100 is likely due to it being a non-ionic surfactant with a hydrophobic head, this will readily link with the ESP dust's hydrophobic shell resulting in an exposed hydrophilic head which reduces the dust's hydrophobic property.

5.3 Surfactant Solutions on ESP Dust

After completing the baseline testing on glass, the same surfactant solutions were then tested on a bed of ESP dust, as was done with water in section 5.1. Results generally followed that seen in the baseline test, although contact angles were higher on average. Starting with the samples containing 0.2 % and 2.0 % TX-100, once again these were the samples which stand out the most when looking at Figure 5.6. As with the glass slide test, a sharp decline in WCA was observed before stabilising over the remainder of the test. However, the initial contact angle was much higher on the ESP dust test, recorded at 79 ° for the 0.2 % TX-100 solution and 89 ° for the 2.0 % TX-100 solution. The contact angle dropped approximately 90% in both tests over the 10-minute period, the two highest percentage drops of contact angle in this test. The initial contact angle is approximately 64 ° lower than the average recorded from water on ESP dust and instead of a steady decline in WCA there is a much more rapid decline. These results again indicate that the addition of TX-100 reduces the hydrophobicity of ESP dust, more effectively than the other surfactants tested.

The 2.0 % soap nut solution also followed observations from the baseline test, with a higher initial contact angle before decreasing more rapidly, again having the lowest final contact angle excluding the TX-100 tests. The initial contact angle of 134.72 ° fell substantially to 31.13 °, at a rate of approximately 10.36 °/min. This was the fastest rate of WCA decline of any test, exceeding the next highest rate of 8.07 °/min recorded in the 2.0 % TX-100 test. Although it had the fastest rate of WCA decline, it had a significantly higher initial contact angle when compared to the TX-100 tests and after 10 minutes it had not reached the same WCA value as the TX-100 tests. Though not as effective as the TX-100 tests, this does suggest that soap nut could be a viable alternative to TX-100, given that it is environmentally friendly and of a lower price point.

The addition of 2.0 % sodium xylene sulfonate appeared to have a slightly more immediate impact on the contact angle compared to 2.0 % soap nut, as its initial contact angle was 119 °. Meaning this was the lowest initial contact angle behind the TX-100 solutions. However, the rate of decline during the test was only 5 °/min, one of the lowest rates. The total WCA decline in this test was only 41 %, meaning it was outdone by the lower concentration of 0.2% soap nut solution which had a 58 % decrease. The 0.2 % sodium xylene sulfonate performed slightly worse than the 2.0 %, with both the lowest rate of contact angle decline (4 °/min) and a total reduction of just 32 %. Indicating that although the sodium xylene sulfonate does have an impact on the WCA of the solution on ESP dust, more effective results can be achieved by using alternative surfactants, even at lower concentrations.

The results from this section highlight that TX-100 is the much more impactful, at concentrations between 0.2 – 2.0 %, surfactant for increasing wettability when compared to soap nut or sodium xylene sulfonate. As it has the greatest impact on initial WCA and over a 10-minute period it results in the lowest WCA. There are also promising results for soap nut powder as a more environmentally sustainable alternative however, with just 0.2 % soap nut inclusion outperforming 2.0 % sodium xylene sulfonate in terms of total WCA reduction and rate of WCA reduction.

Figure 5.7 further highlights the greater impact of TX-100, as images show how the droplet dissipates within 1 minute. The soap nut solution has a much more gradual decline over 10 minutes and there is a minimal impact observed for the sodium xylene sulfonate. The scaling effect observed in the previous section seems to have been mitigated by the addition of surfactants.

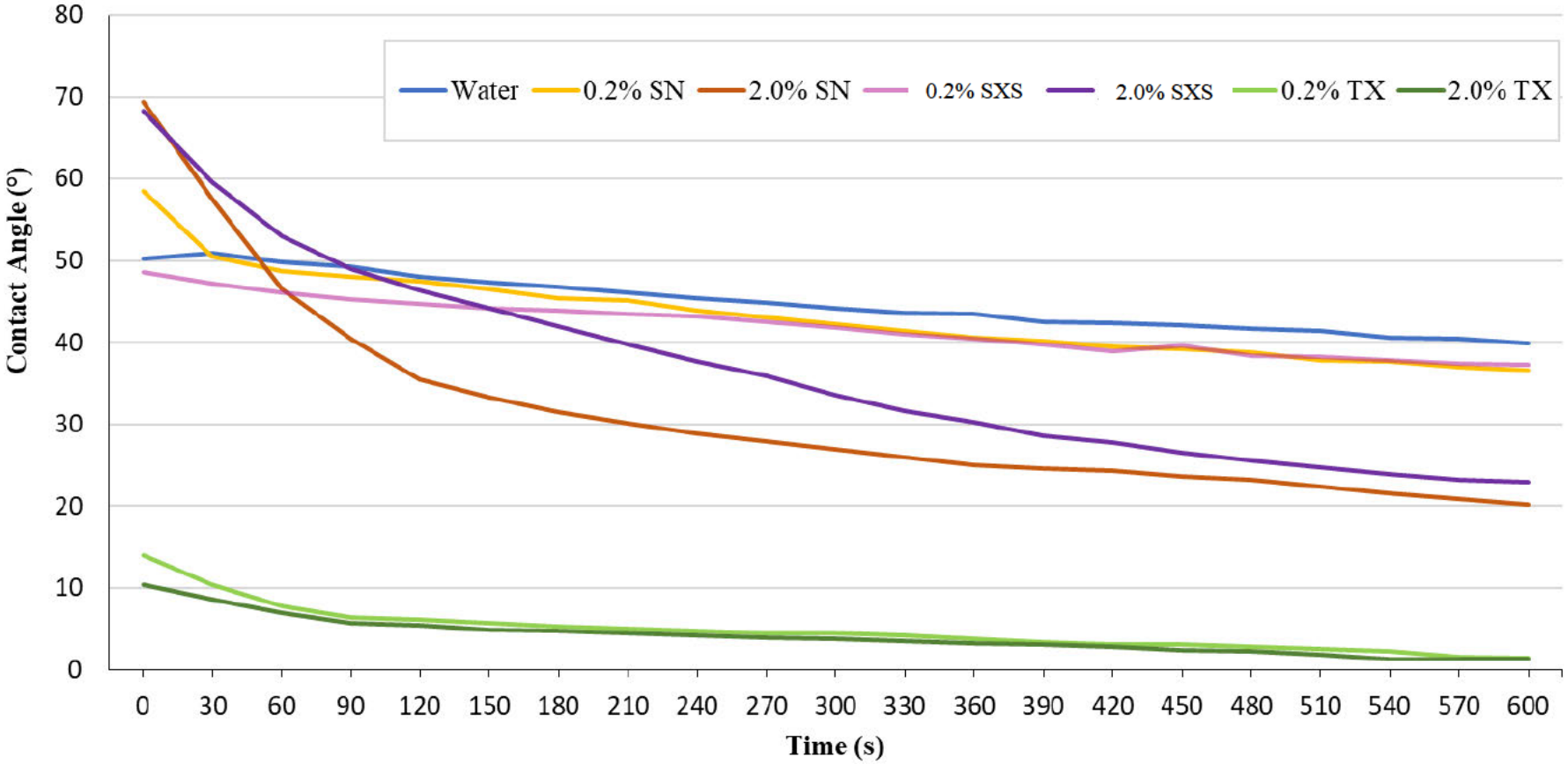

Figure 5.5 Graph depicting change in water contact angle of solution droplets on glass substrate over 10 minutes. Source: Author. SN = Soap Nut, SXS = Sodium Xylene Sulfonate, TX = TX-100.

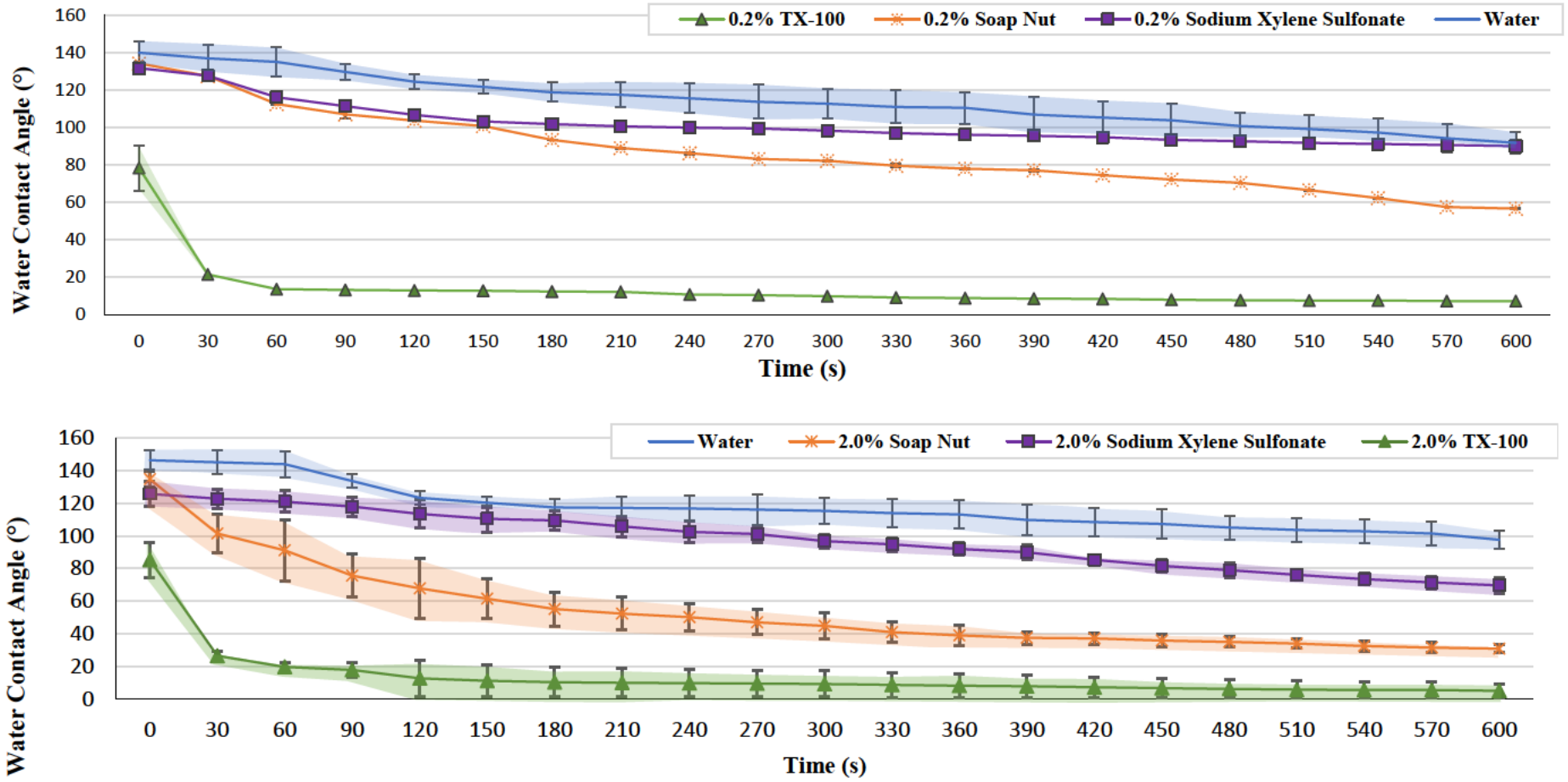

Figure 5.6 Graph depicting change in water contact angle of solution droplets on ESP dust over 10 minutes. Water & 0.2 % surfactants (top) and water & 2.0 % surfactants (bottom).

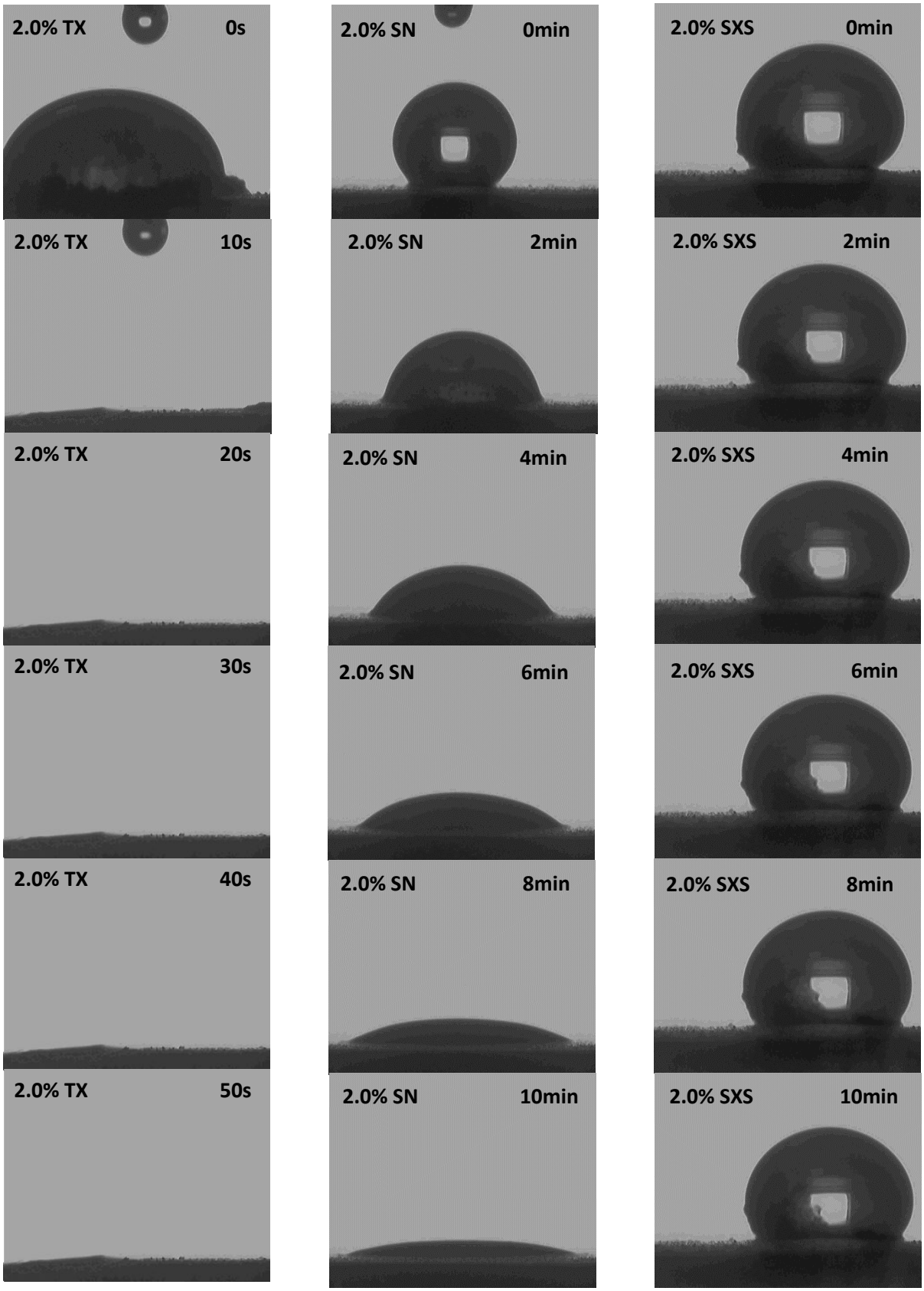

Figure 5.7 Images from 2.0 % surfactant water contact angle tests. Sample and image time are denoted on images. TX = Triton X-100, SN = Soap Nut & SXS = Sodium Xylene Sulfonate.

5.4 Effect of Washing ESP Dust with Surfactants on WCA

WESP dust samples from froth flotation washing tests, outlined in section 4.1.4.2, were retained for water contact angle analysis. The "heavy" and "light" solids were tested separately for 5 minutes with WCA readings recorded every 10 seconds. The motivation for these experiments was to further confirm and quantify the varying characteristics of the materials obtained from the aforementioned testing.

The graph shown in Figure 5.8 illustrates the difference between the heavy and light water-washed solids. The trend displayed echoes that seen in Figures 4.1 and 4.2, with one plot being relatively stable and the other declining more sharply. In this instance, it is the WCA of the heavy solids that declines more than the lighter solids. This is to be as expected as the lighter solids were suspected to be more hydrophobic as they remained on the water's surface even after mechanical stirring. However, interestingly the heavy solid's WCA value does not decline at a similar rate to that of the tests in section 5.1. Whereas the heavy solids from water washing in Figure 5.8 decline at an average rate of 13 °/min (± 2) and the light solids dropped at a rate of 1 °/min (± 1.2). Previously, the WESP dust recorded a rate of 71 °/min (± 14) and ESP only reached 7 °/min (± 0.4) over 5 minutes. The 1 °/min (± 1.2) represents the slowest rate of WCA decline recorded so far. Although these samples were washed using the same method, the method of filtration was different and may account for these differences, these methods are detailed in section 3.15.

The heavy and light solid samples recorded initial WCA readings of 142 ° (± 4) and 126 (± 3) respectively. Although, as previously noted they had differing rates of WCA decline over time which resulted in final WCA values of 77 ° (± 7) for the heavy solids and 119 (± 3) for the light solids, as is clear in Figure 5.8. These results do provide evidence that even after 10 minutes of mechanically stirred water-washing of the dust, highly hydrophobic solids can still be found. Owing to this, this test was then replicated when TX-100 and soap nut had been added to the washing water, to gauge if adding surfactants would impact the surface energy of the dust after washing.

When testing was carried out on dusts washed with 2.0 % TX-100, droplets immediately dissipated on contact with the dust making it impossible to record WCA data. The test was repeated 10 times, on both light and heavy solids, and this effect was observed each time. This

had not been seen in any other WCA test. Considering TX-100 has had the biggest impact on ESP dust WCA during testing this was to be expected.

The droplets on both the heavy and light ESP dust washed in 2.0 % soap nut solution behaved variably during the test. However, they had all collapsed within 2 minutes. Although, as was seen in the water-washed ESP dust, the light dust appeared to behave more hydrophobically. The lighter dust had a slightly lower initial contact angle of 124 ° (± 4.5) compared to the 132 ° (± 4), but as can be seen in Figures 5.8 and 5.9 they did behave similarly for the first 20 seconds before the heavier dust declined much more rapidly. This can be quantified in the WCA reduction rate between the two tests, e.g., the dramatically higher rate of the heavy dusts being 236 °/min compared to 124 °/min recorded in the light soap nut washed solids. This stark difference in WCA reduction rate is largely due to the collapse of the droplets on the heavy dust after approximately 45 seconds, whereas the droplets on the lighter dust declined much more steadily over approximately 90 seconds. As the lighter particles displayed hydrophobic properties in the initial experiment, these results follow on logically.

These tests indicate that washing ESP dust with surfactants results in solids which appear to behave as being more hydrophilic compared to the virgin material. There were also notable differences between the light and heavy solids, apart from the TX-100 washed solids which both exhibited almost instant droplet collapse. The lighter solids in both the water and soap nut tests behaved more hydrophobically, though this clearly varied between the tests. The light portion of the water-washed solids being the most hydrophobic. This may be due to higher concentrations of the hydrophobic functional groups found in ESP dust (30), hindering the washing process. Whilst adding soap nut or TX-100 to the washing solution clearly reduces this effect in the light solids, as droplets on these materials collapsed immediately or within 90 seconds.

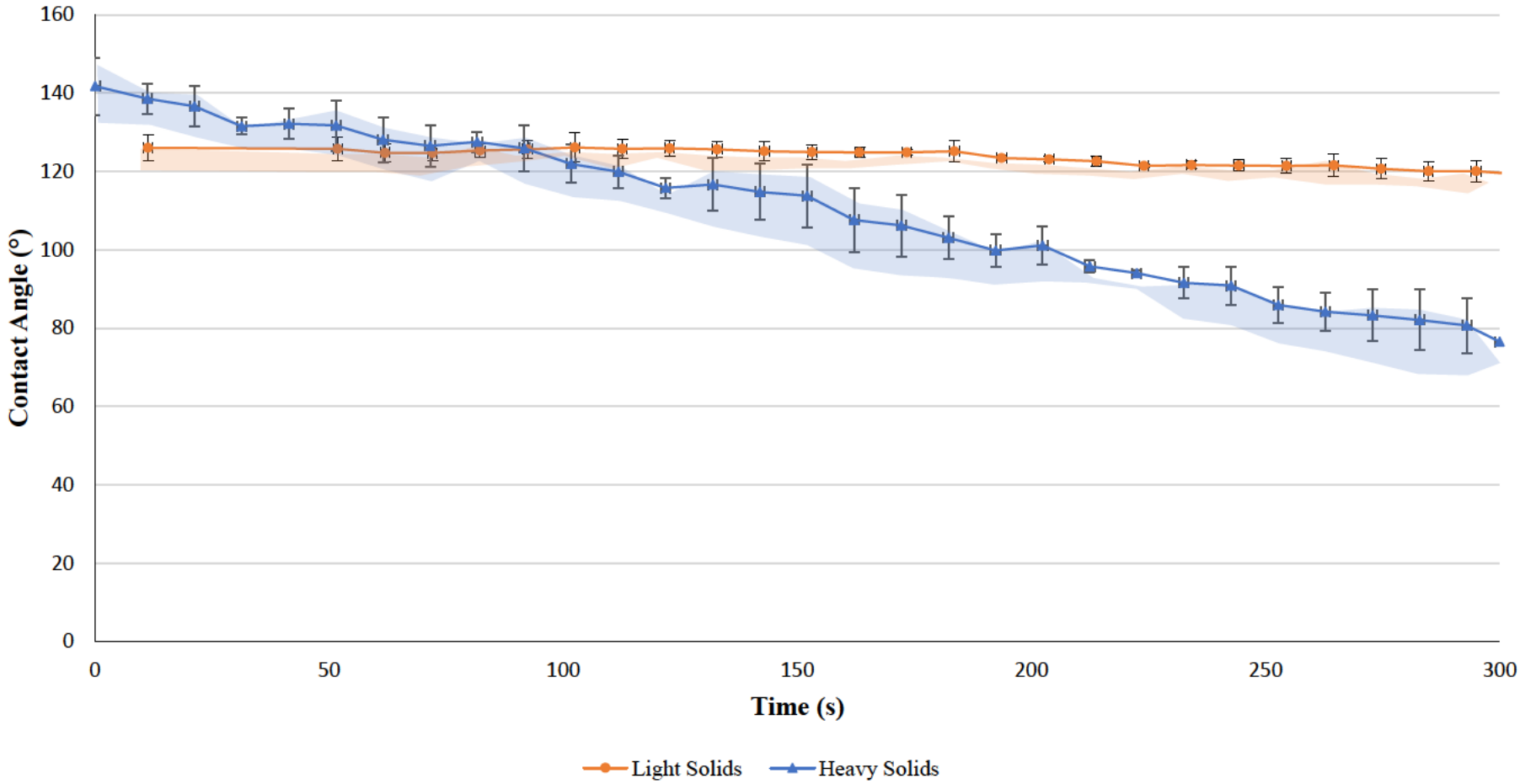

Figure 5.8 Graph displaying water contact angle of water droplets on water-washed ESP dust light and heavy solids over 5 minutes.

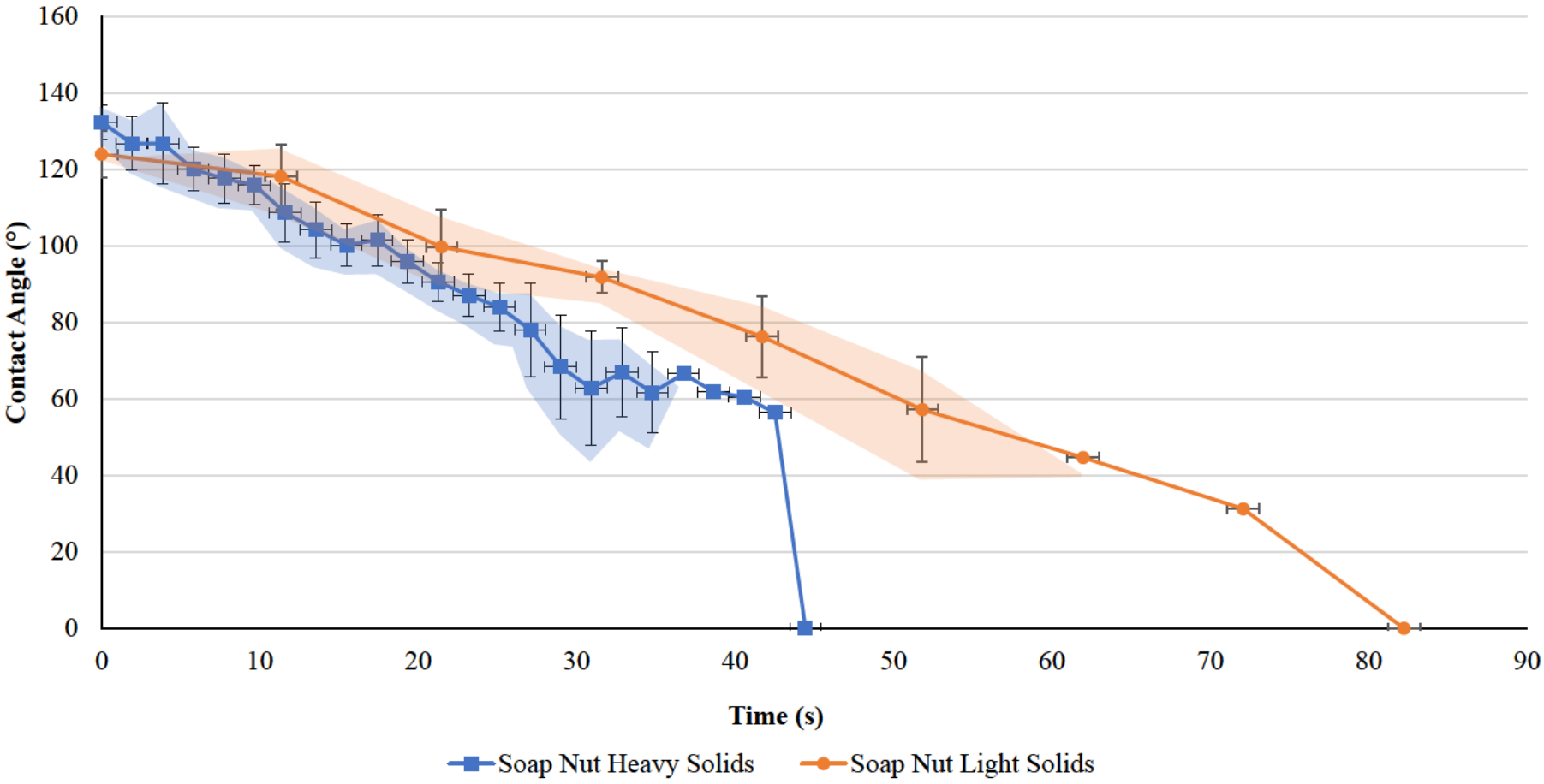

Figure 5.9 Graph displaying water contact angle of water droplets on soap nut-washed ESP dust light and heavy solids over 5 minutes.

5.5 Examples of Hydrophobicity

Several hydrophobic effects were noticed during the WCA testing and are described as follows. So, as previously mentioned, it was observed that the dust samples appeared to 'scale' around the outside of the water droplets, i.e., ESP dust particles climbed around the water droplet to slowly encapsulate it. Figure 5.10 shows this effect on water droplets over different time periods on both ESP dust and WESP dust. The effect is clearly much more pronounced with the droplets on the WESP dust. A comparison of pictures in Figure 5.10 shows how in images A & A' the ESP dust the droplet appears largely pristine, whereas in images B and B', dust can be seen starting to rise along the surface from the base of the droplet and there are also larger particles visible along the silhouette. After 5 minutes on the ESP dust in image A', the droplet has clearly been partially coated by dust. Image B' however shows significant dust coverage after just 10 seconds, to the point where the light source behind the droplet almost cannot be seen.

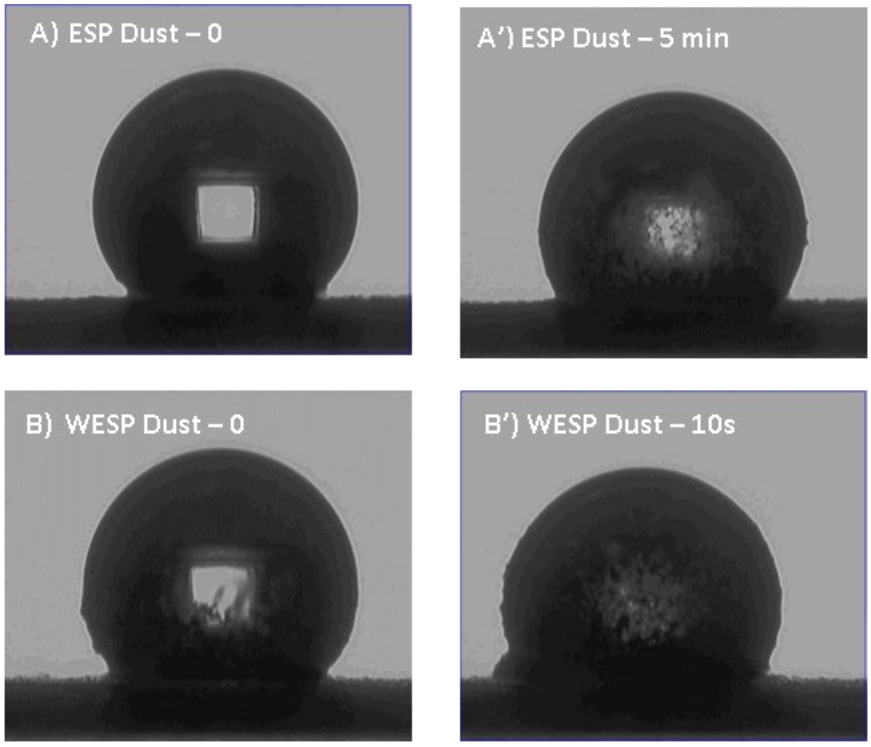

Figure 5.10 Images of depicting 'scaling' effect observed on dust samples during water contact angle measurements. A) ESP dust, 0min. A') ESP dust, 5 min. B) WESP dust, 0min. B') WESP dust, 10 seconds.

As with image B, larger particles can also be seen along the edge of the silhouette and some dust appears to have accumulated towards the bottom left of the droplet. This effect was observed to varying degrees in every test conducted. However, surfactant addition seemed to reduce the effect.

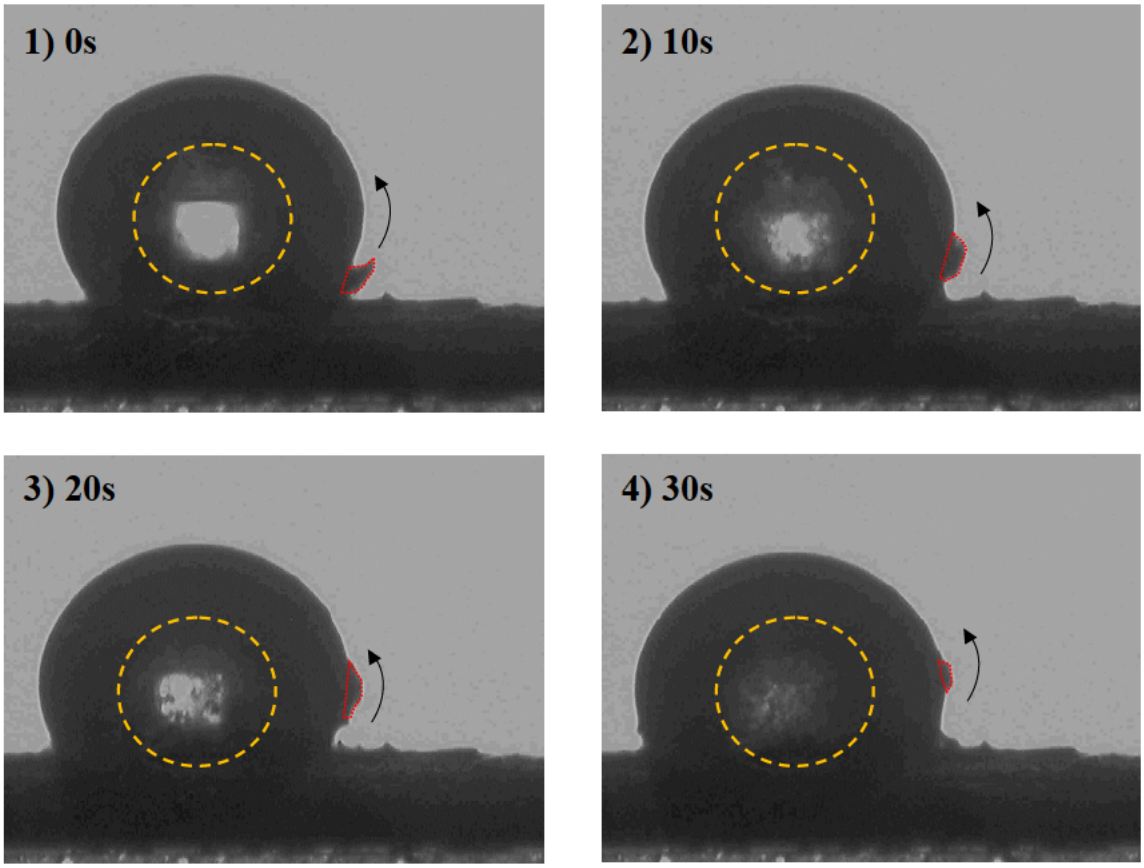

Figure 5.11 Images highlighting scaling effects of WESP dust on a water droplet. Yellow dashed circle highlights smaller particles covering backlight and a larger particle is highlighted in red as it moves up the side of the droplet.

Another impact observed was some of the larger dust particles being pulled up water droplets. This can be seen in Figure 5.11 where the particle is highlighted in red. This figure also again highlights how the finer particles encapsulate the droplet, circled in yellow in images 1-4, to the point where after 30 seconds in image 4 the droplet is almost covered. This effect seemed far more prominent when testing WESP dust and appeared to be linked to the rapid decline in WCA.

To illustrate this further using larger samples of ESP dust, images were taken for water droplets on ESP dust spread across a glass substrate. An image in Figure 5.12 shows 7 water droplets on a substrate of ESP dust with minimal scaling, an image taken several

minutes after placing the droplets. Three of the droplets with a more prominent scaling effect have been circled in yellow to provide better imagery of the effect. Another hydrophobic effect is shown in this figure, when switching samples, it was noticed that droplets on ESP dust samples were anchored in place even when the sample was held close to vertical. Encapsulation of the droplet is again clear.

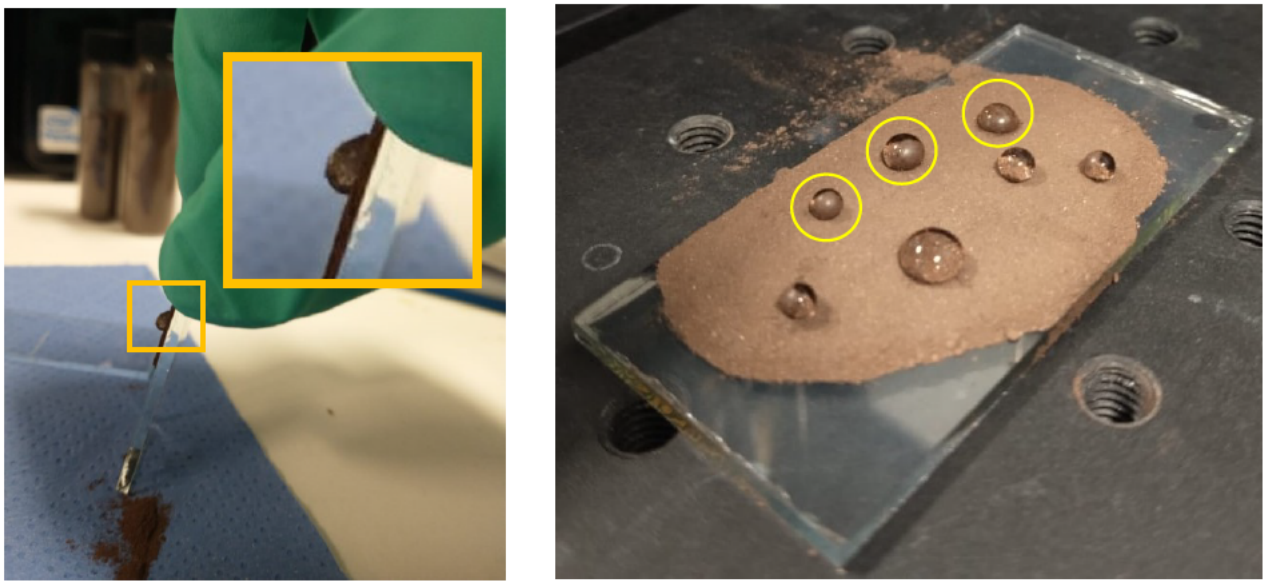

Figure 5.12 Images of hydrophobic behaviour of ESP dust during WCA testing.

Figure 5.13 Image of liquid marbles being formed on ESP dust.

This effect has previously been described as “liquid marbles” (30,32). In this case, liquid marbles could also be formed by carefully rolling water droplets on a bed of ESP dust, as can be seen in Figure 5.13. As discussed in the literature review this is a sign of hydrophobic materials and has been previously recorded in ESP dust. Figure 5.14 shows ESP dust in a glass beaker after being mechanically stirred in water for 10 minutes at 400 rpm. This is yet another example of the highly hydrophobic nature of ESP dust and how it can hinder common washing processes. The image on the left in Figure 5.14 also shows how ESP dust behaves after being added to water without agitation. At the base of the beaker ESP dust can be seen clumping together rather than dispersing and some ESP dust particles can be seen floating on the surface.

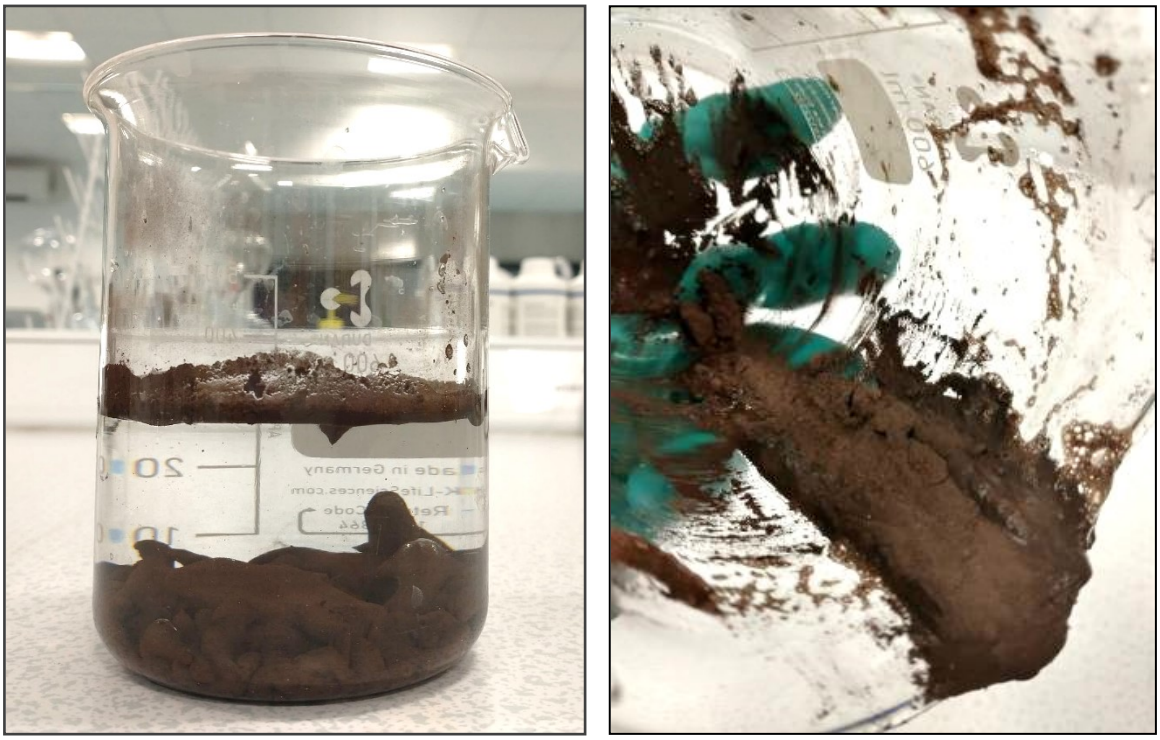

Figure 5.14 Images from ESP dust water washing test. Showing hydrophobic behaviour in water before agitation (left), with post-washing dry ESP dust after washing (right).

5.6 Conclusions

The results from the tests have provided evidence for several significant conclusions. Firstly, the data show that water washing of sinter plant ESP dust clearly results in lower water contact angles and less water contact angle stability. This is likely due to the fact that the process mobilises hydrophobic functional groups from the dust's surface, degrading the materials 'hydrophobic shell.

Including varying concentrations of three surfactants (TX-100, Soap nut and sodium xylene sulfonate) highlighted a range of impacts. Of the three surfactants tested TX-100 had the biggest impact on water contact angle, in terms of WCA over time and initial contact angles. When including 2.0% TX-100 in deionised water, contact angle dropped to 0 ° in < 20 seconds. Soap nut was also effective, showing the biggest impact on WCA, behind TX-100, over a range of timescales. As it is cheaper and more environmentally friendly than TX-100, this makes it an appealing alternative. Sodium xylene sulfonate was seen to have minimal impact on WCA, behaving similarly to water across testing. These results indicate that the addition of TX-100 and soap nut at concentrations between 0.2 – 2.0 % can have an impact on ESP dust WCA, seemingly increasing the effectiveness of hydrophobic functional group mobilisation when compared to solely deionised water.

Numerous examples of the hydrophobicity of ESP dust were recorded during these tests. The most prevalent being the hydrophobic droplet shape instantly observable when adding water droplets to an ESP dust bed. Other examples include portions of dry dust still present even after water washing, the ability to form liquid marbles, droplets anchored to ESP beds even when rotated almost vertically and the scaling effect observed during WCA measurements.

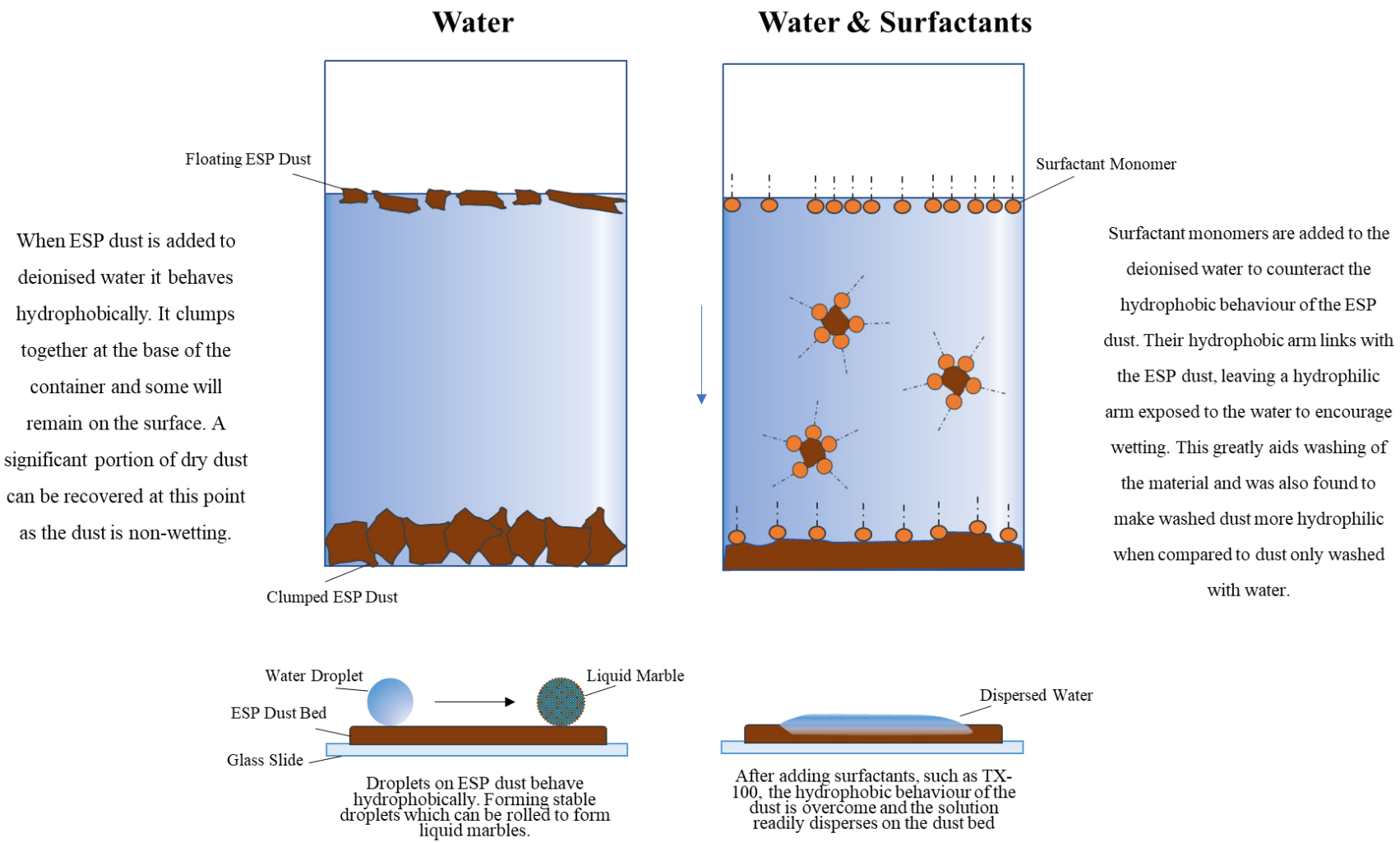

Figure 5.15 Summary annotated diagram highlighting the impacts of surfactants on ESP dust during washing and WCA analysis.

6. INITIAL REVERT AND MICRO-PELLET SINTER POT EXPERIMENTS

This section investigates the implications of utilising up to 5 % of both washed and unwashed ESP dust in sinter pot experiments. This will highlight any impact that water washing of ESP dust would have on the sintering process. As ESP dust is a fine material, some tests were carried out into the micro-pelletisation of fine raw materials, which could be a mechanism of using higher amounts of fines without any detrimental impacts on the process. Analysis will assess whether these alterations impact sintering parameters, final sinter quality and particulate emissions. Sintering quality has been determined by analysis of thermal profile stability, peak temperature, average temperature, cooling rates and the time the sinter bed is above 1000 °C. These are outlined on an annotated sintering thermal profile in Figure 6.1. The quality of sinter produced has been tested in several ways including particle size distribution, dust emission analysis, optical microscopy, XRF and SEM/EDS.

NOTE: Some research was carried out in conjunction with Matthew Thomas (MT) of Swansea University. Any data produced by MT will be credited to him, but all data analysis and interpretation are my own.

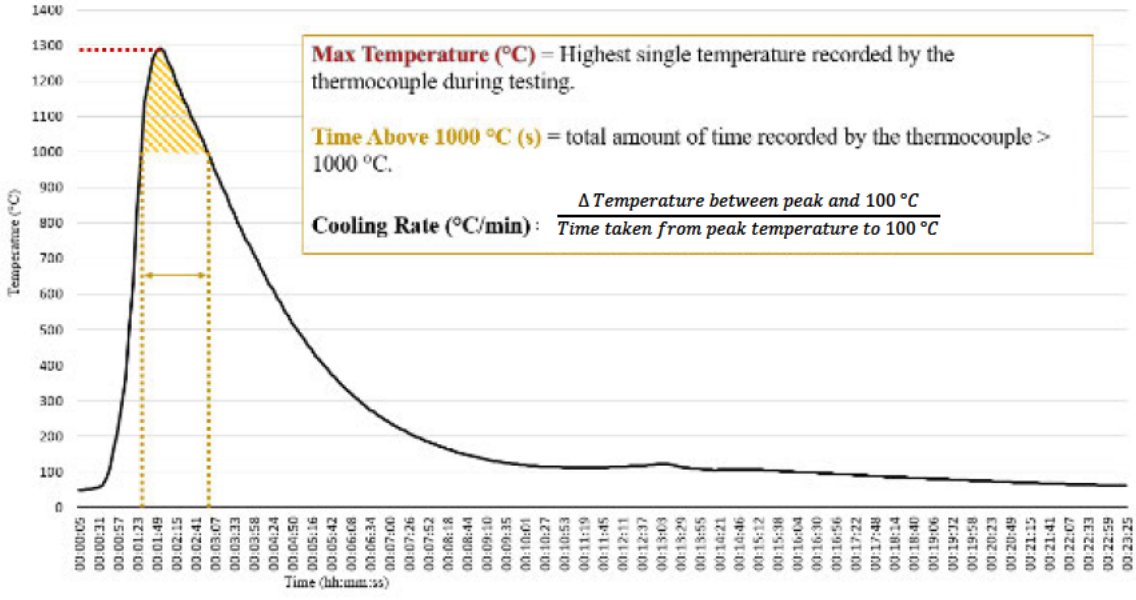

Figure 6.1 An example of a sintering thermal profile graph with key parameters for discussion highlighted.

6.1 Sinter Blend Chemistry & Models

The base blend was an altered version of a previously tested blend, chosen due to its past performance and altered due to availability of materials at the time of testing. Details relating to each blend, including chemistry and particle size distribution, can be found in table 6.1 and figure 6.2. Adaption of the base blend to include reverts and micro-pelletised revert materials was aided by Ryan Davies of Tata Steel UK and the use of the Tata Steel UK blend model calculator. The blend model calculator takes chemistry, particle size and mass of each material into account whilst tracking certain parameters of the blend as a whole. The amount of each material can then be varied to ensure these parameters are within acceptable ranges. Examples of tracked parameters include particle size distribution (PSD) ratio of at least 0.7, $CaO:SiO_2$ ratio of approximately 1.8 and MgO content of approximately 1.9 %, these having been predetermined based on previous Tata Steel UK in house testing. Chemical analysis was completed by Tata Steel UK Labs as is standard procedure for sinter pot testing.

Table 6.1 Summary of tested blend models.

Raw Material (kg)	Base Blend	2.5 % ESP Dust	5.0 % ESP Dust	2.5 % WESP Dust	5.0 % WESP Dust	3.5 % Micro-pellets	7.0 % Micro-pellets
Iron Ore A	**2.21**	**2.14**	**2.06**	**2.14**	**2.06**	**2.55**	**2.55**
Iron Ore B	**3.1**	**2.99**	**2.88**	**2.99**	**2.88**	**3.27**	**2.86**
Iron Ore C	**2.21**	**2.14**	**2.06**	**2.14**	**2.06**	**2.55**	**2.55**
Iron Ore D	**1.33**	**1.28**	**1.23**	**1.28**	**1.24**	**1.53**	**1.53**
Flux A	**1.38**	**1.36**	**1.37**	**1.35**	**1.36**	**1.68**	**1.65**
Flux B	**0.86**	**0.84**	**0.84**	**0.85**	**0.83**	**0.92**	**0.95**
Fuel A	**0.9**	**0.9**	**0.9**	**0.9**	**0.9**	**0.9**	**0.93**
Raw ESP	**0**	**0.32**	**0.65**	**0**	**0**	**0**	**0**
Washed ESP	**0**	**0**	**0**	**0.32**	**0.65**	**0**	**0**
Sinter Fines	**2.32**	**2.32**	**2.32**	**2.32**	**2.32**	**2.38**	**2.53**
BOS slurry	**0.9**	**0.9**	**0.9**	**0.9**	**0.9**	**0**	**0**
Flue dust	**0.8**	**0.8**	**0.8**	**0.8**	**0.8**	**0**	**0**
Micro-pellets	**0**	**0**	**0**	**0**	**0**	**0.61**	**1.3**

Figure 6.2 shows that every sinter blend had a PSD ratio of at least 0.95, well above the acceptable lower limit of 0.7, with the 7.0 % micro-pellet test having the highest value of 1.44. As would be expected the PSD ratio drops as more ESP and WESP dust is added and rises as micro-pellets are added.

Table 6.1 Blend model outlining materials used for sinter pot tests. Some material names excluded at Tata Steel UK's request.

Raw Material (kg)	Base Blend	2.5 % ESP Dust	5.0 % ESP Dust	2.5 % WESP Dust	5.0 % WESP Dust	3.5 % Micro-pellets	7.0 % Micro-pellets
Iron Ore A	2.21	2.14	2.06	2.14	2.06	2.55	2.55
Iron Ore B	3.10	2.99	2.88	2.99	2.88	3.27	2.86
Iron Ore C	2.21	2.14	2.06	2.14	2.06	2.55	2.55
Iron Ore D	1.33	1.28	1.23	1.28	1.24	1.53	1.53
Flux A	1.38	1.36	1.37	1.35	1.36	1.68	1.65
Flux B	0.86	0.84	0.84	0.85	0.83	0.92	0.95
Fuel A	0.90	0.90	0.90	0.90	0.90	0.90	0.93
Raw ESP	0.00	0.32	0.65	0.00	0.00	0.00	0.00
Washed ESP	0.00	0.00	0.00	0.32	0.65	0.00	0.00
Sinter Fines	2.32	2.32	2.32	2.32	2.32	2.38	2.53
BOS slurry	0.90	0.90	0.90	0.90	0.90	0.00	0.00
Flue dust	0.80	0.80	0.80	0.80	0.80	0.00	0.00
Micro-pellets	0.00	0.00	0.00	0.00	0.00	0.61	1.30

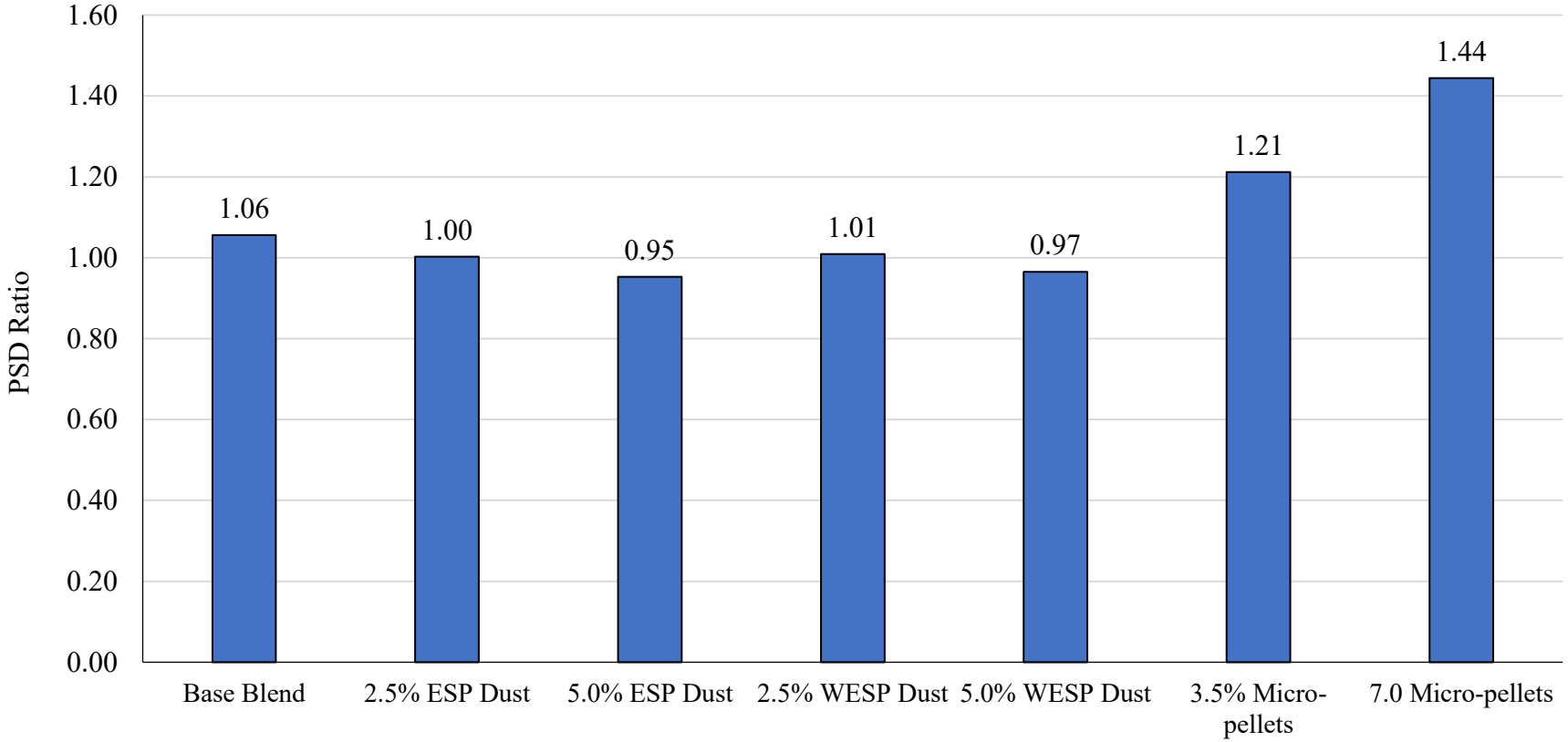

Figure 6.2 Bar chart showing the varying PSD ratios between the sinter blends.

Table 6.2 Raw sinter mix chemistry as reported by Tata Steel UK Laboratories.

Sinter Blend	Base Blend	2.5 % ESP Dust	5.0 % ESP Dust	2.5 % WESP Dust	5.0 % WESP Dust	3.5 % Micro-pellets	7.0 % Micro-pellets
SiO_2	7.98	5.48	5.27	5.41	5.19	5.17	5.57
$Al2O_3$	1.25	1.05	0.97	0.97	1.02	0.59	0.6
TiO_2	0.05	0.07	0.07	0.08	0.09	0.08	0.08
CaO	7.71	8.68	8.09	7.67	9.64	7.83	6.3
MgO	1.18	1.43	1.48	1.35	1.91	1.42	0.87
Fe	46.64	46.38	46.85	44.96	45.54	43.44	50.28
Fe_2O_3	56.41	59.07	60.8	60.81	59.8	51.87	61.67
FeO	9.25	6.52	5.57	3.14	4.79	9.22	9.2
P	0.04	0.029	0.024	0.022	0.027	0.018	0.022
Mn	0.14	0.14	0.13	0.12	0.11	0.09	0.11
Na_20	0.034	0.073	0.093	0.044	0.052	0.032	0.028
K20	0.049	0.08	0.15	0.07	0.073	0.04	0.028
Zn	0.008	0.007	0.019	0.014	0.01	0.009	0.006
Cu	0.001	0.002	0.003	0.003	0.002	0.001	0.001
Cl	0.01	0.024	0.08	0.028	0.059	0.016	0.009
$CaO:SiO_2$	1.78	1.78	1.82	1.78	1.80	1.82	1.82

6.2 Base Blend

The primary aim of the first sintering tests carried out was to establish a baseline of permeability and sintering conditions to highlight differences that occur when the base blend is altered with the addition of reverts and micro-pellets.

6.2.1 Moisture Optimisation

After a blend model was constructed based on available materials, shown in Table 6.1, tests were carried out on the base blend to determine the optimal moisture content for sintering tests. The water content influences granulation rates which in turn will impact permeability and therefore the sintering process.

*Figure 6.3*Figure 6.3 shows images of base blend sinter mixture with 6.0 %, 7.0 % & 8.0 % moisture added. The images show the influence water has on granulation of the base blend so,

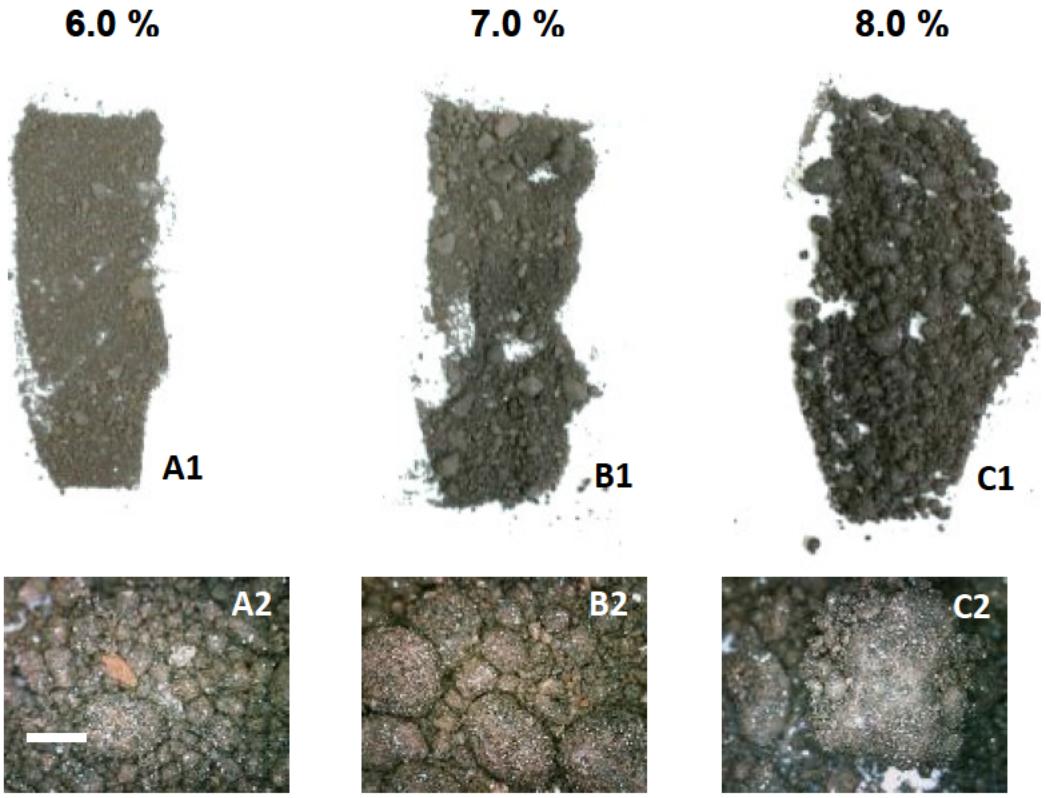

as more moisture is added during the granulation stage, larger granules are observed forming.

Figure 6.3 Image of granulated base blends; A1 = BB1, 6% moisture. B1 = BB2, 7% moisture. C1 = BB3, 8% moisture & close up images; A2 = BB1, 6% moisture. B2 = BB2, 7% moisture. C2 = BB3, 8% moisture (where BB = Base Blend).

Although there is a heterogenous range of granule sizes in all blends, generally the average size increases with more water. Comparing A1 to C1 for example clearly shows more larger granules which is also supported by higher magnification images in A2 and C2.

A2 shows a large number of grains between 1-2 mm indicating that not much granulation has taken place, compared to B2 where there is an increase in average size and C2 where there is clear coalescence on display. 8.0 % moisture is generally a higher level than would be used industrially, this is because excess water in the sinter blend mixer can lead to slurry formation rather than granulation taking place and require excess energy to combat excess moisture which drives up fuel costs. For this reason tests were not extended beyond this point and therefore 8.0 % was selected as the optimal moisture content for the rest of the testing series.

6.2.2 Base Blend Cold Permeability Experiments

Cold permeability testing is the first step in sinter pot experiments and helps to determine the air flow rates though the un-sintered granulated bed in the sinter pot. This is linked to the sintering stage itself as high air flow will have an impact on the sintering rate, flame front width, max temperature etc. Figure 6.4 compares the cold permeability results for the base blends with varied moisture content during the moisture optimisation test.

All thee plots show the same trajectory, a steady rise until approximately 2 minutes into the test before levelling off for the remainder. This is likely due to the initial air flow mobilising loose particles which then fill pore spaces. The blend with 8.0 % moisture clearly had the highest air flow rate with a peak of 9.2 m^3/h & an average of 8.7 m^3/h over the whole test. Compared to averages of 5.8 m^3/h & 5.6 m^3/h and peaks of 6.8 m^3/h & 6.9 m^3/h for BB1 & BB2 respectively. This means that if averaging the values for BB1 and BB2, equalling 5.68 m^3/h, then the average BB3 permeability is approximately 40 % higher.

Although the data for both BB1 and BB2 fluctuates during the cold permeability test, as can be seen in figure 6.4, they both have very similar peaks and averages showing that increasing moisture from 6.0 % to 7.0 % had almost no impact on the cold permeability of this particular sinter blend. However, BB3 has visibly higher air flow rates during the test which is also supported by the peak and average values. This supports the visual observations

of the granules in figure 6.3 that BB3, with 8.0 % moisture, results in the most effective granulation which in turn leads to superior air flow permeability which is preferable for commercial sintering to maximise fuel combustion within the sinter bed.

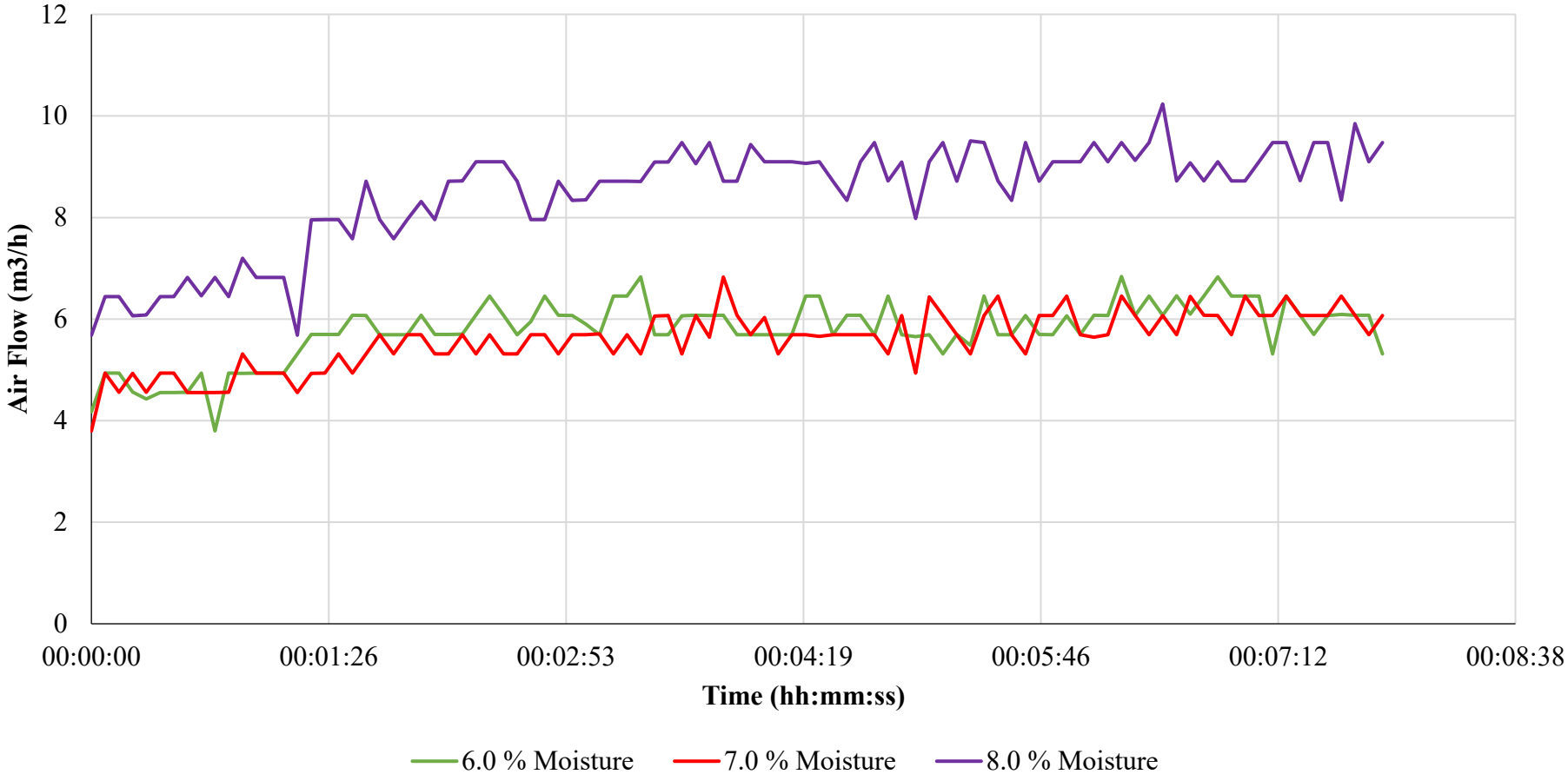

Figure 6.4 Cold permeability test results for base blend moisture optimisation test

6.2.3 Base Blend Sintering Experiments

The sintering thermal profile for the 8 % moisture base blend can be seen in figure 6.5. The 8 % moisture test concludes in approximately 32 minutes and overall displays a typical thermal profile expected from this sinter pot based off previous research (82). The only atypical data being around thermocouples 4 and 5 where the thermal profiles almost have overlapping peaks and identical thermal declines. This will be discussed in more detail below.

Peak temperature throughout the test ranges between 1255.9 ºC at thermocouple 1 to 1353.0 ºC at thermocouple 5, with the greatest temperature of 1412.8 ºC being recorded at thermocouple 4. This is to be expected as the flame front develops early on, resulting in lower temperatures, before propagating as it works though the bed and resident fuel.

The highest average temperature however is seen in thermocouple 2 which averages 488.1 ºC during testing, compared to a low of 280.5 ºC at thermocouple 5. This coincides with the time above 1000 °C also being the highest and lowest at these thermocouples, with thermocouple 2 spending 360 s above 1000 °C whereas thermocouple 5 spends just 140 s, i.e., less than half the time at thermocouple 2.

When looking at figure 6.5 there is a notable difference between the morphology of the peaks of thermocouples 2 and 5 also, with 2 showing a more rounded and wider peak compared to a very sharp and fleeting peak at thermocouple 5. This further indicates how the flame front's behaviour has changed during the test, likely thinning and speeding up as it reached the latter stages. There was only 65 seconds between the peaks of thermocouples 4 and 5, compared to 265 s between thermocouples 2 and 3.

Overall, this blend appeared to perform well and will act as a good baseline for comparison against the tests outlined in upcoming sections.

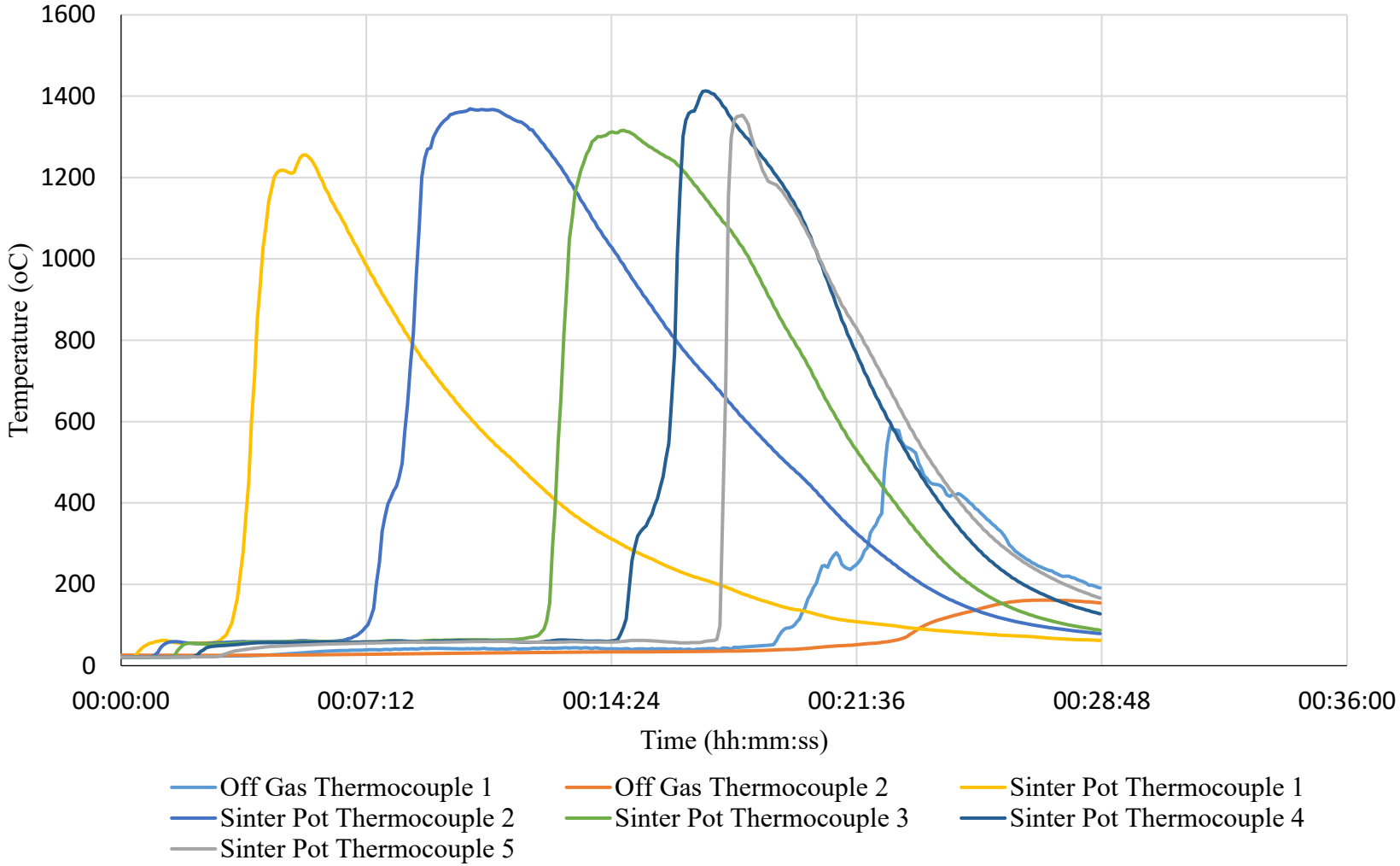

Figure 6.5 Sintering thermal profile for 8 % moisture base blend test.

6.2.4 Base Blend Hot Permeability Experiments

A comparison of hot permeability rates can be seen in figure 6.6. Initially, the same trend is observed that was seen in the cold permeability test, with the 8 % moisture blend presenting a higher permeability compared to the 6 % and 7 % moisture blends. This reinforces observations from the cold permeability test with the early stages of the hot permeability showing the same trend before.

The blend featuring 8 % moisture sees it's inflection much sooner than the lower moisture blends, after approximately 17 minutes compared to around 30 minutes, shown in figure 6.7. The significant point of inflection at after approximately 17 minutes in the 8 % moisture blend coincides with the inflection seen at thermocouple 5 in Figure 6.5. This inflection indicates the point in time where a significant portion of the raw material blend has been sintered, which allows for better air flow due to higher void spaces.

Figure 6.6 compares the average and peak airflow between the blends during sintering, further emphasising that the 8 % moisture blend has superior permeability. This must be due to the improved granulation, as shown in figure 6.3.

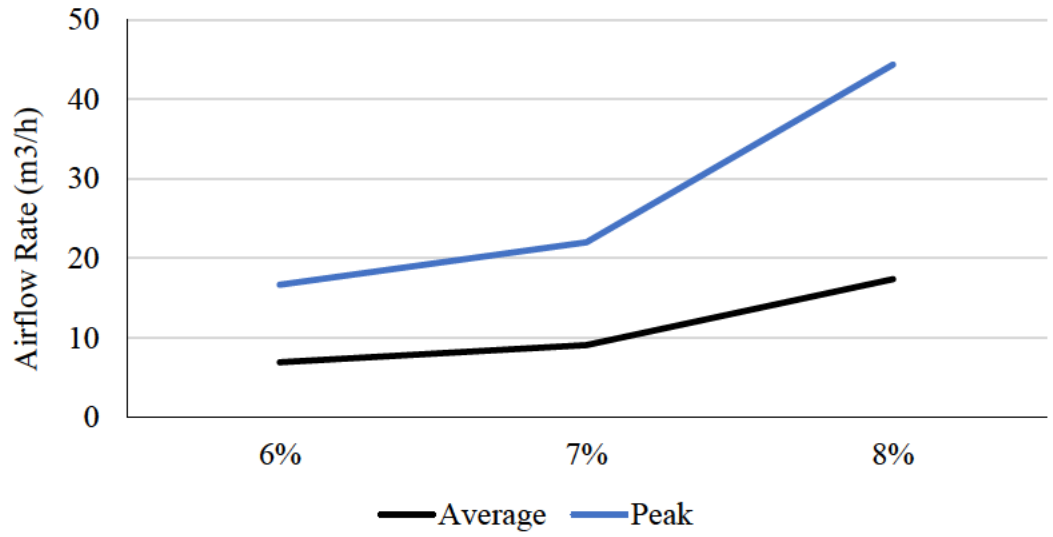

Figure 6.6 Chart showing impact of moisture content on the base blends average and peak airflow rates during sintering.

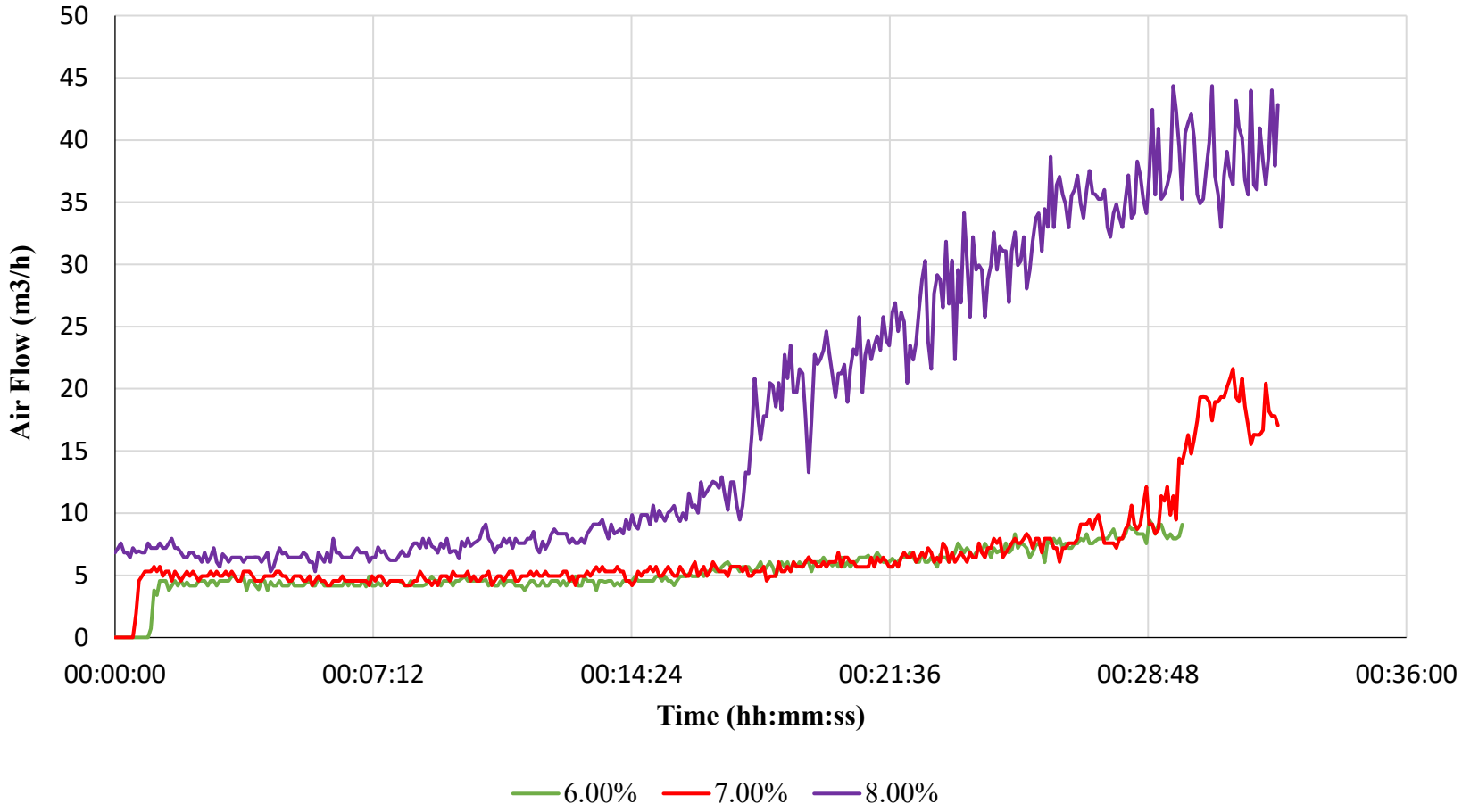

Figure 6.7 Hot permeability test air flow fata for moisture optimisation of base blend.

6.2.5 Base Blend Conclusions

Based on the moisture optimisation tests undertaken 8 % moisture was deemed the optimal moisture content for this blend. As demonstrated, this provided improved granulation, superior permeability, and stable sintering conditions. Testing was not extended beyond 8 % as this would not be reflective of plant operating conditions and excessive moisture content can be detrimental to sintering. The remainder of tests in this section were conducted at a moisture content of 8 %. It was considered that the alteration of the blend composition may have an impact on optimal moisture content however it was recommended by Tata Steel UK to proceed with a moisture content of 8 %.

6.3 Micro-pellets Addition

Micro-pellets were tested at 3.5 % & 7.0 % of the total blend, the aim being to establish if ultra-fine material can be used in higher quantities by pelletising it prior to sintering. Total blend chemistry was matched between the tests.

6.3.1 Micro-pellet Cold Permeability Experiments

The cold permeability tests are displayed in Figure 6.88, and base blend results are also included for ease of comparison. Both micro-pellet tests display higher cold permeability air flow rates than the 8 % moisture base blend, which has the highest readings out of all 3 base blend variations during moisture optimisation. Both micro-pellet tests show similar results with an average of 12.1 m^3/h for MP 3.5 % & 12.9 m^3/h for 7 % micro-pellet blend, ~ 20 % greater than the 10.6 m^3/h average of the base blend.

There is slightly more variance in the peak readings with 13.3 m^3/h & 14.0 m^3/h for MP 3.5 % & MP 7.0 %, respectively. This means that compared to the base blend there is a 25 % rise in peak cold permeability flow rates when including 3.5 % micro-pellets in the blend, rising to 32 % when adding 7.0 % micro-pellets. This indicates that the addition of micro-pellets provides a significant benefit to cold permeability initially. However, the benefit achieved does not appear to be a linear increase as more micro-pellets are added , as shown in the results discussed. Due to this increased permeability, faster sintering rates and potentially higher temperatures would be expected during sinter testing.

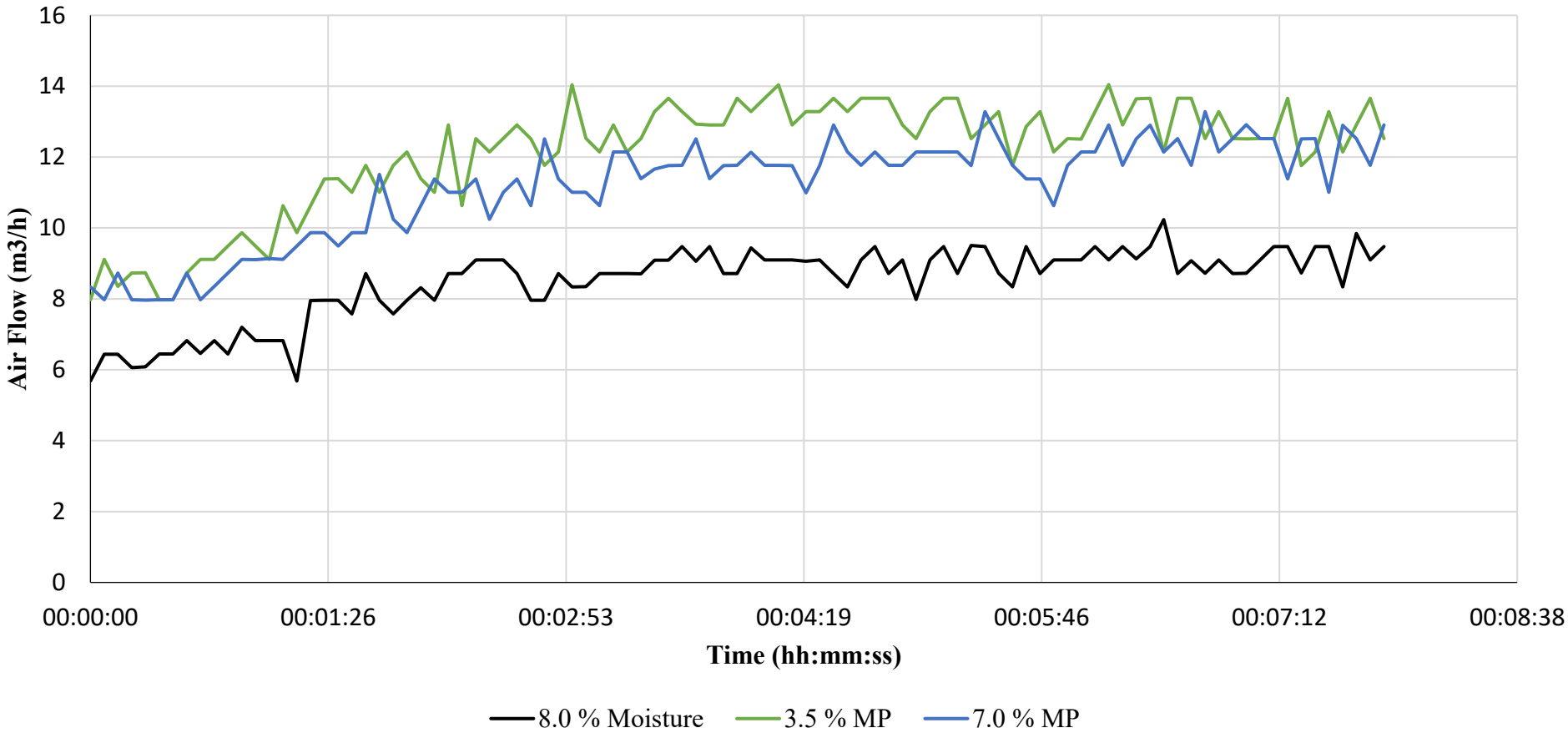

Figure 6.8 Comparison of cold permeability test air flow data for micro-pellet sinter blends, with moisture optimised base blend included for comparison.

6.3.2 Micro-pellet Sintering Experiments

The sintering thermal profiles for the 3.5 % & 7.0 % micro-pellet tests are displayed in Figure 6.10 and Figure 6.10. The data show that it takes approximately 23 minutes for the thermocouples in both tests to read < 100 ºC. This is approximately 10 minutes faster than the optimised base blend. Both micro-pellet profiles are relatively similar overall, although it could be said that the 3.5 % micro-pellet blend is slightly more stable overall in terms of peak temperatures across thermocouples and in terms of uniformity of each thermocouple profile. The blend which included 7.0 % micro-pellets showed irregular sintering profiles during all repeat tests, this is considered to be due to the high PSD ratio of 1.44 (see figure 6.2) due to the high micro-pellet content. The results indicate that this PSD ratio may be detrimental to the sintering process, likely due to allowing too much void space or causing irregular airflow through the bed which disrupts sintering.

6.3.2.1 Thermocouple 1

The peak temperatures recorded at thermocouple 1 are similar in both blends featuring micro-pellets, with the 1291.9 °C of the 3.5 % micro-pellet blend slightly exceeding the 1258.8 °C recorded in the 7.0 % micro-pellet blend. This makes the base blend, which peaks at 1255.9 °C, comparable to the 7.0 % micro-pellet blend in terms of peak temperature.

The average temperature recorded by thermocouple 1 during sintering for the 3.5 % and 7.0 % micro-pellet blends, respectively was 255.0 °C and 258.8 °C. This is significantly lower than the 357.5 °C average temperature in the base blend. This however can be explained by the cooling rates. Whereas the base blend was cooling by approximately 68 °C/min at thermocouple 1 throughout sintering, the micro-pellet tests were cooling at rates of 95.4 °C/min and 136.3 °C/min for the 3.5 % and 7.0 % micro-pellet blends, respectively.

The time spent above 1000 °C was just 85 s and 110 s in the 3.5 % and 7.0 % micro-pellet sintering experiments at thermocouple 1, compared to approximately 175 s in the base blend sintering test. These discrepancies are likely due to the higher permeability forming a faster flame front, as increased airflow pulled the flame front through the bed at a more rapid rate, also seen by the difference in total test times.

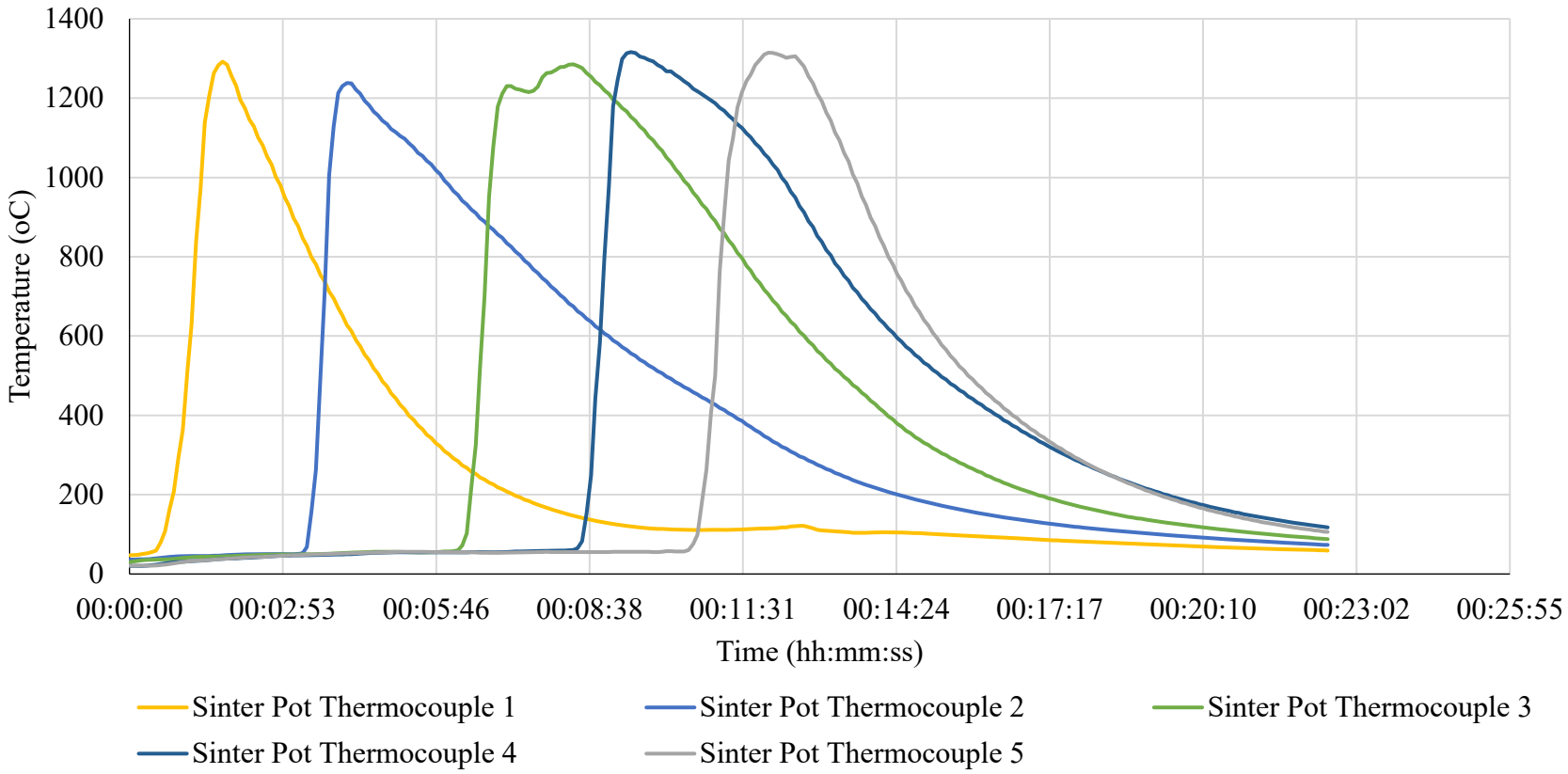

Figure 6.9 Sintering thermal profile of the 3.5 % micro-pellet sinter blend.

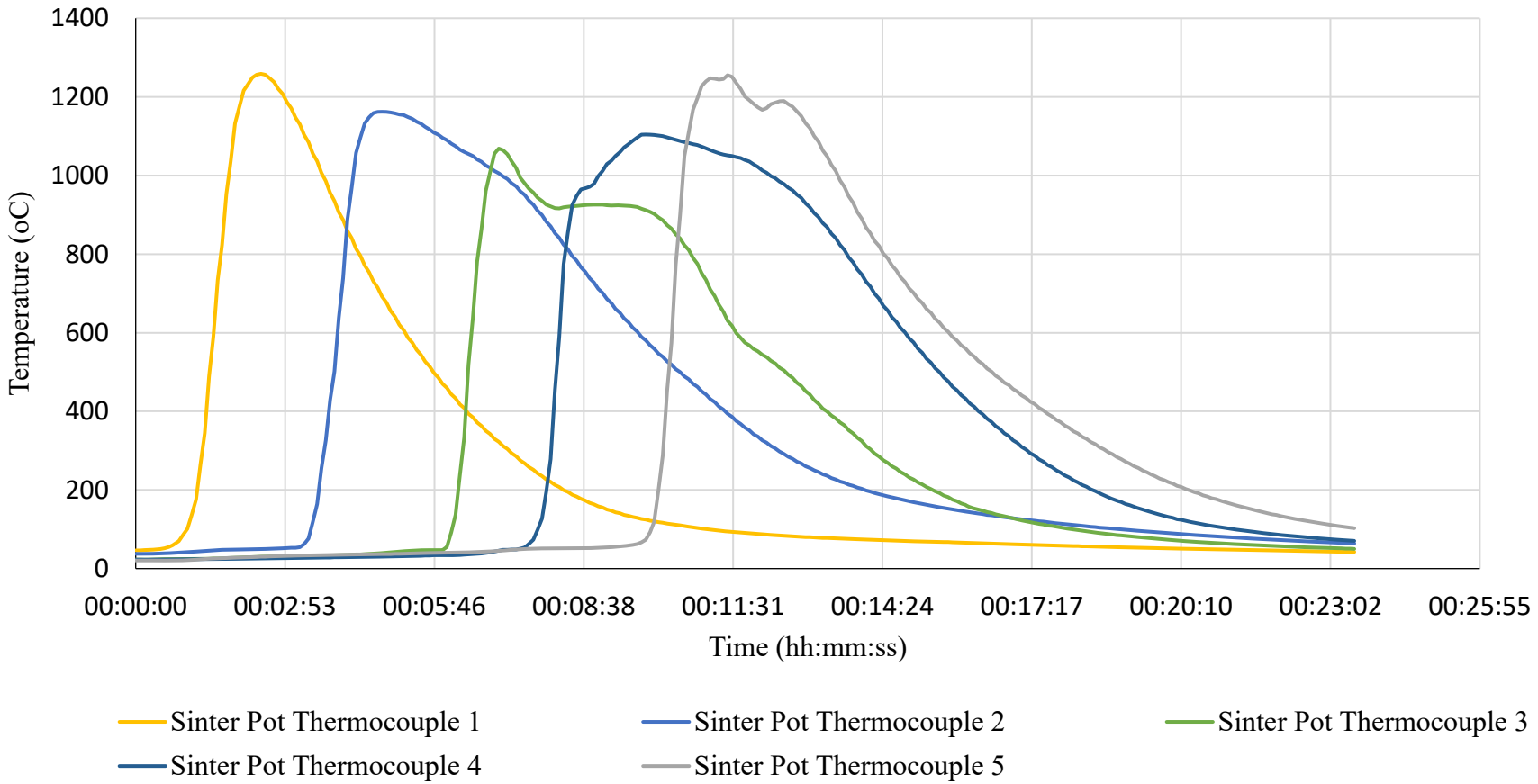

Figure 6.10 Sintering thermal profile of the 7.0 % micro-pellet sinter blend.

6.3.2.2 Thermocouple 2

As the flame front moves on to thermocouple 2 both micro-pellet tests see declines in their peak temperatures. The 3.5 % micro-pellet test temperature falls slightly less to 1238.3 °C, or by approximately 4 %, whereas the 7.0 % micro-pellet test drops to 1162.2 °C, or approximately 7.5 %. Conversely, the base blends peak temperature rose as the flame front progressed to thermal couple 2, rising by approximately 9 % to 1369.1 °C.

The average temperature of both micro-pellet tests and the base blend all rise by at least 100 °C compared to thermocouple 1. This is likely due to the development and widening of the flame front as it consumes more fuel within the bed. The base blend averages 488.1 °C compared to 362.9 °C and 359.5 °C for the 3.5 % and 7.0 % micro-pellet tests, respectively.

Whilst the 3.5 % micro-pellet blend's test only spent 125 s above 1000 °C at thermocouple 2 and the 7.0 % micro-pellet just 165 s, the base blend spent 360 s above 1000 °C. This is testament again to the fact that the base blend appears to induce a much wider and slower flame front. The cooling rates for both micro-pellet tests did fall slightly below that of the base blend's 79.3 °C/min, 74.6 °C/min and 75.9 °C/min for the 3.5 % micro-pellet and 7.0 % micro-pellet, respectively. However, this slightly slower cooling rate was offset by the lower peak temperatures.

6.3.2.3 Thermocouple 3

The only data which does not see a decline in peak temperature at thermocouple 3 is the 3.5 % micro-pellet blend, which rose by 47 °C to 1285.2 °C. Although the base blend declines it does still have the highest peak temperature of 1316.1 C. The 7.0 % micro-pellet blend however falls by a further 94 °C to 1068.6 °C. When looking at Figure 6.1010, there is clearly something unusual occurring at thermocouple 3 during the 7.0 % micro-pellet test. After this low peak temperature, the profile declines before plateauing for roughly 2 minutes before returning to a steady decline for the remainder of the test.

Average temperature of the 3.5 % micro-pellet test increased 32 °C to 394.7 °C, however due to the anomalous profile seen within the 7.0 % micro-pellet test its average temperature fell to 299.5 °C. This is compared to the base blend at this point which averages 398.5 °C. This also results in just 30 s spent above 1000 °C at thermocouple 3 for the 7.0 % micro-pellet test, whilst the 3.5 % micro-pellet test increases its time above 1000 °C by 90 s

to a total of 215 s. Cooling rates rise slightly in both the 3.5 % and 7.0 % micro-pellet tests, to 91.2 °C/min and 88.1 °C/min respectively.

The irregularity seen at thermocouple 3 for the 7.0 % micro-pellet blend could be due to channelling or an uneven flame front, potentially caused by the high number of micro-pellets. It may also have originated closer to thermocouple 2, when the peak temperature fell where a rise would be expected.

6.3.2.4 Thermocouple 4

Peak temperatures rise in both of the micro-pellet tests as the sintering progresses through the bed to thermocouple 4 rising by 31 °C to 1316.1 °C in the 3.5 % micro-pellet test and by 36 °C to 1104.3 °C in the 7.0 % micro-pellet test. Although the 7.0 % micro-pellet test has rebounded somewhat from thermocouple 3, it is still approximately 200 °C and 300 °C lower than the peak at the same stage for the 3.5 % micro-pellet test and the base blend, respectively.

The average temperature of the 7.0 % micro-pellet test's profile at thermocouple 4 did rebound significantly however and even exceeded that of the base blend. The 7.0 % micro-pellet data rises to 365.7 °C, compared to the base blends 349.2 °C and 376.6 °C in the 3.5 % micro-pellet blend's test. This is linked to the 7.0 % micro-pellet test having the slowest cooling rate of 83.7 °C/min, whereas at this point the base blend's cooling rate began to speed up and reached 109.4 °C/min, approximately 20 % faster. This slower cooling rate also results in significantly more time spent above 1000 °C for the 7.0 % micro-pellet test, achieving a total of 200 s. This indicates that whilst not as stable as the other tests, the 7.0 % micro-pellet test has become more stable compared to its behaviour at thermocouple 3.

6.3.2.5 Thermocouple 5

As the flame front progresses to the final thermocouple, the peak temperature in the 3.5 % micro-pellet test remains stable at 1314.7 ºC but the 7.0 % micro-pellet test rose by approximately 150 °C to 1255 °C. However, both of these are lower than the base blend at this point which recorded 1353.0 ºC.

Average temperatures drop in both micro-pellet tests compared to thermocouple 4 although the 3.5 % micro-pellet test's decline is more significant as it falls by 73 °C to 303 °C. Whilst this drop is greater than the 26 °C fall in the 7.0 % micro-pellet blend test, it is similar to the base blend's average temperature drop at thermocouple 5 fell which is a 70 °C drop to 280 °C, making it the lowest average temperature at thermocouple 5.

Time above 1000 ºC falls in both micro-pellet tests, to 150 s and 180 s for the 3.5 % and 7.0 % micro-pellet tests respectively, both slightly greater than the base blend's 140 s. Cooling rates also become faster in both tests as they reached 115.7 C/min and 96.3 ºC/min in the 3.5 % and 7.0 % micro-pellet tests respectively. Conversely the base blend saw its cooling rate decrease by 20 ºC/min to 89.5 ºC/min.

6.3.3 Micro-pellet Hot Permeability Experiments

The hot permeability data again includes the base blend readings for ease of comparison, shown in Figure 6.111. Both micro-pellet tests follow a similar trend, holding relatively steady until 7 minutes into the test before a rapid rise. The 3.5 % micro-pellet test continues this positive course longer than 7.0 % micro-pellet. For example, after approximately 16 minutes, the 7.0 % micro-pellet blend begins to plateau in comparison. This is seen in the average flow rate from 7 minutes, the point of inflection, to the end of test being 28.1 m^3/h for the 3.5 % micro-pellet blend compared to 26.1 m^3/h for the 7.0 % micro-pellet blend. The 3.5 % micro-pellet test also has a higher peak airflow of 48.2 m^3/h compared to 39.8 m^3/h recorded in the 7.0 % micro-pellet test. Despite the much earlier inflections, indicating faster sintering of the blends, the base blend does reach similar air flow rates towards the end of its sintering test.

6.3.4 Micro-pellet Addition Conclusions

Whilst both tests were completed much faster than the base blend, the base blend had higher peak temperatures at every thermocouple apart from thermocouple 1. The reduced test time is almost certainly linked to the improved permeability in the micro-pellet blends, the faster flame front may also contribute to the lower temperatures. However, when comparing the 3.5 % and 7.0 % micro-pellet thermal profiles, the 3.5 % blend appears to have been much more stable and uniform in terms of peak temperatures and profile morphology throughout. This potentially indicates that over a certain concentration the presence of micro-pellets can be a hinderance to sintering. Based off these results it appears that the addition of up to 3.5 % micro-pellet noticeably improves both permeability and sintering performance of this sinter blend.

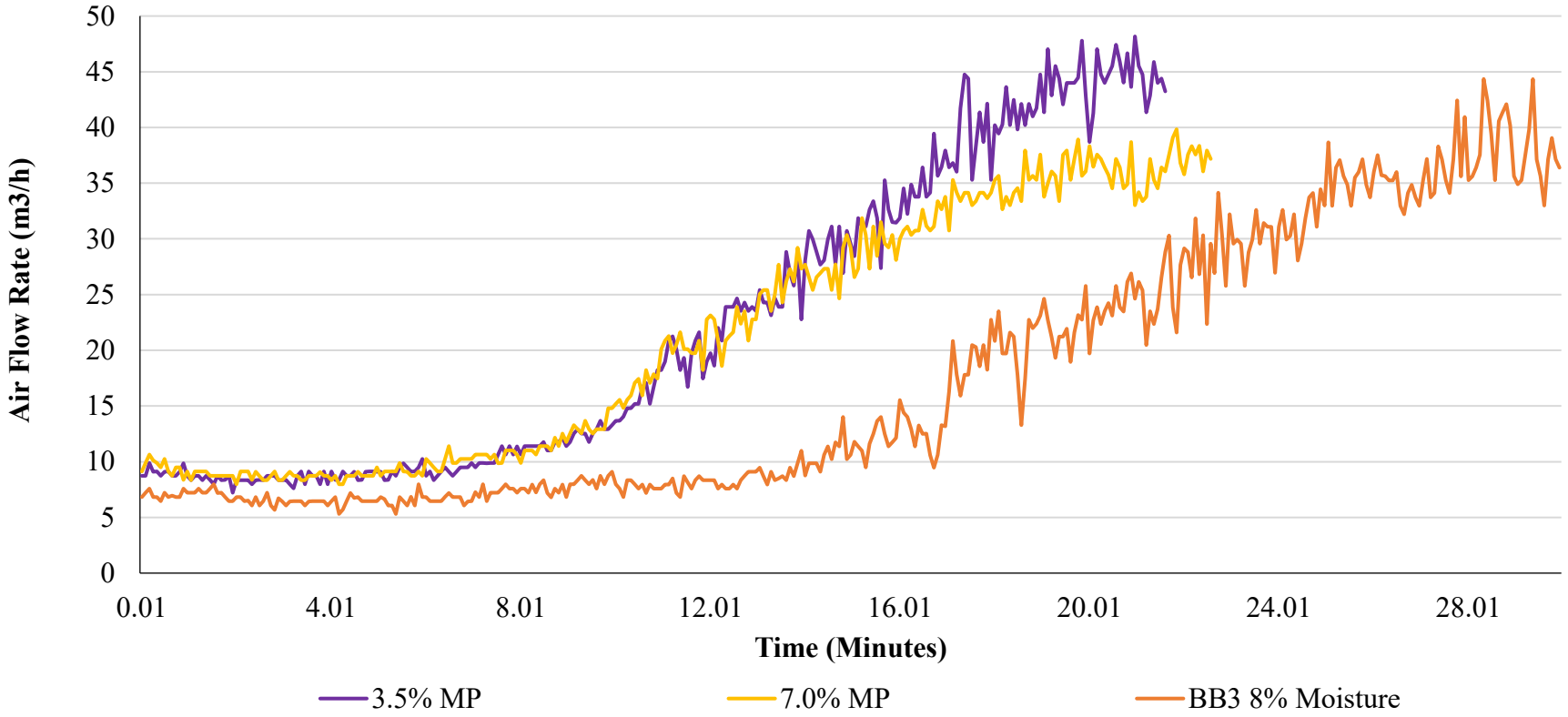

Figure 6.11 Hot permeability test air flow data for micro-pellet blends, base blend included for comparison.

6.4 ESP Dust Addition

The original base blend was amended to account for the inclusion of ESP dust at varying concentrations and the moisture content was held at the selected optimised level of 8.0 % for all tests. The aim of this suite of tests was to assess the how including high concentrations of ESP dust impacts the sintering process and resultant sinter. Water washed ESP dust was also tested at the same concentrations to assess if the washing process impacts the process. Tata Steel UK lab analysis results showed that both the ESP and WESP dust particles were all < 0.1 mm in diameter, meaning they represent ultra-fine materials in terms of the sinter blend.

6.4.1 ESP Dust Cold Permeability Experiments

The cold permeability airflow data for the tests containing ESP dust are displayed in Figure 6.12, with the base blend also included for ease of comparison. There are no major differences between the blends. When analysing the data however there are some slight differences between the blends. The average airflow rate drops in the 5.0 % ESP dust blend compared to the base blend, although only by approximately 0.5 m^3/h to 8.2 m^3/h. The highest average is 9.0 m^3/h in the 2.5 % ESP dust test, which also has the highest peak airflow of 10.6 m^3/h. However due to the fluctuations recorded in all tests it could be argued that the addition of ESP dust has a negligible impact on the cold permeability airflow.

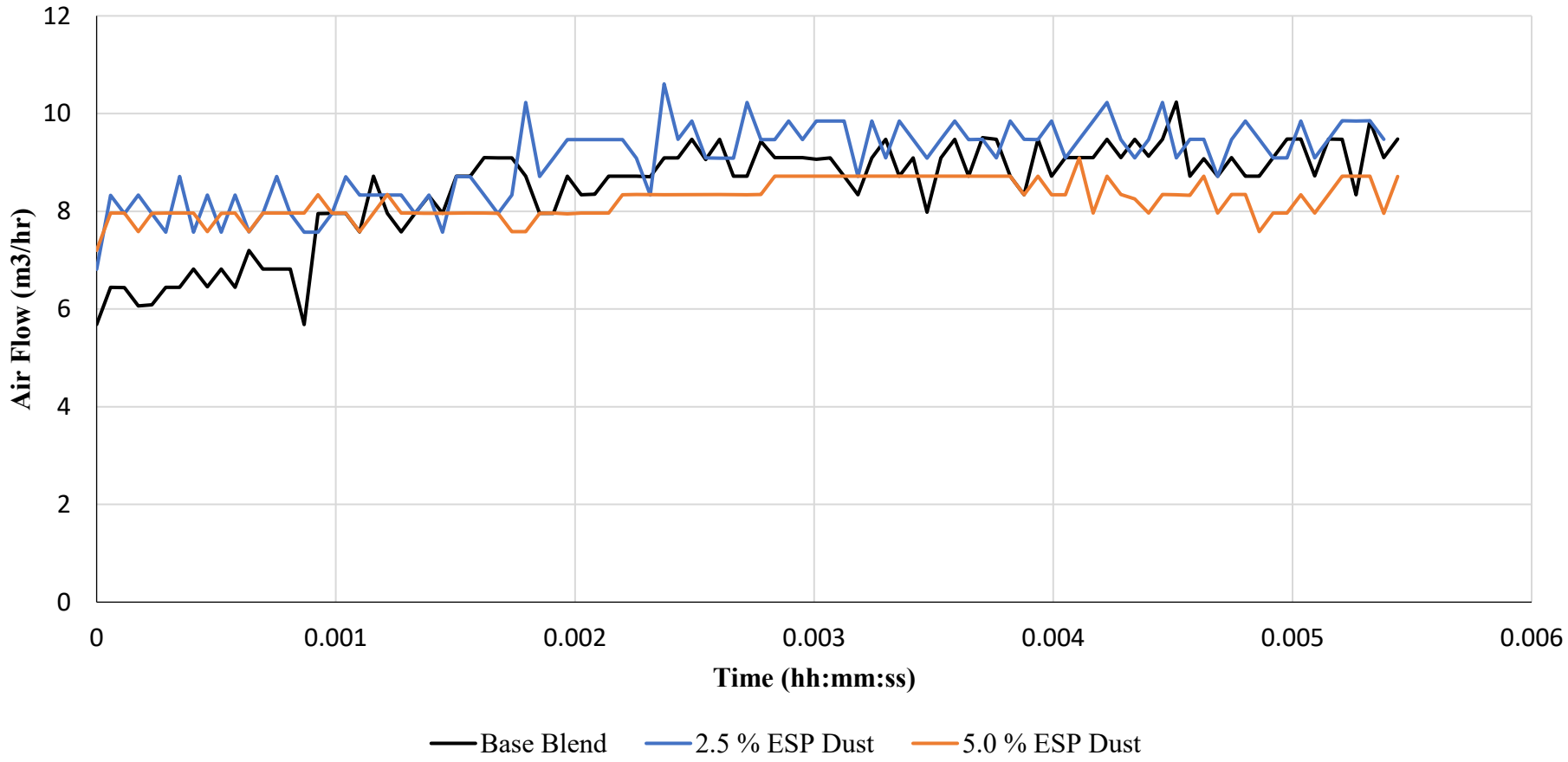

Figure 6.12 Comparison of cold permeability test air flow data for ESP dust blends with moisture optimised base blend included for comparison.

6.4.2 ESP Dust Sintering Experiments

The sintering thermal profiles for the ESP dust blend tests are shown in Figure 6.133 and Figure 6.144. There is a difference in the length of tests between the 2.5 % ESP dust and 5.0 % ESP dust blends, with the two tests lasting approximately 27 minutes and 33 minutes respectively, meaning the higher concentration of ESP dust leads to an approximate 20 % increase in test time. However, if accounting for the variation in the start of data recording, this difference drops to approximately 3 minutes and 30 seconds. The overall thermal profiles of the tests are erratic. This is clear when compared to the 3.5 % micro-pellet blend in Figure 6.99 which displays a typically stable sintering thermal profile.

6.4.2.1 Thermocouple 1

During early stages of sintering at thermocouple 1, the blend containing 2.5 % ESP dust peaks at 1375.4 ºC, approximately 111 ºC higher than the 5.0 % ESP dust which peaks at 1264.2 ºC. Both of these values exceed the base blend's 1255.9 ºC and the 2.5 % ESP dust blend's peak is also higher than either of the micro-pellet tests.

Average temperatures for thermocouple 1 are 299.3 ºC and 284.8 ºC for the 2.5 % and 5.0 % ESP dust blends, respectively. These exceed the average temperatures of the micro-pellet blends at the same stage but the base blend's average of 357.5 ºC remains highest.

The 2.5 % ESP dust blend spends 140 s above 1000 °C at thermocouple 1, slightly less than the 160 s of the 5.0 % ESP dust. Again, this is lower than the 175 s of the base blend but greater than both micro-pellet blends values. Cooling rates are faster than the 68 °C/min recorded in the base blend, being 102.0 °C/min and 80.3 °C/min. These results suggest that the addition of ESP dust to this base blend is more advantageous for early-stage sintering, resulting in higher average temperatures, higher peak temperatures and more time spent above 1000 °C.

6.4.2.2 Thermocouple 2

The sintering thermal profile of the 5.0 % ESP dust blend appears irregular at this point, its sharp inflection tailing off and followed by an unusual small spike in temperature. As the sintering process progresses through the sinter bed towards thermocouple 2, peak temperatures of the ESP dust blends become more similar, as the 2.5 % blend sees a drop to 1289.1 C and the 5.0 % blend rises to 1281.3 C. Though still lagging behind the base blends peak of 1369.1, they remain higher than the micro-pellet blends thermocouple 2 peak temperatures. The average of the ESP dust tests peak temperature are 1285 °C (± 5.7) compared to an average of 1200 °C (± 53.1) in the micro-pellet blends.

The average temperatures both rise sharply from thermocouple 1, reaching 384.2 °C in the 2.5 % ESP dust blend's test and 346.6 in the 5.0 % ESP dust test. This indicates widening or possibly slowing of the flame front. Though experiencing a significant rise from their respective values at thermocouple 1, the base blend averages 488.1 C at thermocouple 2.

Both tests also see rises in their time spent above 1000 °C. The 2.5 % ESP dust test is up 50 % to 210 s and the 5.0 % ESP dust test rises 75 % to 280 s above 1000 °C. The cooling rate of the 2.5 % ESP dust blend declines to 83.2 °C/min, whereas the 5.0 % ESP dust blend hastened to 96.0 °C/min.

6.4.2.3 Thermocouple 3

The 2.5 % ESP dust blend's thermal profile displays a slight double peak at thermocouple 3, indicating some flame front instability. Peak temperatures of the sintering thermal profiles reach 1358.4 ºC and 1272.1 ºC at thermocouple 3 for the 2.5 % and 5.0 % ESP dust blends, respectively. This represents an increase of approximately 69 ºC and a small decline of approximately 9 ºC compared to thermocouple 2, respectively. At this point in the testing although lower on average, the peak temperature of the 5.0 % ESP dust blend appears more stable.

The average temperature of the 2.5 % ESP dust test falls by approximately 40 °C to 346.9 °C, whilst the 5.0 % ESP dust test remains steady at 348.6 °C, comparable to its thermocouple 2 average. For comparison, at this same point the base blend averages 398.5 °C.

Both tests spend a similar amount of time above 1000 °C, being 220 s and 230 s for the 2.5 % ESP dust and 5.0 % ESP dust tests, respectively. This marks a slight increase for the 2.5 % blend but a 50 s decline in the 5.0 % blend compared to the previous thermocouple. Cooling rates again behave variably, with the 2.5 % ESP dust blend's rising to 100.7 ºC/min and the 5.0 % blend dropping down to 75.1 C/min.

6.4.2.4 Thermocouple 4

At thermocouple 4 the thermal profile of the 2.5 % ESP dust blend sees a drop in peak temperature, falling by approximately 240 °C to 1118 ºC, its lowest peak of the test. The 5.0 % ESP dust test however remains fairly stable in terms of peak temperature, rising slightly to 1313 ºC, and does not display any irregularities in its profile. The base blend peaks at 1413 °C at this point.

Average temperature in the blends shows little change from the previous thermocouple. For example, the 2.5 % ESP dust blend reads 347 ºC and the 5.0 % ESP dust averages 336 C, which are comparable to the base blends average of 349 ºC. The time spent above 1000 ºC and cooling rates continue to fluctuate at thermocouple 4 in both tests. The time spent above 1000 ºC drops to 190 s in the 2.5 % ESP dust test and rising to 255 s in the 5.0 % ESP dust test, a disparity of 65 s. Cooling rates of 112 °C/min and 76 ºC/min have been calculated for the 2.5 % ESP dust and 5.0 % ESP dust blends, respectively.

6.4.2.5 Thermocouple 5

This late stage of the test shows irregularities in both test's thermal profiles. The 2.5 % ESP dust blend's profile morphology changes dramatically from the previous thermocouple and the 5.0 % ESP dust test displays 2 peaks. Despite this, the 2.5 % ESP dust blend's peak temperature increases to 1196 ºC, although the 5.0 % blend falls to 1234 ºC. Both of these are significantly lower than the base blend's peak temperature of 1353 ºC.

The average temperatures of the 2.5 % ESP dust and the 5.0 % ESP dust tests are 221.7 ºC and 351 ºC, respectively. This further indicates different causes for the irregularities in their profiles. The time above 1000 ºC is also impacted by these irregularities, a sharp fall to 75 s in the 2.5 % ESP dust blend and 295 s in the 5.0 % ESP dust test. The 2.5 % ESP dust blend records its fastest cooling rate of 112 ºC/min.

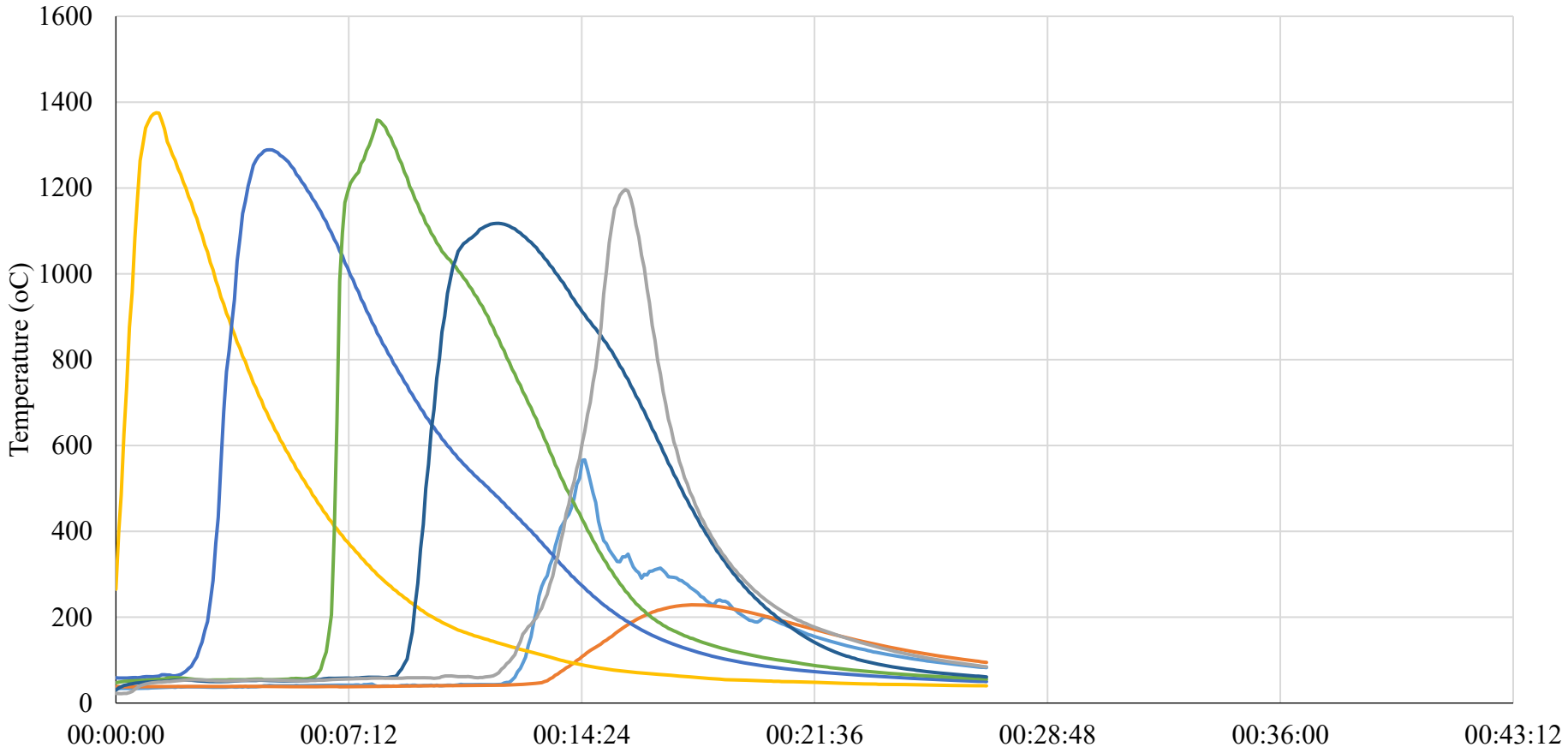

Figure 6.13 Sintering thermal profile for the 2.5 % ESP dust blend test.

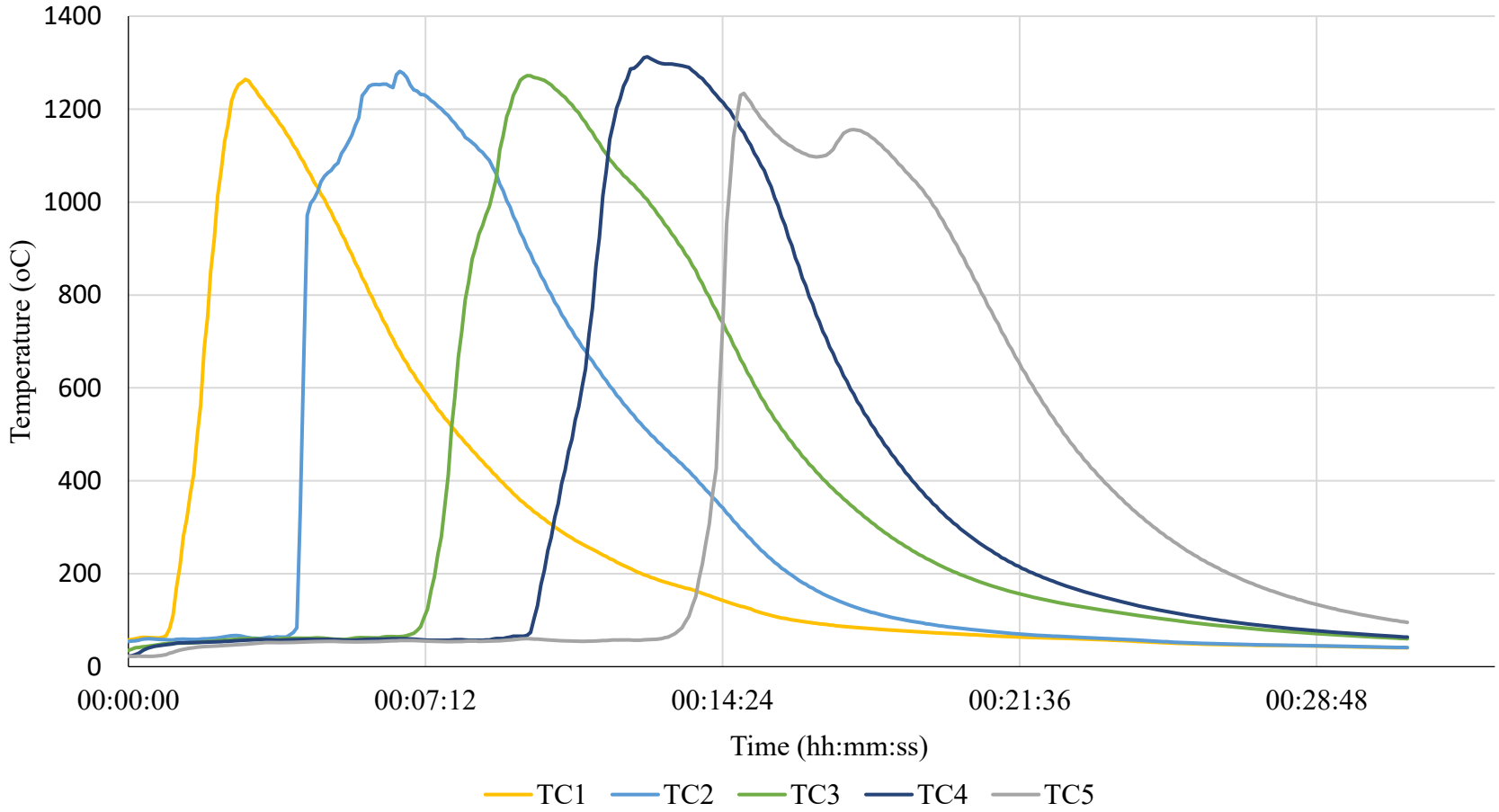

Figure 6.14 Sintering thermal profile for the 5.0 % ESP dust blend test.

6.4.3 ESP Dust Hot Permeability Experiments

The hot permeability results for the ESP dust tests are shown in figure 6.15 which once more clearly shows the difference in sintering test length. Whereas sharp inflections can be seen for the base blend and the 2.5 % ESP dust tests after approximately 17 minutes, the 5.0 % ESP dust test has a more gentle rise throughout the duration of the test. This shows less permeability within the 5.0 % ESP dust blend.

6.4.4 ESP Dust Addition Conclusions

The addition of ESP dust appears to alter sintering stability. The profile for the blend containing 5.0 % ESP dust displayed more consistent temperatures, compared to the 2.5 % ESP dust blend's profile, although there were still clear irregularities within the profile overall. The 2.5 % test displayed a steady decline in temperatures throughout the test and seemed to be much faster, suggesting that the addition of ESP dust leads to irregular flame front behaviour, even when only including 2.5 % in this sinter blend. The cold permeability prior to sintering of the sinter blends showed negligible differences compared to the base blend. However, the hot permeability testing showed the 2.5 % ESP dust had the lowest average air flow initially but showed the sharpest inflection later in the test. This means the flame front moved through the bed faster, this coupled with the low temperatures will likely negatively impact the resultant sinter.

In an industrial setting these impacts could hinder productivity as the sinter bed is much larger, providing more room for variation in the flame front along the strand. Varying flame front speeds could lead to weak or poorly sintered material leaving the strand, increasing return fines and potentially hindering blast furnace permeability. This could also result in more dust emissions from the sinter strand itself, based on these experiments it would not be recommended to include ESP dust in concentrations of 2.5 % or higher of the total blend.

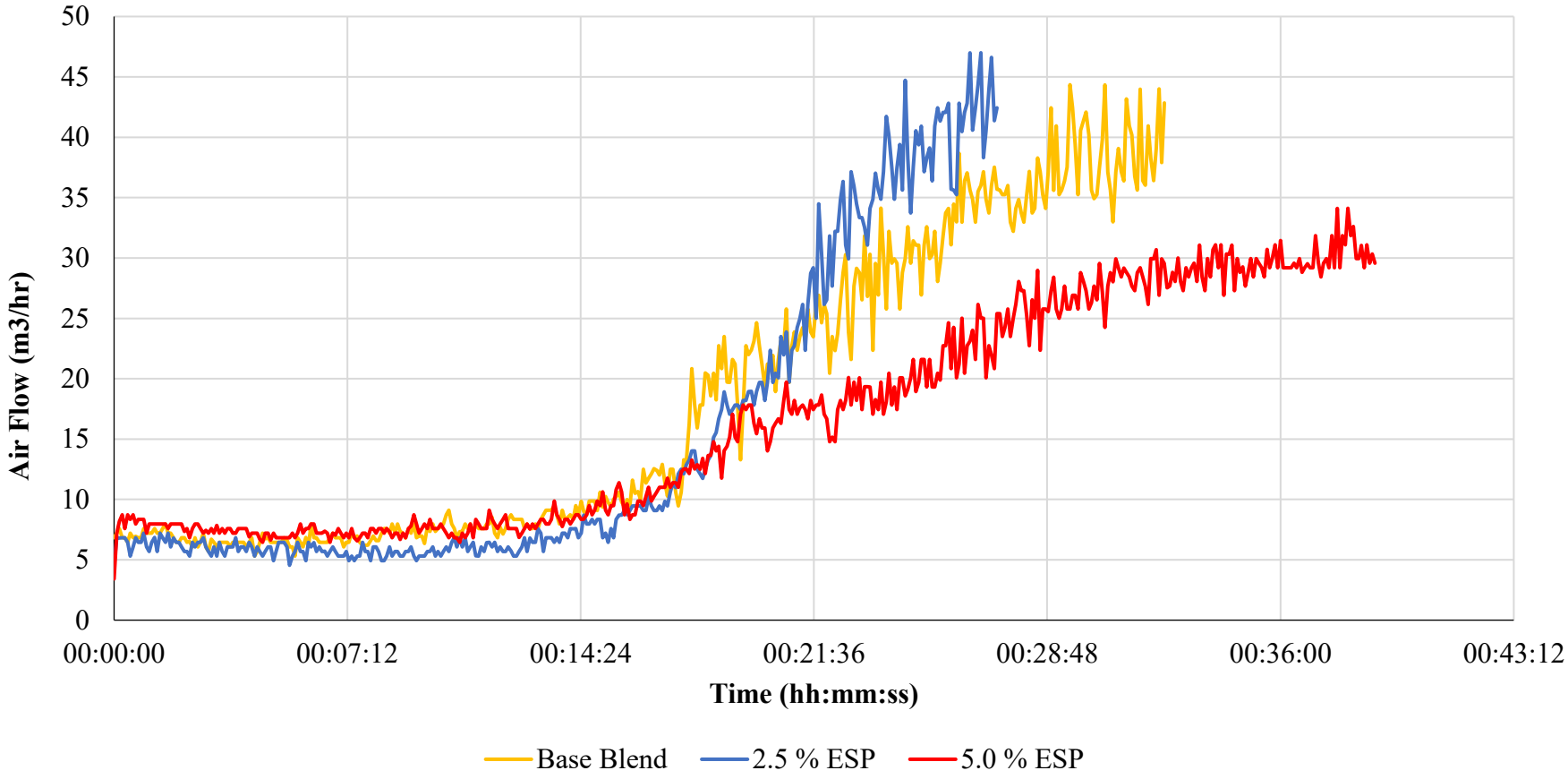

Figure 6.15 Hot permeability test air flow data for ESP dust blends during sintering tests, base blend included for comparison.

6.5 WESP Dust Addition

The original base blend was then also amended to account for the inclusion of WESP dust at varying concentrations and the moisture content was again held at the selected optimised level of 8.0 % for all tests.

6.5.1 WESP Dust Cold Permeability Experiments

The cold permeability results for the WESP dust sinter pot tests are shown in Figure 6.166. In this case, the base blend displays the highest air flow rates with an average of 9.2 m^3/h compared to averages of 8.2 m^3/h for the 2.5 % WESP dust blend & 8.6 m^3/h for 5.0 % WESP dust blend. These results appear in line with the cold permeability testing of the blends containing equal amounts of ESP dust, in Figure 6.122. This suggests that the water washing of the dust does not significantly impact their granulation properties and that the WESP dust behaves similarly to the ESP dust during these tests.

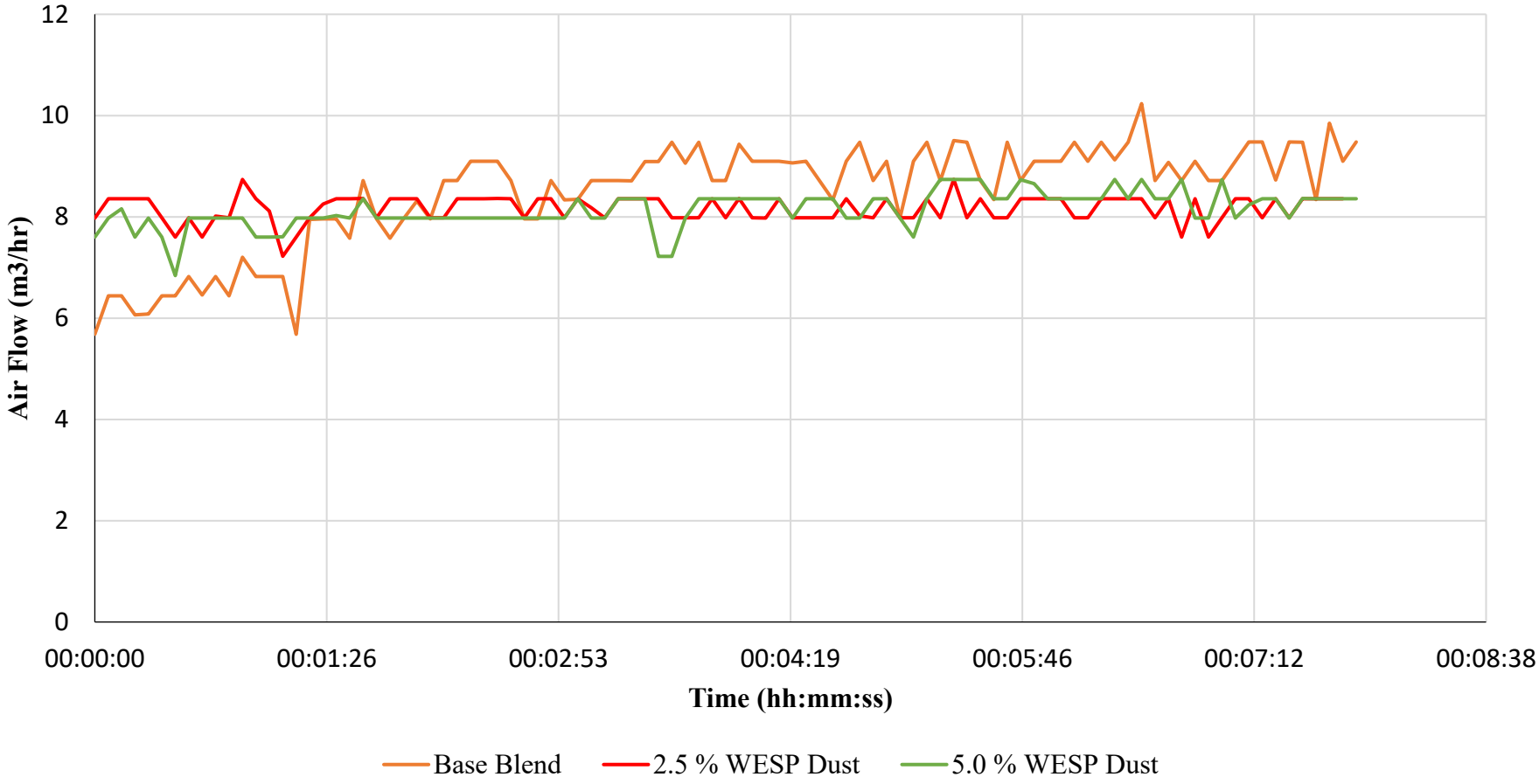

Figure 6.16 Comparison of cold permeability test air flow data for ESP dust blends with moisture optimised base blend included for comparison.

6.5.2 WESP Dust Sintering Experiments

The sinter pot thermal profiles in Figure 6.177 and *Figure 6.18*8 for the WESP dust sintering tests show that each test took longer than the other experiments analysed in this section for all thermocouples to read < 100 °C. For example, the 2.5 % WESP dust test takes approximately 35 minutes, and the 5.0 % WESP dust test takes over 40 minutes. Both test profiles appear largely similar, with a slower start at thermocouple 1 before progressing uniformly.

6.5.2.1 Thermocouple 1

At the first thermocouple, peak temperatures of 1092 °C and 1105 °C are recorded in the 2.5 % and 5.0 % WESP dust blends, respectively. This is notably lower than the blends containing equal amounts of ESP dust and the base blend. The average temperature for the 2.5 % WESP dust test is 392 °C, over 100 °C higher than that of the 5.0 % WESP dust blend. When looking at the shape of the thermocouple 1 profile in *Figure 6.17*7 there is a slight plateau around peak temperature. This appears to be what causes the difference in average temperature between the two blends.

In terms of total time above 1000 °C at thermocouple 1, the 2.5 % WESP dust blend spends 255 s whereas the 5.0 % blend spends 135 s. This is more variable compared to the 140 s and 150 s recorded in the respective ESP dust tests. Cooling rates are markedly lower in the WESP dust blend tests than all other tests run, being as slow as 48 °C/min and 50 °C/min.

6.5.2.2 Thermocouple 2

The peak temperatures at thermocouple 2 rises significantly from the values measured at thermocouple 1 reaching 1209 °C and 1302 °C for the 2.5 % WESP dust and 5.0 % WESP dust blends, respectively. This is a total increase of 198 °C in the latter blend. This indicates that the flame front in both blends is developing as it works through the bed and consumes more fuel. These are also similar peak temperatures to those seen in the ESP dust blend sintering tests.

The average temperature at thermocouple 2 falls by approximately 40 °C in the 2.5 % WESP dust blend to 355 °C, whereas the 5.0 % WESP dust blend exceeds this by averaging 361 °C. The significant drop in average temperature seen in the 2.5 % blend test as its profile

does not plateau near peak temperature, potentially indicating some flame front width variation at thermocouple 1.

The time above 1000 °C changes dramatically from the previous thermocouple. The 2.5 % test only spends 175 s and the 5.0 % test rising to 275 s. Cooling rates however remain low at 53 °C/min and 52 °C/min, respectively.

6.5.2.3 Thermocouple 3

The trend of increasing peak temperatures continues into thermocouple 3 for both tests. For example, the 2.5 % WESP dust blend peaks at 1324 °C, up 116 °C, and the 5.0 % WESP dust blend peaks at 1389 °C, a rise of 87 °C. These peak temperature rises continue to suggest that the flame front within the sinter bed is developing and propagating still.

The average temperatures are more stable when compared to the changes seen between thermocouples 1 and 2. The 2.5 % WESP dust blend averages 359 °C and the 5.0 % WESP dust averaged 368 °C, each representing a slight increase from thermocouple 2. This indicates that the flame front is moving at a steady pace and was evenly distributed at this stage.

The time each test spent above 1000 °C increases in each test by an average of 55 s ± 5 in both blends. The cooling rates do become faster in both tests but are also still lower compared to the other tests at the same stage, whilst the 2.5 % and 5.0 % WESP dust tests have rates of 68 °C/min and 65 °C/min respectively. The base blend is cooling at a rate of 94 °C/min at thermocouple 3.

6.5.2.3 Thermocouple 4

Both thermal profiles at thermocouple 4 appear to deviate from the typical profile shape, more noticeably in the 2.5 % WESP dust test which has a very short peak followed by a variable decline. Its peak temperature is 1245 ºC, which is a drop of approximately 80 °C from the previous thermocouple. The 5.0 % WESP dust test also declines, though only by approximately 50 ºC to 1336 ºC.

In terms of thermocouple 4's average temperature, the 5.0 % WESP dust blend achieves a higher value of 351 ºC, whereas the 2.5 % WESP dust test falls more significantly to 309 ºC.

The time that the 2.5 % WESP dust test spends above 1000 ºC clearly drops in figure 6.17, falling in total by 90 s compared to the previous thermocouple to 145 s. The 5.0 % WESP dust test however actually sees an increase in its time above 1000 ºC, rising by 40 s to 365 s in total. Cooling rates both slow by approximately 8 ºC/min, the 2.5 % test seeing a rate of 60 ºC/min and the 5.0 % WESP dust 54 ºC/min.

6.5.2.4 Thermocouple 5

The final profiles in both tests can be described as irregular for different reasons. In the 2.5 % WESP dust test the peak profile appears flatter than the usual rounded shape that would be expected. It appears similar to that of thermocouple 1. There is however a 10 % rise in the peak temperature to 1369 ºC. The inflection of the 5.0 % WESP dust profile has a shoulder where the heating rate drops between approximately 750 ºC – 950 ºC, this resulted in the peak temperature dropping to 1276 ºC.

Average temperatures decline in both tests, though the drop is much larger in the 5.0 % WESP dust test, as would be expected given its drop in peak temperature. A small drop of 11 ºC results in an average temperature at thermocouple 5 of 298 ºC in the 2.5 % WESP dust blend, whereas the 5.0 % WESP dust blend's average temperature falls by approximately 45 ºC to 306 ºC.

The fluctuation in time spent above 1000 ºC throughout the tests continues to the final thermocouple. The 2.5 % WESP blend spends 240 s above 1000 ºC, up 95 s from thermocouple 4, and the 5.0 % falls drastically by 155 s to 210 s. Cooling rates hasten in both tests, reaching 79 ºC/min and 59 ºC/min respectively.

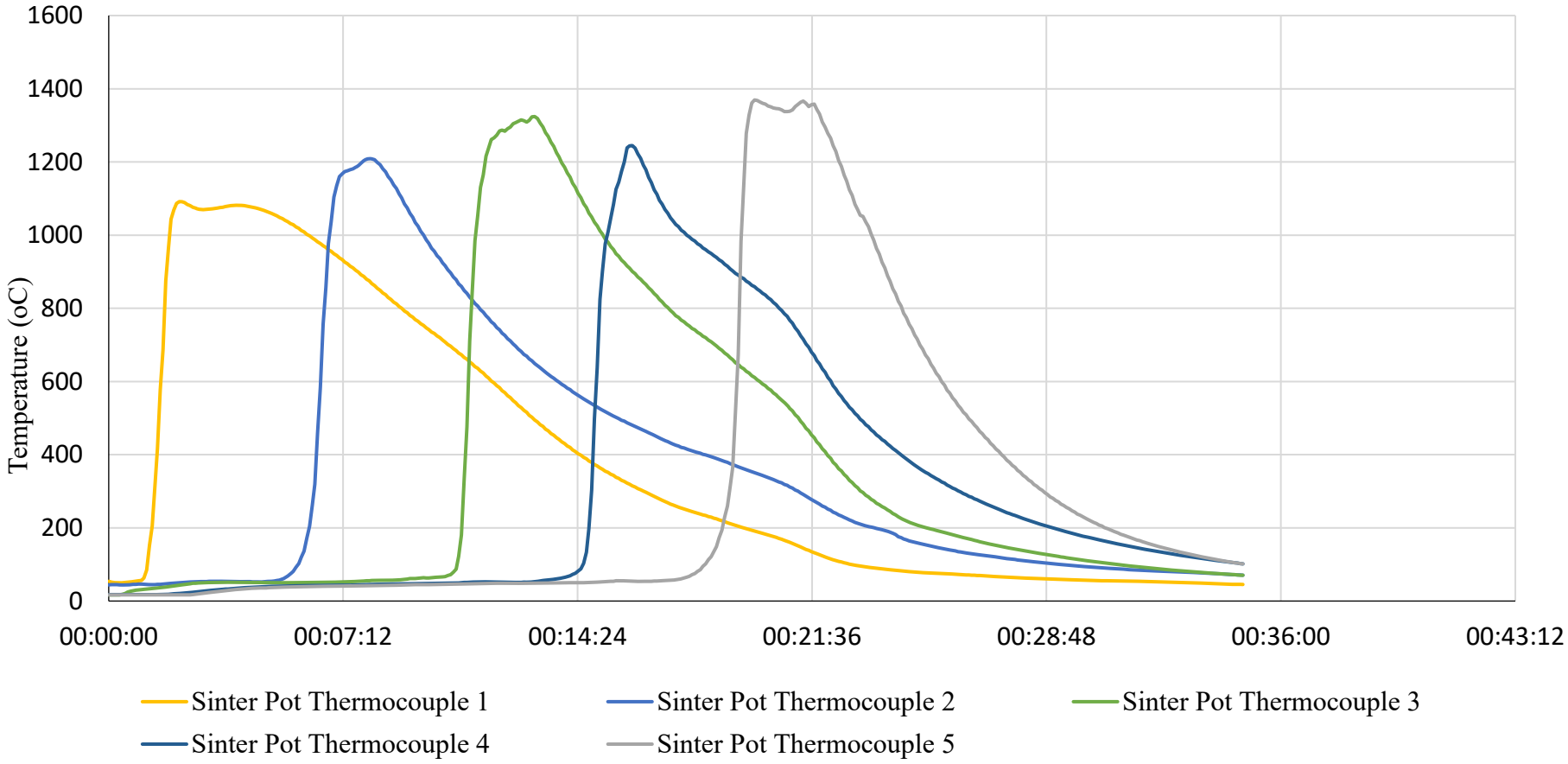

Figure 6.17 Sintering thermal profile for the 2.5 % WESP dust blend tests.

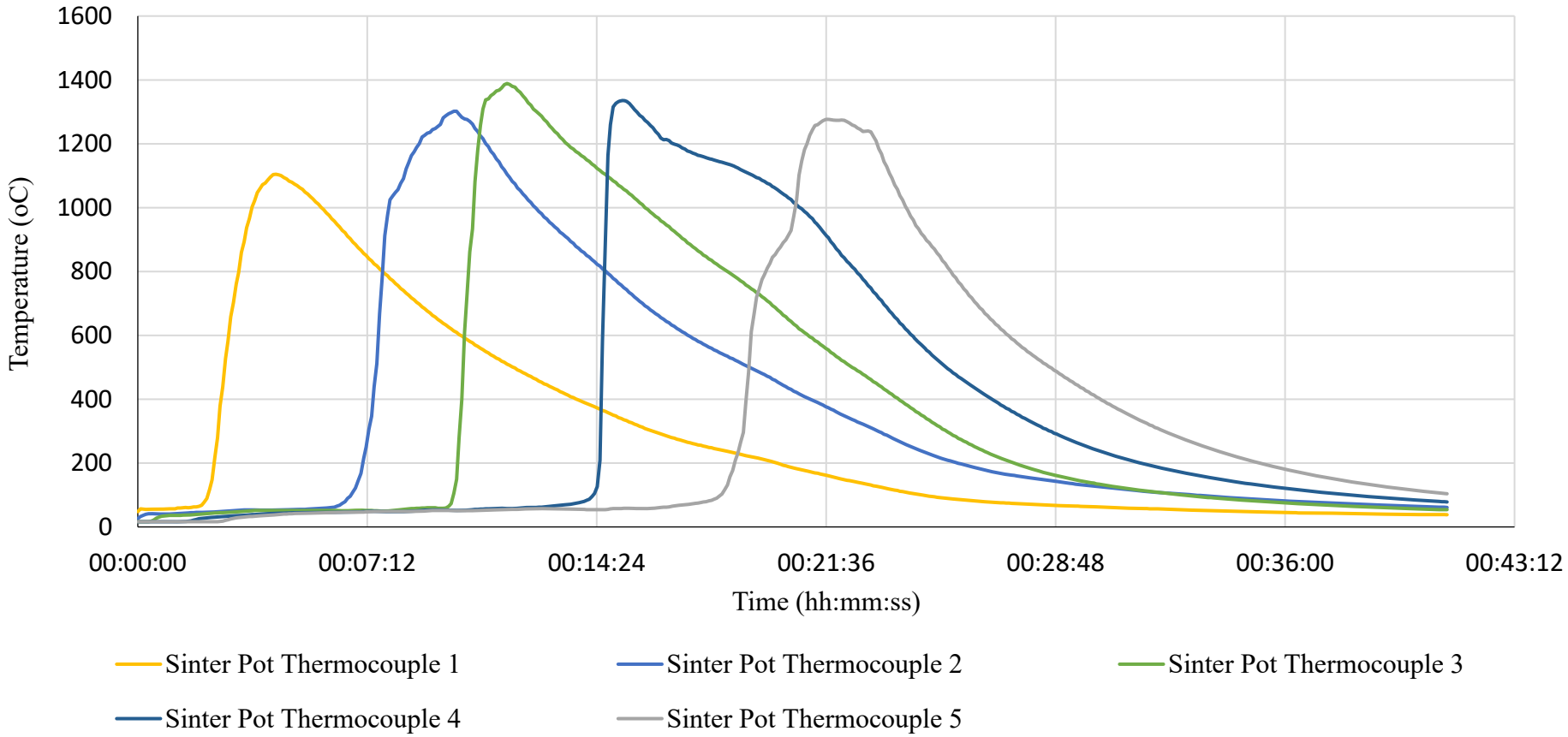

Figure 6.18 Sintering thermal profile for the 5.0 % WESP dust blend test.

6.5.3 WESP Dust Hot Permeability Experiments

As seen in the 5.0 % ESP dust blend testing, the addition of WESP dust to the sinter blend appears to reduce the hot permeability recorded during the sintering tests. This contradicts the 2.5 % ESP dust addition seen in figure 6.15, which seemed to result in an improved air flow. Figure 6.199 shows that the base blend inflects much sooner than the tests which feature WESP dust in the blend, indicating a faster sintering process. This difference in sintering test time is also clear in figure 6.19, with the time increasing as more WESP dust is added to the blend. This is as would be expected as the proportion of fines increase. The 2.5 % WESP and 5.0 % WESP tests inflect at similar points, but a much sharper rise is seen in the 2.5 % WESP dust test. This suggests that the flame front in the 5.0 % test slows down in the latter stages, something visible in Figure 6.188 and when comparing the cooling rates of 79.3 ºC/min and 58.8 ºC/min for the 2.5 % and 5.0 % WESP tests, respectively.

6.5.4 WESP Dust Addition Conclusions

Overall, the sintering thermal profiles appeared stable throughout testing, more so than the ESP dust tests, although total test time is clearly increased as the WESP dust content is increased. The peak temperature of the 5.0 % test at thermocouple 5 is only approximately 2 minutes after the peak in the 2.5 % WESP dust test, however a lower cooling rate drove the longer test time in the 5.0 % test. As the sintering profiles were more comparable than the two ESP dust tests, the higher number of fines may have caused this lower cooling rate. The impact on cold permeability was slightly more pronounced when compared to the ESP dust tests.

As with the addition of ESP dust to the blend, the WESP dust addition had a noticeable impact on sintering performance compared to the base blend. Increased sintering time would be an issue at a full-scale sinter plant as strand speed may have to be reduced, therefore lowering the plant's speed of work and product output. Overall sintering temperatures were better than the ESP dust tests, although a more stable and uniform profile would be desirable for industrial-scale operations. As with the ESP dust test results, there is no strong evidence to support the use of WESP dust at or above 2.5 % of the blend.

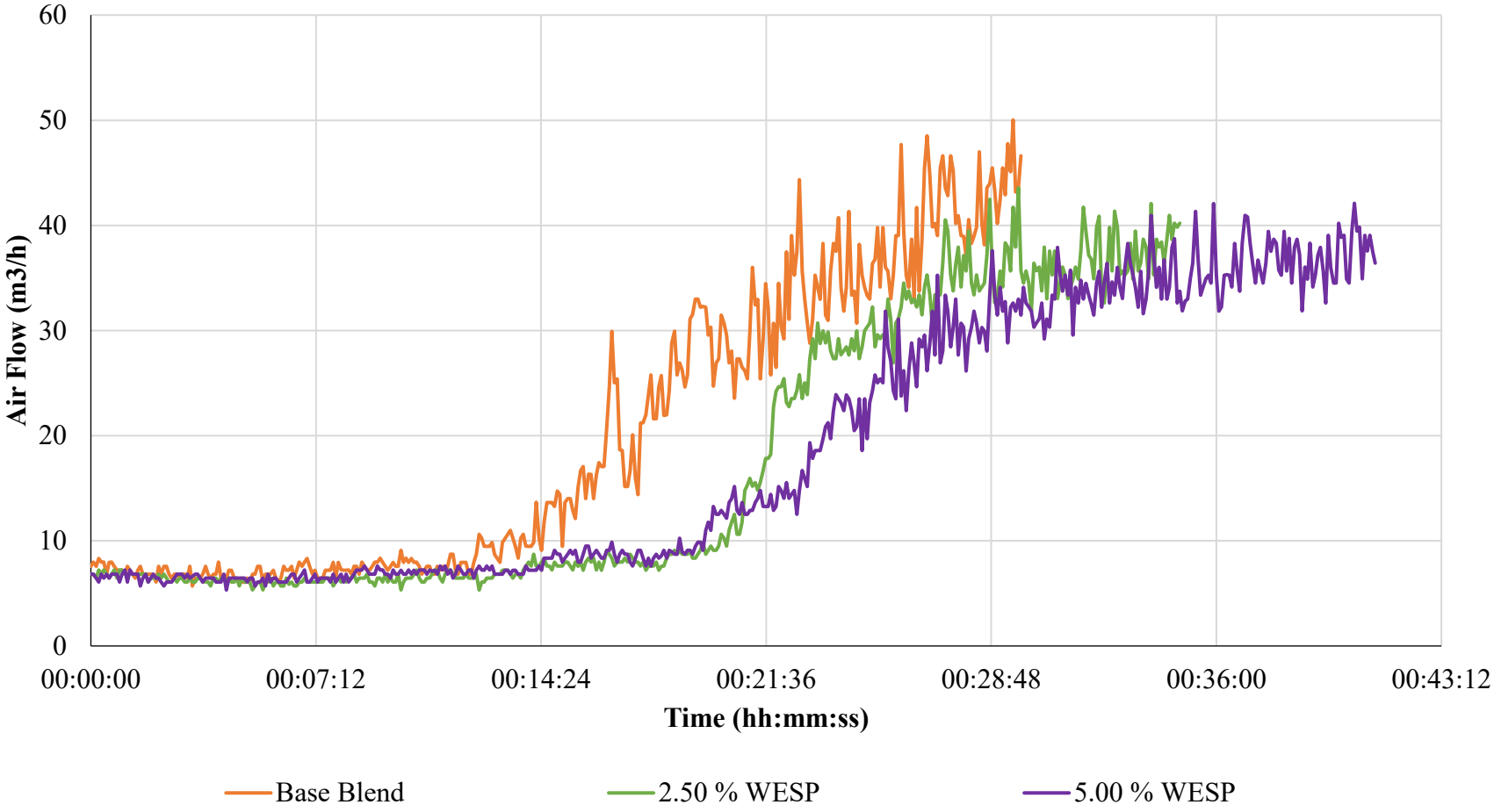

Figure 6.19 Hot permeability test air flow data for WESP dust blend sintering tests, base blend included for comparison.

6.6 Post Analysis

6.6.1 Mechanical Sieving Particle Size Distribution

The mechanical sieving of the sinter highlights some interesting trends. Although the total yield for both micro-pellet tests is very similar, the distribution between size fractions does vary, as can be seen in Table 6.3. In terms of total yield, the test with 2.5 % WESP dust has the lowest output with 5.07 kg compared to a maximum value of 5.79 kg produced from the 3.5 % micro-pellet test. The average total yield observed over every test is 5.40 kg. However, the average for each suite of tests varies somewhat. The sinter produced from the WESP dust tests is again the lowest on average with 5.12 kg, the base blend tests yield is 5.39 kg, ESP dust tests record an average of 5.41 kg and the micro-pellet tests average 5.77 kg.

The only tests which produced sinter > 40 mm after mechanical sieving are the 3.5 % MP & 7.0 % MP, producing 0.34 kg and 0.47 kg, respectively. This may potentially indicate that the base blend, and ESP/WESP dust variations, produce comparatively weak sinter but the addition of micro-pellets may counteract this. The amount of sinter < 1 mm produced in each test also varies. The highest reading is 0.67 kg from the 2.5 % WESP sinter, compared to a low of 0.37 kg in the 3.5 % micro-pellet sinter. However, there is no obvious trend seen when increasing ESP or WESP dust levels. A key observation is that the two micro-pellet blends produced sinter that results in the lowest < 1 mm readings and highest > 40 mm readings, further suggesting that the addition of micro-pellets is conducive to creating stronger sinter.

The distribution between size fractions is plotted in figure 6.21, the data generally shows a uniform distribution in all samples with a slight positive skew. However, the suite with the most normal distribution is the micro-pellet tests. The 16 – 25 mm size fraction had the most mass on average across all tests with 1.39 kg, followed by 10 – 16 mm with 1.20 kg, both 25 – 40 mm & 5 – 10 mm had similar averages of 0.82 kg and 0.80 kg respectively. This is followed by 1-5 mm with 0.61 kg, < 1 mm with 0.49 kg and finally > 40 mm with a 0.09 kg average.

The cumulative particle size distribution curve is shown in Figure 6.22. This helps to establish the percentage of samples within specific size ranges. It can be derived that the highest D90 value (size which encompasses 90 % of total sample mass, marked on the figure with dashed lines) is 31.1 mm for the 7.0 % micro-pellet sinter compared to a low of 19.3 mm for the 2.5 % WESP sinter. When averaging the D90 value for the various sets of

experiments, the micro-pellet tests come out on top with an average of 30.5 mm, followed by the ESP dust tests with 25.2 mm, then base blends with 24.3 mm and finally the WESP tests had the lowest average D90 with 21.8 mm. This further shows that the addition of micro-pellets leads to an increase in overall sinter size after mechanical sieving, suggesting higher strength.

Table 6.3 Summary of sinter particle size distribution after mechanical sieving.

Sizing	Base Blend (kg)	3.5% MP	7.0% MP	2.5% ESP	5.0% ESP	2.5% WESP	5.0% WESP
> 40 mm	0.00	0.34	0.47	0.00	0.00	0.00	0.00
25 - 40 mm	0.81	1.14	1.02	0.96	0.80	0.30	0.65
16 - 25 mm	1.62	1.26	1.21	1.41	1.28	1.27	1.73
10 - 16 mm	1.19	1.24	1.22	1.07	1.14	1.36	1.01
5 - 10 mm	0.84	0.90	0.99	0.70	0.88	0.96	0.67
1 - 5 mm	0.43	0.54	0.47	0.85	0.74	0.52	0.63
< 1 mm	0.51	0.37	0.39	0.41	0.49	0.67	0.48
TOTAL	**5.41**	**5.79**	**5.75**	**5.41**	**5.33**	**5.07**	**5.16**

Figure 6.20 Images of 2.5 % WESP sinter (left) and 7.0 % micro-pellet sinter.

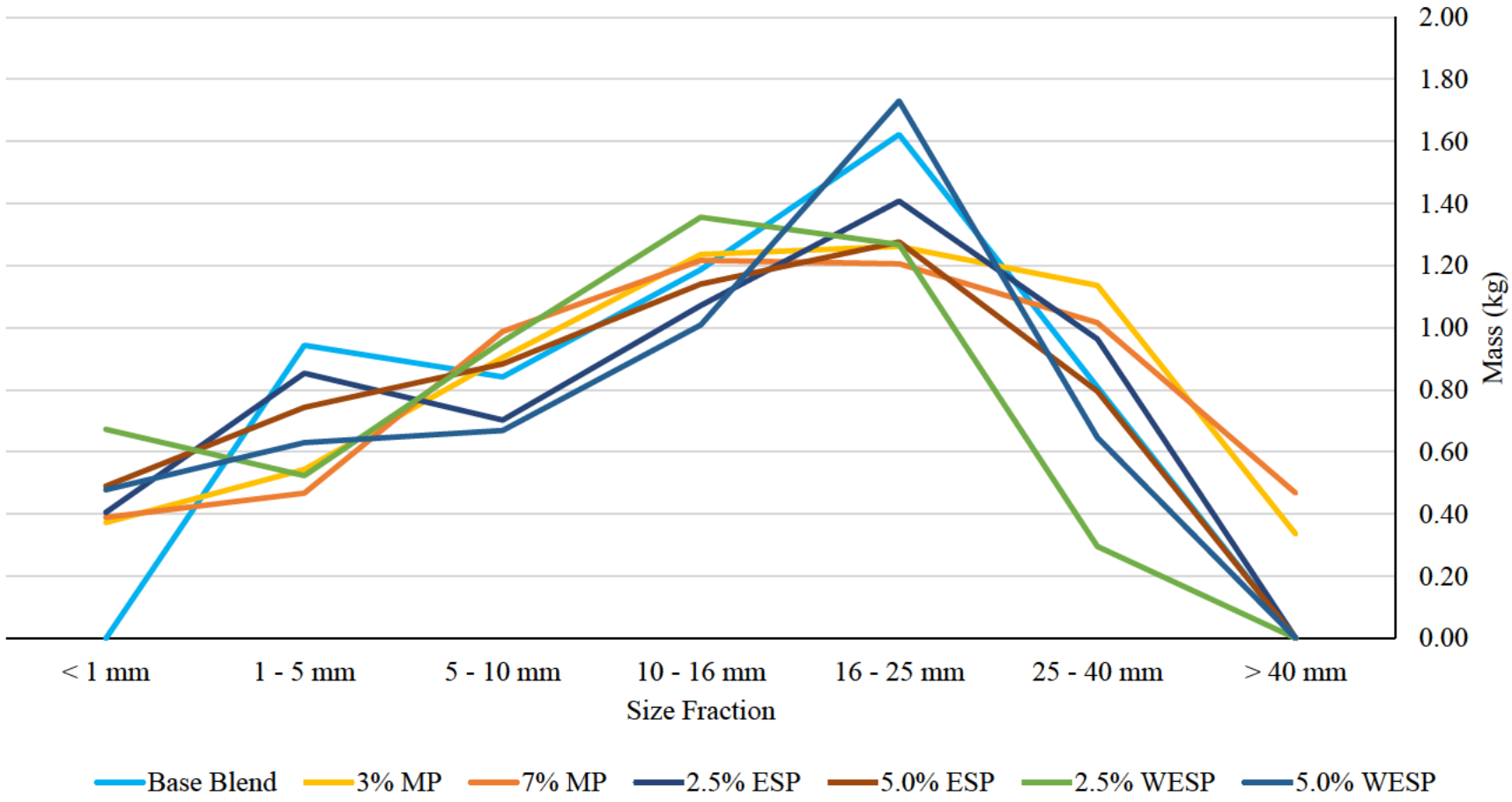

Figure 6.21 Line graph plotting particle size distribution of sinter after mechanical sieving.

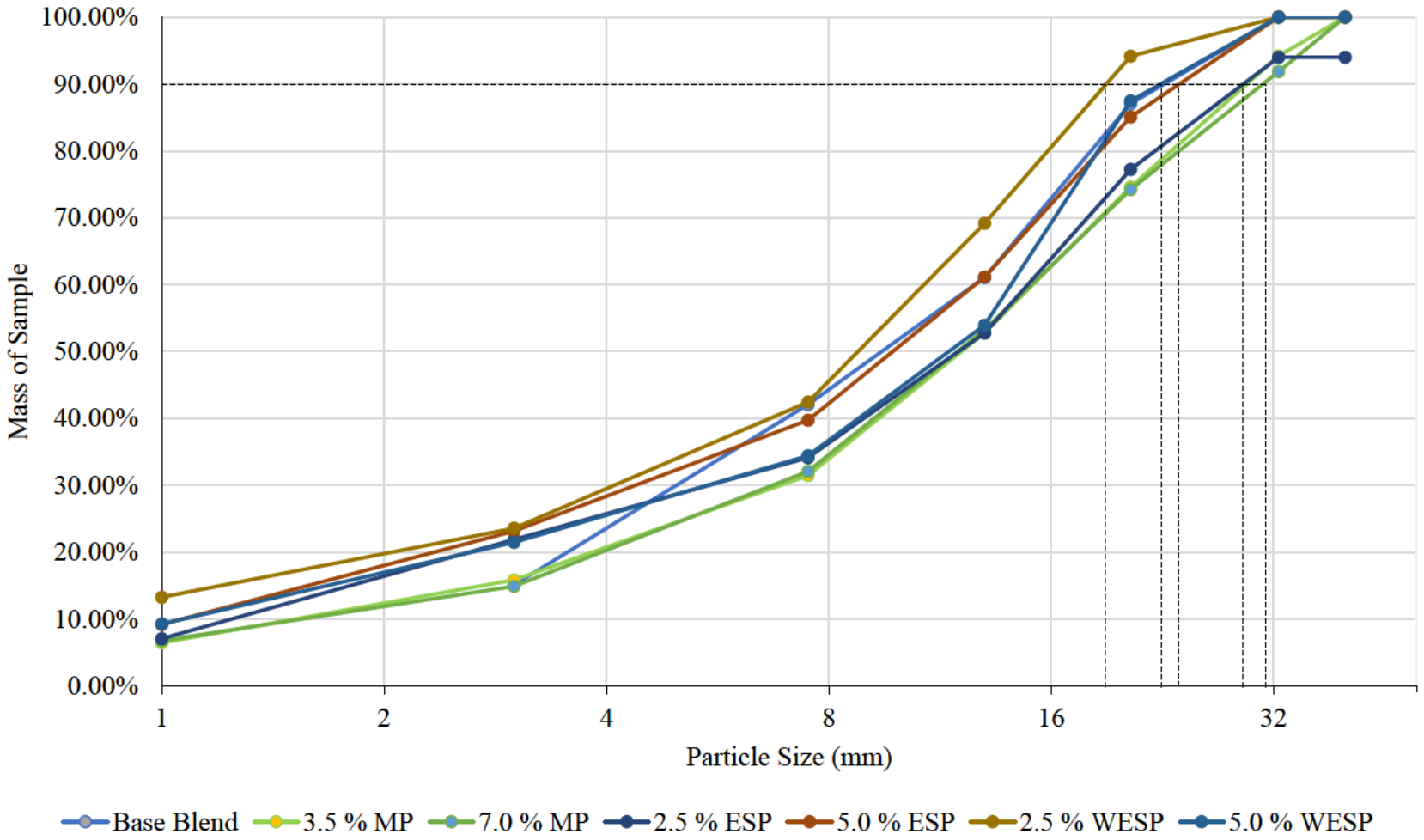

Figure 6.22 Particle size distribution curve of sinter after mechanical sieving. D90 values marked with dashed lines.

6.6.2 Particulate Emission Analysis

Dust emissions were collected for the base blend and micro-pellet tests to assess whether pelletisation of fine materials would reduce particulate emissions. The results from weighing of particulates in the collection tray are shown in Figure 6.233. There is a noticeable drop in the particulates produced by the tests including micro-pellets compared to the base blend test. The base blend averages 21.2 g (± 2.7) of dust produced, which is 89 % and 182 % more than the 3.5 % and 7.0 % micro-pellet tests which recorded 11.2g (± 3.6) and 7.5g (± 1.6), respectively.

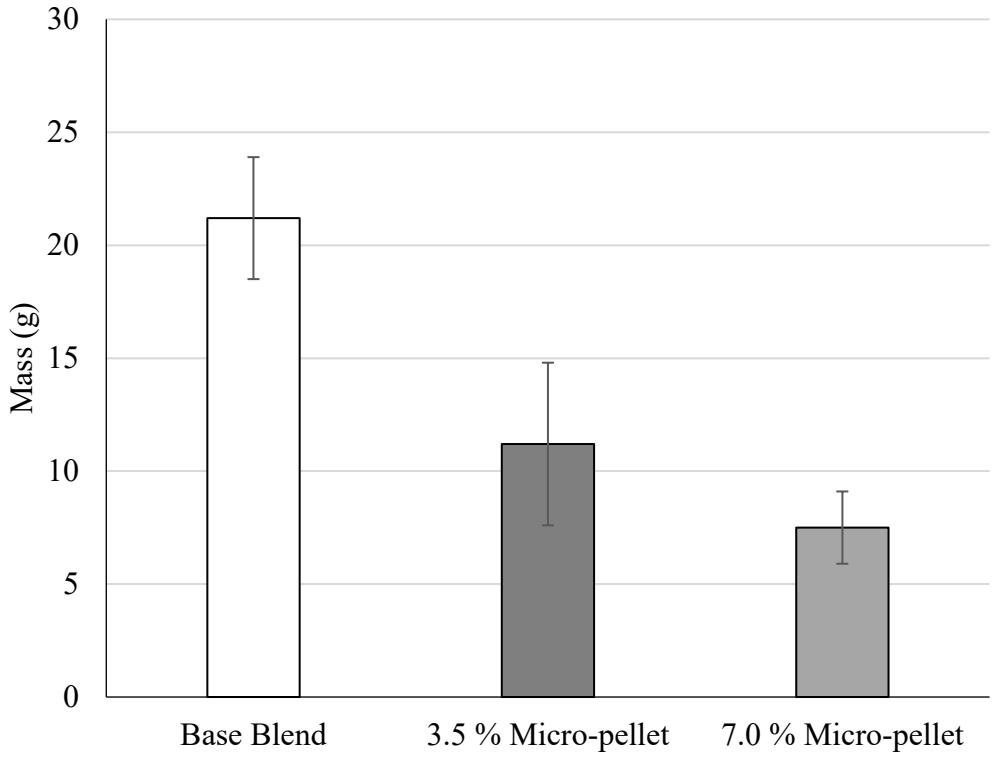

Figure 6.23 Bar chart showing dust emissions collected during sintering tests. Source: Matthew Thomas, Swansea University.

Images of the filter used for these tests is shown in Figure 6.244. This gives a visual indication of the variation in dust emissions. Image A shows the base blend's filter which has clearly collected more ultra-fine particles, whilst the dust described in Figure 6.233 shows the heavy particles which fell out into the tray. The filter would have stopped the particles airborne in the waste gas stream which would otherwise have been emitted to the

environment. These results suggest that the addition of micro-pellets to this base blend has significantly reduced the particulate emissions produced.

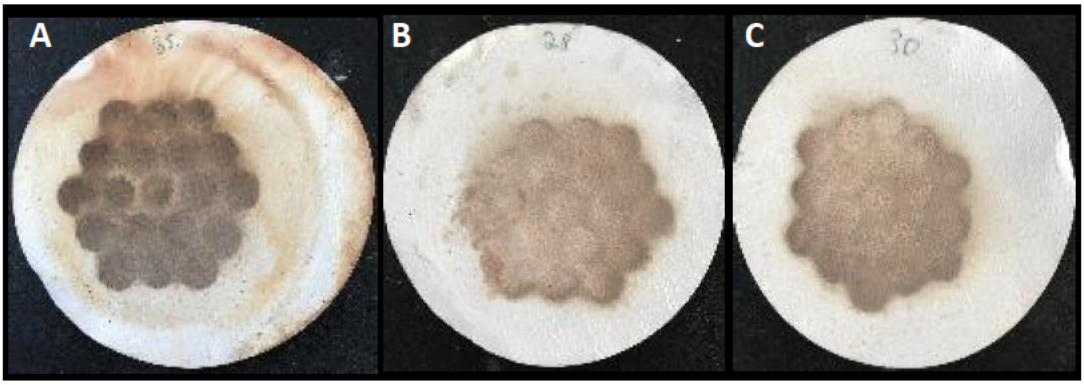

Figure 6.24 Images of particulate emission filters from sinter pot tests. A = base blend, B = 3.5 % micro-pellets & C = 7.0 % micro-pellets.

6.6.3 Sinter Chemistry

The results of XRF analysis of sinter samples produced from these tests is shown in Table *6.4*6.4. The basicity of these sinters is approximately 1.6 in all tests so should not be the cause of any variation in strength or reducibility. Total iron content of the sinters was very similar, ranging between 53.7 – 56.5 %, the iron phases present however showed significant variation. In terms of FeO the lowest reading was 9.2 % in the 7.0 % micro-pellet sinter, compared to the highest value measured which was 27.1 % in the 2.5 % WESP dust sinter. This is likely linked to temperature differences between the tests, as sintering below 1300 °C yields less magnetite and therefore less FeO (65,68).

Chloride is seen to be higher within the ESP dust sinter samples, though still relatively low industrial sinter plants have stringent limits for elements such as chloride due to their relationship with dioxin formation (23). Zinc is also another element with low limits of acceptability due to impacts on the blast furnace, and is again highest in the sinters featuring ESP dust.

Table 6.4 Summary of resultant sinter chemistry.

	Base Blend	**2.50% ESP Dust**	**5.00% ESP Dust**	**2.50% WESP Dust**	**5.00% WESP Dust**	**3.5% Micro-pellets**	**7.0% Micro-pellets**
SiO_2	6.19	5.95	6.03	6.22	6.31	6.02	6.02
Al_2O_3	1.16	1.17	1.19	1.16	1.22	1.06	1.07
TiO_2	0.17	0.07	0.08	0.13	0.11	0.1	0.08
CaO	10.09	10.12	10.07	10.28	10.41	10.49	10.26
MgO	2.04	1.90	1.89	1.92	1.90	2.07	1.99
Fe	55.13	54.74	53.65	54.24	54.49	56.48	54.61
Fe_2O_3	52.7	55.18	57.13	47.48	50.82	60.38	67.85
FeO	23.5	20.78	17.62	27.05	24.37	18.33	9.21
P	0.034	0.028	0.029	0.03	0.032	0.028	0.031
Mn	0.17	0.15	0.14	0.14	0.15	0.15	0.15
Na_2O	0.04	0.10	0.12	0.033	0.031	0.03	0.033
K_2O	0.065	0.065	0.096	0.081	0.089	0.027	0.038
Zn	0.011	0.016	0.016	0.01	0.011	0.005	0.009
Cu	0.000	0.003	0.002	0.000	0.000	0.000	0.000
Cl	0.003	0.009	0.005	0.001	0.001	0.002	0.001

6.6.4 Blast Furnace Simulation

Due to equipment availability, only selective samples could be analysed using the blast furnace simulation rig. This rig simulates the upper section of the blast furnace by varying temperature between 400 – 900 °C and the $CO/CO_2/N_2/H_2$ mixture throughout. Therefore, the base blend and extreme additive mass from each sample suite was tested. The results from the blast furnace simulation test shown in figures 6.25 and 6.26 and display the variation between samples. The sinters that underwent the blast furnace simulation were also subjected to tumble testing to assess any impact of reduction on sinter disintegration rates, the results of this are shown in figure 6.25. Supporting the trends recorded from the mechanical sieving PSD analysis, the addition of ESP/WESP dust made the sinter weaker after reduction whereas the addition of micro-pellets lowered the disintegration index.

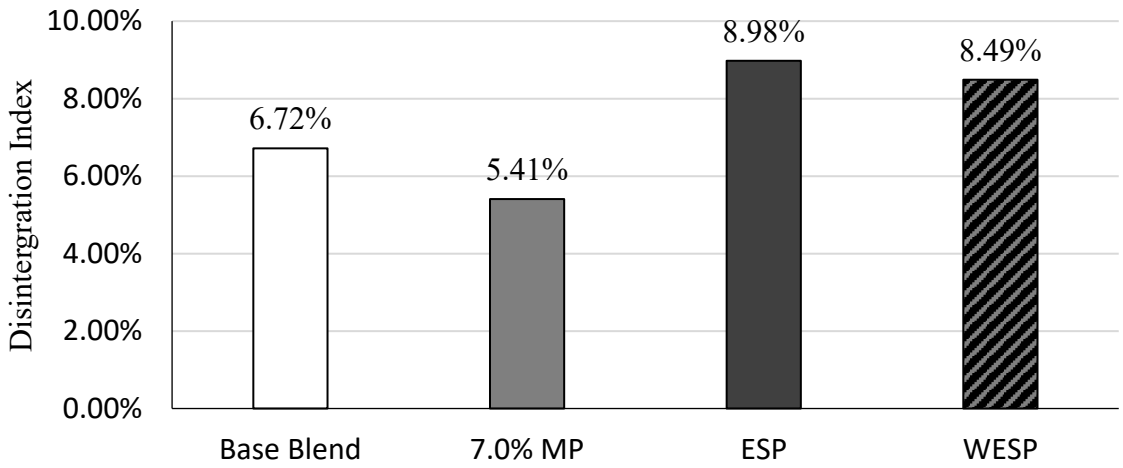

Figure 6.25 Bar chart showing the disintegration index of sinters that underwent blast furnace simulation.

In terms of the blast furnace reduction simulation itself, the base blend test being the longest of the 4 samples tested in terms of test time, losing 64.2 g over 4 hours and 23 minutes, at a rate of 0.24 g/min. The sample featuring micro-pellets lost the most mass, 71.5 g, and had an average mass loss rate of 0.31 g/min over 3 hours and 48 minutes. The sinter sample with ESP dust lost 65.4 g of mass at a rate of 0.28 g/min for 3 hours and 52 minutes. The WESP sample's mass loss rate was 0.29 g/min, although it lost the least mass in total, 62.8 g, and was the fastest test as it finished in 3 hours and 40 minutes. These results will be linked to the chemistry of the sinter, the micro-pellet sinter for example was measured as only having 9.2

% FeO and high FeO contents are linked to poor blast furnace reducibility (96). Factors such as porosity and surface area may also have played a role in the reaction.

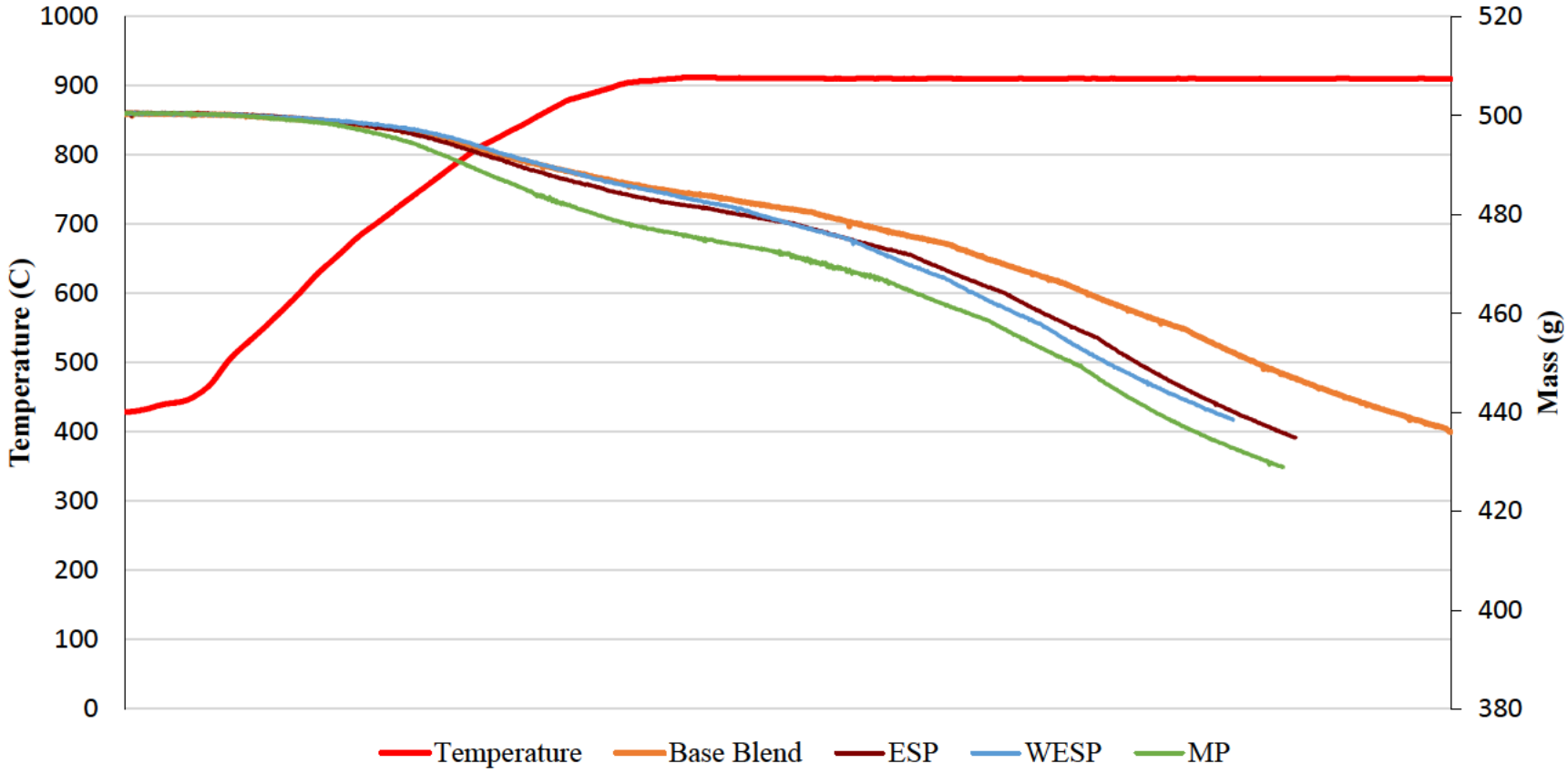

Figure 6.26 Blast furnace Simulation showing sample mass versus temperature.

6.7 Conclusions

In this study the addition of micro-pelletised fine materials notably increased the permeability of the sintering bed compared to that of the control base blend, in turn this resulted in greater airflow and faster sintering. Cold permeability tests averaged 12.5 m^3/hr for the micro-pellet blends compared to 10.6 m^3/hr recorded from the base blend. It was noted that when increasing the micro-pellet content from 3.5 % to 7.0 % of the blend appeared to lead to less stable sintering conditions, visible in the thermal profiles shown in figures 6.9 & 6.10. A summary of key sintering parameters can be seen in table 6.5 which provides quantification of this variation. The average peak temperature across all thermocouples for instances declines from 1289 °C to 1169 °C for the 3.5 % and 7.0 % blends respectively and the 3.5 % micro-pellet blend also recorded a total of 1 minute more above 1000 °C. Whilst the cooling rates were similar, the average being 93 °C/min for the 3.5 % micro-pellet blend and 96 °C/min for the 7.0 % micro-pellet blend, the standard deviations of 15 °C/min and 24 °C/min respectively highlight more variation in the blend featuring more micro-pellets. Micro-pellets increased the PSD ratio and provided more nucleation sites for granulation, resulting in greater airflow. However, excessive loading of micro-pellets may have created pockets of irregular void space within the bed and the increased airflow could have resulted in a turbulent flame front. The addition of ESP dust and WESP dust proved to provide irregular results with no clear trends. There was a negligible impact on the sinter blend permeability although all ESP/WESP dust addition tests, excluding the 2.5 % ESP dust test, prolonged the total test time. This slower test time resulted in more time spent above 1000 °C during these tests, ~18 minutes on average, compared to the micro-pellet blends which only spent ~ 12 minutes on average. The peak temperatures averaged across all thermocouples for these blends ranged between 1248 – 1282 °C.

Other significant differences between the micro-pellet blends and the fine material blends were seen in the dust emissions during sintering and product sinter strength. During sintering of the 7.0 % micro-pellet blend less than half the total dust emissions of the base blend were recorded. Sinter strength after mechanical sieving also showed variation between the fine material blends and the micro-pellet blends. The typical size of ferrous charging materials at the Port Talbot blast furnaces is 10-40 mm in diameter, the fine material blends averaged 3.25 kg of sinter within this range whereas the micro-pellet blends averaged 3.55 kg. The only tests that produced > 40 mm sinter was the micro-pellet blends and the fine

material blends produced ~ 20 % more material < 1 mm. The > 40 mm would be screened out of the sinter bound for the furnaces and be re-crushed to produce material within the 10-40 mm range. The proportion of < 1mm material is an indicator of poor strength, during transport and screening the sinter will breakdown resulting in fines which can either blind sinter screens, reduce furnace permeability or be emitted to atmosphere. There was also less disintegration of the micro-pellets sinter when they were tumbled after blast furnace simulation tests, further suggesting they are better suited to blast furnace reduction without generating fines and reducing permeability.

Overall the results from these experiments show that micro-pelletisation of fine materials, such as ESP dust, can allow for high rates of use without detrimental impacts on key parameters such as sintering conditions, dust emissions and sinter strength. Though there was some sinter instability seen when increasing micro-pellet content to 7%, meaning there may be a tipping point where their inclusion can become detrimental, this is something which will be investigated further in the next chapter.

Table 6.5 From top; Summary of peak temperatures, summary of average temperatures, summary of time spent above 1000 °C (rounded to nearest 5 s interval and summary of cooling rates from sinter pot testing.

	TC1 (°C)	TC2 (°C)	TC3 (°C)	TC4 (°C)	TC5 (°C)
BB	1255.9	1369.1	1316.1	1412.8	1353.0
2.5% ESP	1375.3	1289.0	1358.4	1117.7	1196.3
5.0% ESP	1264.2	1281.3	1272.1	1312.7	1234.1
2.5% WESP	1091.6	1208.8	1324.1	1244.8	1369.4
5.0% WESP	1104.6	1301.9	1388.8	1335.7	1276.3
3.5% MP	1292.0	1238.2	1285.2	1316.1	1314.7
7.0% MP	1258.8	1162.1	1068.6	1104.3	1255.2

	TC1 (°C)	TC2 (°C)	TC3 (°C)	TC4 (°C)	TC5 (°C)
BB	357.5	488.1	398.5	349.2	280.5
2.5% ESP	299.3	384.2	347.0	347.2	221.7
5.0% ESP	284.8	346.6	348.6	336.3	350.5
2.5% WESP	392.2	354.8	359.0	308.9	298.0
5.0% WESP	287.3	360.7	367.9	350.6	305.6
3.5% MP	255.0	362.9	394.7	376.6	303.2
7.0% MP	258.8	359.5	299.5	365.7	339.5

	TC1 (s)	TC2 (s)	TC3 (s)	TC4 (s)	TC5 (s)
BB	175	360	315	240	140
2.5% ESP	140	210	220	190	75
5.0% ESP	160	280	230	255	295
2.5% WESP	255	175	235	145	240
5.0% WESP	135	275	325	365	210
3.5% MP	85	125	215	170	150
7.0% MP	110	165	30	200	180

	TC1 (°C/min)	TC2 (°C/min)	TC3 (°C/min)	TC4 (°C/min)	TC5 (°C/min)
BB	68.0	79.3	93.5	109.4	89.5
2.5% ESP	102.0	83.2	100.7	90.1	112.4
5.0% ESP	80.3	96.0	75.1	86.6	75.6
2.5% WESP	48.4	52.8	68.0	60.3	79.3
5.0% WESP	50.2	52.3	61.4	53.7	58.8
3.5% MP	95.4	74.6	91.2	90.1	115.7
7.0% MP	136.3	75.9	88.1	83.7	96.3

Sintering stability variation was a key observation during these experiments. With the addition of micro-pellets generally improving the stability, apart from when they were used at 7% of the total blend, the flame front properties were also variable in terms of size and speed.

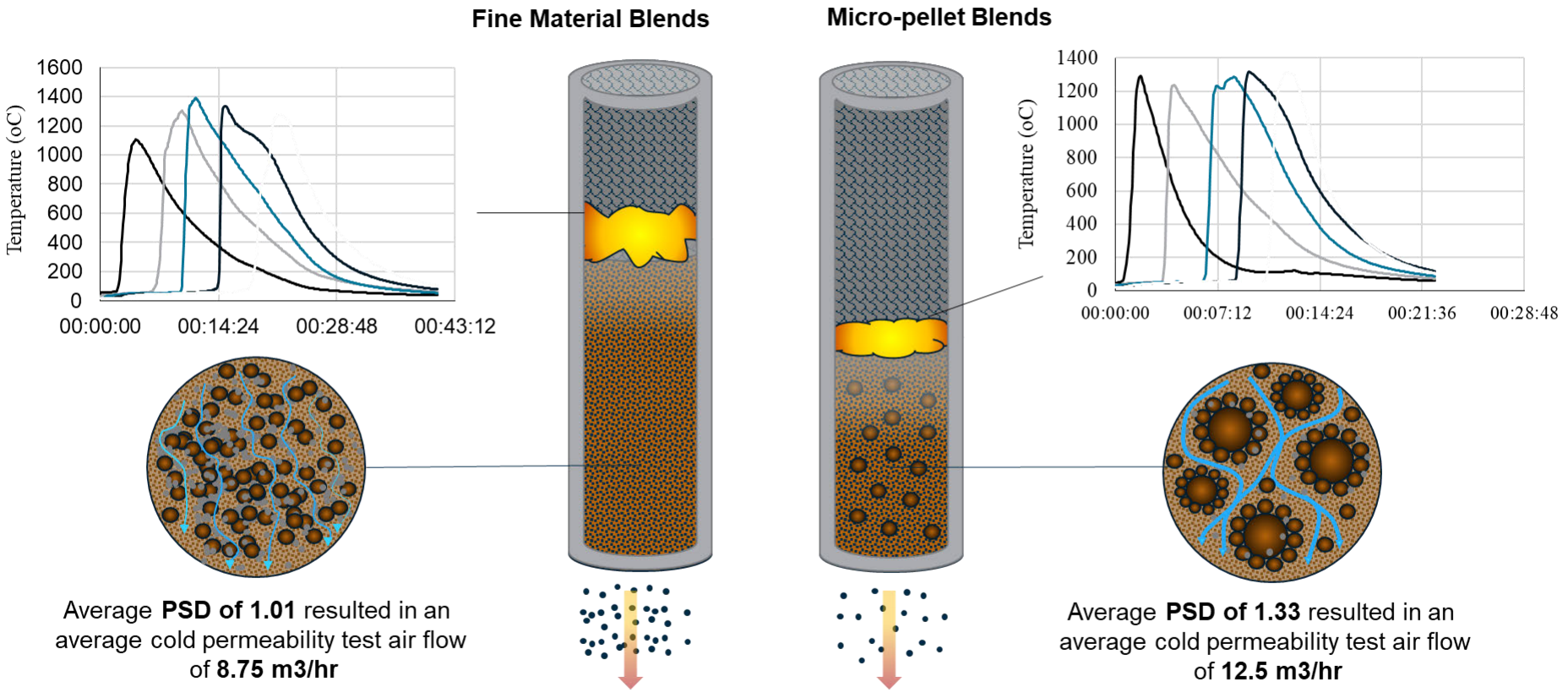

Average **PSD of 1.01** resulted in an average cold permeability test air flow of **8.75 m3/hr**

Average **PSD of 1.33** resulted in an average cold permeability test air flow of **12.5 m3/hr**

Dust emissions were on average **43% lower** when the equivalent material had been micro-pelletised prior to sintering and stronger product sinter was also produced

7. EXTENDED REVERT AND MICRO-PELLET SINTER POT EXPERIMENTS

This section builds on the tests outlined in section 6 by testing higher concentrations of steelmaking by-products, different types of by-products and micro-pellets consisting of only by-products compared to a mixture with iron ore. For example, this chapter will reveal how including up to 10 % of reverts in a sintering blend, both as fines and micro-pellets, can alter sintering parameters, final sinter quality and particulate emissions. Sintering quality has been determined by analysis of thermal profile stability, peak temperature, average temperature, cooling rates and the time the sinter bed is above 1000 °C. The quality of sinter produced has been tested in several ways including particle size distribution, dust emission analysis, optical microscopy, XRF and SEM/EDS.

NOTE: Some research was carried out in conjunction with Matthew Thomas (MT) of Swansea University. Any data produced by MT will be credited to him, but all data analysis and interpretation are my own.

7.1 Base Blend

The base blend was selected from an archive of proven blends, due to its past performance and availability of materials at the time of testing. Details relating to each blend, including chemistry and particle size distribution can be found in Tables 7.1 and 7.2. Adaption of the base blend to include reverts and micro-pelletised revert materials was aided by Ryan Davies of Tata Steel UK and the use of the Tata Steel UK blend model calculator. The blend model calculator takes chemistry, particle size and mass of each material into account whilst tracking certain parameters of the blend as a whole. The amount of each material can then be varied to ensure these parameters are within acceptable ranges. Examples of tracked parameters include particle size distribution (PSD) ratio of at least 0.7, $CaO:SiO_2$ ratio of approximately 1.8 and MgO content of approximately 1.9 %, these having been predetermined based on previous Tata Steel UK in house testing. Table 7.2 denotes the chemistry of revert materials both before and after micro-pelletisation process, chemical analysis was completed by Tata Steel UK Labs using XRF and chemical titration.

Figure 7.1 shows that every sinter blend had a PSD ratio of at least 0.94, well above the acceptable lower limit of 0.7, with the micro-pellet tests having the highest values which all exceeded 1.39. This is due to the fine materials being agglomerated prior to granulation,

resulting in more nuclei sized particles (larger particles which smaller particles can agglomerate to). Some of the other notable differences in chemistry of the raw sinter blends include carbon content and FeO. As is seen in Table 7.1, a consistent amount of coke breeze was added to each blend, this being between 0.64 – 0. 66 kg. However, in Table 7.2 we see that 6 of the 8 blends have carbon contents of 5.97 – 6.16 % but the two blends featuring 5 % and 10 % BOS slurry fines recorded 7.42 % and 8.84 % carbon, respectively.

Total Fe is again consistent between all blends, ranging between 55 – 57 %. However, FeO is notably higher in the BOS fine blends when compared to the other blends, as with carbon, reaching 8.17 and 9.92 % in the 5 % and 10 % BOS slurry blends, respectively. These differences may well impact the experiments and shall be considered when interpreting results in forthcoming sections.

Table 7.1 Sinter blend models for various tests denoting proportions of raw materials used. MP = micro-pellet. Some material names excluded at Tata Steel UK's request.

Raw Material	Base Blend	5% BOS	10% BOS Slurry	10% ESP Dust	10% WESP Dust	10% BS MP	10% Raw ESP MP	10% WESP MP
Iron Ore A	4.75	4.50	4.16	4.76	4.87	4.60	5.56	56
Iron Ore B	2.64	2.91	3.12	2.03	1.82	2.49	0.76	1.62
Iron Ore C	3.17	2.65	2.25	2.83	2.94	2.65	3.49	3.02
BOS Slurry	0.00	0.53	1.06	0.00	0.00	0.00	0.00	0.00
Raw ESP	0.00	0.00	0.00	1.07	0.00	0.00	0.00	0.00
Washed ESP	0.00	0.00	0.00	0.00	1.07	0.00	0.00	0.00
BOS Slurry MP	0.00	0.00	0.00	0.00	0.00	1.08	0.00	0.00
ESP MP	0.00	0.00	0.00	0.00	0.00	0.00	1.09	0.00
WESP MP	0.00	0.00	0.00	0.00	0.00	0.00	0.00	1.08
Sinter Fines	2.32	2.32	2.32	2.35	2.35	2.38	2.39	2.36
Flux A	1.43	1.42	1.39	1.33	1.33	1.10	1.09	1.22
Flux B	1.04	1.03	1.05	0.98	0.98	1.03	0.96	0.99
Fuel A	0.64	0.65	0.65	0.65	0.65	0.66	0.66	0.66

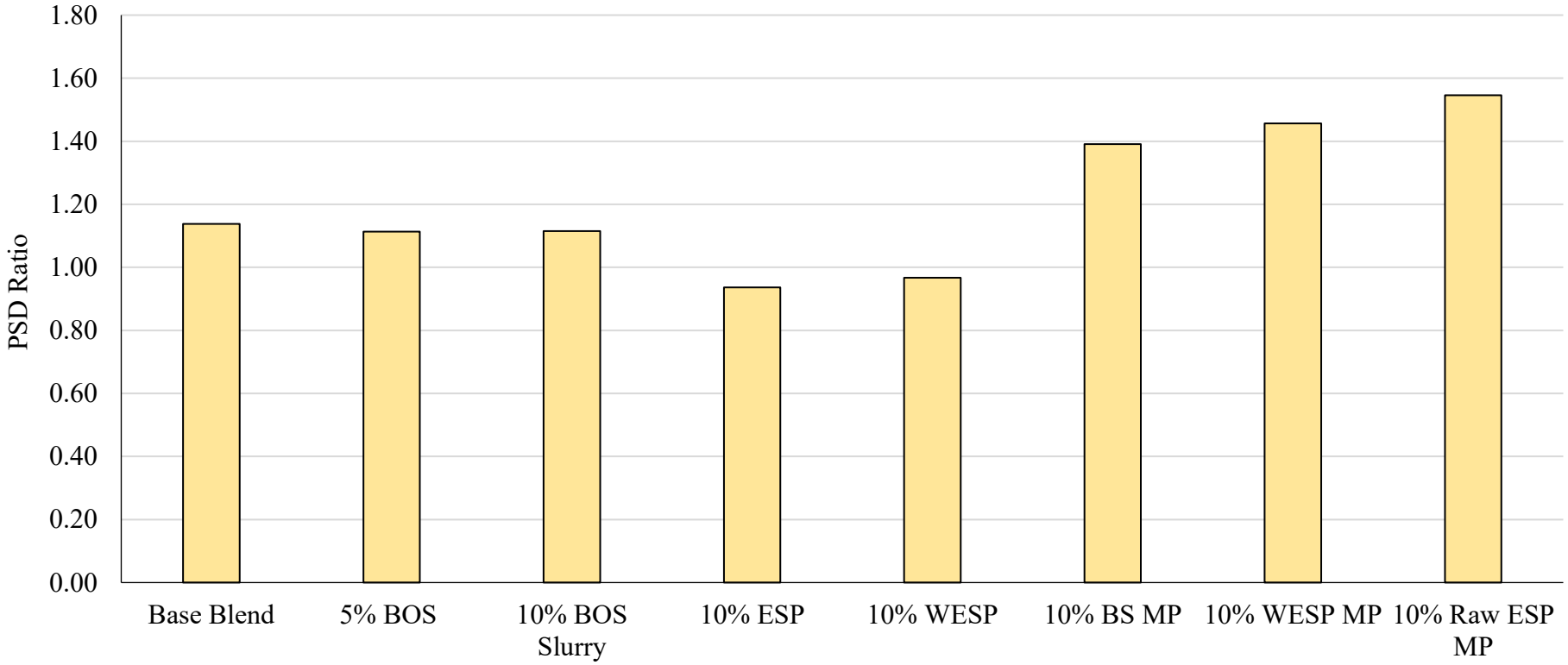

Figure 7.1 Bar chart displaying PSD ratios for sinter blends.

Table 7.2 XRF chemistry and sizing for each blend.

	Base Blend	5% BOS	10% BOS Slurry	10% ESP	10% WESP	10% BOS MP	10% WESP MP	10% Raw ESP MP
Fe_{TOTAL}	56.57	56.51	56.42	55.45	55.86	56.26	56.20	56.29
CaO	9.81	9.83	9.85	9.83	9.83	9.82	9.83	9.78
SiO_2	5.43	5.43	5.43	5.43	5.43	5.41	5.43	5.43
MgO	2.11	2.09	2.09	2.11	2.12	2.11	2.12	2.09
Al_2O_3	0.94	0.93	0.93	0.97	0.98	0.93	0.99	1.06
P	0.04	0.04	0.03	0.04	0.04	0.04	0.04	0.04
Mn	0.13	0.13	0.13	0.13	0.13	0.15	0.14	0.13
S	0.01	0.01	0.01	0.01	0.01	0.01	0.01	0.01
FeO	6.34	8.17	9.92	6.44	6.55	10.31	7.02	7.37
Na_2O	0.03	0.03	0.02	0.05	0.04	0.03	0.03	0.03
K_2O	0.04	0.03	0.03	0.29	0.10	0.03	0.03	0.03
TiO_2	0.06	0.07	0.07	0.07	0.07	0.07	0.07	0.07
C	6.00	7.42	8.84	6.13	6.16	6.00	6.01	5.97
Nuclei	39%	39%	40%	36%	36%	44%	44%	44%
Non-Adhering	27%	26%	24%	26%	26%	24%	26%	28%
Adhering	34%	35%	36%	38%	37%	32%	30%	28%
PSD Ratio	1.14	1.11	1.11	0.94	0.97	1.39	1.46	1.55

7.1.1 Base Blend Cold Permeability Analysis

The base blend demonstrates a stable cold permeability profile with an air flow between 12.5 m^3/h and 14.8 m^3/h throughout the test, as shown in Figure 7.2, the average value being 13.66 m^3/h. This is indicative of a well-mixed blend and shows good permeability within the bed, which is conducive to good sintering performance. The stability of the sintering profile in Figure 7.3 is a testament to this. This is owing to the oxygen demand of the fuel present in the bed to combust effectively, which is a requirement for the sintering reaction to take place. The issue of poor air flow is that it will reduce combustion and sintering rates though the bed, or potentially lead to pockets of un-sintered material.

The higher values and stability of the profile in figure 7.2 when compared to figure 6.4 shows that the base blend used in this set of tests has better permeability prior to sintering. The base blend measured in figure 7.2 had a calculated PSD ratio of 1.14 compared to 1.06 for the base blend from chapter 6.

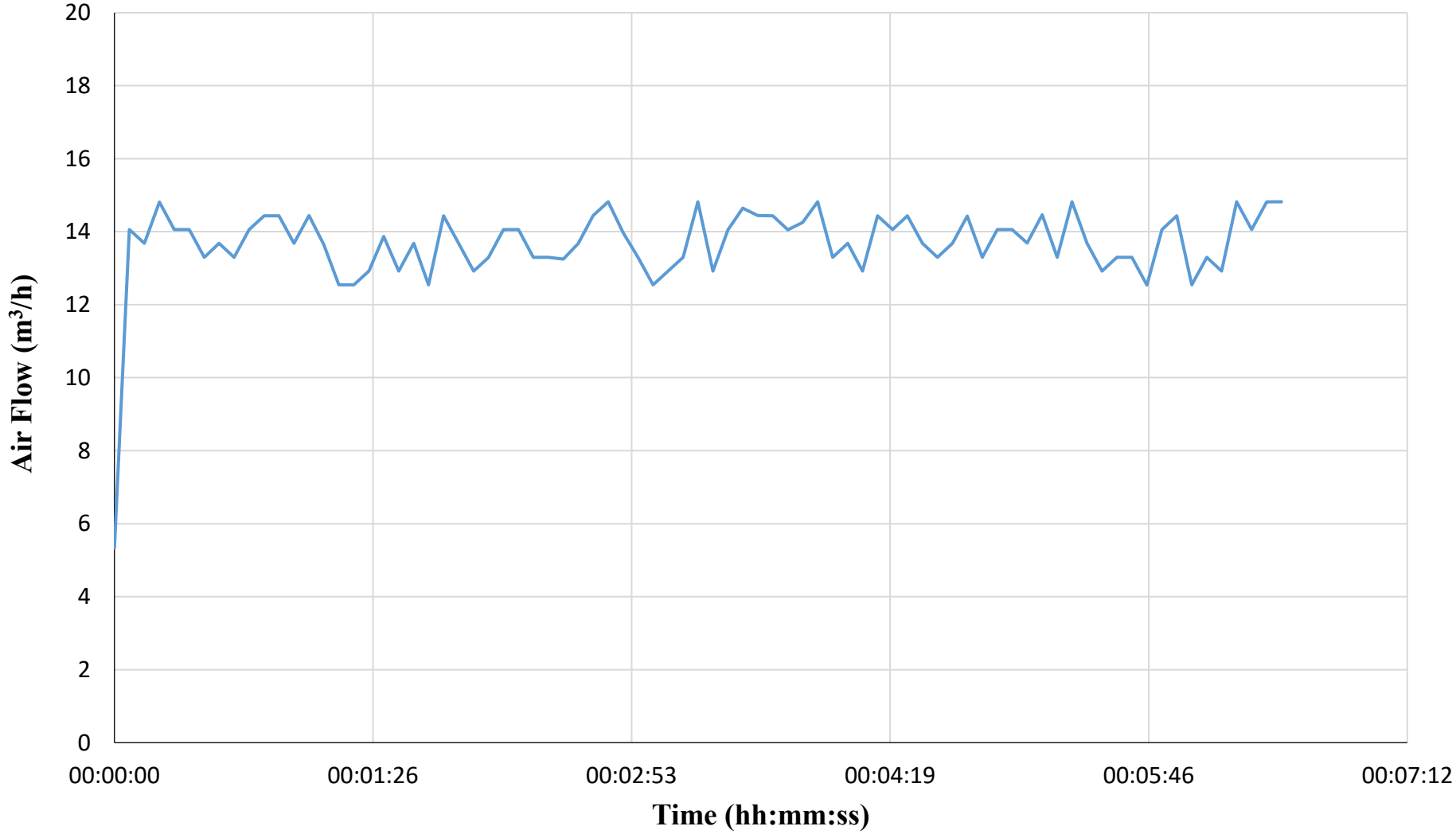

Figure 7.2 Results from the cold permeability air flow during cold permeability test for base blend.

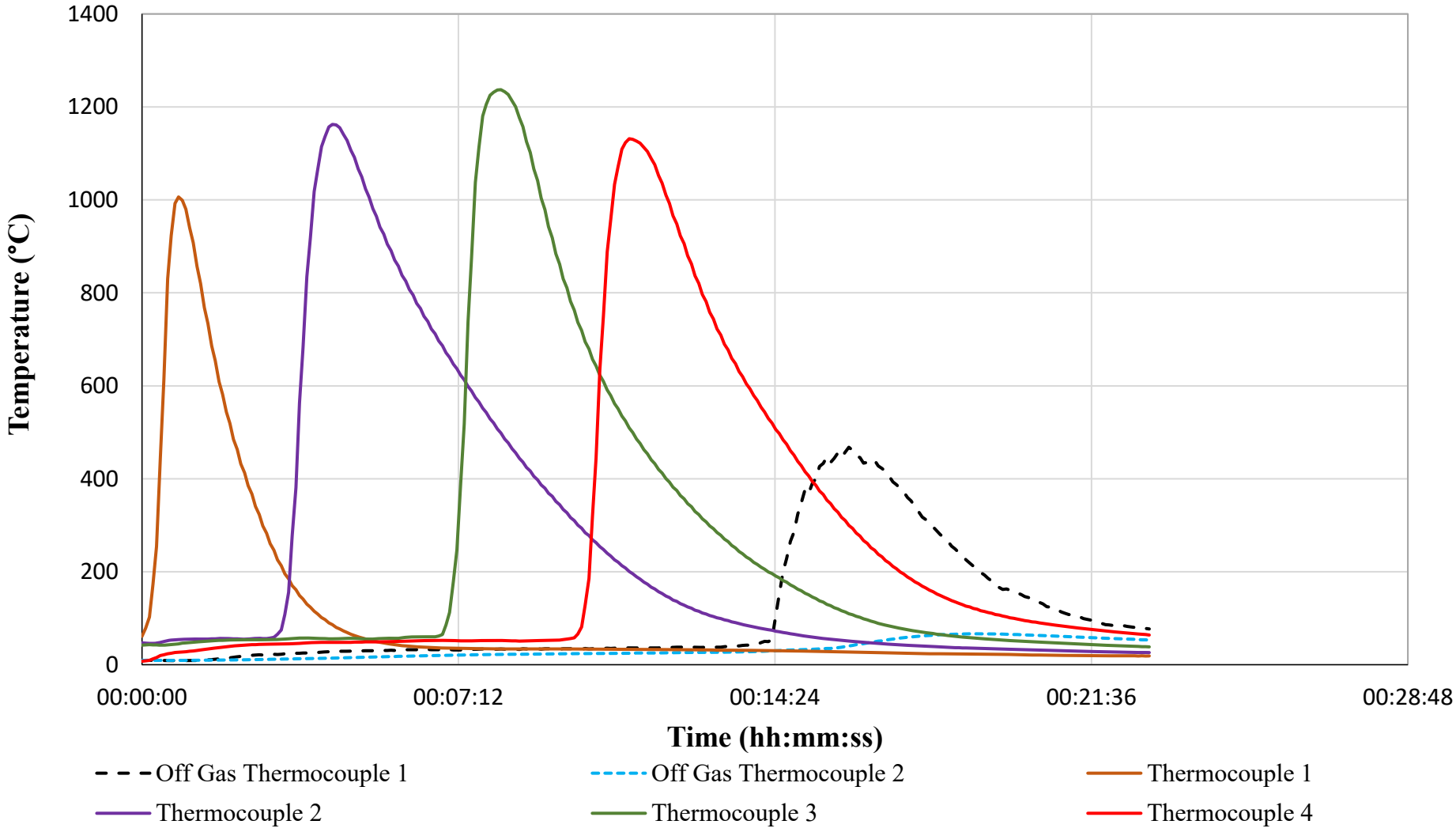

Figure 7.1 Sintering thermal profile during base blend test.

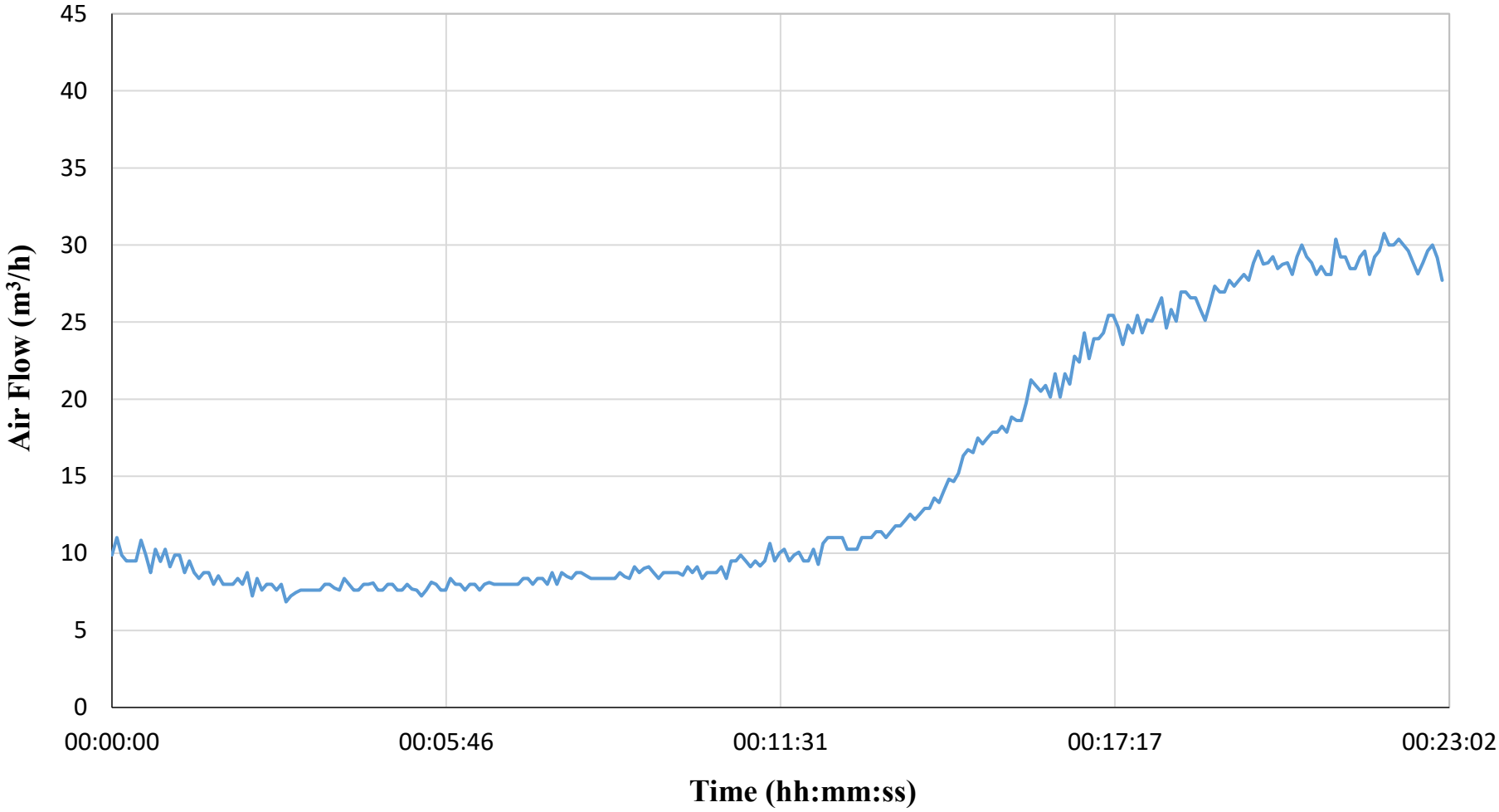

Figure 7.2 Hot permeability testing air flow during sintering test for base blend.

7.1.2 Base Blend Sintering Thermal Profiles

During the base blend testing thermocouple 5 was damaged and failed. For this reason, after base blend testing thermocouple 3 was relocated to thermocouple 5 slot to provide more complete temperature profile data across the whole sinter bed.

The base blend's sintering thermal profile is shown in Figure 7.4. This blend sintered in just under 22 minutes, sintering completion being defined as when all thermocouples recorded < 100 °C. Overall, the thermal profile appeared stable and steadily rose between thermocouples 1-3 before dropping slightly at thermocouple 4. Temperatures recorded at thermocouple 1 are the lowest throughout the test, peaking at just 1006 °C and averaging 108 °C throughout the whole test. The narrow shape of the thermal profile recorded at thermocouple 1 also indicates that the flame front is thin and moving quickly due to the sharp rise followed by a quick decline when compared to the other profiles on the sintering profile.

Once the flame front has moved onto thermocouple 2, it is clear that the combustion and sintering processes have developed. This is indicated by the fact that the peak temperature is higher, and the cooling rate appears significantly lower. The peak temperature is 1162.4 °C, representing an increase of 156.1 °C, or 15.5%, compared to thermocouple 1. The cooling rate change drastically from 275.6 °C/min in thermocouple 1 to 118.3 °C/min in thermocouple 2, a drop of approximately 57.0 %. The time spent above 1000 °C is another important parameter of sintering. In this context, thermocouple 1 only reaches this mark for approximately 10 seconds whereas at thermocouple 2 the flame front spends approximately 70 seconds over 1000 °C. This allows seven times longer for the sinter mix to reach temperature, melt and begin to fuse together.

The trend of increasing temperature continues into thermocouple 3 where the highest temperature recorded during this test was, 1237.1 °C, up approximately 7.0% from the previous thermocouple reading. This indicates that the rate of increase in the overall heating rate is waning at this point, something supported by a slight rise in cooling rate to 137.8 °C/min. However, the time above 1000 °C did rise further to approximately 90 seconds.

Thermocouple 4 sees a decline in every recorded parameter compared to thermocouple 3, further indicating decreasing heat flow and flame front propagation in the sinter pot. Peak temperature drops to 1131.6 °C, the lowest peak temperature apart from thermocouple 1 and a 105.4 °C reduction from the previous peak at thermocouple 3. The time

spent above 1000 °C drops to approximately 70 seconds, similar to that of thermocouple 2 even though the peak temperature is 30.8 °C lower. The cooling rate is approximately 117 °C/min, which is lower than thermocouple 3 but highly comparable to thermocouple 2.

Overall, the base blend sintered well and appears a good baseline for comparison to further tests. This was determined due to similarities to previous Tata Steel UK experiments (82). Sharp rises in thermocouple peaks followed by smooth declines and test length all supported this assertion, all indicative of a steady and effective sintering process.

7.1.3 Base Blend Hot Permeability Analysis

Looking at the airflow rate though the base blend during sintering, otherwise defined as the hot permeability, the graph in Figure 7.5 shows that the air flow drops during the initial stages of sintering. So, over the first 10 minutes the average airflow is 8.36 m^3/h, significantly lower than the 13.66 m^3/h observed in the cold permeability testing. This is likely to be predominantly due to the flame front impeding airflow from the top of the bed, with potentially a small amount of natural consolidation within the material.

After this stage, the air flow begins to rise with an average of 16.89 m^3/h over the next 10 minutes and the final stage of the test where the air flow once again levels off again (average 29.02 m^3/h). The peak air flow rate that is reached in this final stage after approximately 22 minutes is 30.75 m^3/h. This increase in permeability throughout the test is a factor of the flame front's movement and sintering of the raw material such that the agglomeration of the fines to sinter and combustion of fuels throughout the sinter bed results in increased porosity and therefore greater permeability. This same effect was seen in Chapter 6.

7.1.4 Base Blend Conclusions

This overall profile of the base blend's hot permeability in figure 7.1 is typical of others produced using this sinter pot, further supporting the assumption that this base blend test was successful and has provided a good baseline for comparison to later tests.

7.2 Basic Oxygen Steelmaking Slurry Addition

Basic oxygen steelmaking (BOS) slurry is another common revert found within integrated steelworks (described in detail in section 2.2.3). As with ESP dust, there is a strong focus on the recycling of revert materials and BOS slurry typically offers significant iron and carbon content which can offset costly raw material usage. For these tests, BOS slurry was added to the base blend at concentrations of 5 % and 10% alongside a BOS slurry micro-pellet at 10 % concentration. A key objective here is to study the impact of pelletising the higher concentration of BOS slurry in comparison to the test solely utilising BOS slurry fines. One key factor limiting increased utilisation of BOS slurry within the steel industry is the zinc content. As such, in these experiments, zinc levels will be monitored in the in both the sinter and dusts collected in the emissions tray, to ascertain whether pelletisation modifies zinc mobilisation/pathways. As previously discussed, zinc will negatively impact downstream processes within integrated steelworks which often have strict zinc content limits.

7.2.1 BOS Slurry Cold Permeability Analysis

The BOS slurry cold permeability testing data in Figure 7.3.1 clearly shows that the 10 % BOS slurry addition has a significant negative impact on the air flow compared to the other tests. The average flow rate in the 10 % BOS slurry blend is 11.23 m^3/h whereas for the base blend the average is 13.66 m^3/h, or ~ 16 % higher. The 5 % BOS addition has an average flow rate of 13.03 m^3/h and the 10 % BOS slurry micro-pellet test shows a 13.59 m^3/h average air flow. The blend containing 10 % BOS slurry fines also has the lowest peak flow rate, reaching just 12.91 m^3/h, a value lower than the average air flow of the other tests. This indicates that the inclusion of BOS slurry fines reduces permeability, which is perhaps to be expected if the fines fill void spaces. However, this reduction intensifies when increasing BOS slurry concentration from 5 % to 10 %. Interestingly, the addition of micro-pellets appears to have had no impact on the cold permeability of the blend, despite having a greater PSD ratio of 1.39 compared to 1.14 in the base blend. Analysis of the standard deviation of the tests shows that the 10 % BOS slurry micro-pellet test has the tightest distribution with a standard deviation of 0.56 m^3/h compared to 0.67 m^3/h, 0.65 m^3/h and 0.64 m^3/h for the base blend, 5 % BOS slurry & 10 % BOS slurry tests respectively. This indicates less fluctuation in the cold air flow rate when using micro-pellets which is a positive result if this were to be scaled into an industrial scale sintering process.

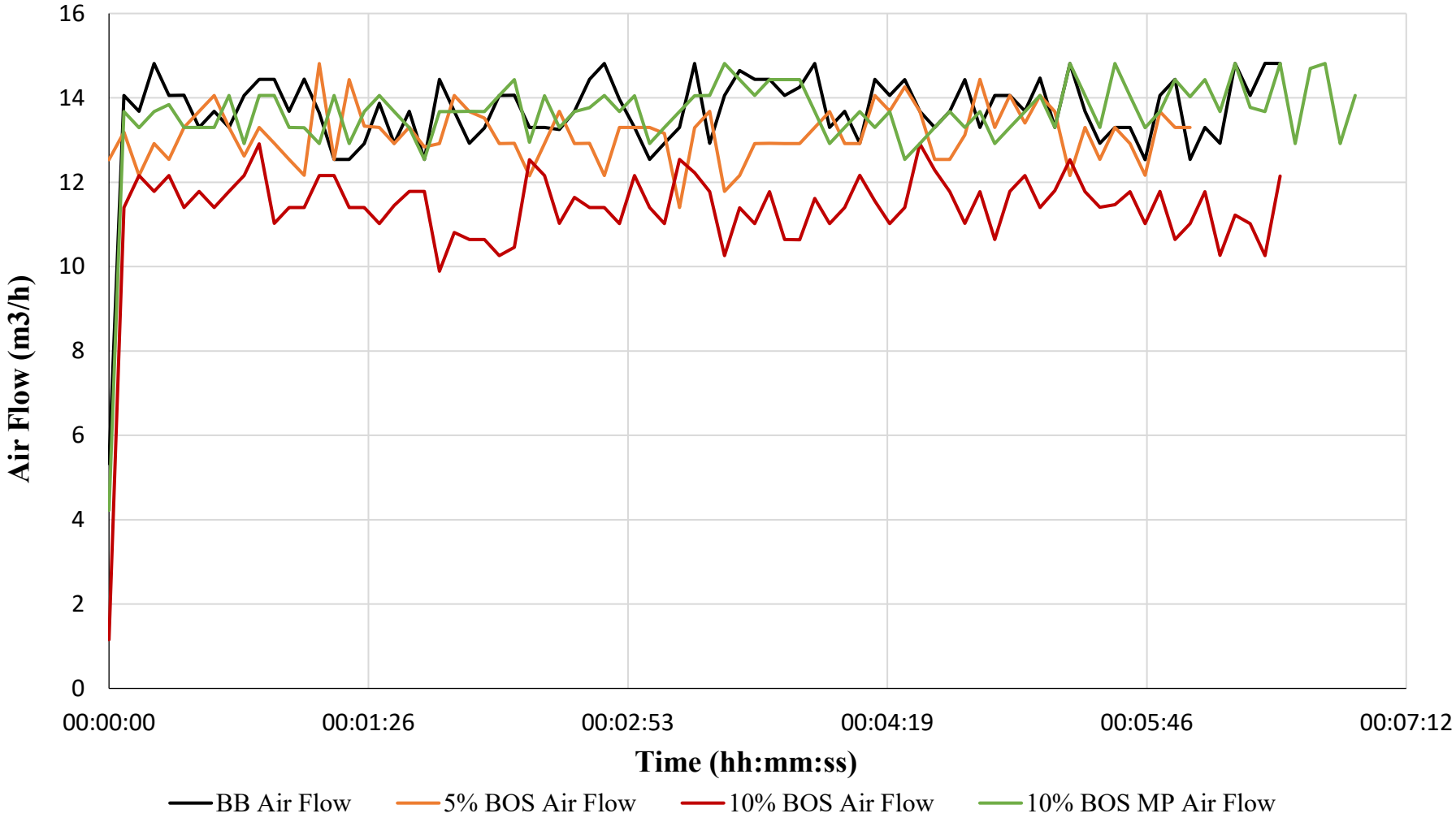

Figure 7.3 Air flow during cold permeability testing for BOS slurry addition tests.

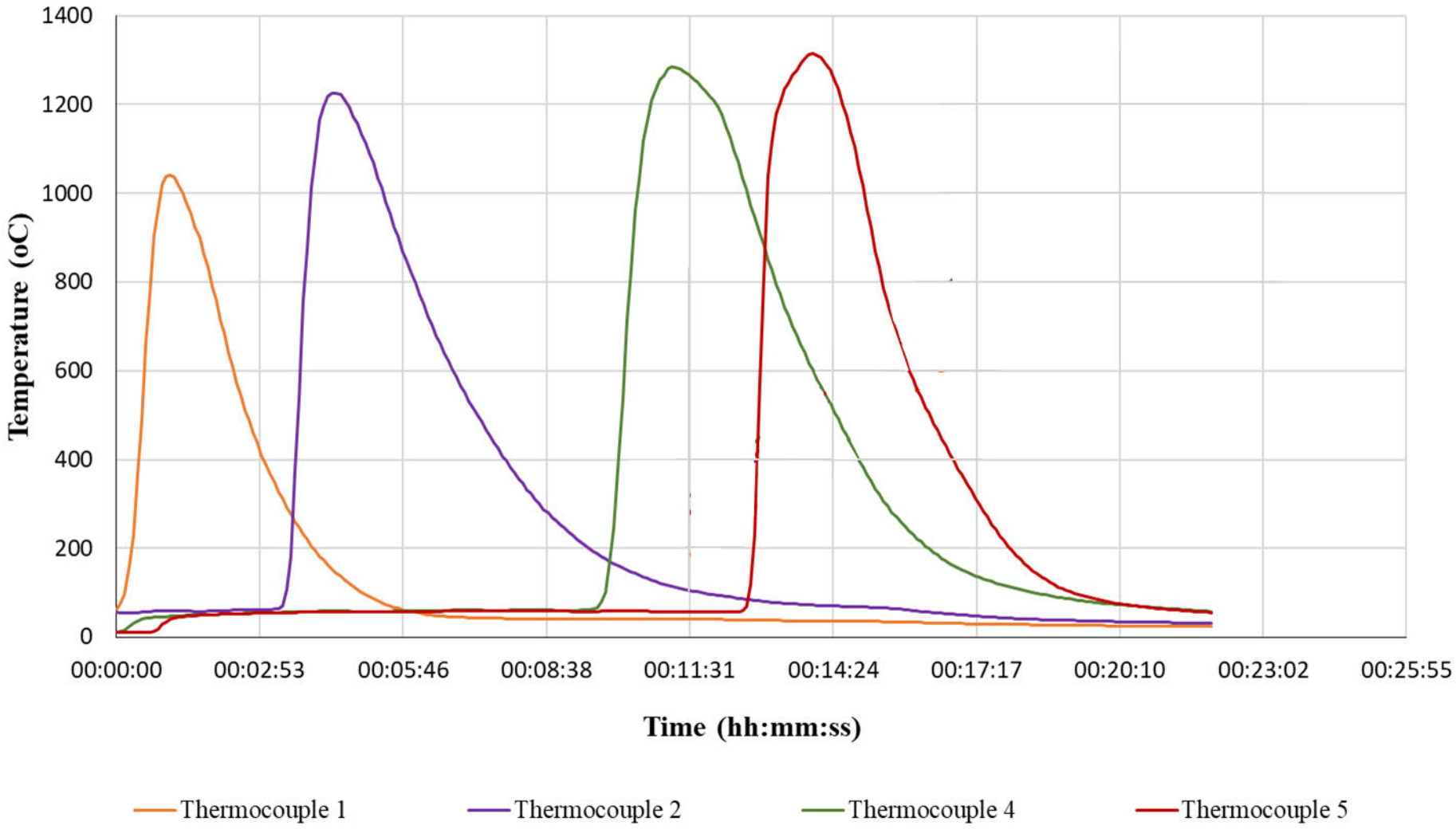

Figure 7.4 Sintering thermal profile for 5% BOS Slurry Test.

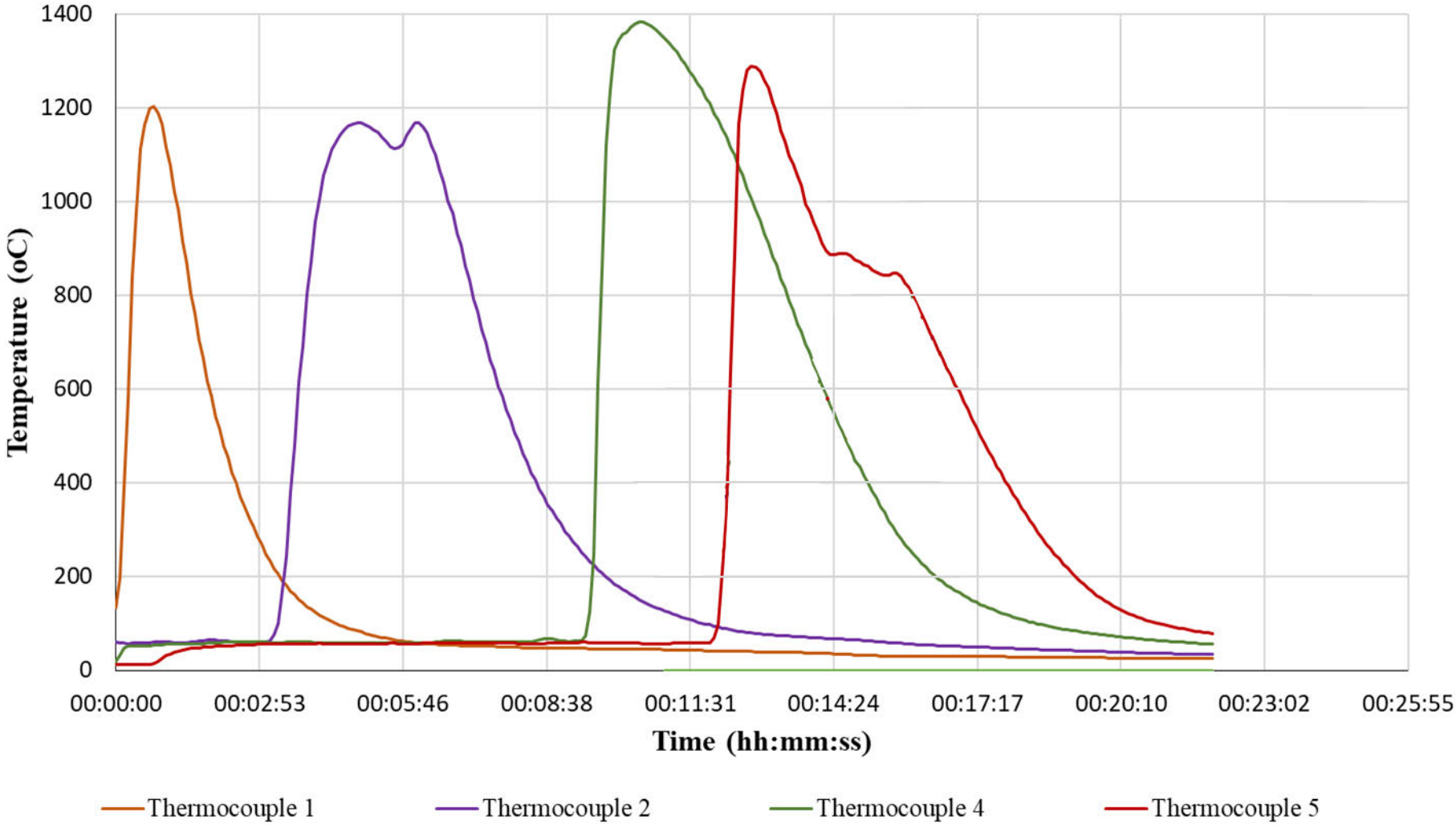

Figure 7.5 Sintering thermal profile for 10% BOS Slurry test.

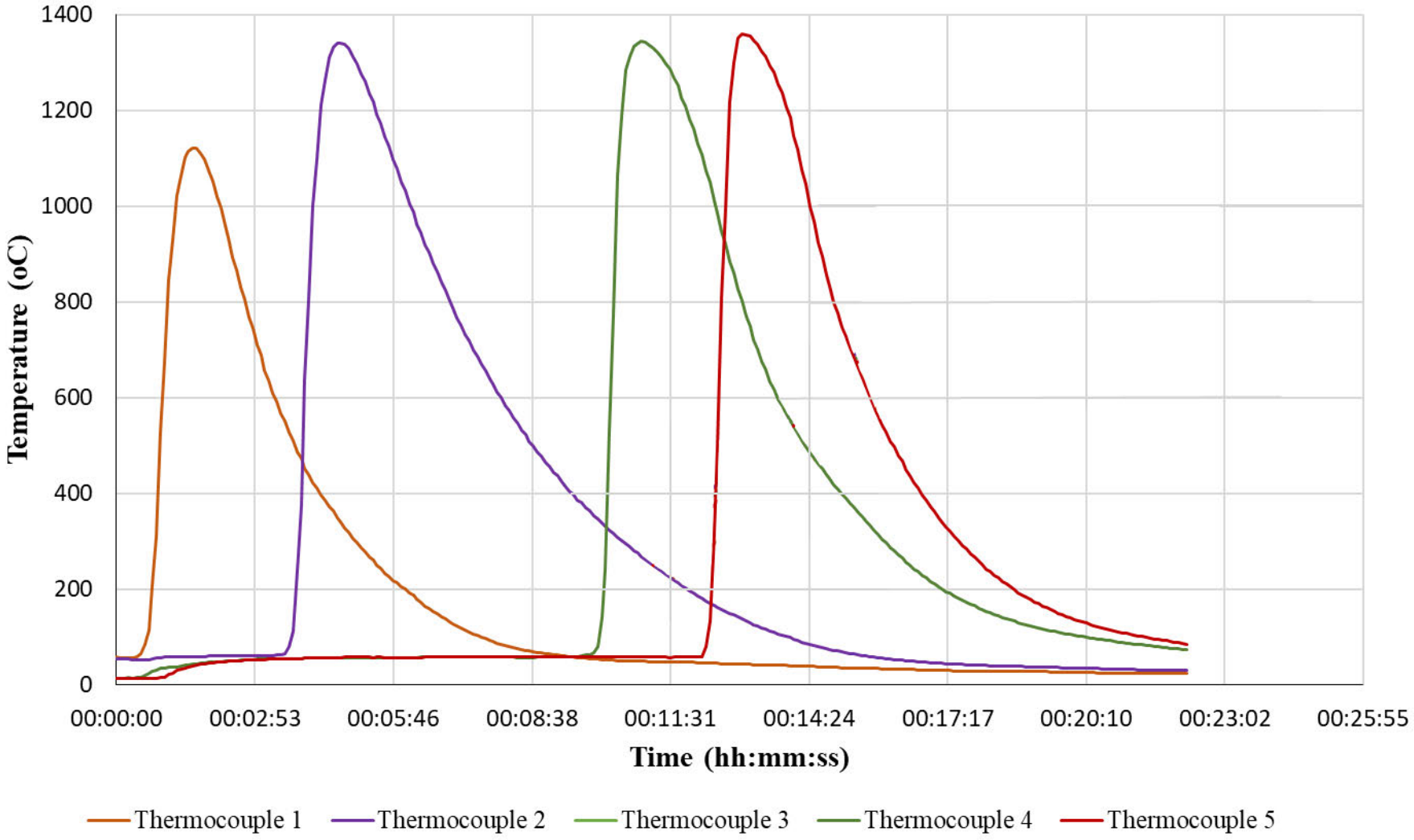

Figure 7.6 Sintering thermal profile for 10% BOS Slurry MP test.

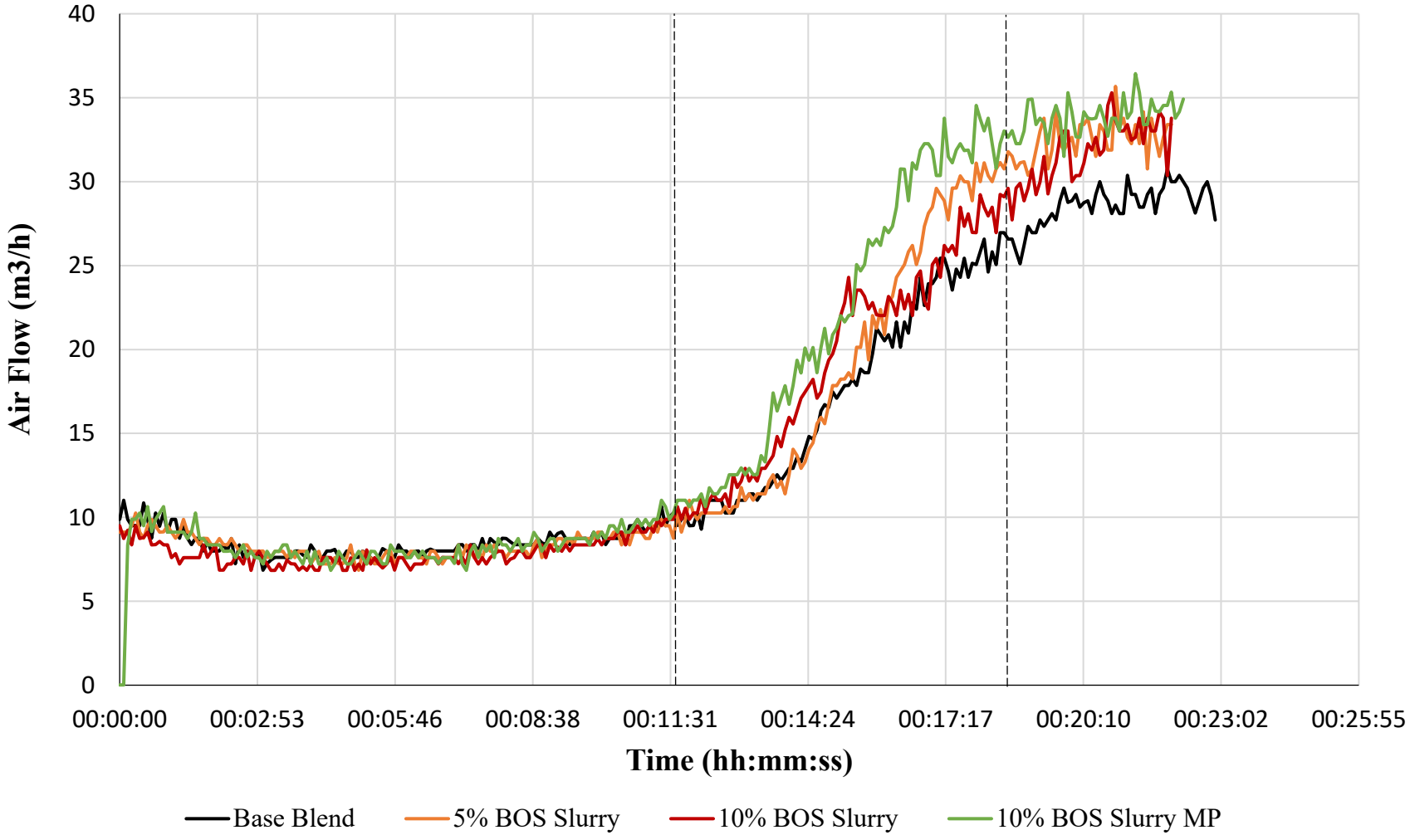

Figure 7.7 Air flow during sintering tests for BOS Slurry additions & base blend.

7.2.2 BOS Slurry Sintering Thermal Profiles

There were notable differences between the test data in terms of the peak temperature reached and time spent above 1000 ºC, with the addition of 10 % BOS slurry fines to the blend seemingly having the most detrimental impacts relative to the other experiments (and in line with the permeability data). By comparison, the 5 % BOS slurry fines and the 10 % BOS slurry micro-pellet tests appear more stable and homogenous throughout in terms of the thermal profiles, as can be seen when comparing Figures 7.3.2, 7.3.3 & 7.3.4. The 10 % BOS slurry fines thermal profile stands out by showing a double peak on thermocouple 2 and an irregular decline in thermocouple 4. This is likely linked to the lower permeability of the 10 % BOS slurry fines blend, seen in Figure 7.3.1, but will be discussed in more detail in this section.

7.2.2.1 Thermocouple 1

As with the overall temperature profile, thermocouple 1 readings from the 5 % BOS slurry fines and the 10 % BOS slurry micro-pellet blends appear similar in terms of their shape, peaking at 1041.9 °C and 1121.8 °C, respectively. However, the 10 % BOS slurry fines test displays a different temperature profile at thermocouple 1, peaking at 1201.8 °C. Compared to the base blend, the peak temperature of the 10 % BOS slurry fines test recorded an increase of 19.4%. However, the 10 % BOS slurry fines test have an average temperature of 137.2 °C during sintering, compared to the nominally higher 139.0 °C for 5 % BOS slurry and the significantly higher average of 181.7 °C observed in the 10 % micro-pellet test.

Supporting the average temperature data are the cooling rates, with the slowest recorded in the 10 % BOS slurry micro-pellet test at 170.3 °C/minute compared to the fastest rate of 293.6 °C/min observed with the 10% BOS slurry fines test. The time spent above 1000 °C during sintering is higher in every test when compared to the base blend; approximately 25 s for the 5 % BOS slurry test, rising to 40 s with 10 % BOS slurry and finally 50 s for the 10 % BOS slurry micro-pellet.

These results from the initial sintering activity at thermocouple 1 indicate that increasing BOS slurry content of sinter blends results in higher temperatures, likely due to the carbon content of the slurry. The differences between the 10 % fines and micro-pelletised BOS slurry tests behaviour indicate that the form of BOS slurry being added does impact sintering parameters such as cooling rates and peak temperature.

7.2.2.2 Thermocouple 2

As the tests moved onto thermocouple 2, the thermal profiles develop as expected, apart from the 10 % BOS slurry fines test which, as described above, show an irregular double peak. However, generally parameters indicate continuation of flame front development and propagation; compared to thermocouple 1. For example, the average peak temperature rises by 123.4 °C to 1245.3 °C, the average temperature rises from 181.7 °C to 290.2 °C, the average cooling rate reduces from 233.1 °C/min to 144.0 °C/min and average time over 1000 °C increases by approximately 322 % to 123.3 s.

Looking at the 5% BOS slurry test, the temperature increases steadily to approximately 1226.0 °C and the micro-pellet test rises significantly to 1341.2 °C. However, the peak temperature for the 10 % BOS slurry fines test only peaks at 1168.5 °C, which is actually a decrease from thermocouple 1 suggesting that this addition hinders combustion.

The average temperatures throughout each test at thermocouple 2 range from 231.7 °C observed in the 5 % BOS slurry test, to 272.2 °C in the 10 % BOS slurry profile to a maximum of 290.2 °C in the 10 % BOS slurry micro-pellet test.

The cooling rate is another parameter which is notably different when compared to thermocouple 1, reducing due to flame front propagation. The cooling rates at thermocouple 2 are 118.3 °C/min, 155.2 °C/min and 152.7 °C/min for the 5 % BOS slurry, 10 % BOS slurry and the 10 % BOS slurry micro-pellet tests, respectively. As previously mentioned, the time above 1000 °C also rises dramatically. 5 % BOS slurry rises by 360 % to 90 s, 10% BOS slurry fines jumped 400% to 160 s and the BOS micro-pellet test also rises by 240 % to 120 s.

Despite a lower peak temperature in the 10 % BOS slurry fines test, it still records a significant increase in time above 1000 °C, average temperature, and a slower cooling rate. This points to a less uniform flame front profile in this test, as the flame front has clearly developed between thermocouples 1 and 2 but, by being less stable, it may not have passed the thermocouple uniformly resulting in a lower reading. This is also supported by the fact that in Figure 7.2.3 the reading for thermocouple 4 shows a high peak temperature and a return to a uniform profile.

7.2.2.3 Thermocouple 4

Thermocouple 4 in each test appears more uniform compared to thermocouple 2, particularly in the 10 % BOS slurry fines test. The average of the parameters analysed here all rise steadily from the previous thermocouple. For example, the average maximum temperature has an increase of 7.5 % to 1338.5 °C, the average temperature throughout the tests rises by 8.0 % to 285.9 °C, the time above 1000 °C decreases by 4.8% to 117.5 s and the cooling rate increases by 6.1% to 152.7 °C/min.

The 10 % BOS slurry fines test records the highest peak temperature from any point during the BOS slurry addition testing, reaching 1383.3 °C. Although this represents an 18.4 % rise compared to the previous thermocouple, as outlined in section 7.3.2.3, the peak temperature at thermocouple 2 for the 10 % BOS slurry fines test may not be completely accurate. The 10 % BOS slurry micro-pellet test peaks at 1343.4 °C, although the second highest value this is only a 0.2 % rise from the previous measurement in the test, marking the smallest increase from thermocouple 2 to 4. The 5 % BOS slurry fines test's peak temperature rises by 5.1 % to 1284.9 °C, whereas the base blend slightly decreases by 2.7 % to 1131.6 °C at this stage of the testing.

By comparison, the 10 % BOS slurry test has the most significant increase in peak temperature. However, the biggest increase in average test temperature is seen in the 5 % BOS slurry test where it rose by 16.7 % to 270.4 °C. This is followed closely by the 10 % BOS slurry test which rises by 15.7 % to 315 °C, the highest value in this suite of tests. Conversely, the 10 % BOS slurry micro-pellet test sees a slight drop in average temperature, down 6.1 % to 272.3 °C, which may have been expected due to its lack of a significant rise in peak temperature compared to the other BOS addition tests. This decrease is like the 5.4 % drop observed in the base blend.

Looking at the cooling rates, these decrease in all tests between thermocouple 1 and 2, between 2 and 4 they all rose slightly with BOS addition. 5.2 % and 5.1 % increases for 5 % BOS slurry and 10 % BOS slurry, respectively. A slightly higher rise of 8.3 % is seen for the 10 % BOS slurry micro-pellet test. The time above 1000 °C sees the 5 % BOS slurry test once again produce the largest increase, rising by 50%, to 135 s total. The 10 % BOS slurry micro-pellet again shows a small rise of 4.2 % to 125 s, and although the 10 % BOS slurry test still recorded the highest time at thermocouple 4 it decreases by 12.5 % from thermocouple 2 to 140 s.

Despite slight increases in peak and average temperatures when compared to those recorded at thermocouple 2, the flame front development is clearly indicating that, at this stage in the experiment, it is reaching a temperature ceiling. The 10 % BOS slurry test records the highest average and peak temperatures at this point in testing and also displays a more typical thermal profile compared to the previous test. This indicates that the addition of BOS slurry at high concentrations in un-pelletised form is conducive to achieving good sintering temperatures but can result in variable flame front behaviour compared to if the same concentration is used when pelletised.

7.2.2.4 Thermocouple 5

As previously mentioned, the base blend does not have values for thermocouple 5 so cannot be compared to the BOS addition tests at this stage.

The fifth and final thermocouple of the tests for the 5 % BOS slurry test and the 10 % BOS slurry micro-pellet show clear increases in peak temperature and look very similar to their preceding profiles. The 10 % BOS slurry test however appears irregular, after a normal start it declines, from a lower peak than thermocouple 4, before a shoulder appears which eventually returns to an expected ending phase. Average peak temperature compared to thermocouple 4 is down by 1.35 % to 1320.4 °C, average temperature during sintering also decreases by 12.6 % to 249.9 °C and time above 1000 °C also declines by 14.9 % to approximately 100 s. The average cooling rate at thermocouple 5 increases, typically inversely linked to the other parameters, by 14.3 % to 174.5 °C/min.

The peak temperature seen in both the 5 % BOS slurry and 10 % BOS slurry micro-pellet tests at thermocouple 5 rises slightly by 2.0 % and 1.2 % to 1314.3 °C and 1359.3 °C, respectively. By comparison, the 10 % BOS slurry fines test's peak temperature decreases from its previous level by approximately 7.0 % to 1287.6 °C. However, as can be seen in Figure 7.3.3, the temperature profile recorded appears anomalous compared to other results. It is dissimilar to the anomaly seen at thermocouple 2 during the same test, suggesting a different cause behind it. The much more dramatic deviation from the expected thermal profile indicates something more profound than flame front variation. In this context, previous tests have seen 'channelling' occur within the sinter pot. This is when a vertical section of material fails to sinter, the causes of which could be various and are hard to

identify but as there is another instance of irregular thermal profiles it is likely due to the specific blends sintering stability.

The data also show that the average temperature throughout the sintering tests declines in every instance when comparing thermocouple 5 to 4. The biggest drop is in the 5 % BOS slurry test which falls 17.3 % to 223.8 °C, losing 46.5 °C overall resulting in the lowest average temperature at thermocouple 5. The average for the 10 % BOS slurry fines test is down 11.4 % to 279.3 °C, which remains the highest average temperature recorded at thermocouple 5. Finally, the 10 % BOS slurry micro-pellet falls to 246.6 °C, seeing the smallest decline of only 9.5 % nearly half of that observed in the 5 % BOS slurry test. This is indicative that the flame front is approaching the base of the sinter pot and is running out of material to sinter.

Time above 1000 °C again sees variation between the BOS addition tests. Although having the biggest drop in average temperature, the 5 % BOS slurry test has the smallest decline in terms of time above 1000 °C, falling by approximately 15 s to 120 s (11.2 %). The 10 % BOS slurry has the largest decline, due to its irregular profile, falling 42.9 % to only 80 s. The test including BOS micro-pellets is down 20.0 % to approximately 100 s. Cooling rates rise across the tests apart from the 10 % BOS slurry test where they drop 10.3 % to 144.00 °C/min. The 5 % BOS slurry and 10 % BOS slurry micro-pellet tests rise by 42.6 % and 10.3 % respectively, resulting in rates of 231.3 °C/min and 148.2 °C/min respectively.

7.2.3 BOS Slurry Addition Hot Permeability Analysis

The air flow during sintering for the BOS slurry addition tests are displayed on a single graph in Figure 7.3.5. The base blend has also been included for ease of comparison. All follow similar overall trends; (1) a slight dip over the initial five minutes of sintering before a gentle increase above initial levels, (2) a sharp and fluctuating inflection and (3) plateau towards the end of the test. These stages are divided by dashed lines on Figure 7.3.5.

The first stage lasts 11 min 35 s (± 52 s) on average, stage 2 averages 6 min 58 s (± 27 s) and the final stage having the lowest average length of 3 min 10s (± 34). These timings show that on average the flame front has passed thermocouple 4 before stage 1 has been completed and stage 2 occurs after the flame front has passed thermocouple 5. This illustrates that once the blend has been fully sintered, the particle size and number of void spaces increases which results in the dramatic increase in airflow. Average airflow rates increase

over the stages, as would be expected as more of the raw blend is sintered and void space increases, rising from 8.16 m^3/h initially, to 20.41 m^3/h before 32.66 m^3/h in stage 3. Peak airflows also follow this trend rising from a high of 10.26 m^3/h in stage 1, 31.84 m^3/h in stage 2 and finally reaching 35.80 m^3/h in stage 3.

There is a noticeable difference between the base blend and 10 % BOS slurry micro-pellets test in stage 3 of 7.3.5, with the base blend having the lowest average airflow of 29.07 m^3/h and the micro-pellets inducing the highest of 33.74 m^3/h, an increase of 16.1 %.

7.2.4 BOS Slurry Addition Conclusions

There are clearly impacts on a range of parameters when varying the level of BOS slurry addition, the most notable negative impacts were seen when including 10 % BOS slurry fines in the sinter blend. From the initial cold permeability test, the high level of BOS fines is impacting air flow in the sinter bed, dropping to 11.23 m^3/h which is the lowest in this suite of tests and lower than the base blend, as opposed to 13.59 m^3/h when including the same amount of BOS slurry but in micro-pellet form.

This is also likely a contributing factor to what causes the unstable sintering thermal profile for the 10 % BOS slurry fines test, clearly seen in Figure 7.3.3. The elevated carbon content of the BOS slurry may also contribute to instability and high peak temperatures, potentially also causing channeling and flame front irregularities which may be observable in thermocouples 2 & 5. This test does however record the highest peak temperature, again likely due to the BOS slurry fines spready throughout the blend.

The test with 10 % BOS slurry micro-pellets behaves very differently however, with the highest average temperature, the most time above 1000 °C and the production of much more stable profiles during sintering. Alongside the improved cold permeability, this indicates that pelletisation of BOS slurry results in better sintering parameters when using concentrations as high as 10 %.

Highest sinter Zn levels were seen in the 10 % BOS slurry sinters, this would be a limiting factor depending on industrial Zn limits. However it is recommended that BOS slurry usage be maximized where possible to reduce fuel rates and use micro-pelletisation to further support this increased usage.

7.3 ESP Dust and WESP Dust Sintering Tests

This section outlines results from tests featuring the addition of 10 % ESP dust, WESP dust, ESP dust micro-pellets and WESP dust micro-pellets. The aim here has been to assess the impact of high levels of dust from the electrostatic precipitators (ESP) - both raw and after being water washed. As such, at least part of this material had been present in a sinter mix but had been blown out of the sinter strand as dust to be captured within the ESP dust capture system. Furthermore, the impact of adding the same amount of each material but micro-pelletised has also been studied.

7.3.1 Cold Permeability Air Flow

It is clear from Figure 7.4.1 that the addition of micro-pellets results in improved air flow in the un-sintered bed when compared to the base blend, 10 % ESP dust and 10 % WESP dust addition tests. This is not unexpected because the micro-pellets would be expected to break up the normal packing on the sinter mix to increase void space within the sinter bed. As such, the two tests that included micro-pellets have the highest maximum and average air flow values when compared to this suite of tests and the base blend. For example, 10 % ESP dust micro-pellets have an 18.23 m^3/h peak flow with an average of 16.47 m^3/h and a 18.05 m^3/h peak with an average of 16.79 m^3/h for the 10 % WESP dust test. This can be compared to the 10 % ESP and 10 % WESP dust, which have peaks of 15.77 m^3/h & 14.44 m^3/h, respectively and average flow rates of 13.59 m^3/h & 13.33 m^3/h, respectively. Standard deviation analysis however highlights that the micro-pellets tests as the most variable.

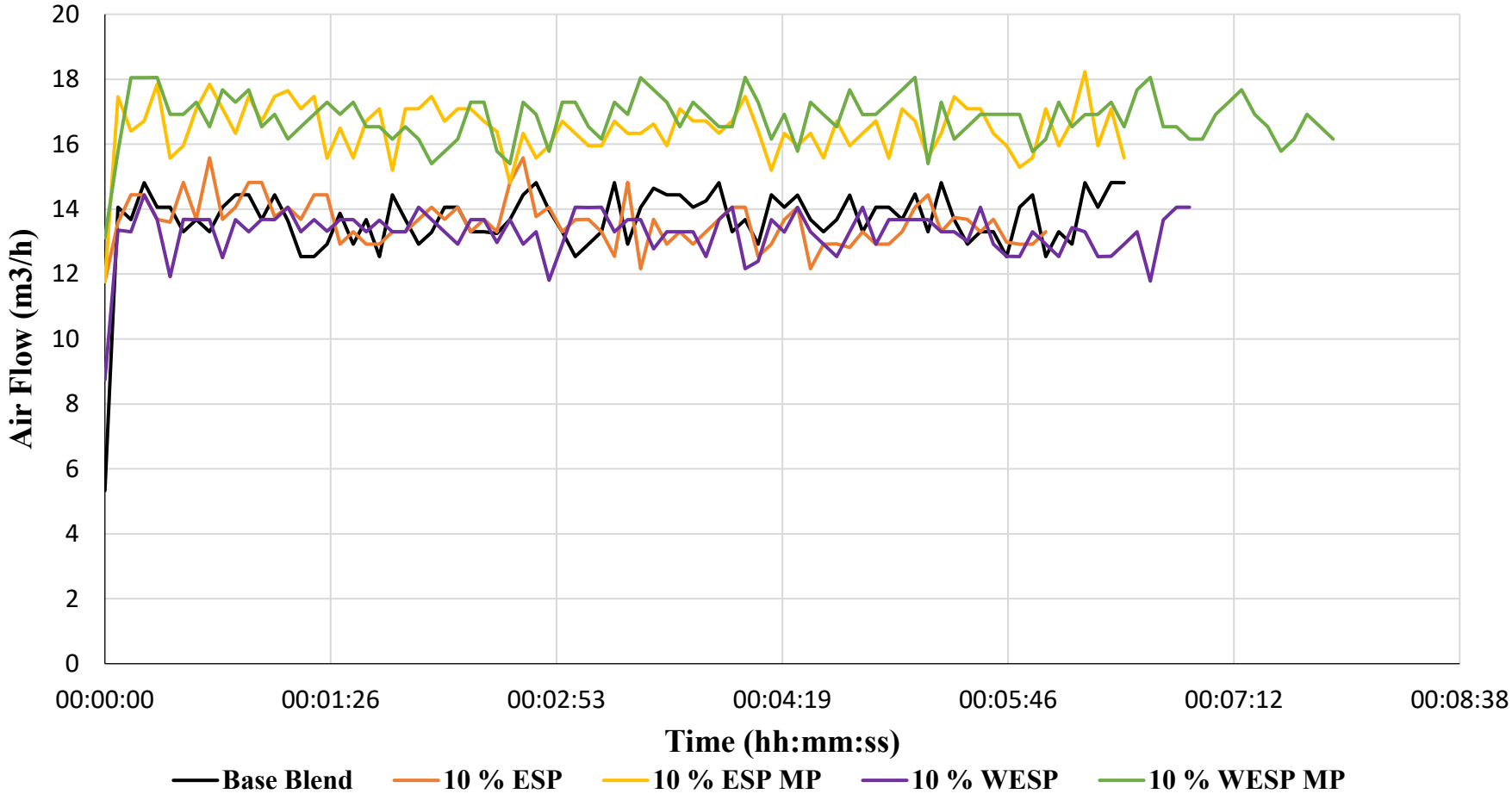

Figure 7.8 Cold permeability air flow graph for base blend and ESP/WESP addition tests.

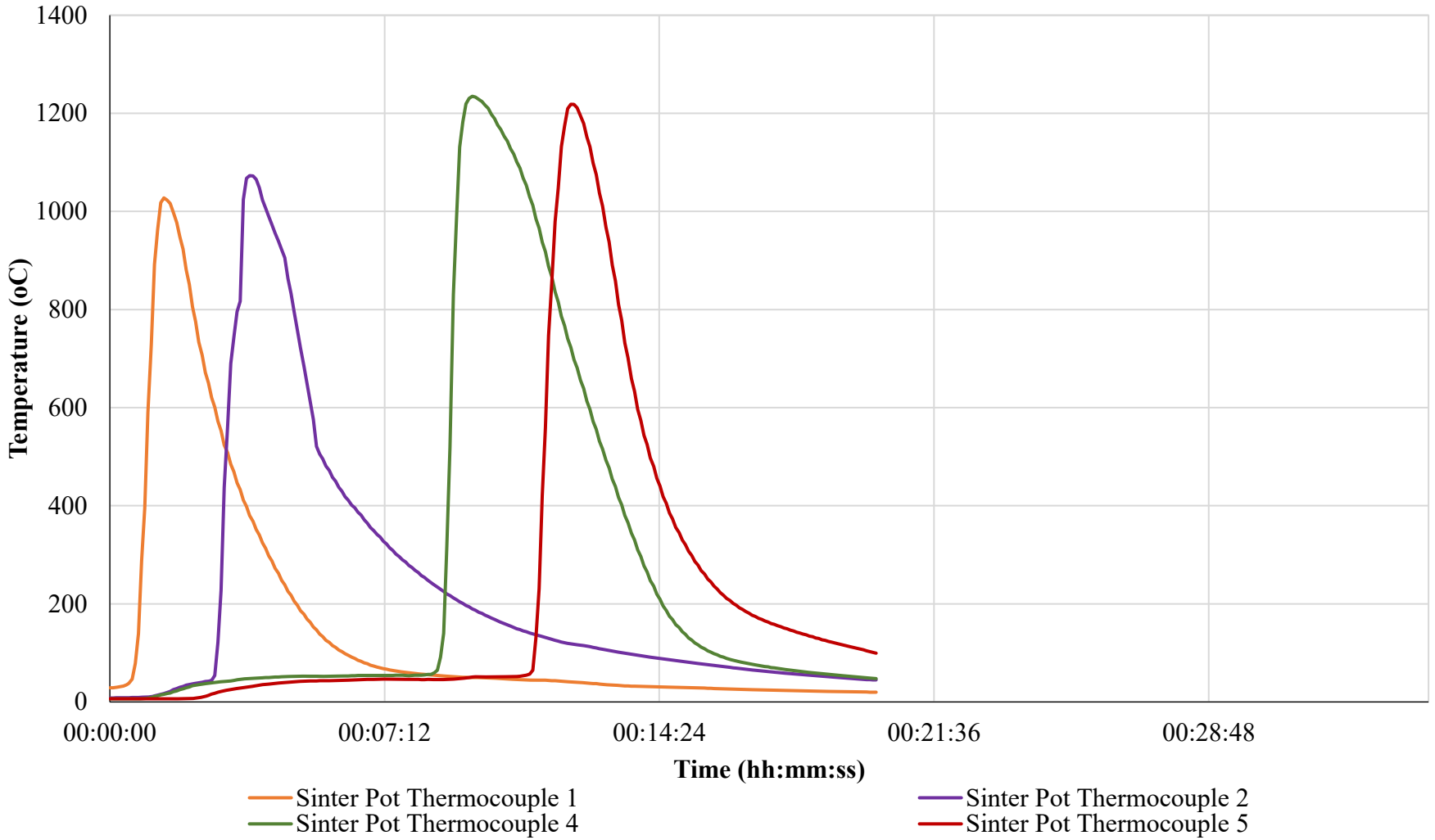

Figure 7.9 Thermal profile for 10 % ESP dust sinter test.

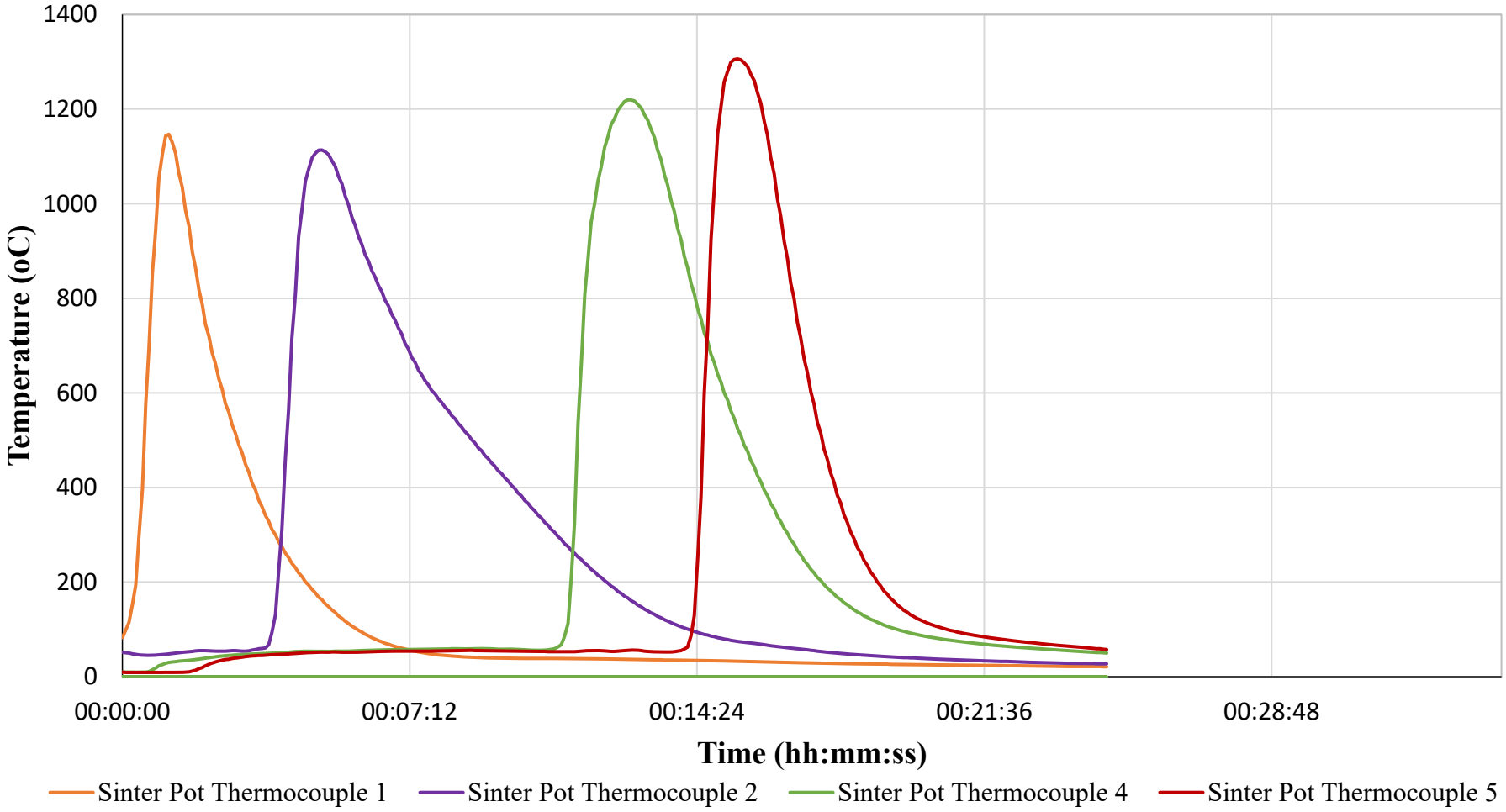

Figure 7.10 Thermal profile for 10 % WESP dust sinter test.

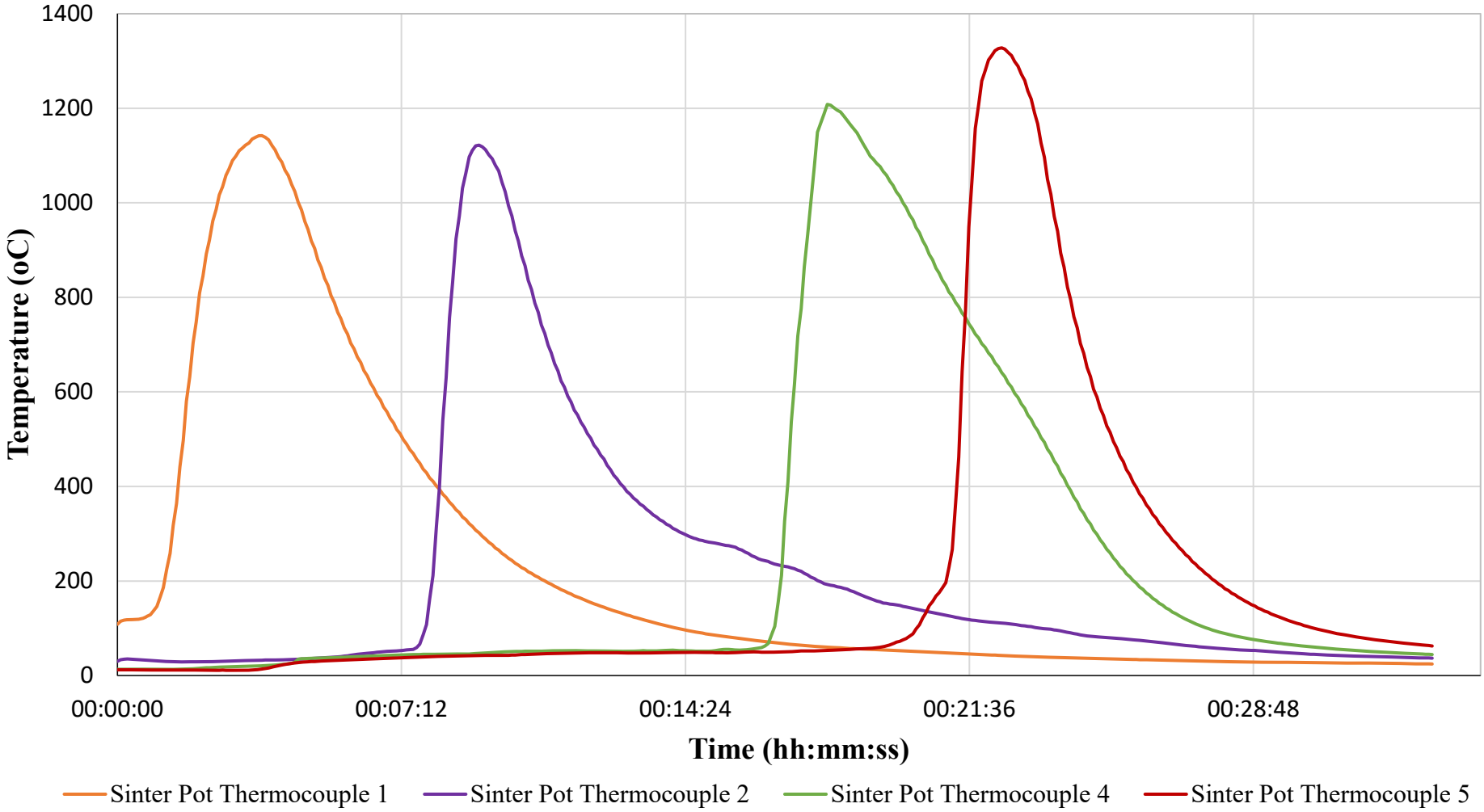

Figure 7.10 Thermal profile for 10 % ESP micro-pellet sinter test.

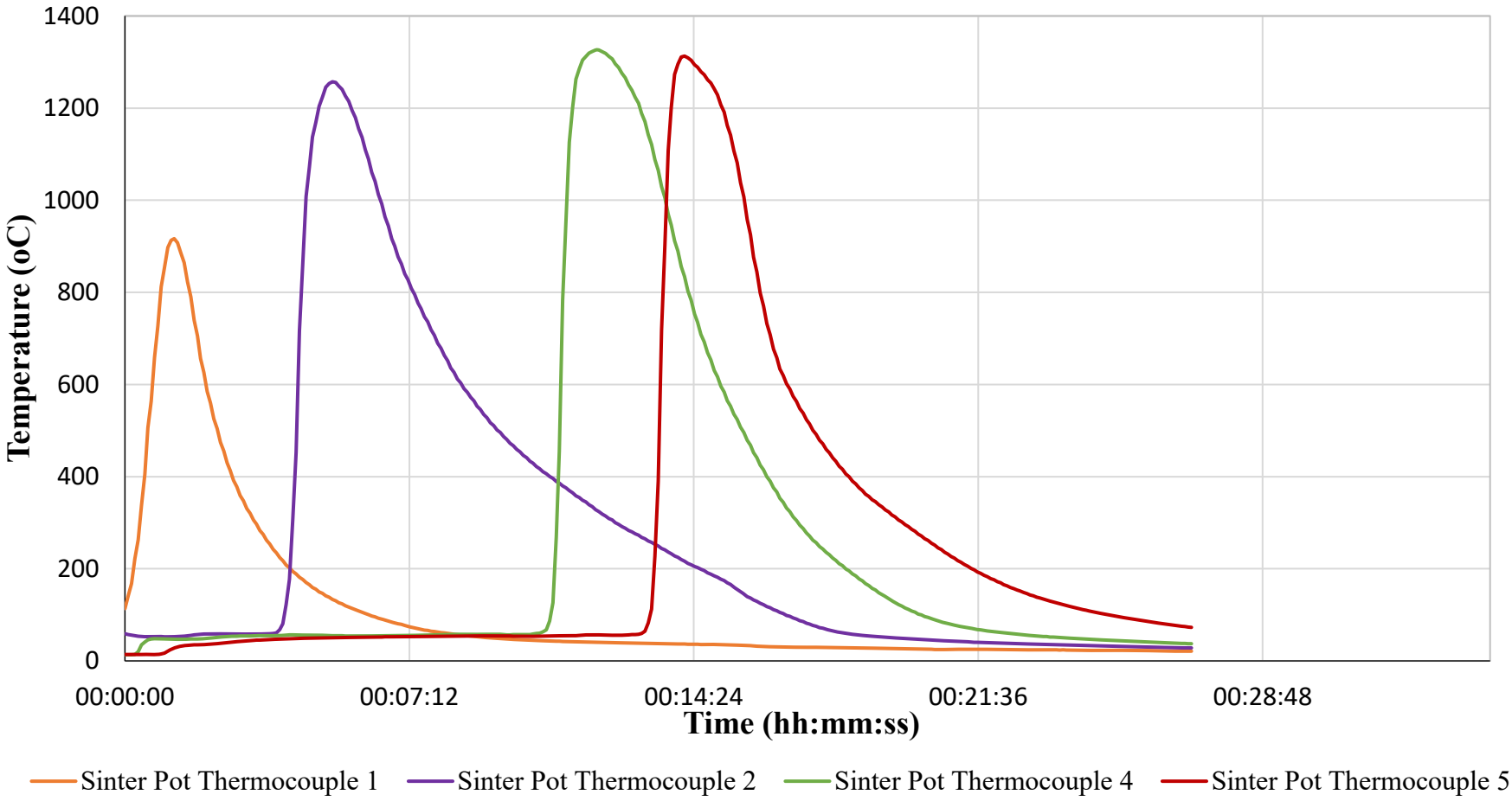

Figure 7.12 Thermal profile for 10 % WESP micro-pellet sinter test

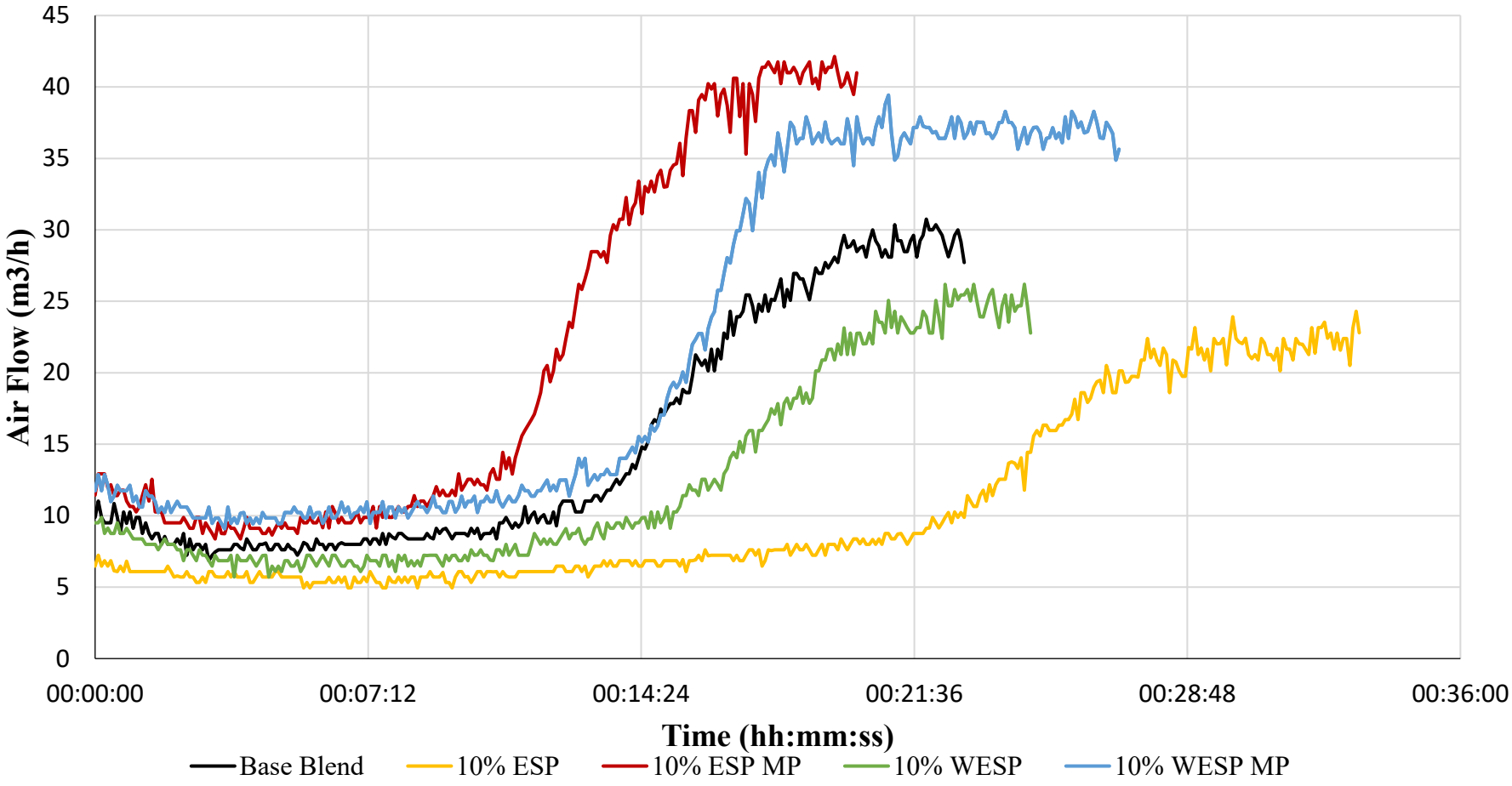

Figure 7.13 Hot permeability air flow test profiles for all sinter test.

7.3.2 ESP/WESP Sintering Thermal Profiles

This suite of tests had much more variable thermal profiles during sintering compared to the BOS slurry addition tests, varying in thermal profile sizes and test time significantly. The variation in test length is evident in Figure 7.4.6. Both tests featuring micro-pellets appear to take longer to heat up to peak temperature, as evident when looking at thermocouple 1 between Figures 7.4.2 – 7.4.5. The 10 % ESP dust test is the slowest overall lasting 33 min 20 s, making it over 50 % longer than the 10 % ESP dust micro-pellet test.

7.3.2.1 Thermocouple 1

As previously mentioned, across all tests the behaviour of the flame front at thermocouple 1 is varied, with the 10% ESP dust test appearing to be the biggest outlier, shown in Figure 7.4.2. The average peak temperature reached at thermocouple 1 is 1058.3 °C, compared to an average of 1121.8 °C observed in the BOS slurry addition tests and 1006.3 °C recorded in the base blend. The average temperature is 159.6 °C, slightly higher than the 152.6 °C seen in the BOS slurry tests. However, both are significantly higher than the 107.2 °C recorded in base blend testing. Time above 1000 °C averages to 43.75 s in the ESP dust tests compared to 38.3 s in the BOS slurry addition tests, both significantly surpassing the 10 s seen in the base blend. The lowest average cooling rate of 175.3 °C/min is seen in the ESP dust addition tests, slower than the 233.1 °C/min and 275.6 °C/min in the BOS slurry tests and base blend, respectively.

More detailed analysis of the peak temperatures at thermocouple 1 across the ESP dust addition tests highlights interesting results. Both the 10 % ESP dust and 10 % WESP dust tests reach the highest and similar temperatures, 1142.1 °C and 1146.8 °C, respectively. The next highest peak temperature is that of the 10 % ESP dust micro-pellet test with a reading of 1027.7 °C, followed by the 10 % WESP micro-pellet test which surprisingly fails to reach 1000 °C, only peaking at 916.6 °C. This means there is a 230.1 °C, or 25.1 %, difference between the lowest and highest peak temperature values.

In terms of average temperature during sintering the 10 % ESP dust test has by far the highest value of 229.4 °C. This value appears to be skewed by the slow frame front. This is followed by the 10 % ESP micro-pellet test with 155.1 °C. Surprisingly, the 10 % WESP dust only has an average sintering temperature of 140.0 °C. Considering it nearly has the highest

peak temperatures, this indicates a faster overall burn, shown by the rapid drop from its peak temperature in Figure 7.4.3. The 10 % WESP micro-pellet test again has the lowest average temperature of 113.9 °C, meaning the ESP dust test has an average temperature over double that of the WESP micro-pellet test.

The trend of the 10 % ESP dust and 10 % WESP dust micro-pellet tests being highest and lowest respectively continued in both the time above 1000 °C and the cooling rate analysis. The ESP dust test is above 1000 °C for 120 s, compared to 0 s in the WESP micro-pellet test. By comparison, the WESP dust test has the second longest time over 1000 °C at 40 s, followed by the ESP micro-pellet test with 15 s. The slowest cooling rate of 99.3 °C/min is seen in the 10 % ESP dust test, in line with its slowest overall test time. The 10 % WESP micro-pellet test has the next slowest cooling rate of 163.2 °C/min, while the ESP micro-pellet and WESP dust test has similar cooling rates of 218.3 °C/min and 220.2 °C/min, respectively.

The slow start in terms of heating in both the ESP and WESP micro-pellet tests is an observation mirrored by the BOS slurry micro-pellet test, seen in Figure 7.3.4. This suggests that, despite aiding permeability, the presence of micro-pellets hinders sintering propagation, at least initially, and despite the chemical difference between the micro-pellets. The ESP dust test's slower flame front is something not seen in the WESP dust test, implying that the water washing process has removed something from the dust that inhibits combustion.

7.3.2.2 Thermocouple 2

As the flame front progresses to thermocouple 2, the data shows that the average peak temperature rises by 83.1 °C from thermocouple 1 to 1141.4 °C. This would be expected due to flame front propagation. When compared to the average peak temperature of BOS slurry addition tests at this stage, the ESP/WESP dust addition test's peak temperature average is found to be 103.8 °C lower. Average temperature during sintering across all tests averaged 208.0 °C, a significant increase of 30.3 % from the previous thermocouple's average. However, as with average peak temperature, this is still 21.4 % lower when compared to the BOS slurry addition tests, which recorded 264.7 °C at thermocouple 2.

As with the previous two parameters, the average time above 1000 °C increases when compared to thermocouple 1, rising 62.9 % to 71.3 s. The BOS slurry addition tests recorded an average time above 1000 °C of 123.3 s, which is 71.2 % higher than the ESP/WESP

addition average at the same stage. The average cooling rate decreases from 175.3 °C/min to 95.6 °C/min between thermocouples 1 and 2 in the ESP/WESP addition tests. The BOS slurry cooling rate at this stage is 66.41 % higher at 144.0 °C/min.

The peak temperature of the 10 % ESP dust test falls by 1.8 % and the 10 % WESP dust test falls by 2.9 %, to 1122.0 °C and 1113.5 °C, respectively. By comparison, the ESP dust micro-pellet test only rises by 4.4 % to 1073.0 °C. The WESP micro-pellet test however rises by 37.2 % to 1257.2 °C, rising from the lowest peak temperature at thermocouple 1 to become the highest at thermocouple 2. However, this is still 83.94 °C lower than the highest peak temperature from the BOS slurry addition tests at the same stage.

All the tests' average temperatures rise when compared to thermocouple 1, excluding the 10 % ESP dust test which decreases by 12.5 % to 200.9 °C. The highest average temperature, and largest increase of 135.6 %, is seen in the WESP micro-pellet test which reaches 268.4 °C. This large increase is due to the surprisingly low temperatures seen at thermocouple 1 during this test, further supporting the idea that micro-pellets cause a slower ignition, which is also observed in the BOS slurry micro-pellet and ESP micro-pellet tests. The second highest rise is 72.5 % taking the 10 % WESP dust test to 241.6 °C which is followed by the ESP dust micro-pellet test which rises by 42.6 % to 221.2 °C. As with peak temperature, the highest average temperature at thermocouple 2 does not exceed the highest seen in the BOS slurry tests, and only the WESP micro-pellet test exceeds the base blends value of 253.0 °C.

At thermocouple 2, the WESP micro-pellet test again has the largest increase and final value when analysing the time above 1000 °C, reaching 120 s which is up from 0 s at thermocouple 1. As can be seen in Figure 7.4.2, the ESP dust test clearly has a decline in its time above 1000 °C from 120 s to 70 s. Both the ESP micro-pellet and the WESP dust tests see steady increases, rising from 15 s to 35s and 40 s to 60 s, respectively. Cooling rates become slower in every ESP/WESP addition test at thermocouple 2. The biggest decrease is in the ESP micro-pellet test, slowing from 218.3 °C/min to 99.3 °C/min. The average decline in the other 3 ESP/WESP tests is 38.9 %, ESP dust reaching 73.0 °C/min, WESP dust 109.6 °C/min and 100.6 °C for the WESP micro-pellet test.

Both tests featuring 10 % or ESP or WESP appear to show minimal development from thermocouple 1 to 2, although the WESP dust test is still sintering faster. The WESP micro-pellet test's thermal profile shows significant development however, resembling the

performance of the BOS slurry micro-pellet shown in Figure 7.3.4. Despite showing some development from the slow start recorded at thermocouple 1, the ESP dust micro-pellet test does not see rises in peak or average temperature as seen in other micro-pellet tests.

7.3.2.3 Thermocouple 4

Once the tests progress to thermocouple 4, average peak temperature in the ESP/WESP tests at thermocouple 4 was up 9.3 % on that of thermocouple 2 to 1247.1 °C. However, this is still 6.8 % below the levels reached in the BOS addition tests at the same point. The average temperature throughout the sintering at thermocouple 4 during the ESP/WESP addition tests is 243.7 °C, up 17.2 % from the previous thermocouple but still 14.7 % below the comparable BOS slurry addition value.

Time above 1000 °C is much less variable compared to the previous thermocouple, the range dropping from 85 s at thermocouple 2 to 30 s in thermocouple 4. The average time also rises 86.0% to 132.5 s, whereas the average across the BOS slurry addition tests at this point only reachesd117.5 s. Average cooling rate rises 54.1 % to 154.1 °C/min, which is very similar to the average of 152.7 °C/min recorded in the BOS slurry addition tests.

Both tests featuring the ESP and WESP micro-pellets have the highest peak temperatures at thermocouple 4, the 10 % WESP micro-pellet dust test peaking at 1326.0 °C and the 10 % ESP dust reaching 1234.9 °C compared to the 1219.5 °C and 1208.2 °C recorded in the WESP dust and ESP dust tests, respectively. Although the WESP micro-pellet test has the highest peak temperature, as is observed at thermocouple 2, it only rises by approximately 5.5 % from the previous thermocouple. This is the smallest percentage increase among all tests at thermocouple 4, the largest being approximately 15 % in the ESP micro-pellet test.

Average temperature values at thermocouple 4 vary somewhat between tests although there are some interesting features. Both the ESP dust and the ESP dust micro-pellet tests see increases of approximately 16.0 % and 17.7 % to 233.8 and 260.4 °C, respectively. By comparison, the tests featuring WESP dust and WESP dust micro-pellets both decline slightly by approximately 4.0% and 7.4% to 232.0 and 248.7 °C, respectively.

The WESP micro-pellet test again has the most time above 1000 °C, which at 150 s is up by 25 % on the previous thermocouple. The lowest value of 120 s is recorded in both the

ESP dust micro-pellet test and the WESP dust tests. However, for the ESP dust micro-pellet test this does represent the biggest increase of 243% between thermocouples 2 & 4. Cooling rates increase by at least 40 °C/min in every test at thermocouple 4. The most significant rise is recorded in the ESP dust micro-pellet test which rises by 80.9 °C/min to 180.1 °C/min. The ESP dust test shows the smallest change, only rising by 42.3°C/min to 115.4 °C/min.

7.3.2.4 Thermocouple 5

The final thermocouple's average peak temperature across the ESP/WESP addition tests is up 44.3 °C to 1291.4 °C, when compared to the average of thermocouple 4. However, this is still lower than the average of the same point from the BOS slurry addition tests which was 1320.4 °C. The average temperature at this point however drops from 243.7 °C at thermocouple 4 to 218.6 °C at thermocouple 5. Again, this does not exceed the values of the BOS slurry testing at this stage, averaging 249.9 °C, making the average temperature in the BOS slurry addition tests 14.4 % higher.

The average time above 1000 °C is approximately 105 s at thermocouple 5, making it 5 seconds longer than the BOS slurry testing at this stage. However, this does represent an approximate decline of 21.0 % when compared to thermocouple 4, which averaged 132.5 s above 1000 °C. The cooling rate slightly increases from 154.1 °C/min at thermocouple 4 to 159.0 °C/min at thermocouple 5. This is still 15.5 °C/min lower than the average cooling rate recorded at the fifth thermocouple during the BOS slurry addition testing. Declining average temperatures and time above 1000 °C alongside hastening cooling rates demonstrate that the sintering process is nearing its end.

As previously mentioned, the average peak temperature rises from thermocouple 4, with only the ESP dust micro-pellet test recording a peak below 1300 °C, that being 1218.5 °C. The other three tests are all within 21.5 °C of each other. The ESP dust test reaches 1327.8 °C, the highest peak temperature of the suite at thermocouple 5. WESP dust peaks at 1306.3 °C and similarly the WESP dust micro-pellet test recorded 1313.0 °C. Interestingly, both the ESP dust and WESP dust tests show increases in peak temperatures from thermocouple 4 whereas both tests featuring micro-pellets began to slightly decrease. Rises of 9.9 % and 7.1% in the ESP dust and WESP dust tests respectively can be contrasted by negligible declines of 1.3% in ESP dust micro-pellet and 1.0% WESP dust micro-pellet tests.

Analysis of average temperature across the tests at thermocouple 5 shows that each test sees a decline compared to the previous thermocouple. However, the WESP dust micro-pellet test's decline is much less significant than the other 3 tests. At thermocouple 4 the average test temperatures are tightly distributed, being within 28.3 °C of each other and with a standard deviation of just 13.4 °C. However, at thermocouple 5 both the range and standard deviation nearly double to 48.0 °C and 22.4 °C, respectively. This is due to the fact that the WESP dust micro-pellet test only declines by 5.1% to 236.2 °C, compared to 19.5% in the ESP dust test to 188.2°C, 19.6% to 209.3 °C in the ESP dust micro-pellet test and 18.4% in the WESP dust test to 189.5 °C. This also highlights higher average temperatures in the tests featuring micro-pellets, a trend seen consistently from thermocouple 2 onwards.

Time above 1000 °C at thermocouple 5 drops in each test from the thermocouple 4 value in varying amounts. The two micro-pellet tests have the biggest drops, with the ESP dust micro-pellet falling to 70 s and the WESP dust micro-pellet reaching 115 s; declines of 41.7% and 23.3%, respectively. ESP dust micro-pellet clearly has the most significant drop overall, whereas the WESP dust test records 115 s which only represents a 4.2% drop from thermocouple 4. Cooling rates again highlight a potential difference between micro-pellets and dust fines. The ESP dust micro-pellet falls 22.4% to 139.8 °C/min and the WESP dust micro-pellet similarly falls by 24.1% to 112.8 °C/min. Conversely the ESP dust test rises by 32.9% to 153.5 °C/min and the WESP dust test increases by 33.5 % to 229.8 °C/min. This analysis indicates cooling rates increase during late stage sintering when using dust fines and slow down when using micro-pellets.

7.3.3 ESP/WESP Addition Hot Permeability

The most obvious observations from Figure 7.4.6 are the difference in total length of tests and significant variation in permeability between tests. The 10 % ESP micro-pellet test is the fastest as it is completed in 20 min 5 s, compared to the longest test which was the 10 % ESP dust test which lasts 33 min 20 s. A slow moving flame front can be a negative from a production point of view, as it could severely reduce sinter yield requiring the use of more expensive blast furnace feed alternatives such as externally supplied iron ore pellets. Too fast a flame front can also be a negative as it may not allow enough time for effective agglomeration and result in a weak sinter. This variance in sintering times will be considered when discussing further analysis such as sinter particle size distribution.

The ESP micro-pellet test also has the highest peak air flow rate of 42.1 m^3/h, just above the WESP micro-pellet which peaks at 39.4 m^3/h, whereas the two lowest peak flow rates belonged to the ESP dust and WESP dust tests, peaking at 24.3 m^3/h and 26.2 m^3/h, respectively. This trend is replicated in the average airflow during the tests. This time the WESP MP came out slightly on top with 21.5 m^3/h compared to 20.8 m^3/h in the ESP MP test. Again, the lowest averages of 10.5 m^3/h and 12.4 m^3/h belong to the ESP dust and WESP dust tests, respectively.

Poor permeability is associated with negative impacts on the sintering process as gases struggle to be drawn through the bed which aid combustion. The flame front is also drawn through the bed in the same way. The inclusion of micro-pellets instead of fines results in more nuclei-sized particles which fines can agglomerate around during the wet granulation process prior to sintering. If fines cannot bind to a nuclei site, they will agglomerate via coalescence Figure 2.7, examples of this in samples tested can be seen in Figure 7.11. Images A1 and A2 show agglomeration around a WESP micro-pellet compared to images B1 and B2 which shows the coalescence of fines from the ESP dust test. In image, A1 the variety of finer particles on the surface are clear and A2 better shows this pattern around the particle's edges. By comparison, in B1 we see the coalesced fine materials in a more sporadic shape and the same particles are shown in B2 after some slightly pressure was applied with a spatula. The PSD ratios are 0.94 and 0.97 for the ESP dust and WESP dust tests respectively, compared to 1.55 and 1.46 for the ESP micro-pellet and WESP micro-pellet tests respectively, also shown in Figure 7.1. This implies more effective granulation likely occurred in the micro-pellet tests which would have improved permeability of the blends.

7.3.4 ESP Addition Conclusions

The cold permeability testing provided the first evidence that the addition of the micro-pellets was beneficial to the air flow in the sinter blend. The addition of the unprocessed ESP and WESP dust did not have a clear impact on the cold permeability as may be expected. During sintering however, the blends featuring the unprocessed fine ESP/WESP dust recorded the two lowest average air flow rates, the 10 % ESP dust blend having lowest average flow and longest test time. This test time likely caused by the fines hindering the air flow and therefore slowing the flame front propagation through the bed.

The sintering process itself was stable in all tests but there was variance in temperatures. The micro-pellet tests had higher average temperatures than the blends featuring dusts however initial temperatures at thermocouple 1 appeared low, perhaps caused by the increased air flow moving the flame front past the thermocouple too quickly before it has a chance to fully develop. These results indicate micro-pelletisation of reverts is far superior to fine dust addition in sintering tests in terms of permeability during airflow.

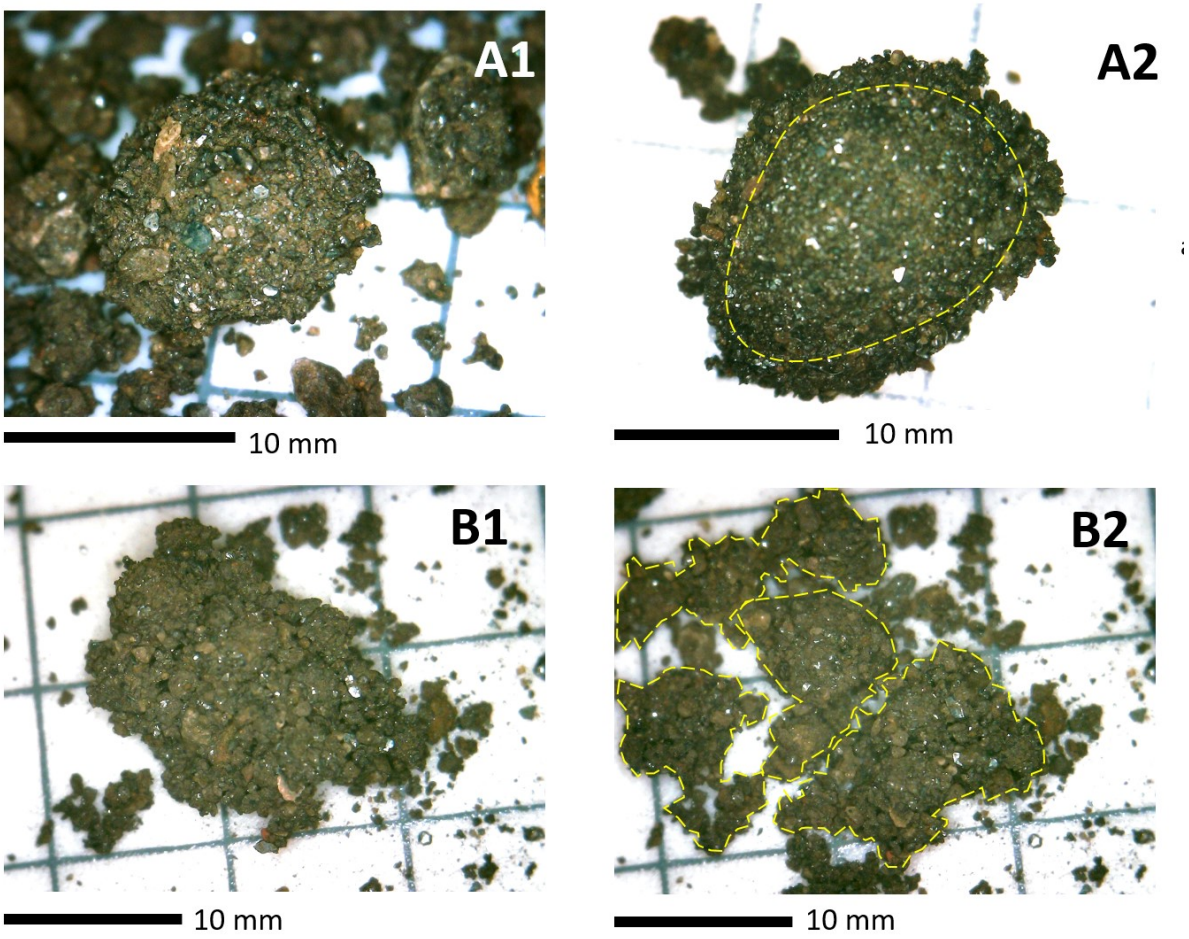

Figure 7.11 Optical microscopy showing examples of granulation around a nuclei particle (A1, A2), fines coalescence (B1) and the breakdown of coalesced fines under slight pressure (B2).

7.4 Gas Emission Temperature Analysis

Generally, all the gas emission temperature profiles in Figure 7.4.8 follow the same trend. A slow and gentle rise in temperature towards 50 °C before a sharp inflection to toward the peak temperature, which varied between 423.4 °C (10 % ESP dust micro-pellet) – 658.2 °C (10% BOS Slurry micro-pellet), which was then followed by a decline until the end of the testing. This sharp inflection appears to be associated with the point where the flame front is approaching thermocouple 5 in the sinter pot testing and the rise in gas permeability also sharply rises upwards. As mentioned in section 7.3.3, due to this being late in the sintering test most of the material will have been sintered which leads to more void space enabling higher gas flows. The fastest test to reach its peak exhaust gas temperature of 423.4 °C is the 10% ESP dust micro-pellet test in just 13 min and 5 s, whereas the 10 % ESP dust test took 25 min and 40 s to reach its peak temperature of 488.1°C.

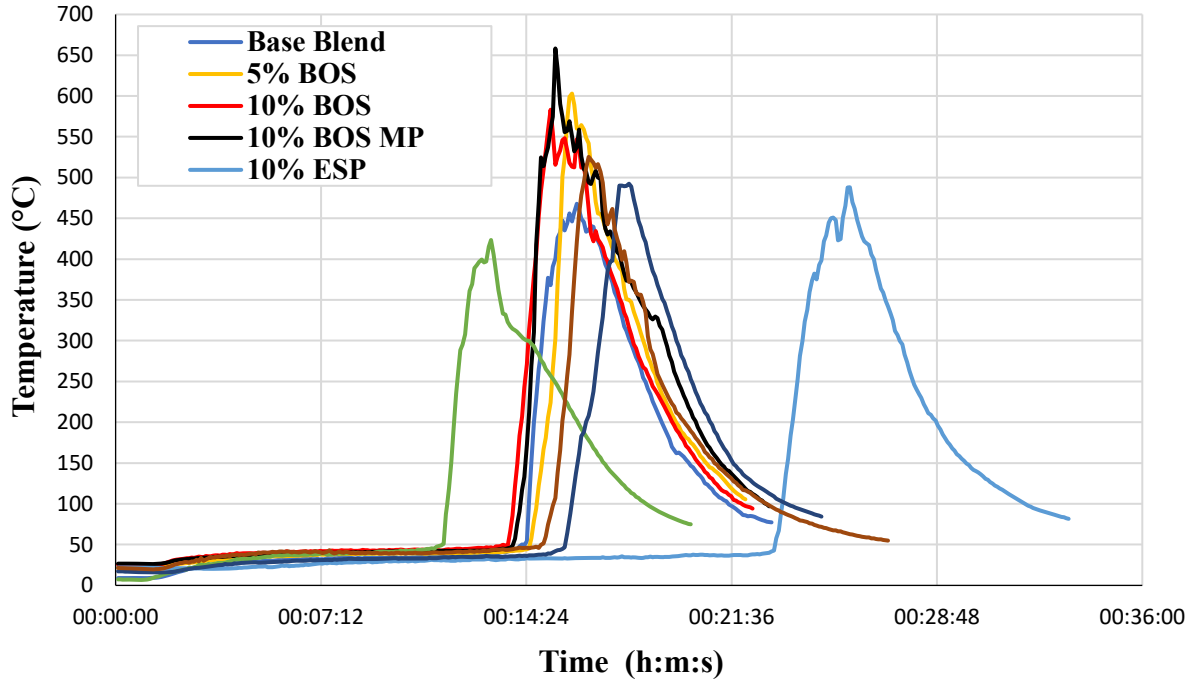

Figure 7.12 Waste gas temperature profiles from all sintering tests.

Although having similar peak gas temperatures, the sintering temperature at thermocouple 5 at the same point varies dramatically. For example, the test featuring 10 % ESP dust only measures 424.6°C compared to 937.9°C in the ESP dust micro-pellet test, highlighting the significant difference in sintering parameters between the two tests. The 10 % ESP dust gas temperature profile also has the lowest average temperature during the test, averaging just

92.5°C, compared to a high of 147.3°C average in the 10 % BOS slurry test. When analysing the data based on material being added, this highlights that the BOS slurry tests have the highest average gas emission temperature of 134.2 °C, compared to ESP dust with 100.9 °C and WESP dust addition with 104.6 °.

7.5 Post Analysis

7.5.1 Sinter Particle Size Analysis

The results of sizing after mechanical sieving are shown in Figure 7.13. With strength of sinter being an important factor for industry, these results reveal how the change in reverts utilised can impact the particle size distribution of sinter.

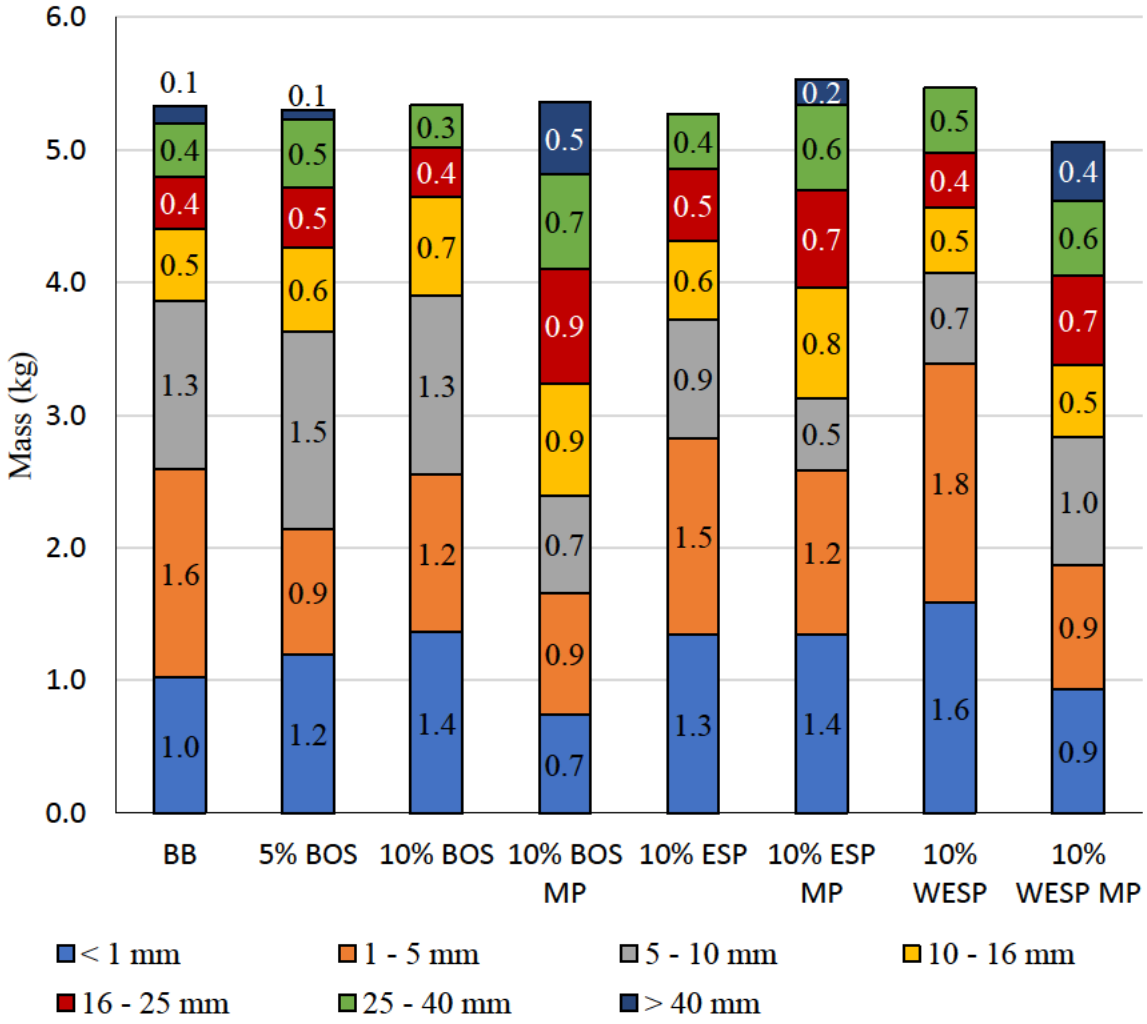

Figure 7.13 Stacked bar chart showing particle size distribution of sinter produced.

During industrial operation, after sintering on a sinter strand, the sinter is broken up using a crusher before being screened. Undersize material can be reused in the sintering process to reduce ore rates, but oversize sinter will have to be crushed until it is a suitable size. The number of fines (< 1 mm) produced is also related to the strength and can be a negative as the sinter will undergo abrasion during transport and furnace loading. If the sinter readily breaks

down in the furnace or during transport this can reduce furnace permeability and cause hot metal production issues.

The results indicate that the most fines originate from the 10 % WESP dust sinter, where they constitute 1.6 kg or 29 % of the total sinter. In total 62.1 % of this sinter was < 5 mm after being mechanically sieved. By comparison, the BOS micro-pellet sinter contains only 31.0 % of the sinter broken down to < 5 mm after sieving. The presence of > 40 mm sinter, whilst not the most desirable sizing, does indicate good sinter strength and notably there is no sinter > 40 mm produced from the 10 % BOS slurry fines, 10 % ESP dust and 10 % WESP dust sinters, whilst only 0.1 kg arises from the base blend sinter and the 5 % BOS slurry fines sinter. The two sinters that produced the most > 40 mm sinter particles after sieving are the WESP micro-pellet sinter and the BOS slurry micro-pellet sinter, this being 0.4 kg and 0.5 kg respectively. In summary, these findings appear to show that the addition of micro-pellets to sinter blends is beneficial to sinter strength, compared to adding the same volume of reverts in their raw fines form.

7.5.2 Sinter Chemistry

Sinter samples were submitted to Tata Steel UK laboratories for chemical XRF analysis after sieving, as is standard procedure, the results are shown in Table 7.1.

Sinter chemistry analysis showed similarities between all samples in terms of their basicity as they ranged between 1.5 – 1.7. Total iron content ranged between 53.25 – 56.71 % and there was much less variation between Fe phases compared to the sinter produced in the previous chapter. FeO ranging between 2.94 % in the 10 % BOS slurry micro-pellet test and a maximum of 4.77 % in the 10 % BOS slurry fines sinter. Fe2O3 was highest in the 10 % BOS slurry micro-pellet test with 77.83 % with the lowest value being 72.47 % in the 10 % ESP dust micro-pellet test. A notable point is the zinc level throughout the sinters. Whilst between 0.007 – 0.009 in the base blend, ESP/WESP dust and ESP micro-pellet tests a step up to 0.012 in the 10 % BOS slurry test and a further rise to 0.042 in the 10 % BOS slurry micro-pellet sinter. Suggesting that by micro-pelletising BOS slurry Zn becomes trapped within the sinter, whereas if sintered as a fine material it is more likely to be released in a dust form.

Table 7.1 Summary of sinter chemistry from XRF analysis. WESP micro-pellet sinter sample was lost during transport.

	Base Blend	10% ESP	10% WESP	10% ESP MP	10% BOS	10% BOS MP
SiO2	5.53	4.99	4.97	5.64	5.55	5.63
Al2O3	0.98	0.86	0.83	1.12	1.01	1.02
TiO2	0.06	0.09	0.07	0.11	0.07	0.12
CaO	9.61	7.93	8.14	8.44	8.95	9.09
MgO	2.25	2.01	1.98	1.86	2.3	2.26
Fe	54.35	54.88	54.69	53.25	55.96	56.71
Fe2O3	72.96	74.51	74.78	72.47	74.72	77.83
FeO	4.28	3.57	3.08	3.31	4.77	2.94
P	0.029	0.016	0.016	0.028	0.027	0.03
Mn	0.14	0.17	0.18	0.16	0.15	0.19
Na2O	0.051	0.054	0.04	0.037	0.102	0.052
K2O	0.051	0.078	0.08	0.082	0.046	0.052
Zn	0.007	0.008	0.007	0.009	**0.012**	**0.042**
Cu	0.001	0.002	0.002	0.001	0.001	0.002
Cl	0	0.001	0.001	0.001	0	0.001
C	0.218	0.155	0.144	0.211	0.196	0.188
S	0.001	0.002	0.002	0.003	0.004	0.001

7.5.3 Particulate Emissions

During the sintering process, fine particles are carried by gas streams to wind mains before an abatement technique, such as electrostatic precipitators, wet scrubbers, or bag filters, is used to arrest the dust from the gas stream before it is emitted to the atmosphere. Minimising dust production during sintering therefore puts less strain on these abatement systems and is also desirable as regulations become stricter. A simple dust capture device was installed on the sinter pot system at Tata Steel UK to catch particulates, aiming to see variation in dust produced and to allow sampling. Figure 7.5.2 shows the difference in total mass of dust collected during each sintering test.

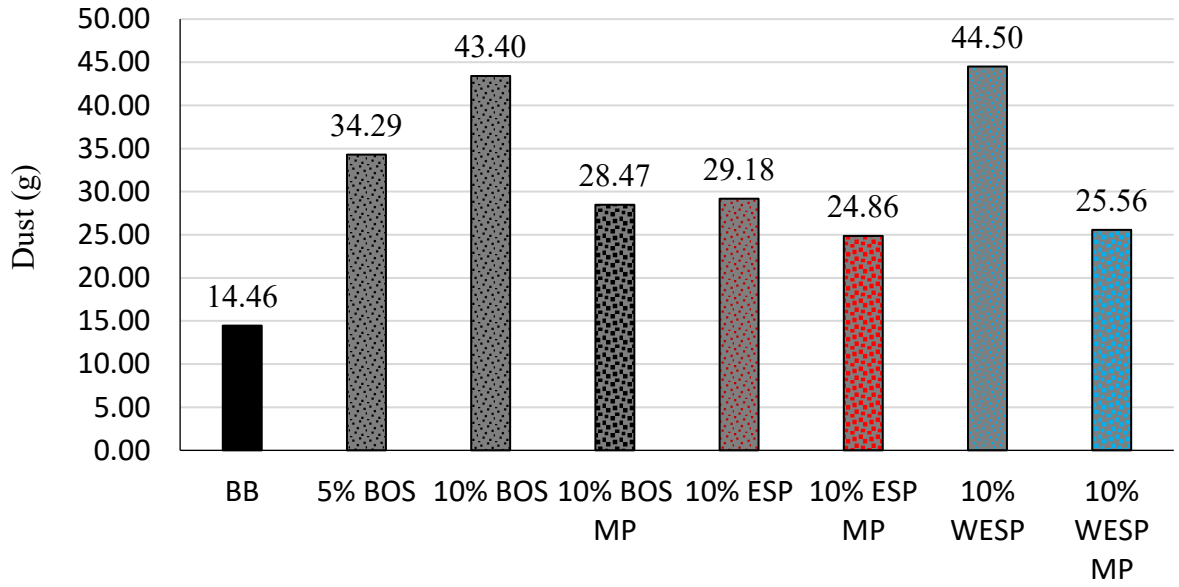

Figure 7.14 Bar chart showing variation in the mass of dust produced during sintering experiments.

At a glance it is clear that the two samples with the most dust collected are seen in the 10 % WESP dust and 10 % BOS dust sinter tests with 43.5 g and 43.4 g, respectively. The base blend records the lowest dust at 4.5 g, suggesting that the addition of reverts, even when micro-pelletised, does lead to higher dust emissions during sintering although including them as fines does result in more dust compared to the micro-pellet form.

Interestingly pelletisation of the ESP dust does not appear to be as effective compared to the other micro-pellet results. This is potentially linked to that experiment's relatively poor sintering performance and sinter particle size distribution testing also indicating more fines compared to other micro-pelletised samples.

One experiment was carried out on a filter paper from the 10 % BOS slurry test using SEM EDS to image the filter and gain an idea of the chemistry of material that would otherwise have been emitted. The results are shown in Figure 7.15 and highlight many particles < 100 µm of varying chemistry, such as Ba, Na, K, Fe, Zn, and Cl, which would have otherwise been emitted. The high wt% of O and Si is owing to this composition of the filter paper. Going forward this could be a good means of analysis to better understand finer dust emissions and how changing sinter blends can impact them.

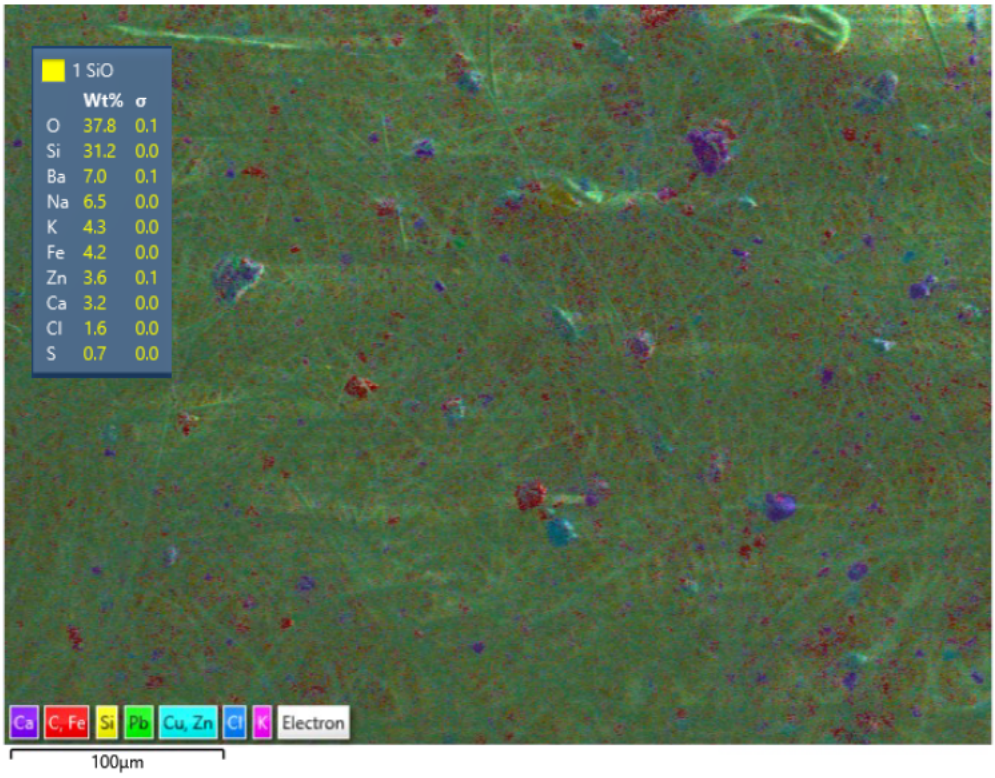

Figure 7.15 SEM EDS image of a filter paper used during 10% BOS slurry sinter pot testing which highlights fine dust particles arrested from gas stream.

7.6 Conclusions

This chapter aimed to build on the previous by investigating the use of micro-pellets made exclusively from reverts with no ores mixed in. After discussions with Tata Steel staff, the maximum content of materials was increased from 7.0 % in Chapter 6 to 10.0 % to confirm if the same detrimental impacts would be seen from high micro-pellet usage. Another revert, BOS slurry, was also included to allow comparison and identify any benefits from using a carbon rich revert.

Generally the same benefits from using micro-pellets compared to equivalent levels of unprocessed fine materials were seen. The impact of micro-pellets on cold permeability airflow was less pronounced compared to the blend tested in Chapter 6 although the hot permeability measurements during sintering tests still indicated higher airflow rates and flame fronts. The difference was less pronounced in the BOS slurry tests although this is likely due to the higher fuel rate. Sintering itself was generally much more stable overall, the 10.0 % BOS slurry blend however displayed a very erratic profile. The higher proportion of carbon may not have distributed itself evenly during granulation and, combined with the lower PSD, this could have contributed to and uneven flame front. Both the 10.0 % ESP dust and WESP dust micro-pellet blends produced stable thermal profiles however the ESP micro-pellet blend was approximately 7 minutes faster.

As expected the additional carbon provided by the BOS slurry resulted in higher peak and average temperatures across all thermocouples in those tests compared to the ESP dust and WESP dust tests. The average peak temperatures being 1257 °C, 1169 °C and 1199 °C respectively and the average temperatures being 239 °C, 212 °C and 209 °C respectively. If operating conditions allow this would mean that the fuel rate of blends can be reduced and offset by BOS slurry usage.

More comprehensive particulate emission data was available for these tests and supported observations from the previous Chapter. Across all fine materials and their micro-pelletised equivalent, and average decline of 31 % was seen in particulate emissions. The post mechanical sieving data also followed observations from Chapter 6, with a greater proportion of sinter from the micro-pellet tests falling in the 10-40 mm range compared to the fine material sinters, 2.13 kg compared to 1.43 kg respectively. These are lower than the blends tested in the previous chapter but it must be assumed that this blend was coherently weaker by design as there was a much more significant 0-10 mm fraction across all tests. The > 40

mm sinter was again predominantly only seen in the micro-pellet tests, with ~ 0.1 kg also recorded in the base blend and the 5.0 % BOS slurry blend sinters.

Though some variation compared to results seen in Chapter 6 it has to be remembered that these were fundamentally different blend compositions and therefore variation was to be expected. The results do show that the link between micro-pellet usage and sintering speed/stability is not as linear as the previous chapter suggested. Generally, the use of micro-pellets does appear to support optimal sintering conditions, less dust emissions and stronger sinter. Perhaps this is not a strictly uniform relationship however, with factors such as specific blend composition/PSD and ensuring high quality granulation playing a key role in the maximum level of micro-pellets that can be included in sinter blends.

Table 7.2 From top; Summary of peak temperatures, summary of average temperatures, summary of time spent above 1000 °C (rounded to nearest 5 s interval and summary of cooling rates from sinter pot testing.

Maximum T	TC1 (°C)	TC2 (°C)	TC3 (°C)	TC4 (°C)	TC5 (°C)
BB	**1006.3**	**1162.4**	**1237.1**	**1131.6**	
10% ESP	1142.1	1122.0		1208.2	1327.8
10% ESP MP	1027.7	1073.0		1234.9	1218.5
10% WESP	1146.8	1113.5		1219.5	1306.3
10% WESP MP	916.6	1257.2		1326.0	1313.0
5% BOS	1041.9	1226.0		1288.9	1314.3
10% BOS	1201.8	1168.5		1383.3	1287.6
10% BOS MP	1121.8	1341.2		1343.4	1359.3

Average T	TC1 (°C)	TC2 (°C)	TC3 (°C)	TC4 (°C)	TC5 (°C)
BB	**107.2**	**253.0**	**243.6**	**239.5**	
10% ESP	229.4	200.9		233.8	188.2
10% ESP MP	155.1	221.2		260.4	209.3
10% WESP	140.0	241.6		232.0	189.5
10% WESP MP	113.9	268.4		248.7	236.2
5% BOS	139.0	231.7		270.4	223.8
10% BOS	137.2	272.2		315.0	279.3
10% BOS MP	181.7	290.2		272.3	246.6

T > 1000 °C	TC1 (s)	TC2 (s)	TC3 (s)	TC4 (s)	TC5 (s)
BB	**10**	**80**	**90**	**70**	
10% ESP	120	70		140	120
10% ESP MP	15	35		120	70
10% WESP	40	60		120	115
10% WESP MP	0	120		150	115
5% BOS	25	90		135	120
10% BOS	40	160		140	80
10% BOS MP	50	120		125	100

Cooling Rate	TC1 (°C/min)	TC2 (°C/min)	TC3 (°C/min)	TC4 (°C/min)	TC5 (°C/min)
BB	**275.6**	**118.3**	**138.7**	**117.2**	
10% ESP	99.3	73.0		115.4	153.5
10% ESP MP	218.3	99.3		180.1	139.8
10% WESP	220.2	109.6		172.2	229.8
10% WESP MP	163.2	100.6		148.6	112.8
5% BOS	235.5	155.2		163.3	231.3
10% BOS	293.6	152.7		160.4	144.0
10% BOS MP	170.3	124.1		134.4	148.2

8. CONCLUSIONS & RECOMMENDATIONS FOR FUTURE WORK

8.1 Conclusions & Discussion

This research project aimed to optimise the environmental performance of iron ore sinter plants by building on previous work, with a focus on developing the remediation and recycling of sinter plant ESP dusts.

A detailed literature review was carried out initially to establish the current landscape of research in the field. This showed that water washing was an effective method of ESP dust washing to mobilise chlorides and that at least one surfactant had been used to improve this process. Some work had also been carried out investigating the impacts of recycling ESP dust to the sintering process. These highlighted areas of interest which were either underrepresented or had not been previously investigated.

A comprehensive set of testing was carried out focusing on the water washing of ESP dust and how it could be optimised in a variety of ways. Initial work confirmed literature findings before more novel experiments were undertaken. Once confirmed that 95 % of soluble chloride could be mobilised in one washing cycle, experiments focused on recycling washing solutions to wash more dust. This proved successful over 5 cycles initially before being extended to 10 cycles, though still effective a decline in chloride mobilisation was noted from approximately 7 cycles onwards. Analysis of washing solutions also showed that rubidium also continually amassed in the washing solution during recycling, potentially providing more effective recovery due to its higher concentrations.

A variety of surfactants were trialled whilst recycling ESP dust washing solutions, with concentration and washing parameters being varied to assess their impact. All were found to reduce ESP dust hydrophobicity and improve the handleability of the dust during washing. There was also evidence showing that the presence of surfactants aided chloride mobilisation during washing.

Water contact angle analysis of the surfactants used in ESP dust washing tests was also carried out on ESP dust samples. It was shown that liquid marbles would form on ESP dust, indicating highly hydrophobic material, but after washing this phenomenon was not observed. A droplet of water can sit on a bed of ESP dust for in excess of 10 minutes without

much reduction in contact angle, whereas once washed the WESP dust particles begin to 'scale' the droplet and the droplet would rapidly collapse. When surfactants were added to the droplets the rate of the drop in contact angle on a bed of ESP dust was significantly increased.

Sinter pot research was carried out using variations of two blends. Initially up to 5 % of ESP and WESP dust was included and a micro-pellet containing iron ores and reverts was tested up to a maximum of 7 % in the same blend. Impacts on permeability were noted as it increased with micro-pellet addition and decreased with the dust additions, likely owing to the impact on the blend particle size distributions and granulation. The sintering performance of the tests featuring the dusts was erratic compared to the base blend and micro-pellet blends. Suggesting high concentrations of ESP and WESP dusts are detrimental to sintering performance. The sinter produced from these tests suggested the micro-pellets aided production of stronger sinter, with particulate emission analysis also suggesting that the micro-pellets reduce dust emission.

Further sinter pot tests were carried out at a later date on a different blend. ESP and WESP dust concentrations were extended to 10.0 % both in fines and micro-pellet form and another revert, BOS slurry, was also tested to the same levels. The results showed no loss in sintering stability whilst increasing micro-pellet content beyond 7.0 %, suggesting that micro-pellet inclusion limits are dependent on each particular blend they are used in and should be determined as such. Positive improvements to sinter dust emissions and product sinter strength were again prevalent. Overall both studies suggest that higher levels of fine materials can be achieved by micro-pelletising the fines prior to sintering.

In summary this research suggests that recycling of sinter plant ESP dust washing solutions is an effective way to reduce water consumption, mobilise chlorides and concentrate elements in the solution for extraction or treatment. A range of surfactants were shown to aid this process. Addition of washed or unwashed ESP dust to the sintering process at high concentrations had detrimental impacts to the process itself and resultant sinter. However, micro-pelletisation of reverts prior to sintering appeared to offset these impacts and should be considered in future.

8.2 Recommendations for Future Work

Larger scale washing experiments would highlight any scaling issues of surfactant utilisation or recycling of washing solutions which should encourage the uptake of the methodology by industry. There is also scope for more surfactants to be trialled in the water washing of ESP dust but also other hydrophobic materials which require wetting for processing or remediation. Testing of environmentally friendly surfactants, such as soap nut saponin is encouraged to minimise environmental impacts of such research.

The recycling of ESP dust washing solutions was shown to concentrate soluble elements such as chloride and rubidium. This would make recovery of these elements more cost-effective and could be used to offset remediation costs.

Research carried out during this project further highlighted the ability of a range of surfactants to combat the hydrophobicity of sinter plant ESP dust. Further work could investigate how surfactants could be used to aid the agglomeration of hydrophobic ores or sinter blends. As iron ores can vary greatly in their wettability owing, to differing chemical or morphological features, the addition of surfactants to the granulation solution could reduce freshwater requirements.

Rubidium was seen to concentrate within the washing solution as it was recycled over washing cycles. This could provide potential to extract rubidium from recycled ESP dust washing solutions in future, if a viable method can be proven. This would help to offset the costs of industrial scale ESP dust washing. Research should be carried out into cost-effective rubidium recovery from recycled ESP dust washing solutions.

Further research into micro-pelletisation of reverts to optimise their sintering performance is recommended as this research showed promising results. Modelling or sinter pot testing investigating the optimal mixture of materials for micro-pelletisation should aid the sintering process and resultant sinter quality. This would also lead to higher revert usage rates, offsetting prime ore rates in sinter blends which saves the money in the long term.

Sinter pot trials with more staggered levels of revert addition. This work aimed to use extreme levels to highlight impacts, however future work could use smaller intervals between concentrations to observe if impacts are linear or not. This could identify a point where the benefits of utilising more revert materials, therefore reducing virgin iron ore consumption thus saving money, may be outweighed by negative impacts on the process or resultant sinter.

More focus on dust emission analysis would provide greater insight into how changes in sinter blends, and increasing revert material usage, impacts emissions. Initial experiment completed using SEM EDS in this work showed promising results.

Investigations into the impact of micro-pelletising zinc rich reverts, such as BOS slurry, to ascertain whether this causes retention of zinc in product sinter. This may be detrimental to the integrated works as a whole and may make micro-pelletisation of BOS slurry less favourable compared to BOS slurry fines. Work should look to further confirm this and establish mechanisms behind it.

Bibliography

1. World Steel Association. 2022 World Steel in Figures. 2022.
2. Remus R, Aguado-monsonet MA, Roudier S, Sancho LD. JRC REFERENCE REPORT Best Available Techniques (BAT) Reference Document for Iron and Steel Production (Integrated Pollution Prevention and Control). 2013.
3. Parry S. History of the Steel Industry in the Port Talbot Area 1900-1988. 2011;
4. Menad N, Tayibi H, Carcedo FG, Hernández A. Minimization methods for emissions generated from sinter strands: A review. J Clean Prod. 2006;14(8):740–7.
5. Gan M, Fan X, Chen X, Ji Z, Lv W, Wang Y, et al. Reduction of pollutant emission in iron ore sintering process by applying biomass fuels. ISIJ International. 2012;52(9):1574–8.
6. Anderson DR, Fisher R. Sources of dioxins in the United Kingdom : the steel industry and other sources. 2002;46:371–81.
7. Choi SD, Baek SY, Chang YS. Atmospheric levels and distribution of dioxin-like polychlorinated biphenyls (PCBs) and polybrominated diphenyl ethers (PBDEs) in the vicinity of an iron and steel making plant. Atmos Environ. 2008;42(10):2479–88.
8. Van Larebeke N, Hens L, Schepens P, Covaci A, Baeyens J, Everaert K, et al. The Belgian PCB and dioxin incident of January-June 1999: Exposure data and potential impact on health. Environ Health Perspect. 2001;109(3):265–73.
9. Ji Z, Huang B, Gan M, Fan X, Chen X, Zhang Y, et al. Insight into a novel technique to regulate the emission profile of hazardous PM2.5 during iron ore sintering process. Process Safety and Environmental Protection [Internet]. 2020;133:88–96. Available from: https://doi.org/10.1016/j.psep.2019.10.029
10. Peng C, Zhang F, Guo Z. Separation and Recovery of Potassium Chloride from Sintering Dust of Ironmaking Works. 2009;49(5):735–42.
11. F. Schorcht, I. Kourti, B.M. Scalet SR and LDS. Best Available Techniques (BAT) Reference Document for the Production of Cement , Lime and Magnesium Oxide. European Commission. 2013;
12. Xiong G, Li S, Chen S, Zhang X, Yao Q. Development of advanced electrostatic precipitation technologies for reducing PM2.5 emissions from coal-fired power plants. Proceedings of the Chinese Society of Electrical Engineering. 2015;35(9):2217–23.
13. Fisher R, Anderson DR, Wilson DT, Aries E, Hemfrey D, Fray TAT. EFFECT OF CHLORIDE ON THE FORMATION OF PCDD / Fs AND WHO-12 PCBs IN IRON ORE SINTERING Figure 1 : Schematic of a typical sinter. 2004;66(June):1116–23.
14. Peng C, Guo ZC, Zhang FL. Existing state of potassium chloride in agglomerated sintering dust and its water leaching kinetics. Transactions of Nonferrous Metals Society of China (English Edition). 2011;

15. Tang H, Zhao L, Sun W, Hu Y, Ji X, Han H, et al. Hydrometallurgy Extraction of rubidium from respirable sintering dust. Hydrometallurgy [Internet]. 2018;175(June 2017):144–9. Available from: https://doi.org/10.1016/j.hydromet.2017.11.003

16. Vehlow J. Air pollution control systems in WtE units: An overview. Waste Management. 2015;37:58–74.

17. Steel T, Plant P, Steel T, Plant S, Steel T. Characterisation of ESP Dust Sample from Sinter Plant. 2010;50(11):1719–21.

18. Nakano M, Hosotani Y, Kasai E. Observation of Behavior of Dioxins and Some Relating Elements in Iron Ore Sintering Bed by Quenching Pot Test. 2005;45(4):609–17.

19. Pei Y dong, Wu S li, Chen S guo, Zhao Z xing, An G, Cheng Z ming, et al. Sintering of solid waste generated In Iron and steel manufacturing process in Shougang Jingtang. Journal of Iron and Steel Research. 2017;24:697–704.

20. Gan M, Ji Z, Fan X, Chen X, Zhou Y, Wang G, et al. Clean recycle and utilization of hazardous iron-bearing waste in iron ore sintering process. J Hazard Mater. 2018;353(932):381–92.

21. Qie JM, Zhang CX, Shangguan FQ, Li XP, Zhou JC. Effect of Iron-Bearing By-products on the Emission of SO2 and NOx in the Iron Ore Sintering Process. Transactions of the Indian Institute of Metals [Internet]. 2020;73(1):35–45. Available from: https://doi.org/10.1007/s12666-019-01801-1

22. Chean T, Lu L. Chemosphere Formation and mitigation of PCDD / Fs in iron ore sintering. Chemosphere. 2011;85(3):291–9.

23. Aries E, Anderson DR, Fisher R, Fray TAT, Hemfrey D. PCDD / F and ‘“ Dioxin-like ”’ PCB emissions from iron ore sintering plants in the UK. 2006;65:1470–80.

24. Zhan G, Guo Z cheng. Water leaching kinetics and recovery of potassium salt from sintering dust. Transactions of Nonferrous Metals Society of China [Internet]. 2013;23(12):3770–9. Available from: http://dx.doi.org/10.1016/S1003-6326(13)62928-3

25. Tang HH, Sun W, Han HS. A novel method for comprehensive utilization of sintering dust. Transactions of Nonferrous Metals Society of China (English Edition). 2015;

26. Zhan G, Guo ZC. Preparation of potassium salt with joint production of spherical calcium carbonate from sintering dust. Transactions of Nonferrous Metals Society of China (English Edition). 2015;

27. Stec M, Słowik K, Iluk T, Czaplicki A. A pilot study for treatment and thickening of wastewater from sintering dust dechlorination. Proceedings of the 10th European Metallurgical Conference, EMC 2019. 2019;4:1417–30.

28. Young J, Reardon M. TATA STEEL EUROPE Revert Washing Trial Summary. 2018.

29. Chandler D. Two faces of water. Vol. 417, Nature. Nature Publishing Group; 2002. p. 491.

30. Tang H, Zhao L, Sun W, Hu Y, Han H. Surface characteristics and wettability enhancement of respirable sintering dust by nonionic surfactant. Colloids Surf A Physicochem Eng Asp [Internet]. 2016;509:323–33. Available from: http://dx.doi.org/10.1016/j.colsurfa.2016.09.041

31. Hapgood KP, Khanmohammadi B. Granulation of hydrophobic powders. Powder Technol. 2009;189(2):253–62.

32. Aussillous P, Quéré D. Liquid marbles. Nature. 2001;411(6840):924–7.

33. Jiang Y, Wang P, Liu R, Pei Y, Wu G. An Experimental Study on Wetting of Coal Dust by Surfactant Solution. 2020;

34. Fan T, Zhou G, Wang J. Preparation and characterization of a wetting-agglomeration-based hybrid coal dust suppressant. Process Safety and Environmental Protection. 2018 Jan 1;113:282–91.

35. Cybulski K, Malich B, Wieczorek A. Evaluation of the effectiveness of coal and mine dust wetting. Journal of Sustainable Mining. 2015 Jan 1;14(2):83–92.

36. Chu W, Chan KH. The mechanism of the surfactant-aided soil washing system for hydrophobic and partial hydrophobic organics. Vol. 307, The Science of the Total Environment. 2003.

37. Ugwu E, Sen Gupta B, Meza-Figueroa D, Razo Soto I. An investigation on the Lead Removal from Soil Contaminated by Mining and Industrial Wastes Using Soapnut in Batch Washing Process.

38. Chang J, Zhang ED, Zhang LB, Peng JH, Zhou JW, Srinivasakannan C, et al. A comparison of ultrasound-augmented and conventional leaching of silver from sintering dust using acidic thiourea. Ultrason Sonochem. 2017;

39. Tsubouchi N, Kuzuhara S, Kasai E, Hashimoto H, Ohtsuka Y. Properties of Dust Particles Sampled from Windboxes of an Iron Ore Sintering Plant: Surface Structures of Unburned Carbon. ISIJ International. 2006;46(7):1020–6.

40. Lanzerstorfer C. Mechanical properties of dust collected by dust separators in iron ore sinter plants. Environmental Technology (United Kingdom). 2015;36(24):3186–93.

41. Food and Agriculture Organisation of the United Nations. World fertilizer trends and outlook to 2022. 2019;

42. Jensen JT, Creinin MD. Family planning, population growth, and the environment. Contraception. 2020;101(3):145–7.

43. al Rawashdeh R, Maxwell P. Analysing the world potash industry. Resources Policy. 2014;41(1):143–51.

44. Lanzerstorfer C. Potential of industrial de-dusting residues as a source of potassium for fertilizer production – A mini review. Resour Conserv Recycl. 2019;143(September 2018):68–76.

45. Greenwood N, Earnshaw A. Chemistry of the Elements. 2nd ed. Oxford: Butterworth-Heinemann; 1999. 321 p.

46. United States Geological Survey. Rubidium - Mineral Commodity Summaries, January 2022. 2022.

47. Wagner FS. Kirk-Othmer encyclopedia of chemical technology: Rubidium and rubidium compounds. 4th ed. New York: Wiley & Sons; 1997. 591–600 p.

48. Xing P, Wang C, Chen Y, Ma B. Rubidium extraction from mineral and brine resources: A review. Hydrometallurgy [Internet]. 2021;203:105644. Available from: https://doi.org/10.1016/j.hydromet.2021.105644

49. Naidu G, Jeong S, Choi Y, Song MH, Oyunchuluun U, Vigneswaran S. Valuable rubidium extraction from potassium reduced seawater brine. 2017; Available from: https://doi.org/10.1016/j.jclepro.2017.11.042

50. Ball DF. Agglomeration of Iron Ores. Heinemann Educational Books, London. 1973.

51. Ratio M. Formation of Pores in Iron Ore Sinter * By Haruo KOKUBU ,** Takuma KODAMA ,** Hiroshi and Yukio OGUCHI ** proximated by vertical shrinkage and collapse of voids in sinter cake by crushing was estimated by comparing the void fraction of the sinter cake wit. 1986;(182).

52. Zandi M, Martinez-Pacheco M, Fray TAT. Biomass for iron ore sintering. Miner Eng. 2010;23(14):1139–45.

53. Yu Y, Zheng M, Li X, He X. Operating condition influences on PCDD/Fs emissions from sinter pot tests with hot flue gas recycling. Journal of Environmental Sciences. 2012;24(5):875–81.

54. Zhang G liang, Wu S li, Su B, Que Z gang, Hou C gang, Jiang Y. Influencing factor of sinter body strength and its effects on iron ore sintering indexes. International Journal of Minerals, Metallurgy and Materials. 2015;22(6):553–61.

55. Mao H, Zhang R, Lv X, Bai C, Huang X. Effect of Surface Properties of Iron Ores on their Granulation Behavior. ISIJ International [Internet]. 2013 [cited 2021 May 17];53(9):1491–6. Available from: http://dx.doi.org/10.2355/isijinternational.53.1491

56. MAEDA T, FUKUMOTO C, MATSUMURA T, NISHIOKA K, SHIMIZU M. Effect of Adding Moisture and Wettability on Granulation of Iron Ore. ISIJ International. 2005;45(4):477–84.

57. Gan M, Fan XH, Ji ZY, Chen XL, Yin L, Jiang T, et al. Ironmaking & Steelmaking Processes, Products and Applications Optimising method for improving granulation effectiveness of iron ore sintering mixture Optimising method for improving granulation effectiveness of iron ore sintering mixture. 2014 [cited 2021 Jun 28]; Available from: https://doi.org/10.1179/1743281214Y.0000000237

58. Iveson SM, Litster JD, Hapgood K, Ennis BJ. Nucleation, growth and breakage phenomena in agitated wet granulation processes: A review. Vol. 117, Powder Technology. Elsevier; 2001. p. 3–39.

59. Zhou H, Liu Z, Cheng M, Liu R, Cen K. Effect of flame-front speed on the pisolite-ore sintering process. Appl Therm Eng. 2015 Jan 22;75:307–14.

60. Ji Z, Zhang Y, Gan M, Fan X, Yuan X. Importance of intensive mixing on sintering with fine-grained iron ore materials: characterization and function mechanism [Internet]. Journal of materials research and technology. 2020 [cited 2021 May 17]. Available from: chrome-extension://dagcmkpagjlhakfdhnbomgmjdpkdklff/enhanced-reader.html?openApp&pdf=https%3A%2F%2Fpdf.sciencedirectassets.com%2F286905%2F1-s2.0-S2238785420X0007X%2F1-s2.0-S2238785420319037%2Fmain.pdf%3FX-Amz-Security-Token%3DIQoJb3JpZ2luX2VjEKn%252F%252F

61. Zhu J, Wu SL, Bei JC, Zhang GL, Zhai XB. Effects of particle characteristics on the granulation ability of iron ores during the sintering process. International Journal of Minerals, Metallurgy and Materials. 2015;22(9).

62. Charles-Williams H, Hounslow M, Wengeler R, Flore K, Feise H, Salman A. Granulation behaviour of increasingly hydrophobic mixtures [Internet]. Powder Technology. 2012 [cited 2021 May 17]. p. 64–76. Available from: https://pdf.sciencedirectassets.com/271376/1-s2.0-S0032591013X0004X/1-s2.0-S0032591012003968/main.pdf?X-Amz-Security-Token=IQoJb3JpZ2luX2VjELD%2F%2F%2F%2F%2F%2F%2F%2F%2F%2FwEaCXVzLWVhc3QtMSJHMEUCIQDB9F68WFzEdvd0RoZlwayCSYG8Q%2BRF8vJQoWQ4wNHydgIgM6hd4c3saj

63. Aulton M, Banks M. Influence of the hydrophobicity of the powder mix on fluidised bed granulation. In: International Conference on Powder Technology in Pharmacy. Basel; 1979.

64. Nyembwe AM, Cromarty RD, Garbers-Craig AM. Effect of concentrate and micropellet additions on iron ore sinter bed permeability. https://doi.org/101080/03719553320161180033 [Internet]. 2016 Jul 2 [cited 2023 Mar 25];125(3):178–86. Available from: https://www.tandfonline.com/doi/abs/10.1080/03719553.2016.1180033

65. Umadevi T, Karthik P, Mahapatra PC, Prabhu M, Ranjan M. Optimisation of FeO in iron ore sinter at JSW Steel Limited. http://dx.doi.org/101179/1743281211Y0000000080 [Internet]. 2013 Apr [cited 2023 Mar 25];39(3):180–9. Available from: https://www.tandfonline.com/doi/abs/10.1179/1743281211Y.0000000080

66. Nandy B, Chandra S, Bhattacharjee D, Ghosh D. Assessment of blast furnace behaviour through softening–melting test. http://dx.doi.org/101179/174328106X94744 [Internet]. 2013 Apr [cited 2023 Mar 25];33(2):111–9. Available from: https://www.tandfonline.com/doi/abs/10.1179/174328106X94744

67. Clout JMF, Manuel JR. Fundamental investigations of differences in bonding mechanisms in iron ore sinter formed from magnetite concentrates and hematite ores. Powder Technol. 2003 Feb 19;130(1–3):393–9.

68. Yang LX, Witchard D. Sintering of Blends Containing Magnetite Concentrate and Hematite or/and Goethite Ores. ISIJ International. 1998;38(1):998.

69. Fernández-González D, Ruiz-Bustinza I, Mochón J, González-Gasca C, Verdeja LF. Iron Ore Sintering: Quality Indices. https://doi.org/101080/0882750820171323744 [Internet]. 2017 Jul 4 [cited 2023 Mar 27];38(4):254–64. Available from: https://www.tandfonline.com/doi/abs/10.1080/08827508.2017.1323744

70. Umadevi T, Nelson K, Mahapatra PC, Prabhu M, Ranjan M. Influence of magnesia on iron ore sinter properties and productivity. http://dx.doi.org/101179/174328109X445741 [Internet]. 2013 Oct [cited 2023 Mar 27];36(7):515–20. Available from: https://www.tandfonline.com/doi/abs/10.1179/174328109X445741

71. Zhang M, Coe MS, Andrade MW. Effect of sinter basicity on sinter productivity and quality with high rate of recycled materials. Drying, Roasting, and Calcining of Minerals [Internet]. 2016 Jan 1 [cited 2023 Mar 31];259–67. Available from: https://link.springer.com/chapter/10.1007/978-3-319-48245-3_32

72. Nicol S, Chen J, Pownceby MI, Webster NAS. A Review of the Chemistry, Structure and Formation Conditions of Silico-Ferrite of Calcium and Aluminum ('SFCA') Phases. ISIJ International [Internet]. 2018 Dec 15 [cited 2023 Mar 31];58(12):2157–72. Available from: https://doi.org/10.2355/isijinternational.ISIJINT-2018-203

73. Wang Y, Ding L, Shi Q, Liu S, Qian L, Yu Z, et al. Volatile organic compounds (VOC) emissions control in iron ore sintering process: Recent progress and future development. Chemical Engineering Journal. 2022 Nov 15;448:137601.

74. Zhang X, Zhong Q, Liu C, Rao M, Peng Z, Li G, et al. Partial substitution of anthracite for coke breeze in iron ore sintering. Springer [Internet]. 123AD [cited 2023 Mar 31];11:1540. Available from: https://link.springer.com/content/pdf/10.1038/s41598-021-80992-4.pdf

75. Zhao JP, Loo CE, Dukino RD. Modelling fuel combustion in iron ore sintering. Combust Flame. 2015 Apr 1;162(4):1019–34.

76. Wong G, Fan X, Gan M, Ji Z, Ye H, Zhou Z, et al. Resource utilization of municipal solid waste incineration fly ash in iron ore sintering process: A novel thermal treatment. J Clean Prod. 2020;263:121400.

77. Lanzerstorfer C, Bamberger-Strassmayr B, Pilz K. Recycling of blast furnace dust in the iron ore sintering process: Investigation of coke breeze substitution and the influence on offgas emissions. ISIJ International. 2015;55(4):758–64.

78. Debrincat D, Loo CE. Factors Influencing Particulate Emissions during Iron Ore Sintering. ISIJ International. 2007;47(5):652–8.

79. Stewart D. Value Generation by Recovering By-Products from Steelmaking Processes Dezincification of Basic Oxygen Steelmaking Slurry [Internet]. 2022 [cited 2023 Mar 26]. Available from: https://cronfa.swan.ac.uk/Search/Results?lookfor=Value+Generation+by+Recovering+By-

Products+from+Steelmaking+Processes%3A+Dezincification+of+Basic+Oxygen+Steelmaking+Slurry&type=AllFields&limit=20&sort=relevance

80. Steer J, Griffiths A, Heinrich T, Thomas A, Barnes C. Correlation of BOS process variables with dust mass formation and zinc content. http://dx.doi.org/101179/1743281213Y0000000152 [Internet]. 2014 [cited 2023 Mar 26];41(7):554–60. Available from: https://www.tandfonline.com/doi/abs/10.1179/1743281213Y.0000000152

81. Dasgupta R, Reddy PSR. Sintering by recirculation of ferrogenous waste. Transactions of The Indian Institute of Metals [Internet]. 2010 [cited 2023 Mar 26];63:859–62. Available from: www.springerlink.com

82. Al-Haji T. Developments in iron ore sintering using a laboratory scaled development platform [Internet]. Swansea University EngD Thesis. 2022 [cited 2023 Mar 26]. Available from: https://cronfa.swan.ac.uk/Search/Results?lookfor=Developments+in+iron+ore+sintering+using+a+laboratory+scaled+development+platform&type=AllFields

83. Roshan V, Kumar K, Kumar R, Nageswara Rao GVS. Preparation of Iron Ore Micro-pellets and Their Effect on Sinter Bed Permeability. Transactions of the Indian Institute of Metals [Internet]. 2018 Sep 1 [cited 2023 Mar 26];71(9):2157–64. Available from: https://link.springer.com/article/10.1007/s12666-018-1347-3

84. Linhares FM, Victor CCF, Lemos LR, Bagatini MC. Effect of three different binders and pellet feed on granulation behaviour of sintering mixtures. https://doi.org/101080/0301923320191659001 [Internet]. 2019 Oct 20 [cited 2023 Mar 26];47(9):991–7. Available from: https://www.tandfonline.com/doi/abs/10.1080/03019233.2019.1659001

85. Pal J. Innovative Development on Agglomeration of Iron Ore Fines and Iron Oxide Wastes. https://doi.org/101080/0882750820181518222 [Internet]. 2018 Jul 4 [cited 2023 Mar 26];40(4):248–64. Available from: https://www.tandfonline.com/doi/abs/10.1080/08827508.2018.1518222

86. Singh PK, Avala Lava K, Katiyar PK, Maurya R. Agglomeration behaviour of steel plants solid waste and its effect on sintering performance. Journal of Materials Research and Technology. 2017 Jul 1;6(3):289–96.

87. Brouwer P. THEORY OF XRF Getting acquainted with the principles. 2003 [cited 2023 Mar 29]; Available from: www.panalytical.com

88. Thermo Scientific Operator's Manual. Dionex Integrion HPIC System. 2016.

89. Balaram V. Microwave plasma atomic emission spectrometry (MP-AES) and its applications – A critical review. Microchemical Journal. 2020 Dec 1;159:105483.

90. Zhan G, Guo Z. Basic properties of sintering dust from iron and steel plant and potassium recovery. J Environ Sci (China) [Internet]. 2013;25(6):1226–34. Available from: http://dx.doi.org/10.1016/S1001-0742(12)60168-5

91. Goodall TM, North CP, Glennie KW. Surface and subsurface sedimentary structures produced by salt crusts.

92. McHugh CM, Groeneveld J, Henderiks J, Renema W, de Vleeschouwer D, Christensen BA, et al. Miocene Wet and Extreme Arid Climatic Conditions in the Southeast Indian Ocean off Western Australia Revealed by the Lithology of Roebuck and Perth Basins. AGUFM [Internet]. 2016 [cited 2022 Sep 2];2016:PP42A-04. Available from: https://ui.adsabs.harvard.edu/abs/2016AGUFMPP42A..04M/abstract

93. Abdioğlu E, Arslan M, Aydinçakir D, Gündoğan I, Helvaci C. Stratigraphy, mineralogy and depositional environment of the evaporite unit in the Aşkale (Erzurum) sub-basin, Eastern Anatolia (Turkey). Journal of African Earth Sciences. 2015 Nov 1;111:100–12.

94. Abrantes FR, Nogueira ACR, Soares JL. Permian paleogeography of west-central Pangea: Reconstruction using sabkha-type gypsum-bearing deposits of Parnaíba Basin, Northern Brazil. Sediment Geol. 2016 Jul 15;341:175–88.

95. Feng L, Li S, Li Y, Li H, Zhang L, Zhai J, et al. Super-hydrophobic surfaces: From natural to artificial. Advanced Materials. 2002 Dec 17;14(24):1857–60.

96. Cores A, Babich A, Muñiz M, Ferreira S, Mochon J. The Influence of Different Iron Ores Mixtures Composition on the Quality of Sinter. ISIJ International. 2010 Aug 15;50(8):1089–98.